

Dissertation
submitted to the
Combined Faculties of the Natural Sciences and Mathematics
of the Ruperto-Carola-University of Heidelberg, Germany
for the degree of
Doctor of Natural Sciences

Put forward by
M. Sc. Rico Jean-André Agnelo Pires
born in: Heidelberg, Germany
Oral examination: July 21st, 2014

Efimov Resonances in an Ultracold Mixture with Extreme Mass Imbalance

Referees: Prof. Dr. Matthias Weidemüller
 Prof. Dr. Selim Jochim

Zusammenfassung. Die vorliegende Arbeit berichtet über die Untersuchung der Wenigteilchenphysik in einem ultrakalten Gasgemisch mit stark unterschiedlichen Massen bei großen Streulängen. Zu diesem Zweck wurde ein neues Experiment für die Erzeugung von quantenentarteten ^6Li und ^{133}Cs Gasen aufgebaut. Darin haben wir 19 interspezies Feshbach Resonanzen in den jeweils zwei Hyperfeinzuständen mit den niedrigsten Energien der beiden Spezies bei Temperaturen im μK Bereich gemessen. Wir verwenden eine *Coupled-Channels* Rechnung, das *Asymptotic Bound-state* Modell, und die *Multichannel Quantum Defect* Theorie um die Positionen der Feshbach Resonanzen zu errechnen und vergleichen diese drei Modelle. Alle Modelle liefern eine konsistente und präzise Beschreibung der Zweikörperstreuresonanzen des Gasgemisches. Dreikörperverlustkoeffizientmessungen im Bereich negativer Streulängen nahe einer breiten Feshbach Resonanz im energetisch niedrigsten Hyperfeinzustand bei Temperaturen von 450 nK weisen zwei aufeinanderfolgende Efimov Resonanzen auf. Die zugehörigen Streulängen ergeben einen Skalierungsfaktor, welcher mit universellen Vorhersagen bei Nulltemperaturen im Resonanzlimit konsistent ist. Die vorliegenden Messungen erlauben zum ersten Mal universelle Wenigteilchentheorien von Mischungen mit unterschiedlichen Massen zu überprüfen.

Abstract. This thesis reports on the investigation of few-body physics in an ultracold mass-imbalanced mixture at large scattering lengths. For this purpose, a new apparatus for the creation of quantum degenerate ^6Li and ^{133}Cs gases has been built. We measure 19 interspecies Feshbach resonances in the two energetically lowest hyperfine channels of each species of an ultracold mixture with temperatures on the μK scale. We apply and compare a coupled-channels calculation, the asymptotic bound-state model, and the multichannel quantum defect theory for the calculation of the Feshbach resonance positions. All models provide a consistent and accurate description of the two-body scattering resonances in the mixture. Three-body loss rate measurements on the negative scattering length side of a broad Feshbach resonance in the energetically lowest hyperfine channel at 450 nK reveal two consecutive Efimov resonances. The scattering lengths assigned to the two Efimov resonances yield a scaling ratio that is consistent with a universal prediction in the zero temperature and resonant limit. The presented measurements provide the first test for universal few-body theories of mixed-species systems with large mass-imbalance.

Parts of the work presented in this thesis are based on the following manuscripts and publications:

- *R. Pires, J. Ulmanis, S. Häfner, M. Repp, A. Arias, E.D. Kuhnle, M. Weidemüller*
Observation of Efimov Resonances in a Mixture with Extreme Mass Imbalance
Submitted, arXiv:1403.7246
- *R. Pires, J. Ulmanis, M. Repp, E.D. Kuhnle, M. Weidemüller, T. G. Tiecke, C.H. Greene, B.P Ruzic, J.L. Bohn and E. Tiemann*
Analyzing Feshbach Resonances- A ${}^6\text{Li}$ - ${}^{133}\text{Cs}$ case study
Manuscript in preparation
- *M. Repp, R. Pires, J. Ulmanis, R. Heck, E.D. Kuhnle, M. Weidemüller, E. Tiemann*
Observation of interspecies ${}^6\text{Li}$ - ${}^{133}\text{Cs}$ Feshbach resonances
Physical Review A **87**, 010701 (2013)
- *M. Repp, R. Pires, J. Ulmanis, S. Schmidt, R. Müller, K. Meyer, R. Heck, E.D. Kuhnle, M. Weidemüller*
A helical Zeeman slower for sequential loading of two elements with large mass difference into optical dipole traps
Manuscript in preparation

In addition, the author has contributed to the following publication:

- *R. Pires, M. Ascoli, E.E. Eyler, P.L. Gould and A. Derevianko*
Upper limit on the magnetic dipole contribution to the $5p - 8p$ transition in Rb by use of ultracold atom spectroscopy
Physical Review A **80**, 062502 (2009)

Contents

1	Introduction	1
2	Creation of Ultracold Li-Cs Mixtures near Quantum Degeneracy	9
2.1	Overview of the Experimental Apparatus	10
2.2	Scheme for Trapping, Cooling and Combining Both Species	26
2.3	Creation of a ^{133}Cs BEC	32
2.4	Creation of a Molecular ^6Li BEC	41
2.5	Requirements for Combination of Both Species at Higher Phase Space Densities	45
3	Analyzing Feshbach Resonances	51
3.1	Measurement of Feshbach Resonances	54
3.2	Formalism for Scattering at Ultracold Temperatures	60
3.3	Three Models for the Calculation of Feshbach Resonances	72
3.4	Application of the models to the ^6Li - ^{133}Cs System	84
3.5	Comparison of the Performance of the Three Models	95
4	Observation of Efimov Resonances	99
4.1	The Efimov Effect	101
4.2	Experimental Procedure for the Detection of Efimov Resonances . . .	120
4.3	Three-Body Loss Coefficient and Atom Loss Measurements	122
5	Conclusion and Outlook	133
	Bibliography	137
	Acknowledgements	159

Chapter 1

Introduction

In the early 1970's, Vitali Efimov made a bizarre and controversial prediction during his study on the quantum mechanical three-body problem. He concentrated on a system of three bosons with equal mass m , at energies sufficiently low to neglect all higher partial waves, hence requiring only the s -wave scattering length a for its description. When at least two pairwise interactions are characterized by $|a| \gg r_0$, where r_0 is the range of the interaction potential, Efimov found that a number of three-body bound states with geometrically spaced binding energies exist in the energy range between $\hbar^2/(mr_0)$ and $\hbar^2/(ma)$, where \hbar is the Planck's constant¹. As $|a|$ increases, more of these bound-states appear, resulting in an infinite amount for $a \rightarrow \infty$ [Efimov, 1970; Efimov, 1971; Efimov, 1979]. Counterintuitively, the trimer states persist even for negative scattering lengths, where no shallow dimer states are supported. Moreover, the size of these trimers also increases for each higher lying state with a universal scaling factor. These findings challenged the former understanding of quantum physics. However, attempts to prove it wrong only resulted in additional proof for this effect [Amado and Noble, 1971; Amado and Noble, 1972], ultimately leading to the acceptance of the theoretical predictions.

Efimov's findings are linked to a remarkable result in the three-body sector, obtained by Thomas in 1935 [Thomas, 1935] during his study on the triton. He considered the case of a generic two particle potential with depth V_0 that only supports a single bound state. In the zero-range limit, i.e. $r_0 \rightarrow 0$ and $V_0 \rightarrow -\infty$, he found that the binding energy of the deepest bound trimer diverges to infinity when the dimer energy is kept fixed. It is outstanding that a potential which only allows for a single two-body bound state supports a trimer state with infinite binding

¹For the remainder of the thesis we follow the commonly known standard notation for the natural constants, and only introduce specific constants where necessary.

energy. This behavior can be ascribed to the large s -wave scattering length $a \gg r_0$ resulting from the zero-range limit. Obviously, in realistic systems, one has to account for short-range effects, which introduce a lower bound for the depth of this three-body bound state.

One of the reasons why the results described above were and still are somewhat difficult to grasp intuitively is the enormous complexity of the three-body problem. In contrast, the two-body problem allows for a much simpler treatment. Due to angular momentum conservation it can be reduced to solving an ordinary second-order differential equation in a single spatial coordinate, allowing for intuitive analytical results. The addition of only one particle increases the degrees of freedom to a point where no general effective mathematical methods exist for the calculation of the resulting second-order partial differential equations in three dimensions. However, profound knowledge of the interactions in simple three-body system is inevitable for the understanding of few- and many-body phenomena arising in samples with a larger atom number. In some cases, for example, the theoretical methods for the description of three-particle interactions could be generalized to predict the behavior of more particles, still described within a few-body approach [Blume and Greene, 2000; Mehta et al., 2009; von Stecher, 2010]. In the many-body sector, the study of three-component fermionic systems provides intriguing prospects for deepening the understanding of many-body effects [Heiselberg et al., 2000; Honerkamp and Hofstetter, 2004; Paananen et al., 2006; Cherng et al., 2007; Zhai, 2007; Rapp et al., 2007; Catelani and Yuzbashyan, 2008; Rapp et al., 2008; Bedaque and D’Incao, 2009]. A remarkable result connecting the two fields is the transition from a few- to a many-body system, as studied by the group of Selim Jochim at the University of Heidelberg. Investigations on a single impurity immersed in a one dimensional Fermi sea with variable atom number have shown how this system evolves from the few- to the many-body regime when adding particles one by one. Surprisingly, the situation is well-described by a many-body calculation already for four (non-impurity) particles [Wenz et al., 2013].

Besides laying the foundation for the understanding of many-body physics, the three-body problem in general is relevant to a variety of systems in many different areas of physics. In the realm of molecular and chemical physics, for example, the three-body problem emerges from applying the Born-Oppenheimer approximation to separate out the electronic motion [Yuan and Lin, 1998; Launay and Dourneuf, 1982; Honvault and Launay, 1998; Cornelius and Glöckle, 1986; Nielsen et al., 1998; Esry et al., 1996b]. This description also finds application in atom-molecule systems [Robicheaux, 1999; Li and Lin, 1999; Yamazaki, 1999]. On much smaller dis-

tance scales, the interaction of three-nucleon systems [Carlson and Schiavilla, 1998] calls for improved models. These can also help understand the behavior of more complex nuclear clusters, that can be approximated by three-body models [Carlson and Schiavilla, 1998; Zhukov et al., 1993; Johannsen et al., 1990; Bang and Thompson, 1992; Fedorov et al., 1994a; Fedorov et al., 1994c; Fedorov et al., 1994b]. Even the neutrons themselves involve interesting three-body problems [Richard, 1992], as they consist of three quarks. The above mentioned examples are not directly connected to the Efimov effect, which occurs only in ensembles with resonant scattering lengths. However, techniques created in this limit might be generalizable to treat non-resonant cases, as well.

A more exotic specimen, which is closer related to the studies by Efimov and Thomas, is the class of Borromean systems [Zhukov et al., 1993], which refers to systems that support a three-body bound state, even though the two-body subsystems do not exhibit bound states. Two conspicuous examples for Borromean states with mass-imbalanced constituents are the ${}^6\text{He}$ and ${}^{11}\text{Li}$ neutron halos [Riisager, 1994; Hansen et al., 1995; Tanihata, 1996] near the neutron drip line, where a ${}^4\text{He}$ or ${}^9\text{Li}$ core, respectively, is surrounded by two loosely bound neutrons.

A specific example for a three-body system where the Efimov effect is expected is the ${}^4\text{He}_3$ trimer, which was incidentally considered the prime candidate for its experimental confirmation [Lim et al., 1977]. The scattering length² of $a = 189 a_0$ is much larger than the effective range $r_s = 14 a_0$ and the van der Waals length $10 a_0$ of the potential. A single two-body bound state with binding energy $E_2 = 1.3 \text{ mK}$ is supported by the potential, whereas two three-body bound states with energies $E_3^{(0)} = 126 \text{ mK}$ and $E_3^{(1)} = 2 \text{ mK}$ have been predicted. The ground state $E_3^{(0)}$ has been observed in 1994 [Schöllkopf and Toennies, 1996], but there is an ongoing discussion whether this state qualifies as an Efimov state (see Sect. 6.8 in Braaten and Hammer, 2006). The excited state $E_3^{(1)}$, which is widely accepted as belonging to the class of universal Efimov states, has not yet been detected. In fact, the Efimov states remained unobserved for 35 years after their prediction in all systems probed, due to a lack of a suitable system with natural parameters that allow for their observation.

The progress in atomic physics stimulated new interest in low energy few- and many-body processes, since in ultracold gases the structure and dynamics are dominated by the mutual interaction and not the entropy. The considerable advantage as compared to the experiments in other subfields of physics is the unprecedented

²For the following discussion of ${}^4\text{He}_3$ we employ the values of the TTY potentials [Tang et al., 1995]. An extensive comparison of different potentials can be found in Braaten and Hammer, 2006.

level of control over all atomic degrees of freedom. Most notably, the binary interaction between particles can be controlled by use of Fano-Feshbach resonances³. The formalism for these energy dependent resonances, which arise due to coupling of a bound-state to the continuum scattering state of two atoms, was independently developed by Herman Feshbach in the context of nuclear physics [Feshbach, 1958; Feshbach, 1962] and by Ugo Fano in the realm of atomic physics [Fano, 1961]. The magnetic field dependence of these resonances relevant for low energy scattering was found by Stwalley, 1976, and Tiesinga et al., 1993 proposed that the resonances can be used to change the value and sign of the *s*-wave scattering length, which is the dominant parameter for the description of interactions in ultracold samples. Feshbach resonances were first observed in ultracold gases in 1998 [Inouye et al., 1998; Courteille et al., 1998], and have since then been applied to control the interactions in a variety of systems (see e.g. Chin et al., 2010 and references therein).

The advance in the experimental study of ultracold interactions goes hand in hand with the progress in the theoretical investigation, with experiments stimulating new theoretical work and vice versa. Particularly the description of two-atom collisions in the sub-mK regime had to be put on solid mathematical footing [Weiner et al., 1999; Gao et al., 2005; Gao, 2008; Mies and Raoult, 2000; Raoult and Mies, 2004; Burke, 1999; Burke et al., 1998], because earlier *ab initio* calculations were not accurate enough for the precise prediction of Feshbach resonances and field dependent scattering lengths. Moreover, typical molecular spectroscopy experiments (e.g. Staunum et al., 2007) did not probe the relevant region near the asymptote of the interatomic potentials, which exhibits a dominant influence on the low-energy scattering behavior. With the appropriate measurement data from ultracold experiments available, these potentials can be refined to the point where an accurate assignment of the magnetic field dependent scattering lengths is obtained. For ⁶Li and ¹³³Cs intraspecies interactions, for example, this has only been achieved recently [Zürn et al., 2012; Berninger et al., 2013]. Even with sufficient experimental data one cannot obtain an exact analytical solution of the Schrödinger equation, as it contains terms that couple to an infinite amount of electronic configurations. However, several approximations from different areas of research on collisional processes are available for tackling this problem.

The most rigorous and straightforward numerical approach is the coupled-channels calculation [Hutson, 1994], which has already been extensively used in the realm of chemistry and chemical physics. However, the calculations typically include a large

³For reasons of brevity we refer to them as Feshbach resonances throughout this thesis.

number of states and are computationally expensive. Often, the physical interpretation of the results are obscure. The analysis of the first measurement of Feshbach resonances between different species [Stan et al., 2004; Gacesa et al., 2008], for example, turned out to be false [Schuster et al., 2012]. Hence, it is useful to compare the results of the numerical calculations with simpler models that allow for much more intuitive insight into the scattering process, while reducing the computational effort enormously.

One such model is the multichannel quantum defect theory [Seaton, 1983], which has been reformulated and adapted to describe all sorts of interactions [Greene et al., 1979; Greene et al., 1982] (see also Croft et al., 2011 and references therein), including the collision between ultracold atom pairs. Its main advantage is the separation of length scales, because at long-range the wavefunctions often take on a simple and known analytical form. Thus, the numerical calculation only has to be performed at short range, where couplings can often be neglected. Additionally, the behavior of the wavefunction in the inner part is smooth, so that it is sufficient to calculate it only for a few energies, and interpolate between these sampling points, often referred to as quantum defects. In some cases, the calculation of one quantum defect describes the scattering behavior near the asymptote and the bound-states excellently.

Another simple way of calculating Feshbach resonance positions is the use of the asymptotic bound-state model [Tiecke et al., 2010]. It is based on earlier work by Moerdijk et al., 1995, and employs only bound-state energies and their wavefunction overlap as adjustable free parameters for the description of Feshbach resonances. Thus, the spatial part of the Schrödinger equation is not explicitly solved and the calculation reduces to a low-order matrix diagonalization. As a result, one can obtain an overview over the expected resonance structure with minimal computational effort.

Besides the advances in the treatment of two-body interactions, tremendous progress has also been made in the description of three-particle interactions in the framework of atomic physics [Botero and Greene, 1986; Bohn et al., 1998; Lin, 1981; Koyama et al., 1989; Zhou et al., 1993; Esry et al., 1996b; D’Incao et al., 2009; Blume and Greene, 2000; Rittenhouse et al., 2010; von Stecher and Greene, 2009]. The interest originates from the fact that atomic systems can be prepared in the energetically lowest state, making inelastic two-body collisions an endothermic process and suppressing the associated losses (see e.g. [Söding et al., 1998; Mies et al., 1996; Leo et al., 1998; Arlt et al., 1998; Guery-Odelin et al., 1998; Hopkins et al., 2000]). Hence, the leading loss mechanism then becomes three-body losses.

These occur in a triatomic scattering event when two atoms form a molecule whose binding energy is carried away by both the molecule and the third atom, resulting in losses from the trap. Formerly viewed as undesirable effect that limits lifetime and stability of condensates, it was the achievement of C.H. Greene and collaborators [Esry et al., 1996a] to find the intimate connection between three-body losses and Efimov physics [Nielsen and Macek, 1999; Braaten and Hammer, 2001; Bedaque et al., 2000; Esry et al., 1999] in the universal regime, where the scattering length is the dominating length scale. It was concluded that the three-body loss rate coefficient L_3 , which behaves as $L_3 \propto C(a)a^4$ in this regime, is subject to periodic modulations in the coefficient $C(a)$. These modulations are caused by the universal three-body bound states predicted by Efimov [Efimov, 1970; Efimov, 1971].

They have first been observed in the group of R. Grimm in Innsbruck [Kraemer et al., 2006] in a sample of ultracold ^{133}Cs atoms. Several other experiments with equal mass systems have subsequently also found evidence for the energetically lowest Efimov state [Gross et al., 2009; Ottenstein et al., 2008; Pollack et al., 2009; Wild et al., 2012; Huckans et al., 2009; Zaccanti et al., 2009; Berninger et al., 2011a; Roy et al., 2013]. The excited state was found in a three-component mixture of ^6Li atoms [Williams et al., 2009], where the interpretation of the Efimov effect is more complex than for a one or two component sample [Braaten et al., 2010]. The scaling factor in this case is the same as for an equal mass system.

For the confirmation of the scale invariance predicted by Efimov, it is necessary to measure a series of at least three Efimov resonances. If the first resonance is found at $a_-^{(0)}$, the N -th excited state can be found at $a_-^{(N)} = a_-^{(0)} \exp(\pi N/s_0)$. This means that for $a_-^{(0)} \sim 1000 a_0$, as is the case for ^{133}Cs , the first excited state is positioned at $a_-^{(1)} \sim 23000 a_0$, since the scaling factor for equal mass bosons is 22.7. In order to probe this regime, one requires an extremely stable magnetic field control, because small field fluctuations at such high a values result in enormous fluctuations of the scattering length, thus lowering the signal from an Efimov resonance due to averaging. Moreover, extremely low temperatures on the order of ~ 1 nK are necessary for the validity of the zero temperature limit. For higher temperatures, the thermal de Broglie wavelength is on the order of $a_-^{(1)}$, and L_3 is unitarity limited [D’Incao et al., 2004]. The Grimm group has reported the measurement of an excited Efimov state in a recent publication [Huang et al., 2014] during the completion of this work, owing to a model [Rem et al., 2013] that allows to take finite temperature effects into account by means of an S-matrix formalism [Efimov, 1979; Braaten et al., 2008]. However, the measurement of a third resonance is too involved for the current temperature and magnetic field control regimes of single species experiments.

Several publications have pleaded for the use of a mass-imbalanced system for the detection of a series of resonances [D’Incao and Esry, 2006; Bloom et al., 2013; Greene, 2010], because here the scaling factor is drastically reduced, e.g. to 4.9 for ${}^6\text{Li}$ - ${}^{133}\text{Cs}$ [Braaten and Hammer, 2006; D’Incao and Esry, 2006], or 6.9 for ${}^6\text{Li}$ - ${}^{87}\text{Rb}$ [D’Incao and Esry, 2006]. Nonetheless, the only mixture that has been employed for the investigation of Efimov resonances up to the time of this work is K-Rb [Barontini et al., 2009; Bloom et al., 2013]. However, the results are not consistent, and the scaling factor of 131 impedes the detection of excited states.

In this thesis, we present the first detection of two consecutive Efimov resonances in a system with extreme mass imbalance via three-body loss rate measurements. To this end, we start by introducing the new experimental apparatus that allows to create ultracold ${}^6\text{Li}$ - ${}^{133}\text{Cs}$ mixtures in Chap. 2. While this apparatus also allows to bring both gases to quantum degeneracy separately, the control of the temperature in a mixture is more involved, as discussed in Sect. 2.5. In Chap. 3 we present experimental data to refine the existing ${}^6\text{Li}$ - ${}^{133}\text{Cs}$ potentials [Staanum et al., 2007] by measuring 19 interspecies Feshbach resonances in the two lowest spin states of each species at temperatures in the μK regime. The resonance positions are analyzed via three different models: The coupled channels calculation, the multichannel quantum defect theory, and the asymptotic bound-state model. All models are consistent and reproduce the resonance positions with sub-G accuracy. Together with 6498 rovibrational transitions from Fourier transform spectroscopy, the resonance positions are used to obtain precise molecular ${}^6\text{Li}$ - ${}^{133}\text{Cs}$ potentials and field-dependent scattering length, which is essential for an accurate analysis of Efimov resonances.

In the last part of the thesis (Chap. 4) we turn to the detection of Efimov resonances. A broad Feshbach resonance in the energetically lowest hyperfine channel allows for an excellent control of the interspecies scattering length. Atom loss features at specific fields provide an indication of three consecutive Efimov states. The time-dependent three-body losses are analyzed by use of a simple model, yielding the three-body loss coefficient L_3 . Two distinct resonances in L_3 mark the position where Efimov states merge into the three free atom continuum. The third resonance is deeply in the unitarity-dominated regime and can therefore not be resolved in our L_3 measurements. The finite temperature might even have an effect on the position of the second resonance. Our measurements provide the first tests for the mass dependence of the universal scaling factor. An assignment of scattering length to the field positions of the two resonances allows us to compare this ratio with theoretical values calculated with simplifying approximations [D’Incao and Esry, 2006; Braaten and Hammer, 2006; Wang et al., 2012b; Esry et al., 2008]. While measured and

calculated ratios are consistent, the error is too large to quantitatively test specific models. Also, there are currently no models that account for possible shifts of the first resonance due to finite range effects or the changing value of the background ^{133}Cs - ^{133}Cs scattering length. The model in Rem et al., 2013 has not yet been implemented for the heteronuclear case in order to account for finite temperature effects. We conclude our discussion by summarizing our results and giving an outlook on future plans and applications for our experiment in Chap. 5.

Chapter 2

Creation of Ultracold Li-Cs Mixtures near Quantum Degeneracy

Parts of this chapter are based on the following publications:

*M. Repp, R. Pires, J. Ulmanis, R. Heck, E.D. Kuhnle, M. Weidemüller, E. Tie-
mann*

Observation of interspecies ^6Li - ^{133}Cs Feshbach resonances

Physical Review A **87**, 010701 (2013)

*M. Repp, R. Pires, J. Ulmanis, S. Schmidt, R. Müller, K. Meyer, R. Heck, E.D.
Kuhnle, M. Weidemüller*

**A helical Zeeman slower for sequential loading of two elements with large
mass difference into optical dipole traps**

Manuscript in preparation

For the experiments discussed in this work, we require a ^6Li - ^{133}Cs mixture at extremely low temperatures and high phase-space densities. A clear observation of Efimov resonances, for example, requires at least temperatures on the order of hundreds of nK. Otherwise, the cross-section for binary s -wave collisions (as derived in Sect. 3.2.1) is limited to $\sigma = 4\pi/k^2$ already at relatively low values of a , which results in unitarity limited three-body loss rates that do not allow to resolve Efimov features (see Chap. 4). For the observation of Feshbach resonances, as demonstrated in Chap. 3, the temperatures only need to be on the order of a few μK , since here it is sufficient to observe losses connected to the increase of the scattering length

without resolving additional structure in the loss feature.

In this chapter, we introduce our approach to the creation and investigation of an ultracold ${}^6\text{Li}$ - ${}^{133}\text{Cs}$ mixture. As we describe our experimental setup extensively in our earlier work [Repp et al., 2013; Repp, 2013; Repp et al., 2014], we only give a coarse overview over the experimental apparatus in Sect. 2.1. Our method for the creation and combination of ultracold ${}^6\text{Li}$ and ${}^{133}\text{Cs}$ gases at temperatures in the μK range, as employed for the detection of Feshbach resonances (Chap. 3), is described in Sect. 2.2. Yet, for the upcoming experiments we need an even colder sample. It is straightforward to bring both species to quantum degeneracy separately, as discussed in Sect. 2.3 for ${}^{133}\text{Cs}$ and Sect. 2.4 for ${}^6\text{Li}$. Bringing the combined species together to the temperatures required for the study of Efimov physics or even to quantum degeneracy, however, is more involved. We discuss the obstacles and describe our approach to overcoming them in Sect. 2.5.

2.1 Overview of the Experimental Apparatus

The main components of our setup for cooling and trapping of ${}^6\text{Li}$ - ${}^{133}\text{Cs}$ mixtures are presented in this section. The different segments of our vacuum chamber, which are required to reach ultra-high vacuum (UHV), are explained in Sect. 2.1.1. The magnetic field coils, which are important for the manipulation of the ultracold atoms, are introduced in Sect. 2.1.2 and an overview of the lasers required for cooling and trapping both atomic species is given in Sect. 2.1.3. We briefly introduce the computer control of the experiment in Sect. 2.1.4 and demonstrate our methods for the extraction of the sample properties in Sect. 2.1.5.

2.1.1 Vacuum Chamber

Experiments with ultracold atoms require ultrahigh vacuum in order to minimize interactions with room temperature background gas particles that lead to atom losses. However, we need to evaporate the condensed samples of ${}^{133}\text{Cs}$ and ${}^6\text{Li}$ in order to load the atoms into optical traps. The temperatures required to reach vapor pressures for sufficient atom fluxes from the ${}^{133}\text{Cs}$ (375 K) and ${}^6\text{Li}$ (625 K) reservoir lead to partial pressures of 10^{-3} and 10^{-5} mbar, respectively. These pressures are several orders of magnitude too high for our experiments with cold atoms, as collisions with the particles of the background gas would prevent loading and storing the cold atoms. To resolve this dilemma, we divide our chamber into different segments, as depicted in Fig. 2.1, in order to control the vacuum conditions in the different

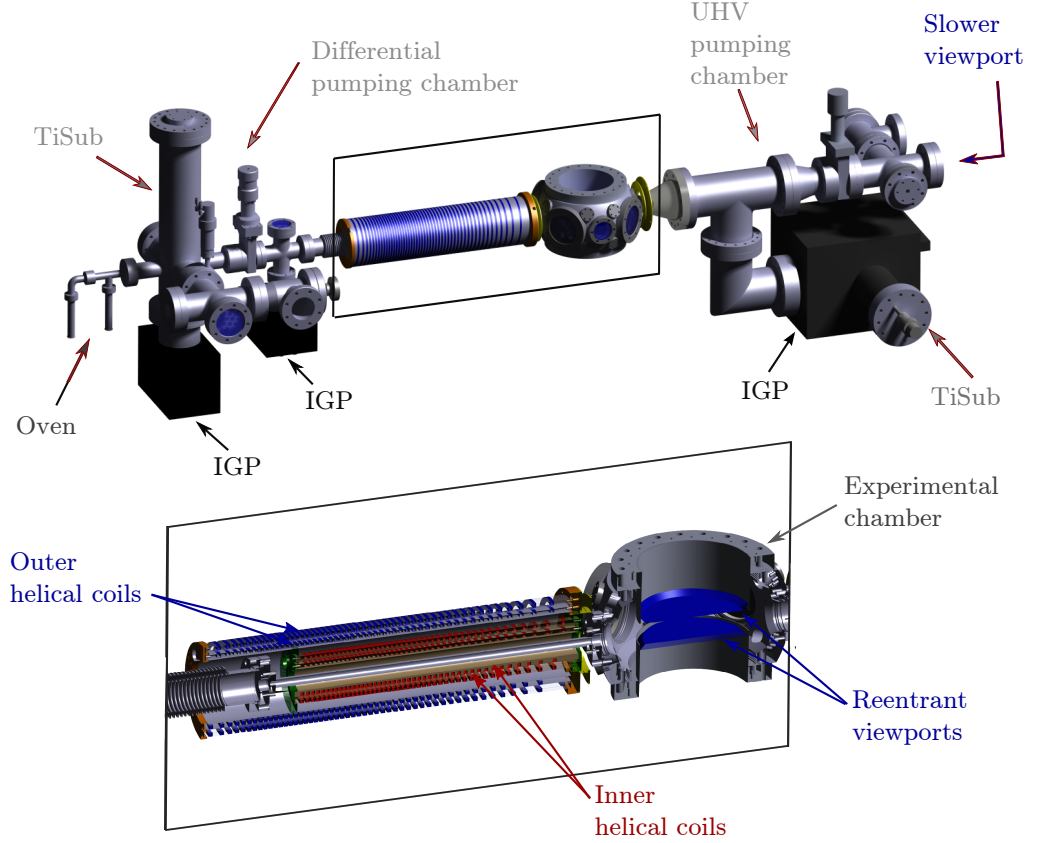


Figure 2.1: Overview of the experimental apparatus. The upper panel gives an overview over the complete setup, the lower channel a zoom into the Zeeman slower and experimental chamber part. The labeled sections of the vacuum setup are described in Sect. 2.1.1. Figure taken from Repp, 2013.

regions individually via the technique of differential pumping.

As a source for the atoms we use a double species effusive oven (see Fig. 2.1), modified from the Ketterle design [Stan and Ketterle, 2005] to account for the ^6Li and ^{133}Cs properties (for details see [Repp, 2013]), which allows for an individual control of the atomic ^6Li and ^{133}Cs fluxes via the temperatures of the separate ^6Li and ^{133}Cs reservoirs. The vapor pressure in this section is regulated by a combination of an ion getter¹(IGP) and a titanium sublimation pump²(TiSub). The oven segment is connected to the next section, the differential pumping chamber, via a 103 mm long tube with 7 mm inner diameter, which limits the flux of particles from the oven section. An additional ion getter pump³ in this chamber leads to a further

¹Starcell, Varian, 75 l/s pumping speed.

²From Varian.

³Starcell, Varian, 45 l/s pumping speed.

reduction of the vapor pressure. The aforementioned components are connected to the main experimental chamber⁴ via a 500 mm long tube with an inner diameter of 10 mm. This section is also used for slowing the atomic beam via light forces (see Sect. 2.1.2). The low vacuum conductivity through this tube and a non-evaporable getter coating [Benvenuti et al., 1999] in the main chamber, which is connected to a UHV pumping chamber that contains an ion getter and titanium sublimation pump⁵, lead to vapor pressures on the order of 10^{-10} mbar and 1/e atom lifetimes of ~ 4 s in the "Experimental chamber" (see Fig.2.1), which is sufficient for the Feshbach spectroscopy experiments in Chap. 3. We speculate that the reason for these relatively high pressures are angle valves with Viton⁶ seals, which were heated above their specified maximum temperature during the bake-out process. Both leaks and outgassing might cause these pressures. As the lifetimes of 4 s are not sufficient for the creation of a ^{133}Cs BEC, we exchange all valves by all-metal valves and remove the gate valve in the UHV section (see Fig. 2.1) for the experiments performed in Sect. 2.3, Sect. 2.4, and Chap. 4. The acquired pressures on the order of $\sim 10^{-11}$ mbar yield 1/e atom lifetimes of ~ 40 s.

The main chamber provides optical access in the horizontal direction via four CF63 and two CF40 viewports. The vertical optical access is ensured by two custom made CF150 reentrant viewports⁷ (see Fig. 2.1), which allow the placement of magnetic field coils at a distance of 19.5 mm from the center point of the chamber (see Fig. 2.2), where the atoms are trapped. All main chamber viewports are anti-reflective (AR) coated for the appropriate wavelengths and are made from Suprasil 3001, which maximizes the transmission of the required high power 1064 nm dipole trap lasers and thus reduces thermal lensing effects. The access for the laser beams that are used to slow the atomic beam emitted from the oven section is provided by the "Slower viewport", as indicated in Fig. 2.1. It is made from high temperature resistant kodial, which allows for heating of this viewport in order to prevent deposition of atoms from the atomic beam. The same AR coating as used for the main chamber viewports has been applied to the slower viewport.

2.1.2 Magnetic Field Coils

Magnetic fields are a main handle for the manipulation of ultracold atoms besides light fields. They are employed for slowing the atomic beam emitted from the

⁴MCF800-EO200080.16, Kimball physics Inc.

⁵VacIon Plus 150 Starcell Kombipumpe, Varian.

⁶From MDC.

⁷Bought from UKAEA Culham.

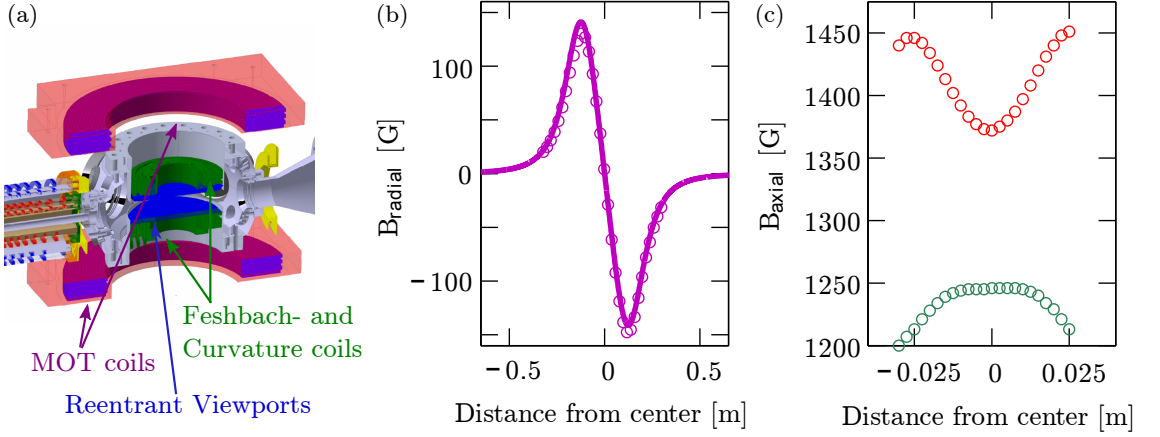


Figure 2.2: Overview of the relevant magnetic field coils. (a) Position of the MOT (violet) and Feshbach and curvature (green) coils with respect to the chamber. (b) The measured (circles) and calculated (solid line) fields of the MOT coils for a current of 97.7 A. (c) The inhomogeneities of the magnetic field of the Feshbach coils at 400 A (red circles) can be compensated for by the curvature coils (green circles) operated at a current of ~ 208 A. Figure taken from Repp, 2013.

oven, cooling and trapping the atoms in a MOT, Raman sideband cooling of ^{133}Cs , selective imaging of different magnetic sublevels, and last but not least for the tuning of intra- and interspecies scattering lengths. The following section introduces the coils that are required for these processes.

- Zeeman slower coils.** The Boltzmann distribution of ^{133}Cs (^6Li) atoms at a typical oven operating temperature of 375 K (625 K) peaks around 400 m/s (1700 m/s). These velocities are about two or three orders of magnitude above typical MOT capture velocities, which are on the order of a few m/s. Therefore, we slow the atomic beam by use of a Zeeman slower. The atoms that are emitted from the oven are illuminated with a laser beam that propagates in the opposite direction of their movement. Absorption of the light leads to momentum transfer in the direction of the laser beam propagation. The momentum an atom acquires from spontaneous emission is zero, when averaged over many emission processes, due to the isotropy of the spontaneous emission process. The resulting net momentum transfer leads to a reduction of the atom velocities. However, since this slowing leads to a change of the Doppler shift, we apply magnetic fields to keep the atoms resonant with the light. The required magnetic field B , which scales as $B \propto \sqrt{1/m}$ [Repp et al., 2014], where m is the atomic mass, is about a factor of five larger for ^6Li atoms as

compared to ^{133}Cs atoms. Instead of using two different slowers, which would limit the optical access to the experimental chamber, we use a construction similar to the one pitch coil presented by Bell and colleagues [Bell et al., 2010]. However, instead of using one coil, we use four interleaved coils (see Fig. 2.1), where the two "Outer helical coils" (operated at a current of 30 A) are designed in a way that results in optimal slowing fields for the ^{133}Cs atoms. All four coils together ("Outer helical coils" and "Inner helical coils"), operated at a current of 75 A, provide the fields necessary to slow ^6Li . This composition allows for a fast switching between the two different configurations of ^6Li and ^{133}Cs . The scheme of the coils is chosen in such a way that the last part of the magnetic field for deceleration is provided by the MOT coils. In order to assure a smooth transition from Zeeman slower to MOT fields, two additional coils are used. One is mounted between the Zeeman slower and the main chamber, the other one is on the opposite side of the main chamber. To remove the heat generated by the high currents, we apply water cooling inside the hollow core wires. For more details on this novel Zeeman slower scheme we refer to Repp, 2013 and Repp et al., 2014.

- **MOT coils.** The quadrupole fields for the MOTs are created by a pair of coils in anti-Helmholtz configuration. A total of 6 layers with 12 windings each, with a minimal radius of 100 mm and a minimal distance to the chamber center of 102 mm, generate gradients of $\partial B_{\text{Cs}}^{\text{axial}}/\partial z = 9.5 \text{ G/cm}$ ($\partial B_{\text{Li}}^{\text{axial}}/\partial z = 31 \text{ G/cm}$) at currents of $I_{\text{Cs}} = 30 \text{ A}$ ($I_{\text{Li}} = 97.7 \text{ A}$) for the ^{133}Cs (^6Li) MOT (see Fig. 2.2(b)). As mentioned earlier, the fields are also used as the last stage of the Zeeman slower. The heat is dissipated by water cooling through the hollow core wire. The time required for switching off the MOT coils from their operating values exceeds 10 ms, a limit which is given by eddy currents in our setup.
- **Compensation cage.** Magnetic stray fields, as well as the earth's magnetic field, are compensated for by three pairs of rectangular coils with dimension $800 \text{ mm} \times 1380 \text{ mm} \times 660 \text{ mm}$. Homogeneous fields of up to 2 G can be created in the center of the cage by 100 windings in one horizontal and the vertical direction and 150 windings in the other horizontal direction at operating currents of 2.5 A. Due to the large number of windings, the inductance of the coils limits the times for switching between different fields to no less than $\sim 20 \text{ ms}$ per 200 mG.

- **Raman coils.** The small magnetic fields required for Raman cooling or fast displacement of the MOT position are created by three pairs of coils that are wound around the CF63 and CF150 viewports of the chamber. While the resulting magnetic fields are not as homogeneous as the ones from the compensation cage, the switching times for a few 100 mG are only on the order $\sim 1\text{-}2$ ms, due to the low winding number of 13 windings. The field created by these coils is typically on the order of $150 - 300$ mG/A.
- **Feshbach coils.** The high field coils for the tuning of the scattering length consist of four windings in axial direction, and six layers in radial direction. The spacing of 5 mm between neighboring windings and layers provides enough space for the glass fiber tube⁸ that is used for electrical isolation. To reduce inhomogeneities, we use a point symmetric design for upper and lower coil. The desired fields of the coils are calculated by use of elliptic integrals [Bergeman et al., 1987], and the appropriate profiles for the inner layers are milled into a peek mount with a CNC milling machine. A low viscosity epoxy is used to glue the wire, and the profiles for the outer layers are milled into the epoxy after an age hardening process. A minimal inner radius of 39.1 mm and a distance from the center of the chamber of 19.5 mm yields fields in the center of the chamber of ~ 1350 G at a current of 400 A. The electric heat is dissipated by pumping water with a pressure of 10 bar through the hollow core wire with a round inner hole of 2.8 mm diameter and a quadratic cross section of $4\text{ mm} \times 4\text{ mm}$. A custom made industrial water cooling unit⁹ stabilizes the temperature of the cooling water to $\Delta T < 0.3$ K, in order to keep changes of the magnetic field due to thermal expansion of the coils to a minimum. The dimension of the coils follow the geometry of the reentrant viewports, which keeps the coils from reaching a Helmholtz configuration. As can be seen in Fig. 2.2(c), the field in the center of the chamber is inhomogeneous. A fit to the measured field values shows that the axial field is well described by the functional form $B_z = B + \alpha B z^2$, where $\alpha = 0.0145\text{ cm}^{-2}$. The field is actively stabilized by using a feedback loop with a current transducer¹⁰ and a PID controller.
- **Curvature coils.** In order to compensate for the inhomogeneities of the Feshbach coil, we place a pair of coils inside the Feshbach coils. Each of the two coils have two windings, two layers, a minimal inner radius of 20.1 mm,

⁸BasTech GSG500.

⁹WKW100, efcooling.

¹⁰LEM IT-600S.

and a distance from the center of the chamber of 20.5 mm. The fields of these coils are curved much stronger than the ones of the Feshbach coils. This can be quantified by a fit of measured field values to the function $B_z = B + \alpha Bz^2$, which yields an order of magnitude larger $\alpha = 0.170 \text{ cm}^{-2}$ as compared to the Feshbach coil. Superposing both fields in opposite directions yields a homogeneous axial field (see green circles in Fig. 2.2(c)) with less than 1 % field deviation over an interval of 1.4 mm in the center on the coil axis. The material, as well as the production, symmetry and cooling procedure is the same as for the Feshbach coils. However, because the MOT coil switching times limit the Raman sideband cooling for the ^{133}Cs atoms, we use the curvature coils in a quadrupole magnetic field configuration in the current setup. The faster switching times of $\sim 1\text{-}2$ ms between different field gradients on the order of 10 G/cm enable an efficient cooling of the ^{133}Cs atoms into the Raman lattice.

2.1.3 Laser Setup for Cooling and Trapping of ^6Li and ^{133}Cs

For the cooling and trapping of the ^6Li and ^{133}Cs atoms we require laser light of several different frequencies, powers and beam waists. In this section we provide an overview on all lasers that are used in our experiments.

^6Li MOT lasers

The light for the cooling of ^6Li is generated by a commercially available fiber coupled external cavity diode laser ¹¹(ECDL) at 671 nm (referred to as "Li TA"), which is internally amplified by a tapered amplifier (TA) chip. The output power of ~ 200 mW is used to create the cooling and repumping beams for MOT and slower, and for absorption imaging of the atoms when no magnetic fields are present. We frequency stabilize this laser 166 MHz below the $2^2S_{1/2} |f = 1/2\rangle \rightarrow 2^2P_{3/2}$ transition via frequency modulation spectroscopy [Bjorklund et al., 1983] (see Fig. 2.3). The choice of this frequency allows us to generate the required frequencies for transitions of the two different hyperfine sublevels of ^6Li by use of acousto-optic modulators¹²(AOMs). A detailed overview over the frequencies are presented in Fig. 2.3, and for more details on the optical setup we refer to the diploma thesis of Romain Müller [Müller, 2011]. Due to slow offset drifts of the error signal, possibly induced by temperature drifts, we change to a modulation transfer locking scheme [McCarron et al., 2008] for

¹¹Toptica TA pro 671.

¹²From Crystal Technologies and IntraAction Corp.

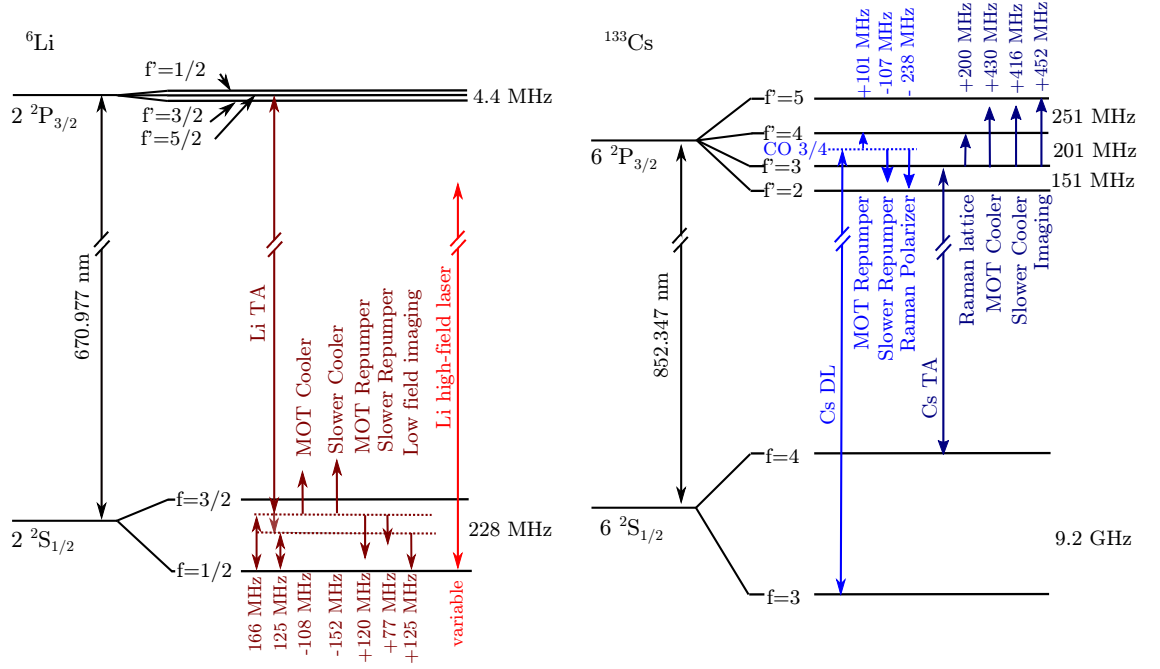


Figure 2.3: Overview of the frequencies required for cooling ${}^6\text{Li}$ and ${}^{133}\text{Cs}$.

The frequency shifts generated by AOMs are indicated. For further details see Sect. 2.1.3. Figure adapted from Repp, 2013.

the experiments shown in Sect. 2.3, Sect. 2.4 and Chap. 4. The details of this setup are presented in the master's thesis of Stephan Häfner [Häfner, 2013]. The light with a frequency corresponding to the $2^2S_{1/2} |f=1/2\rangle \rightarrow 2^2P_{3/2}$ ($2^2S_{3/2} |f=3/2\rangle \rightarrow 2^2P_{3/2}$) transition is referred to as repumping (cooling) light. In order to observe the atom number and distribution at high magnetic fields or to expel one of the hyperfine magnetic sublevels from the trap, we employ a homemade ECDL [Salzmann, 2007] with ~ 15 mW output power, which is stabilized to the Li TA via a tunable offset lock [Schünemann et al., 1999], as described in the master's thesis of Robert Heck [Heck, 2012]. This laser is replaced by a more stable, commercially available fiber coupled ECDL¹³ of 12 mW output power for the experiments presented in Sect. 2.4 and Chap. 4.

${}^{133}\text{Cs}$ MOT lasers

Due to the large hyperfine splitting of ${}^{133}\text{Cs}$ of 9.2 GHz [Steck, 2008], we use two different lasers for the cooling and repumping transitions. An amplified fiber coupled ECDL¹⁴ at a wavelength of 852 nm with ~ 400 mW output power is used for the

¹³Toptica DL pro 671.

¹⁴Toptica TA pro 852.

transitions originating from the $6^2S_{1/2} |f = 4\rangle$ state (cooling laser). It is stabilized via modulation transfer spectroscopy [McCarron et al., 2008] to the $6^2S_{1/2} |f = 4\rangle \rightarrow 6^2P_{3/2} |f' = 3\rangle$ transition, and the desired frequencies are generated by four AOMs, driven by the frequencies indicated in Fig. 2.3. For the transitions originating from the $6^2S_{1/2} |f = 3\rangle$ state (repumping laser) we use a fiber coupled ECDL¹⁵ at a wavelength of 852 nm with ~ 70 mW output power, which is stabilized via frequency modulation spectroscopy to the $6^2S_{1/2} |f = 3\rangle \rightarrow 6^2P_{3/2} |X_{34}\rangle$ transition, where X_{34} denotes the spectroscopy crossover peak between the $6^2P_{3/2} |f' = 3\rangle$ and $6^2P_{3/2} |f' = 4\rangle$ state. Due to fluctuations of the error signal background, we change this spectroscopy to modulation transfer spectroscopy for the experiments presented in Sect. 2.3 and Chap. 4, as given in the master's thesis of Arthur Schönhals [Schönhals, 2013]. Here, we also use AOMs to create the desired laser frequencies, as illustrated in Fig. 2.3. Specifics to this setup as used in Chap. 3 can be found in Stefan Schmidt's diploma thesis [Schmidt, 2011]. The experiments presented in Chap. 4 apply high-field imaging of ^{133}Cs . Contrary to the case of ^6Li , there is no closed transition for the ^{133}Cs atoms in the energetically lowest state at sufficiently high magnetic fields. Thus we use two different lasers, where one is used for pumping the atom population into the $|f = 4, m_f = 4\rangle$ state (see also Sect. 2.1.5), and another one is used for the absorption imaging (see Sect. 2.1.5) of this state. Both lasers are offset locked to the cooling and repumping lasers following the scheme presented in Schönhals, 2013. However, due to the large linewidth of the DBR lasers¹⁶ employed in Schönhals, 2013, only a part of the imaging light is on resonance, which reduces the effective absorption cross section and thus the imaging signal. To resolve this, we exchange the imaging laser by a ECDL¹⁷ with an approximately factor of ten narrower line width in this work.

Optical distribution system for diode laser light

All the above mentioned diode lasers are placed on an optical table next to the one containing the vacuum setup. The light is delivered to the experiment by use of optical fibers. All the beams needed for cooling ^6Li are superposed and distributed by a custom made fiber port cluster¹⁸. The light for imaging of lithium is also delivered to the vertical axis of our main chamber through this cluster (see right panel of Fig. 2.4 "AbsorbI"), however, the linear polarization inside the fiber is

¹⁵Toptica DL pro 852.

¹⁶Laser diode: SDL-5712-H by Spectra Diode Lasers Inc.

¹⁷Radiant Dyes NarrowDiode 852.

¹⁸Delivered by Schäfter&Kirchhoff.

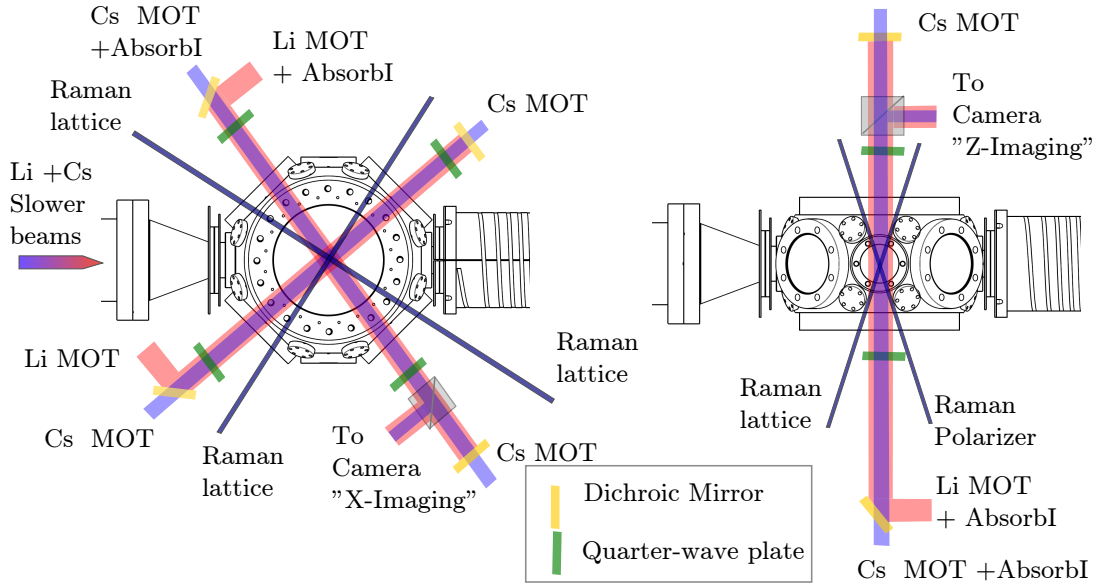


Figure 2.4: Arrangement of beams for optical cooling of ^6Li and ^{133}Cs . A top view (left) and side view (right) is shown. See text for a detailed description. Figure taken from Repp, 2013.

perpendicular to the one of the MOT light. For the horizontal imaging we use a separate fiber, because of difficulties with a stable polarization in the fiber port cluster (see also left panel of Fig. 2.4 "AbsorbI"). The ^{133}Cs MOT and imaging light is also distributed by a fiber port cluster¹⁹ in the same manner, but unlike the ^6Li MOT, which uses a retro-reflected three beam configuration, here we use a six beam configuration, as we have ample power available. The Zeeman slowing cooling and repumping beams, as well as the optical pumping beam for the Raman cooling are delivered by three separate fibers, while the beams for the Raman lattice use another fiber port cluster²⁰. As we require certain sections of the viewports for the Raman sideband cooling and dipole traps beams, we superpose the ^{133}Cs MOT beams with those of ^6Li using dichroic mirrors²¹ (see Fig. 2.4) before entering the science chamber, in order to reduce the optical access used by these beams. The circular polarization is generated by quarter-wave plates²² optimized for both wavelengths, namely 671 nm and 852 nm. The arrangement of all the beams with respect to the chamber is summarized in Fig. 2.4.

¹⁹See footnote 18.

²⁰See footnote 18.

²¹Custom made from Laser Components.

²²Custom made from Doehrer Elektrooptik GmbH.

Dipole trap lasers

Because the temperatures available by optical cooling techniques are fundamentally limited (see e.g. [Metcalf and van der Straten, 1999]), we also perform forced evaporative cooling [Ketterle and van Druten, 1996] in optical dipole traps [Grimm et al., 2000] in order to reach temperatures below these limits. The working principle of these traps is based on the interaction of a polarizable atom with an alternating electric field of the trapping beam with amplitude \mathbf{E} . The induced dipole moment \mathbf{d} of the atom leads to a potential $U_{\text{dip}}(x, y, z) = -\frac{1}{2}\mathbf{d} \cdot \mathbf{E} = \frac{1}{2\epsilon_0 c} \text{Re}[\alpha(\omega)] I(x, y, z)$, where $\alpha(\omega)$ is the polarizability of the atom and $I(x, y, z)$ the intensity of the light. The trapping potential can be rewritten in terms of laser frequency ω as [Grimm et al., 2000]

$$U_{\text{dip}}(x, y, z) = -\frac{3\pi c^2}{2\omega_0^3} \left(\frac{\Gamma}{\omega_0 - \omega} + \frac{\Gamma}{\omega_0 + \omega} \right) I(x, y, z). \quad (2.1)$$

For the laser frequencies used in our experiment, the underlying assumption that the detuning from the atomic resonance frequency ω_0 is much larger than the natural linewidth Γ is justified. From Eq. (2.1) it is evident that for a red detuned ($\omega < \omega_0$) laser beam the potential minimum lies in the beam focus, which enables the trapping of atoms at this position. As the confinement along the direction of the beam is typically orders of magnitude wider than the transversal confinement, we use a crossed dipole trap (CDT) configuration, where a second beam enforces the trapping along the first beam's propagation direction.

In thermal equilibrium the atoms confined in a CDT only probe the bottom of the potential. Here, $U_{\text{dip}}(x, y, z)$ can be approximated by harmonic potential

$$U_{\text{dip}}(x, y, z) = \frac{1}{2}m(\omega_x^2 x^2 + \omega_y^2 y^2 + \omega_z^2 z^2), \quad (2.2)$$

where ω_x, ω_y and ω_z are referred to as trapping frequencies. The thermal density distribution, which follows the Boltzmann distribution $n(x, y, z) = n_0 \exp(-U(x, y, z)/k_B T)$ [Grimm et al., 2000] at a temperature T , where n_0 is the peak density, can then be written as

$$n(x, y, z) = n_0 \exp\left(-\frac{x^2}{2\sigma_x^2}\right) \exp\left(-\frac{y^2}{2\sigma_y^2}\right) \exp\left(-\frac{z^2}{2\sigma_z^2}\right), \quad (2.3)$$

with

$$\sigma_i = \omega_i^{-1} \sqrt{k_B T / m}. \quad (2.4)$$

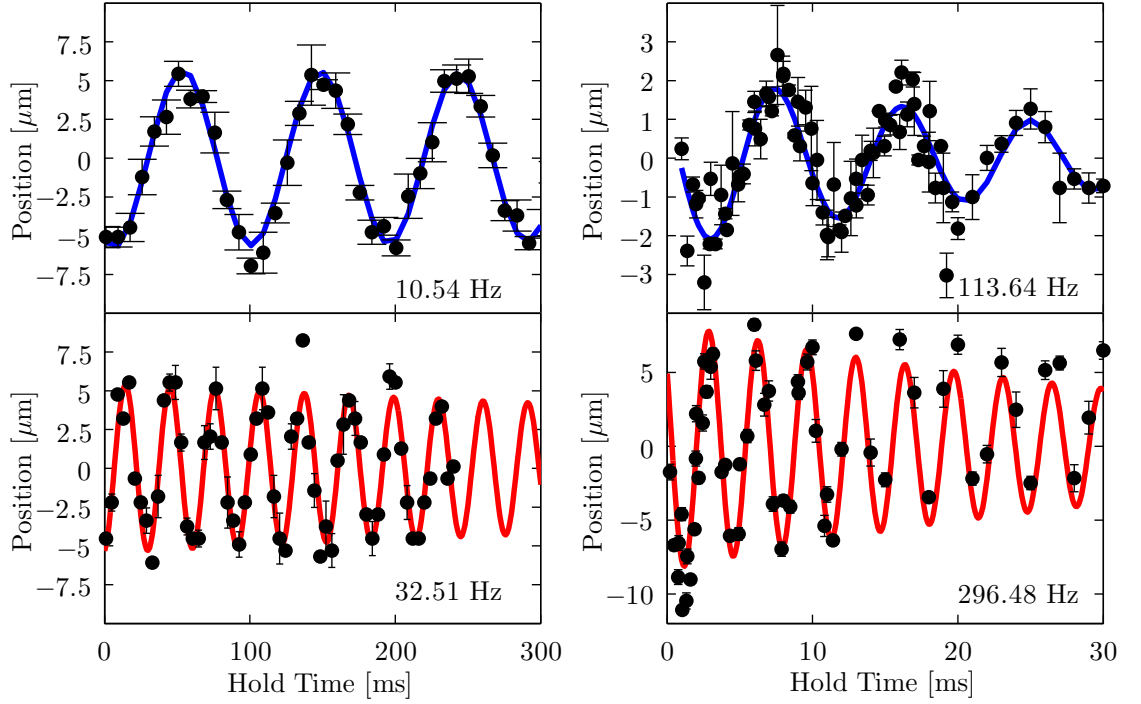


Figure 2.5: Oscillations of ${}^6\text{Li}$ and ${}^{133}\text{Cs}$ in the dipole trapping potential.

The data points show the center position of the cloud and the solid lines are a damped sine fit to determine the ${}^6\text{Li}$ (red) and ${}^{133}\text{Cs}$ (blue) trapping frequencies in the axial (left) and radial (right) direction of the cigar shaped trap at 200 mW. The resulting trap frequencies are also given for each scenario. In cases where more than one data point was taken, the mean value is shown and the error bars represent the standard error.

In order to calculate the peak density

$$n_0 = N \bar{\omega}^3 \left(\frac{m}{2\pi k_B T} \right)^{3/2}, \quad (2.5)$$

with the mean trapping frequency $\bar{\omega} = \sqrt[3]{\omega_x \omega_y \omega_z}$ and total atom number N , we fit the trapping frequencies to oscillations in our traps. For this purpose, we load a sample at a lower trap depth and quickly ramp up the laser power to the value of interest. The resulting oscillations of the center position of the density distribution are illustrated in Fig. 2.5 for the trap laser powers used in Chap. 4.

Due to the specific requirements of trapping frequencies, beam sizes and wavelengths, we use the following dipole traps in the experiments performed in this thesis:

- **Li high power/ ${}^{133}\text{Cs}$ dimple trap.** Because the momentum recoil $p = \hbar k$

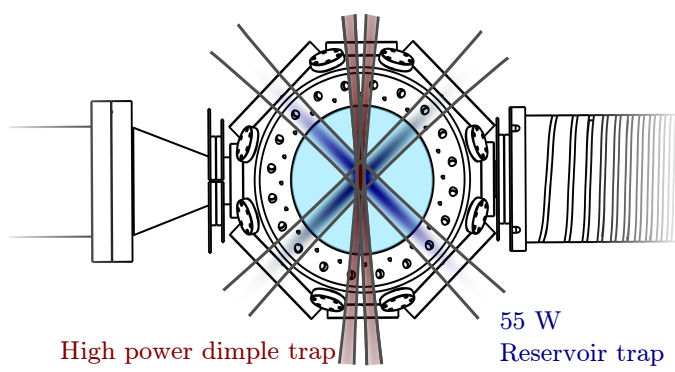


Figure 2.6: Top view on the arrangement of dipole trap beams. The dimple trap beams are shown in red, the Cs reservoir trap in blue. The tune-out wavelength trap will be superposed with the high power dimple trap at a later stage. The figure is adapted from Ref. [Repp, 2013].

from spontaneous emission results in large atom velocities in a ${}^6\text{Li}$ -MOT due to the low mass, the lowest achievable temperatures are limited to $\sim 200\text{--}300\ \mu\text{K}$ [see e.g. Metcalf and van der Straten, 1999]. In order to create a sufficient trapping potential that is able to capture a large fraction of MOT atoms, we use a commercially available Yb doped fiber laser²³ with 200 W output power at 1070 nm for our dipole trap. Two crossed beams (see Fig. 2.6) at an angle of $\sim 8.4^\circ$ with $60\ \mu\text{m}$ waists yield a trapping depth of 1.6 mK, which is sufficient to capture a few million atoms from the MOT. This design has proven to be successful for the evaporative cooling of ${}^6\text{Li}$ to the quantum degenerate regime and is adapted from the group of Prof. Selim Jochim at the University of Heidelberg (see [Ottensstein, 2010; Lompe, 2011]). More details on our setup can be found in Robert Heck’s master’s thesis [Heck, 2012]. Aside from the evaporative cooling of lithium, we also use this trap for the combined loading of ${}^6\text{Li}$ and ${}^{133}\text{Cs}$ in Sect. 2.2 and Sect. 4.3 in order to measure Feshbach and Efimov resonances, respectively. In Sect. 2.3 we apply this trap at low powers for a local increase in phase-space density via the dimple trick [Stamper-Kurn et al., 1998; Pinkse et al., 1997] for ${}^{133}\text{Cs}$, which allows us to create a BEC. Hence we also refer to it as dimple trap.

- **Cs reservoir trap.** The ${}^{133}\text{Cs}$ atoms can be optically cooled to temperatures below $1\ \mu\text{K}$, and therefore only require trapping depths of about $10\ \mu\text{K}$ for capturing them in a CDT. However, with a background scattering length of $\sim 2000\ a_0$, large three-body loss rates [Weber et al., 2003a] are expected.

²³IPG YLR-200-LP-WC.

Since these scale with $\propto n^3$, we keep the ^{133}Cs densities on the order of $\sim 10^{11}$ atoms/cm by using a large volume reservoir trap. Two crossed beams with $\sim 300\ \mu\text{m}$ beam waist and 90° crossing angle (see Fig. 2.6), derived from an amplified Nd:YAG solid-state laser²⁴ with 55 W output power at 1064 nm, provide suitable trapping potentials for this purpose. The trap is characterized in the master's thesis of Alda Arias [Arias, 2014], and is implemented for the condensation of ^{133}Cs , as presented in Sect. 2.3. This trap is also used for a separate loading of displaced ^{133}Cs atoms in Chap. 4.

- **Tune-out wavelength trap.** In Sect. 2.5 we show that the trapping potentials from the dimple laser differ strongly for ^6Li and ^{133}Cs (see also Fig. 2.12). Thus, the atomic species with higher temperature can heat the other species via collisions, which leads to atomic losses of the latter. Another complication is the fact that the potential gradient associated with the gravitational force on the heavier ^{133}Cs leads to a shift of the equilibrium position of ^{133}Cs . Thus, at low potential depths the spatial overlap is drastically reduced. These obstacles can be overcome by use of a so called tune-out wavelength trap [LeBlanc and Thywissen, 2007], frequency stabilized to a wavelength of 880 nm, which is blue detuned from the D_1 and red detuned from the D_2 line of ^{133}Cs . The potential contributions from the two transitions cancel and the ^{133}Cs atoms experience no trapping force. However, heating still arises due to the scattering of photons, which limits the lifetime of the sample. Since this frequency is red detuned for the ^6Li D_1 and D_2 transitions, this dipole trap, derived from a titanium sapphire laser²⁵ with ~ 3 W output power, acts as a species selective trap for the manipulation of ^6Li . It can be used, e.g. to shift the equilibrium position of ^6Li in order to increase the overlap of both species at low temperatures. The design is presented in Stephan Häfner's master's thesis [Häfner, 2013]. In Sect. 2.5 we present results of proof-of-principle experiments to verify that this laser does not provide a trapping force for ^{133}Cs and can thus be used in a scheme for the combination of both species.

2.1.4 Computer Control of the Experimental Sequence

We require precise control and timing of all involved equipment and parameters during our experiments. For this purpose we employ a homemade²⁶ modular FPGA

²⁴Coherent Mephisto MOPA.

²⁵Coherent MBR-110 pumped by a Verdi V-18.

²⁶By the Electronics Workshop of the Physikalisches Institut, Universität Heidelberg.

design with a 100 MHz internal clock and < 100 ns jitter. The upload of the sequence parameters and timings is handled by a LabView interface²⁷.

2.1.5 Detection of the Sample Properties

The relevant information of our experiments is extracted after each individual experimental cycle by means of absorption imaging [Ketterle et al., 1999]. This is done by recording three pictures with a CCD²⁸ camera either from a horizontal or vertical perspective (see Fig. 2.4 "X-Imaging" and "Z-Imaging"). The first picture contains the intensity distribution $I_{abs}(x, y)$ of a light beam that has passed through a cold atomic cloud, where absorption has occurred. The second picture records the intensity distribution $I_{div}(x, y)$ of the laser light without atoms present, and the third picture consists of the intensity distribution $I_{back}(x, y)$ on the camera pixels when no laser light is present. Following Beer's law, the transmission $T(x, y)$ of an incident beam with intensity $I_0(x, y)$ is given by

$$T(x, y) = \frac{I(x, y)}{I_0(x, y)} = \frac{I_{abs}(x, y) - I_{back}(x, y)}{I_{div}(x, y) - I_{back}(x, y)} = e^{-\sigma \int n(x, y, z) dz}, \quad (2.6)$$

where $I(x, y)$ is the intensity distribution after absorption. The atomic column density $n(x, y) = \int n(x, y, z) dz$, which contains the integration along the propagation axis z of the incident beam, is related to the transmission via the formula

$$n(x, y) = -1/\sigma \ln[T(x, y)], \quad (2.7)$$

where σ denotes the absorption cross section, given by $\sigma_{Cs} = 3.468 \cdot 10^{-9} \text{ cm}^2$ [Steck, 2008] and $\sigma_{Li} = 2.150 \cdot 10^{-9} \text{ cm}^2$ [Gehm, 2003] for imaging at zero magnetic offset fields. The projection of circularly polarized light propagating perpendicular to the magnetic field axis leads to a reduction by a factor of four in the case of high-field imaging of ^6Li [Heck, 2012]. In order to obtain atom number N and $1/e^2$ cloud radii Δ_x, Δ_y , we fit the following equation to the observed column density:

$$n(x, y) = \frac{N\sigma}{\sqrt{2\pi}\Delta_x\sqrt{2\pi}\Delta_y} e^{-[\alpha(x-x_0)^2 + 2\beta(x-x_0)(y-y_0) + \gamma(y-y_0)^2]}, \quad (2.8)$$

where $\alpha = \frac{\cos^2(\theta)}{2\Delta_x^2} + \frac{\sin^2(\theta)}{2\Delta_y^2}$, $\beta = -\frac{\sin(2\theta)}{4\Delta_x^2} + \frac{\sin(2\theta)}{4\Delta_y^2}$ and $\gamma = \frac{\cos^2(\theta)}{2\Delta_y^2} + \frac{\sin^2(\theta)}{2\Delta_x^2}$. Here, (x_0, y_0) denote the coordinates of the cloud center, and θ denotes the angle between

²⁷Written by Juris Ulmanis and Hanna Schempp.

²⁸Guppy-38B from Allied Vision Technology

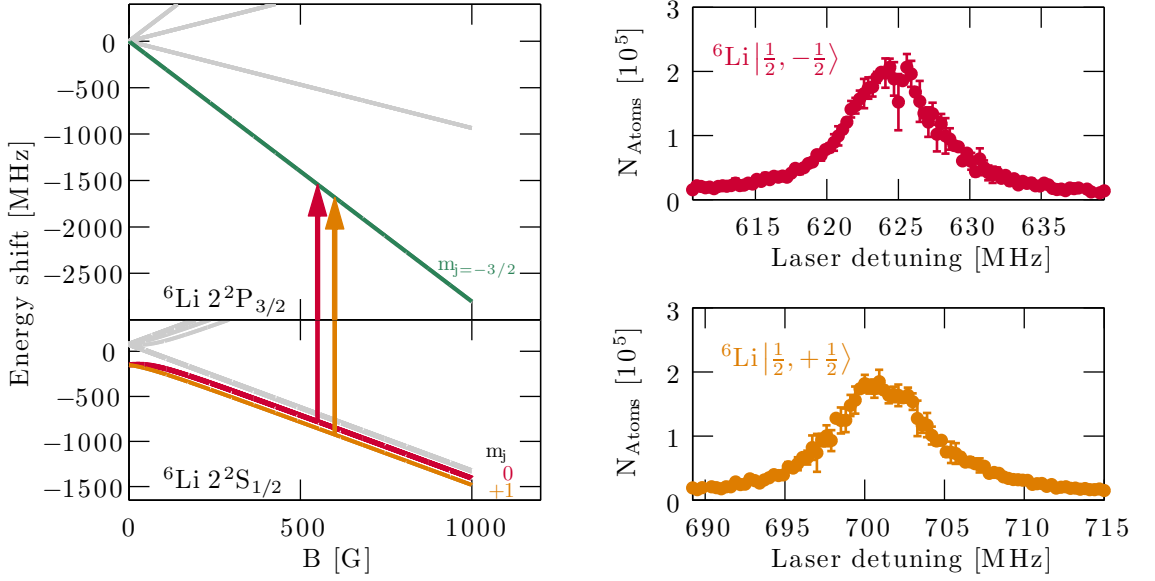


Figure 2.7: Spin selective detection of ${}^6\text{Li}$ at high magnetic fields The shift of levels in the ${}^6\text{Li } 2^2\text{S}_{1/2}$ and ${}^6\text{Li } 2^2\text{P}_{3/2}$ states in dependence of magnetic field is given on the left. The transition used for spin selectively removing and imaging atoms in the $m_j = 0$ ($m_j = 1$) state, corresponding to the $|1/2, -1/2\rangle$ ($|1/2, +1/2\rangle$) state at zero magnetic field, is indicated by a red (orange) arrow. The frequency dependent atom number at a magnetic field of 507.9 G, corresponding to atoms in $|1/2, -1/2\rangle$ ($|1/2, +1/2\rangle$) state is depicted in the right upper (lower) panel (data points are taken from Heck, 2012). The figure is taken from Ref. [Repp, 2013].

the axis from camera to cloud center and the normal axis of the camera. The time t dependent cloud sizes after free ballistic expansion allow us to determine the temperature T of the cloud via the relation

$$\Delta_{x/y}(t) = \sqrt{\frac{T k_B}{m} t^2 + \Delta_{x/y}(t=0)}. \quad (2.9)$$

In cases where we apply magnetic fields on the order of 800 G, we use the ${}^6\text{Li}$ high field imaging laser (see Sect. 2.1.3) in order to directly image the atoms in that field region. The magnetic field dependent energies for the lowest levels, as well as their quantum numbers m_J , which are good quantum number in the Paschen-Back regime, are depicted in Fig. 2.7. We also show the transitions we use for the detection and the dependence of the recorded atom number from the detuning of the high field imaging laser in this figure. More details on this are presented in the master's thesis of Robert Heck [Heck, 2012]. The measurement of three-body loss coefficients of ${}^{133}\text{Cs}$ uses a high-field imaging scheme in order to detect atoms at

fields of about 850 G. The field dependent energies and the transitions utilized for this are shown in Fig. 2.8.

2.2 Scheme for Trapping, Cooling and Combining Both Species

With the experimental setup and methods being introduced in the last section, we are now set to describe our experimental sequences for the production of the ultracold mixture at μK temperatures, which is the starting point for the Feshbach resonance measurements presented in Chap. 3. We discuss the individual steps of the creation of our cold ${}^6\text{Li}$ sample in Sect. 2.2.1. In Sect. 2.2.2 we show how we load a ${}^{133}\text{Cs}$ sample and combine it with ${}^6\text{Li}$.

2.2.1 Magneto Optical Trapping and Forced Evaporation of ${}^6\text{Li}$

We start the preparation of the mixture by loading $\sim 10^8$ atoms in 1 s into a ${}^6\text{Li}$ MOT. Three retro-reflected beams (see Fig. 2.4) with $1/e^2$ diameters of 25 mm and about 3 mW in each of the cooling and repumping beams²⁹ are employed for MOT loading, and a total of 34 mW of light for cooling and repumping transitions are guided to the Zeeman slower (for frequencies see Fig. 2.3). After MOT loading, we turn off the slower coils and beams, and wait for 20 ms before we ramp down the MOT coils from 16 G/cm to 0 G/cm within 20 ms. At the same time we ramp up the curvature coils from 0 G/cm to 28 G/cm in order to compress the MOT and move the atoms to the center of the curvature coil. After another 20 ms, the detuning is reduced to approximately half a natural linewidth, as this minimizes the temperature [Metcalf and van der Straten, 1999], and the power of the cooling (repumping) light is reduced to 0.2 mW (0.05 mW) to reduce heating related to photon scattering. This scheme is summarized in Fig. 2.9.

We turn off the repumping laser 200 μs before the cooling laser, in order to optically pump the atoms into the $2^2S_{1/2} |f = 1/2\rangle$ state. Simultaneously we turn on the ${}^6\text{Li}$ high power trap at 150 W, thus providing a trapping potential of 1.6 mK for the 300 μK cold MOT, which is sufficient to capture $\sim 2 \times 10^6$ atoms. Forced evaporation within 900 ms to a laser power of 0.9 W at a field of 760 G yields a temperature of $T_{\text{Li}} = 2.5 \mu\text{K}$ after 200 ms of plain evaporation and thermalization.

²⁹All involved laser powers are listed in great detail in Repp, 2013.

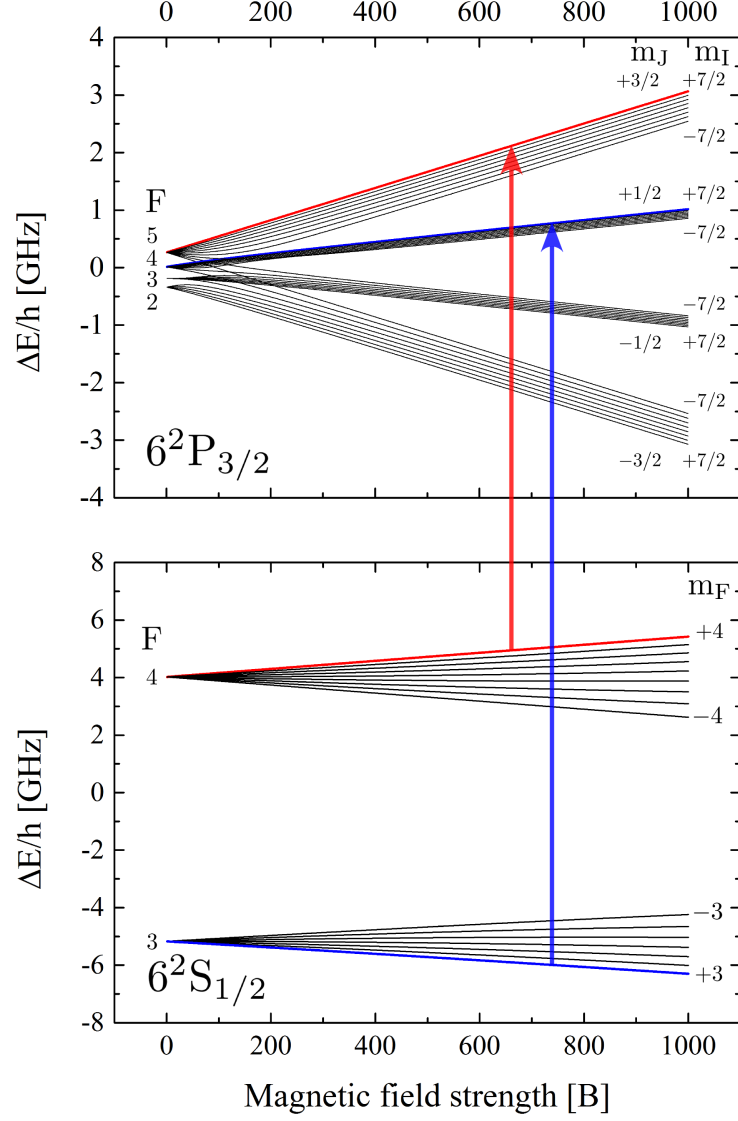


Figure 2.8: Zeeman splitting of ^{133}Cs energy levels at high magnetic fields.

The energies for the $6^2S_{1/2}$ (lower panel) and the $6^2P_{3/2}$ (upper panel) are plotted as a function of magnetic field. The transitions used for imaging (red arrow) and optical pumping (blue arrow) are also shown. Figure taken from Schönhal, 2013.

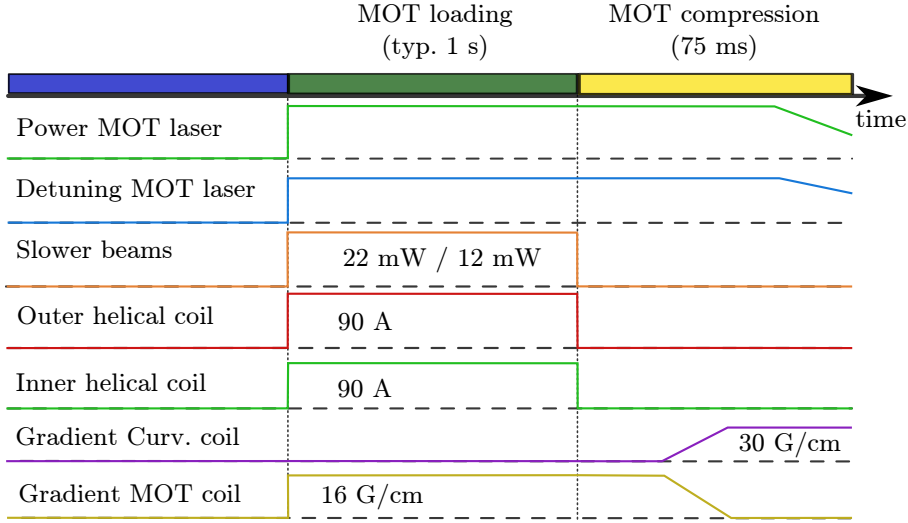


Figure 2.9: Scheme for loading and compressing a ^6Li MOT. For a description of the steps see text.

Before we load the ^{133}Cs atoms, we now slowly ramp up the power to 1.8 W within 100 ms. The fact that the trap depth scales linearly with laser power for an adiabatic ramp, while the temperature scales with the square root of the power, allows for a deeper confinement of the ^6Li atoms in the trap. It turns out that this is necessary to prevent losses due to the subsequent switching of magnetic field gradients during ^{133}Cs MOT loading, which affect the ^6Li trapping potentials.

2.2.2 Cooling of ^{133}Cs and Creation of a ^6Li - ^{133}Cs Mixture

With the ^6Li atoms confined in a CDT at low power, we now want to add ^{133}Cs into the trap. Due to the known problems of inelastic collisions between ground state ^6Li atoms with excited state ($6^2P_{3/2}$) ^{133}Cs atoms [Schlöder et al., 1999], we displace the position of the ^{133}Cs MOT by ~ 1 mm via a small magnetic offset field in the horizontal direction. We load 10^7 atoms in 50 ms in a six beam MOT with $1/e$ diameters of 20 mm and $\sim 7 - 14$ mW (0.5 mW) laser power in the cooling (repumping) beams and 18 mW (3 mW) in the Zeeman slower cooling (repumping) beam. After loading the MOT, we turn off the Zeeman slowing beams and coils, wait for 30 ms and perform a compression phase [DePue et al., 2000], where the MOT coils are ramped from 10 G/cm to 0 G/cm within 5 ms, while the curvature coil is ramped up from 0 G/cm to 22 G/cm within 20 ms. The last step allows us to exchange the MOT for the curvature coils enabling us to switch off the gradient field faster (see Sect. 2.1.2), which is advantageous for the subsequent degenerate Raman sideband cooling cycle. At the same time the cooling (repumping) power

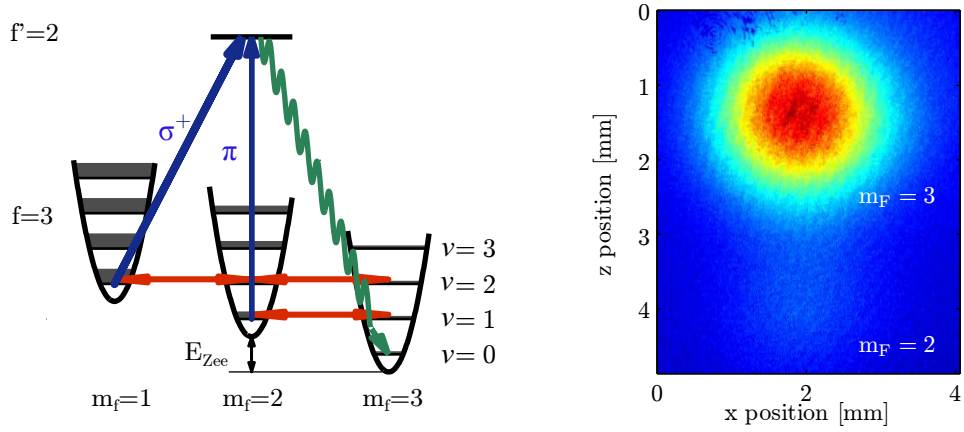


Figure 2.10: Degenerate Raman-Sideband Cooling. Left: Scheme for DRSC.

The pumping by σ_+ and π -polarized light is shown as blue arrows, the spontaneous decay as green arrow. The Raman transitions between degenerate states are indicated as red arrows. The splitting between different Zeeman levels is given by E_{Zee} . Figure inspired by Kerman et al., 2000 and adapted from Repp, 2013. Right: Absorption image of the Stern-Gerlach type experiment after DRSC. Approximately 85% are prepared in the $|3, 3\rangle$ state and the remaining fraction mainly populates the $|3, 2\rangle$ state. Figure adapted from Repp, 2013.

is decreased to 4 mW (0.05 mW) and 5 ms later the detuning is increased from 20 MHz (0 MHz) to 96 MHz (10 MHz) within 25 ms [Drewsen et al., 1994] in order to achieve temperatures on the order of $10 \mu K$. We turn off all fields and optically pump the atoms into the $6^2P_{3/2}, f = 3$ manifold by turning off the repumping laser before the cooling laser.

With these optimized starting conditions we load the atoms with 2 ms delay into a so called Raman lattice created by four linearly polarized beams (see Fig. 2.4) with ~ 30 mW power per beam at ~ 9 GHz detuning³⁰. After 1 ms we add a 10 MHz red detuned³¹ pumping beam of $\sim 100 \mu W$ power (see "Raman polarizer" in Fig. 2.4) with circular polarization in order to perform three dimensional degenerate Raman sideband cooling (DRSC) following the approach by the Stanford group [Kerman et al., 2000; Treutlein et al., 2001]. The fields of ~ 100 mG, which are required to bring the excited vibrational $|f = 3, m_f = 3, \nu = 1, 2\rangle$ states of ~ 100 kHz spacing into degeneracy with the lower lying vibrational $|3, 2, \nu = 0, 1\rangle$ and $|3, 1, \nu = 0\rangle$ states (see Fig. 2.10), is generated by the Raman coils (see Sect. 2.1.2). Via the

³⁰Derived from the cooling laser as shown in Sect. 2.1.3

³¹The detuning compensates light shifts that are caused by the lattice.

compensation cage we slightly tilt the absolute magnetic field vector away from the Raman coil axis, which effectively adds a π -polarization component to the pumping beam. The strong σ^+ -component of the pumping beam allows for pumping from the $|3, 1, 0\rangle$ into the $|3, 2, 0\rangle$ and $|3, 3, 0\rangle$ via the $6^2P_{3/2}, f' = 2$ state. The vibrational quantum number does not change during this pumping cycles, as the system is in the Lamb-Dicke regime, where the spacing between vibrational levels on the order of 100 kHz is much larger than the recoil energy of 2 kHz [Steck, 2008]. Atoms that decay to the $|3, 2, 0\rangle$ states are in a dark state for light of this polarization, however, the weak π -polarized component pumps these atoms into the $|3, 3, 0\rangle$ state. The atoms in the higher vibrational $|3, 3, \nu = 1, 2\rangle$ and $|3, 2, \nu = 1\rangle$ states are transferred to the degenerate $|3, 1, 0\rangle$ or $|3, 2, 0\rangle$ levels via Raman transitions induced by the lattice beams (indicated by the red arrows in Fig. 2.10). Thus, the only remaining dark state is the lowest vibrational $|3, 3, 0\rangle$ state.

Due to the Gaussian shape of the lattice beams, atoms that are captured in the wings of the beam experience lower vibrational lattice spacings than atoms in the center and are therefore not efficiently cooled. We resolve this by ramping down the magnetic fields and laser powers in 2 ms following 20 ms of DRSC, which reduces the temperature and optimizes the optical pumping. As the potential energy of the $|3, 1, 0\rangle$ state is lower than the other states with $\nu = 0$, the photon from the spontaneous emission effectively removes energy on the order of the lattice spacing from the kinetic energy of the atoms. Thus, we acquire a sample of 10^6 atoms at temperatures of $\sim 1 \mu\text{K}$. While all other hyperfine sublevels are subject to rapid loss due to inelastic two-body collisions [Guéry-Odelin et al., 1998; Söding et al., 1998], the energetically lowest $|3, 3\rangle$ state is the only stable state, owing to the fact that only elastic two-body scattering processes are energetically allowed. A summary for a typical MOT loading, compression and DRSC process, similar to the one described above, is given in Fig. 2.11.

We check the degree of polarization by performing a Stern-Gerlach type experiment. We levitate the atoms in the $|3, 3\rangle$ state after DRSC. After a short time of separation, where the atoms in the $|3, 2\rangle$ states fall down due to gravitation, we image the clouds and fit two Gaussians to the two clouds in Fig. 2.10. We determine that 85 % (15 %) of the population is in the $|3, 3\rangle$ ($|3, 2\rangle$) state. The small population in the energetically higher state adds additional channels for the Feshbach resonance spectroscopy, and allows us to observe further Feshbach resonances (see Sect. 3.1), which enables a more precise calculation of the underlying molecular potentials (see Chap. 3).

During the DRSC we ramp the power of the dipole trap back down to 0.9 W

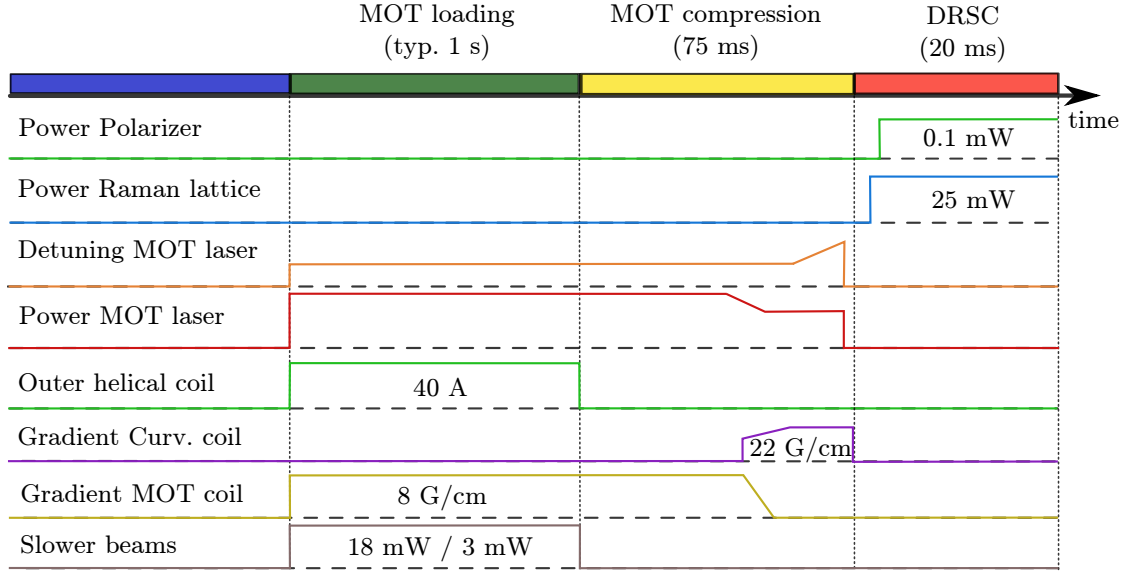


Figure 2.11: Scheme for loading and compressing a ^{133}Cs MOT with subsequent DRSC. For a description of the steps see text.

within 50 ms. We apply a magnetic offset field of 81 G shortly after switching of the optical pumping beam in order to provide a magnetization axis to keep the atoms polarized in the $|3,3\rangle$ state. 5 ms later we turn off the lattice beams and load the atoms into the dipole trap, which already contains ^6Li . The spatial extension of the ^{133}Cs cloud is larger than the width of the dipole trap beams, thus heating the atoms at the edge of the trap by converting potential energy to kinetic energy. The observed oscillations along the weak axis of the trapping potential damp out within 125 ms.

At this point we have 5×10^4 (2×10^5) ^{133}Cs (^6Li) atoms at temperatures of 8 μK (2 μK). This difference in temperature can be explained by the factor of four between the polarizabilities of the two species at a wavelength of 1070 nm, which leads to a difference in trapping potentials, as depicted in Fig. 2.12 and further discussed in Sect. 2.5. In order to measure the trapping frequencies, we prepare the sample at lower laser powers and abruptly ramp up to 0.9 W. This leads to oscillations, which we observe by varying the hold time before imaging the atoms. The obtained trapping frequencies of $\omega_{\text{Cs}}/2\pi = (380, 380, 30)$ Hz and $\omega_{\text{Li}}/2\pi = (900, 900, 65)$ Hz yield peak densities of $n_{\text{Cs}} = 3 \times 10^{11} \text{ cm}^{-3}$ and $n_{\text{Li}} = 1 \times 10^{12} \text{ cm}^{-3}$.

The ^6Li sample still contains a mixture of the $2^2S_{1/2}|1/2, +1/2\rangle$ and $2^2S_{1/2}|1/2, -1/2\rangle$ states. We first remove one of the two in order to unambiguously assign the observed Feshbach resonances in Chap. 3 to the appropriate channel. This is done via optical light forces by illuminating the sample for 800 μs with resonant light from the offset

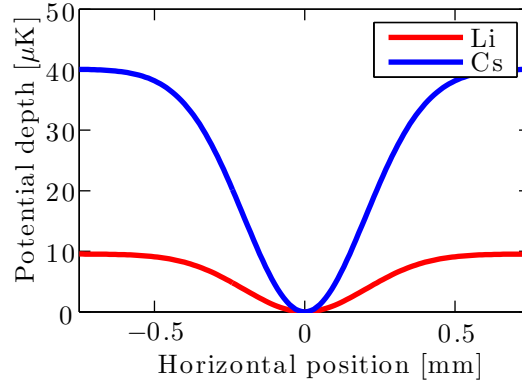


Figure 2.12: Optical trapping potentials for ${}^6\text{Li}$ (red) and ${}^{133}\text{Cs}$ (blue) at a laser power of 0.9 W in the dimple trap. The ${}^{133}\text{Cs}$ (${}^6\text{Li}$) temperature is $8\ \mu\text{K}$ ($2\ \mu\text{K}$) during the Feshbach resonance measurements. The difference in temperature is caused by the difference in trapping potentials, owing to a factor of four between the polarizabilities of ${}^{133}\text{Cs}$ and ${}^6\text{Li}$. Figure taken from Repp, 2013.

locked ${}^6\text{Li}$ high field imaging laser (see Sect. 2.1.3 and Fig. 2.7). We perform this procedure at a field of 530 G, where the scattering length between the two states is zero [Jochim et al., 2002; O’Hara et al., 2002], which minimizes heating of the atoms in the non resonant state.

The loading procedure of the mixture is schematically summarized in Fig. 2.13, and for a more detailed description we refer to the PhD thesis of Marc Repp [Repp, 2013]. The sample prepared in the way described above provides excellent starting conditions for Feshbach resonance measurements.

2.3 Creation of a ${}^{133}\text{Cs}$ BEC

For some experiments, lower temperatures are desirable. These cannot be obtained easily in the mixture (see Sect. 2.5). For a single species, however, the reduction of temperature down to quantum degeneracy is straightforward. The ${}^{133}\text{Cs}$ atom is very well suited for laser cooling techniques [Kastberg et al., 1995; Boiron et al., 1996], because of the large mass and hyperfine splitting. Hence, it was originally predicted to be the first atom to reach Bose-Einstein condensation [Monroe et al., 1993]. However, this prediction could not be fulfilled due to several subtleties in the ${}^{133}\text{Cs}$ - ${}^{133}\text{Cs}$ collisional behavior. The first attempts employed the magnetically trappable stretched $|4, 4\rangle$ state, where spin-exchange collisions are prohibited. It turned out that the second-order spin-orbit interaction is greatly enhanced in ${}^{133}\text{Cs}$, which results in inelastic loss-rates that impede Bose-Einstein condensation [Söding et al., 1998;

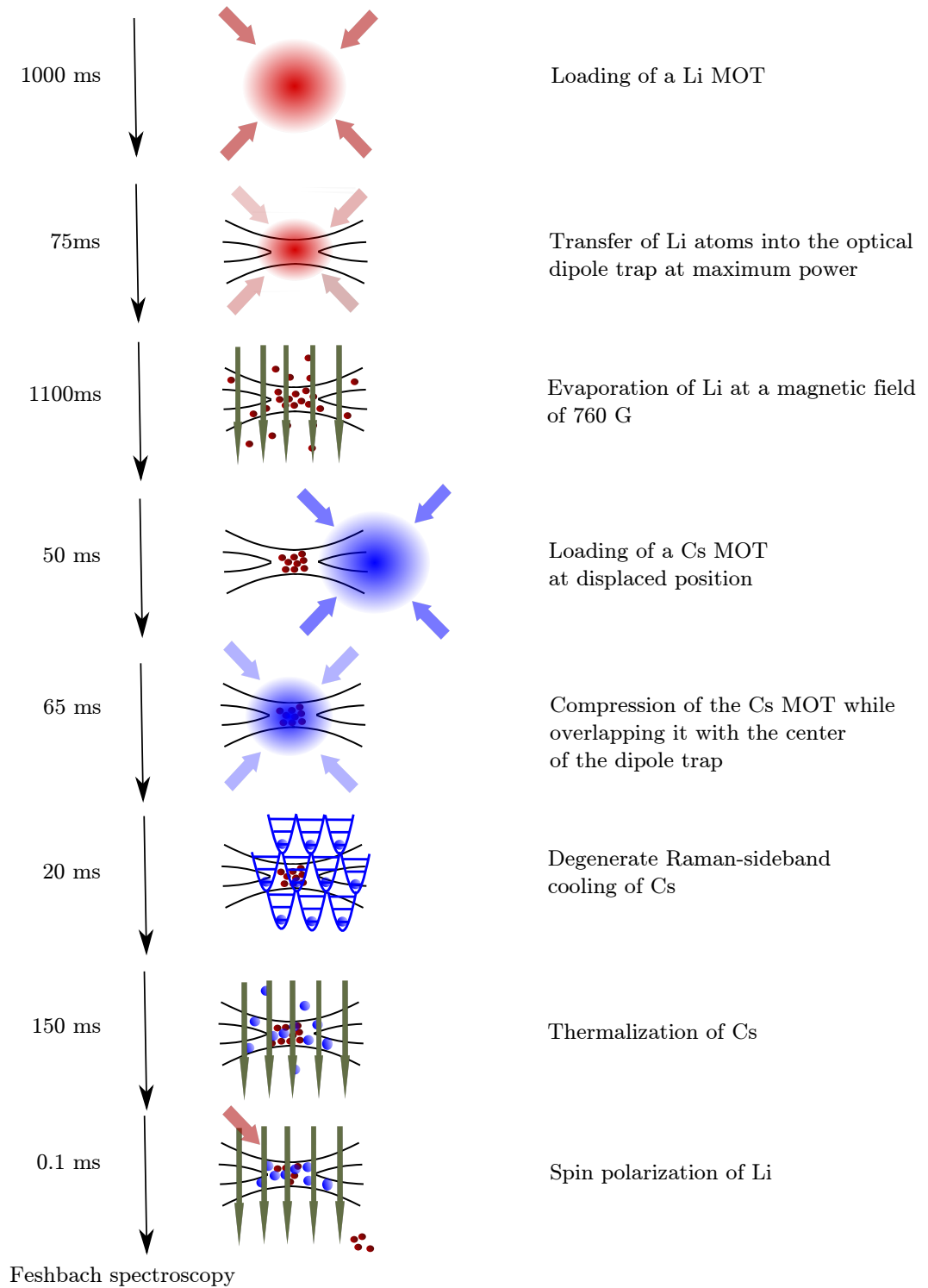


Figure 2.13: Scheme for combining ^6Li and ^{133}Cs . For a description of the steps see text. Figure taken from Repp, 2013.

Mies et al., 1996; Leo et al., 1998; Arlt et al., 1998]. A change to the $|3, -3\rangle$ state, where hyperfine changing collisions are avoided, only brought the sample within two orders of magnitude of quantum degeneracy. High inelastic collision rates also prevented these experiments from reaching quantum degeneracy [Guery-Odelin et al., 1998; Hopkins et al., 2000]. The first creation of a ^{133}Cs BEC was reported in Weber et al., 2003b, where the $|3, 3\rangle$ state was used in connection with an optical reservoir trap and a tightly focused dimple trap [Stamper-Kurn et al., 1998]. The former had to be sufficiently large in order to keep the ^{133}Cs density n_{Cs} low, because the large background scattering length with a magnitude of $\sim 2000 a_0$ would otherwise cause fast three-body losses which scale as n_{Cs}^3 . As it turned out, a three-body recombination minimum due to the Efimov effect was coincidentally used for achieving a sufficient ratio of elastic to inelastic collisions [Kraemer et al., 2006]. A later experiment presented a different approach, where the reduction of the magnetic field levitation gradient, instead of the optical trap depth, was used to evaporatively cool the atoms and reach Bose-Einstein condensation [Hung et al., 2008]. Initial attempts in our group did not succeed to reproduce the latter results, mainly because the reported trap parameters and trapping frequencies are not consistent [Repp, 2013]. Therefore, we present a new approach, which employs elements of both concepts. The experimental procedure for this method is discussed in Sect. 2.3.1 and the results are presented in Sect. 2.3.2.

2.3.1 Experimental Scheme for the Creation of a ^{133}Cs BEC

We start our experiments by loading a ^{133}Cs MOT followed by Raman sideband cooling which yields 2×10^7 atoms at $\sim 1 \mu\text{K}$. As these steps essentially follow the procedure given in Sect. 2.2.2 we do not give further details. We turn on the ^{133}Cs reservoir trap (see Sect. 2.1.3) at 4 W and a magnetic levitation gradient of 31 G/cm, 2 ms before we switch off the Raman lattice beams. As this gradient leads to an anti-trapping potential in the horizontal direction, we ramp up the homogeneous fields of the Feshbach coils to 70 G, where their field curvature (see Fig. 2.2) approximately cancels the anti-trapping effect of the gradient field. A detailed explanation of this process is given in Repp, 2013. The scattering length at 70 G is on the order of $1000 a_0$, which allows for fast thermalization. The three-body losses do not play a significant role, as the densities in this trap are sufficiently low, and the trap is only used as a reservoir for the subsequent loading of a dimple.

At this stage we also ramp up the dimple laser (see Sect. 2.1.3) to a power of 300 mW within 100 ms. This creates a dip in the total optical potential consisting

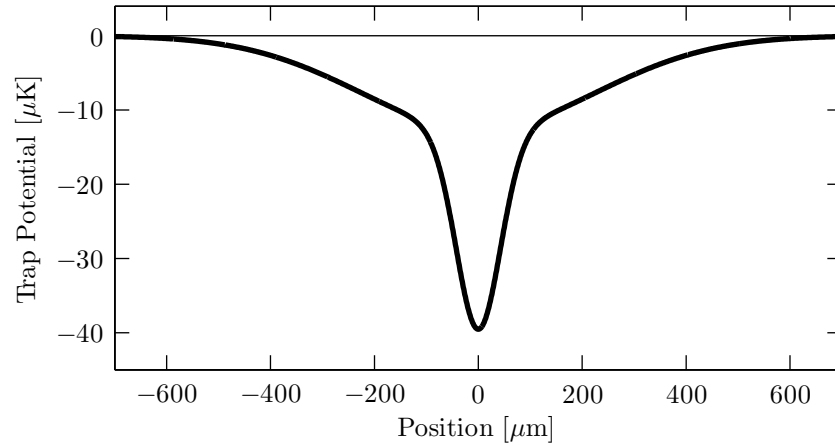


Figure 2.14: Trap potential for ^{133}Cs reservoir and dimple trap. A horizontal cut through the trap center is shown. The broad component of the trapping potential results from the reservoir trap, the narrow feature in the center from the dimple trap.

of both traps, as shown in Fig. 2.14. While the density is locally increased, the atoms in the dimple are still in thermal contact with the atoms in the reservoir trap, thus increasing the phase-space density locally. More details on this concept are given in Pinkse et al., 1997 and Hopkins et al., 2000. After additional 600 ms of thermalization and plain evaporation, we obtain a cloud of 2×10^6 atoms at temperatures of $1 \mu\text{K}$.

Instead of following the scheme of Weber et al., 2003b, where the optical power is reduced for forced evaporation, we linearly reduce the magnetic-field gradient to 29.8 G/cm within 1 s. This is similar to the scheme of Hung et al., 2008 and allows to maintain high trapping frequencies, which results in faster thermalization rates. As we ultimately want to optimize the loading into the dimple trap, where the peak density is much higher as compared to the reservoir, we reduce the homogeneous offset field to 22.8 G . At this field, the scattering length is only $\sim 300 a_0$. A three-body recombination minimum due to an Efimov resonance [Kraemer et al., 2006] provides high collision rates with minimal three-body losses at the high densities of the atoms in the dimple. In a second ramp, we completely turn off the magnetic field gradient within 1100 ms in order to efficiently load the dimple trap, since the reservoir does not exhibit a trapping potential without a gradient field applied. At this point we are left with 4×10^5 atoms at temperatures of 800 nK in the dimple trap. The reservoir trap laser is turned off, and the dimple trap power is reduced to 200 mW within 500 ms, yielding 2×10^5 atoms at $\sim 200 \text{ nK}$. In a last step, we reduce the power within 2 s to a variable end value P_{end} between 120 mW and

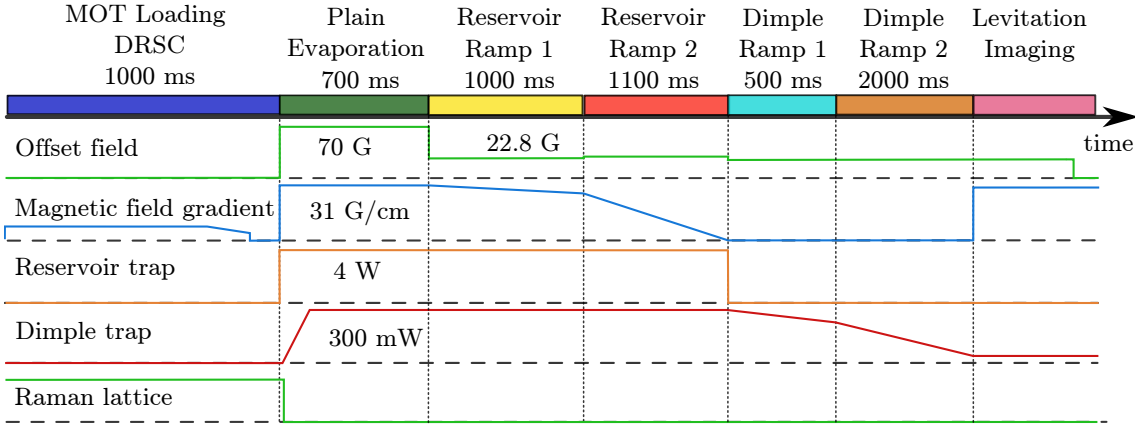


Figure 2.15: Experimental sequence for loading of a ^{133}Cs BEC. Schematic diagram for the timings of selected parameters. For more details see text.

140 mW. Depending on the magnitude of P_{end} , the sample is either on the onset of quantum degeneracy for higher laser intensities, or deeply in the BEC regime for lower values. For the detection of the density distribution, we turn on the levitation gradient in order to allow the atoms to expand for long time-of-flights, while still remaining in the imaging region. The homogeneous field is set to a value near the zero crossing of the scattering length at 17 G, where the mean-field effects are reduced (see Sect. 2.3.2). After 70 ms of expansion we image the cloud at zero field, by turning off the offset field shortly before the imaging pulse. This sequence is summarized in Fig. 2.15. The final results of these experiments and a characterization of the evaporation process are given in the next section.

2.3.2 Characterization of the Evaporation Process and the ^{133}Cs BEC

Bose-Einstein condensation occurs when the thermal de Broglie wavelength

$$\lambda_{dB} = \frac{h}{\sqrt{2\pi\mu k_B T}} \quad (2.10)$$

is on the order of the mean interparticle spacing $n^{-1/3}$. The phase-space density (PSD)

$$D = n\lambda_{dB}^3 \quad (2.11)$$

reaches unity for this case. The macroscopic occupation of the sample's ground state can best be understood by considering the mean occupation number [Mandl, 1988]

$$N_\nu = \frac{1}{e^{(\epsilon_\nu - \mu)/(k_B T)} - 1}, \quad (2.12)$$

of a single-particle state ν with energy ϵ_ν , where the chemical potential μ is fixed by $N = \sum_\nu N_\nu$. N_ν is much less than unity for high temperatures, as the particles distribute among many energy levels. This also means that the chemical potential is much less than the ground-state energy ϵ_0 . When the temperatures are lowered, μ rises, since N must be conserved. The maximum value it can take must be below ϵ_0 , because else the particle number in the ground-state would be negative or diverging, which is unphysical. For $\mu \rightarrow \epsilon_0$ the sum of the occupation numbers in the excited states ($\nu \geq 1$) takes on its maximum value

$$N_{ex,max} = \sum_{\nu=1}^{\infty} \frac{1}{e^{(\epsilon_\nu - \epsilon_0)/(k_B T)} - 1}. \quad (2.13)$$

The onset of Bose-Einstein condensation occurs when the temperature drops below the temperature T_C where $N_{ex,max} < N$. The atoms that are not in the excited states populate the ground-state macroscopically. The critical temperature for this distinct phase-transition is given by

$$T_C = 0.94 \frac{\hbar \bar{\omega}}{k_B} N^{1/3} \quad (2.14)$$

for a gas of noninteracting atoms in a harmonic trap. The condensate fraction $f_C = N_0/N = 1 - (T/T_C)^3$ for a harmonically trapped gas also depends on this parameter. However, the temperature would not be a good criterion to characterize the progress of the condensation procedure, as it depends on atom number and trap frequencies, which are subject to change during evaporation. A more suited parameter is the peak phase-space density

$$D_P = N \left(\frac{\hbar \bar{\omega}}{k_B T} \right)^3, \quad (2.15)$$

which is acquired by inserting Eq. (2.5) into Eq. (2.11). When T_C is introduced into this expression, we obtain the critical value $D_P \approx 1.202$ for Bose-Einstein condensation. Eq. (2.15) is independent of parameters that vary in the course of the experiment. Thus, D_P will be used as a benchmark for the condensation procedure.

We measure the temperature via time-of-flight measurements (see Eq. (2.9)) and the trap frequencies via the method explained in Sect. 2.2.2 at each of the evaporation steps. The results for D_P after each step are shown in Fig. 2.16(a) as a function of time t , where $t = 0$ denotes the start of the MOT loading. A total of 6.3 s is required to create a ^{133}Cs BEC. For the final PSD value at 6.3 s in Fig. 2.16 we chose a sample directly at the phase transition to a BEC.

Efficient evaporation occurs when the fraction of lost atoms is small compared to the fractional increase in phase-space density. Fig. 2.16(b) shows the evolution of D_P as a function of atom number. A quantitative way of examining the efficiency of the evaporation process is to consider the evaporation efficiency [Ketterle and van Druten, 1996]

$$\Gamma = \frac{\ln \frac{D}{D_0}}{\ln \frac{N_0}{N}}, \quad (2.16)$$

where D_0 and N_0 denote the phase-space density and atom density before the evaporation ramp, respectively, and D and N give these quantities after the ramp. This parameter gives a measure on the orders of magnitude gain in phase-space density in comparison to an order of magnitude loss in the atom number. In our experiment, the timings for all evaporation ramps were experimentally determined to optimize Γ . We also varied the homogeneous offset fields from 21.7–25 G during the evaporation in the dimple, which also has an influence on Γ , as it changes the scattering length and recombination rate. We show Γ for each step in the evaporation in Fig. 2.16(b).

In order to understand the density distribution of the trapped gas, we consider the general many-body Schrödinger equation in second quantization for interacting bosons. A simplified ansatz for its solution was proposed in Bogoliubov, 1947 using a mean-field approach and a decomposition of the boson field operator

$$\hat{\Psi}(r, t) = \phi(r, t) + \hat{\Psi}'(r, t) \quad (2.17)$$

into its expectation value $\phi(r, t) = \langle \hat{\Psi}(r, t) \rangle$, which is also referred to as order parameter or condensate wavefunction. The first-order perturbation term $\hat{\Psi}'(r, t)$ describes the excitations of the gas. For $T \ll T_C$, $\hat{\Psi}'(r, t)$ can be neglected, and the stationary Schrödinger equation is given by [Gross, 1961; Pitaevskii, 1961]

$$\left(-\frac{\hbar^2 \nabla^2}{2m} + U(r) + g\phi(r)^2 \right) \phi(r) = \mu\phi(r), \quad (2.18)$$

which is also referred to as Gross-Pitaevskii equation. The trapping potential in Eq. (2.18) is denoted as $U(r)$, and the particle interactions enter via $g = 4\pi\hbar^2 a/m$,

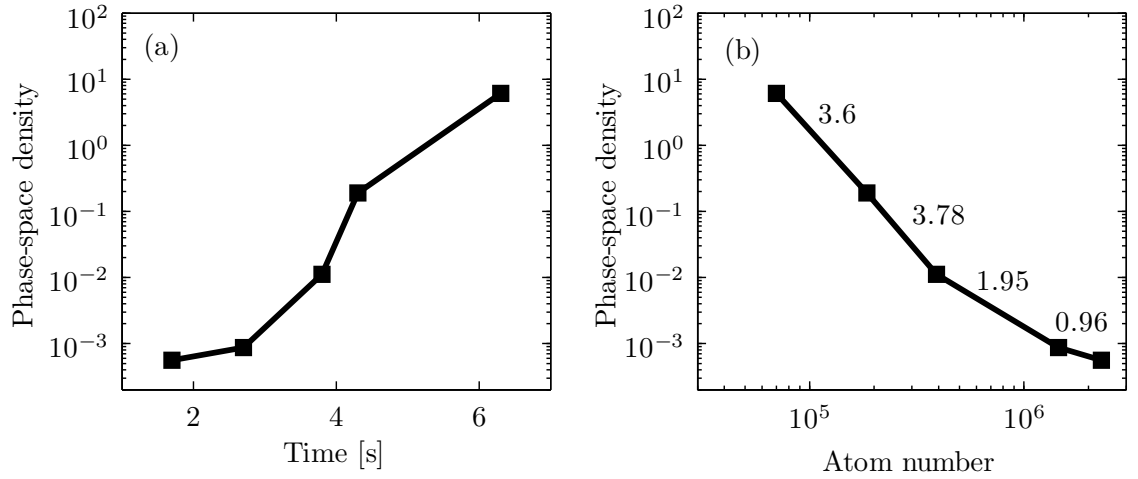


Figure 2.16: Characterization of the ^{133}Cs evaporation process. (a) Phase-space density as a function of time, where $t = 0$ marks the start of the MOT loading procedure. (b) Phase-space density as a function of atom number. The numbers in the plot indicate the evaporation efficiency Γ (see Eq. (2.16)) of each evaporation ramp.

where a is the intraspecies scattering length. The solution to this equation is well understood in the following two limiting cases

In the ideal gas limit, namely $a = 0$, the interaction term vanishes and the ground-state wave function takes on the form [Bongs and Sengstock, 2002; Dalfovo et al., 1999]

$$\phi(r) = \left(\frac{m\bar{\omega}}{\pi\hbar}\right)^{3/4} \exp\left(-\frac{m}{2\hbar}(\omega_x x^2 + \omega_y y^2 + \omega_z z^2)\right), \quad (2.19)$$

which means that the density distribution $n(\mathbf{r}) = |\phi(\mathbf{r})|^2$ is also of Gaussian shape. The width of this Gaussian distribution is given by $\sigma_i = \sqrt{\hbar/(m\omega_i)}$ for $i = x, y, z$.

In the Thomas-Fermi limit, the interaction term in Eq. (2.18) with the scattering length $a \rightarrow \infty$ dominates, and the kinetic energy term can be neglected. In this case the density is given by

$$n(\mathbf{r}) = \begin{cases} \frac{\mu - U(\mathbf{r})}{g}, & \text{for } \mu - U(\mathbf{r}) > 0 \\ 0, & \text{otherwise.} \end{cases} \quad (2.20)$$

In partly condensed clouds, however, the sample is in an intermediate regime, and the choice of the density profile somewhat arbitrary [Ketterle et al., 1999]. Because of the levitation gradient that we apply to keep the atoms within the imaging region during the expansion, additional forces from the resulting gradient in the horizontal

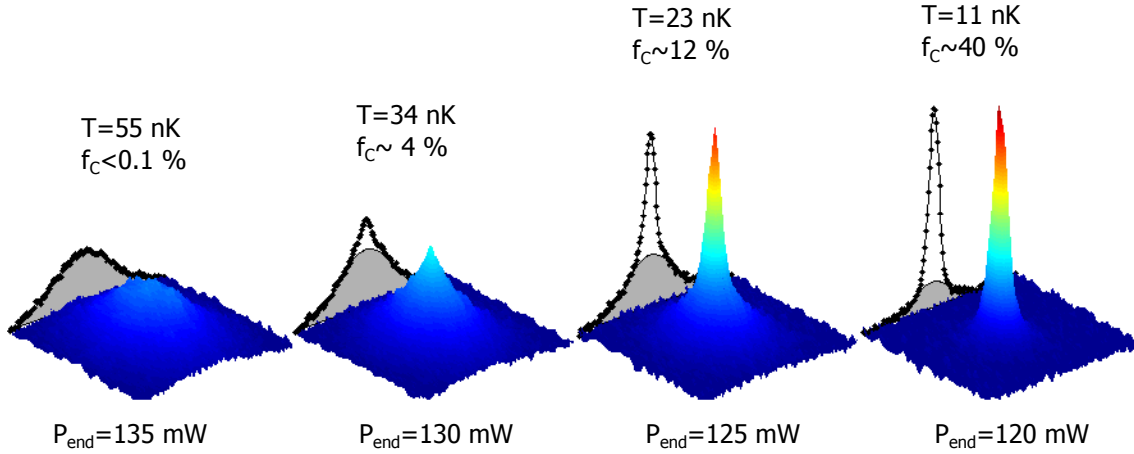


Figure 2.17: Bose-Einstein condensation of ^{133}Cs . The two dimensional column densities for four different laser powers P_{end} are shown. The projections illustrate a cut through the vertical axis (points), the bimodal distribution (solid line), and the thermal Gaussian profile (gray area). The indicated temperatures T are extracted from the profile via Eq. (2.22), and the condensate fraction f_c is obtained from a fit to Eq. (2.21).

direction alter the density profile. Therefore, we fit only a cut through the vertical z -axis to the bimodal density distribution

$$n(z) = \frac{1 - f_c}{\sqrt{2\pi}w_{th}} A e^{-z^2/2w_{th}^2} + \frac{f_c}{\sqrt{2\pi}w_c} A e^{-z^2/2w_c^2} \quad (2.21)$$

(cf. Ketterle et al., 1999; Kohnen, 2008), where f_c denotes the condensate fraction, w_{th} (w_c) the rms-width of the thermal (condensed) cloud, and A is a normalization factor that is proportional to the number of atoms. The second summand is only used in the region where the second Gaussian term is relevant, and we include offsets for the position and the density. The ideal gas limit was chosen in this case because the offset field was set close to the zero crossing of the ^{133}Cs scattering length at 17 G during the expansion. We note that using a parabola to describe the density distribution of the condensate instead, which accounts for residual interactions, yields condensate fractions that differ by less than 25%. The results of this fit are illustrated for several final values P_{end} of the dimple trap power in Fig. 2.17. Depending on P_{end} , we obtain either a thermal gas, or condensate fractions of up to 45 %. The temperature of the sample in Fig. 2.17 is extracted from the thermal

wings of the distribution via [Ketterle et al., 1999]

$$k_B T = \frac{1}{2} m \left(\frac{\omega_z^2}{1 + \omega_z^2 t^2} z_{th}^2 \right), \quad (2.22)$$

where a time-of-flight of $t = 70$ ms was used.

2.4 Creation of a Molecular ${}^6\text{Li}$ BEC

The behavior of ${}^6\text{Li}$ at ultracold temperatures is fundamentally different than that of ${}^{133}\text{Cs}$. With a total spin of $3/2$, the atoms follow Fermi statistics, which prevents the atoms from accumulating in a single quantum state due to Pauli blocking. The mean occupation number

$$\langle n_F^i \rangle = \frac{1}{e^{(\epsilon_i - \mu)/k_B T} + 1} \quad (2.23)$$

can only take on the values 0 for $\epsilon_i > \mu$ or 1 for $\epsilon_i < \mu$ when $T = 0$. In this zero temperature limit, the quantum states are filled up to the Fermi energy

$$E_F = \mu(N, T = 0), \quad (2.24)$$

which is given by $E_F = (6N)^{1/3} \hbar \bar{\omega}$ for a sample in a harmonic trap. Reaching these temperature scales via evaporation in a single component Fermi gas of alkali atoms is impeded by Pauli blocking, which prevents thermalization and renders efficient evaporation impossible.

A common loophole from this complication is the use of a mixed sample with two different hyperfine states involved. Here, collisions between the distinguishable particles allows for thermalization and thus evaporation to quantum degeneracy. A desirable side effect is the suppression of three-body losses, because two of these three-particles are identical fermions. Pauli blocking forbids them to come sufficiently close together. As a result, the evaporation process is experimentally much less demanding as compared to ${}^{133}\text{Cs}$. While for the latter efficient evaporative cooling can only be performed close to an Efimov minimum (see Sect. 2.3), ${}^6\text{Li}$ is extremely insensitive to the specific value or sign of the scattering length.

On the $a > 0$ side of a broad Feshbach resonance [Zürn et al., 2012], a two-component Fermi mixture forms universal dimers (see Sect. 3.2.2) for kinetic energies below the binding energy $\epsilon_B = -\hbar^2/2ma^2$ [Jochim et al., 2003; Chin and Grimm, 2004]. As these molecules composed of two fermions exhibit integer spin, their

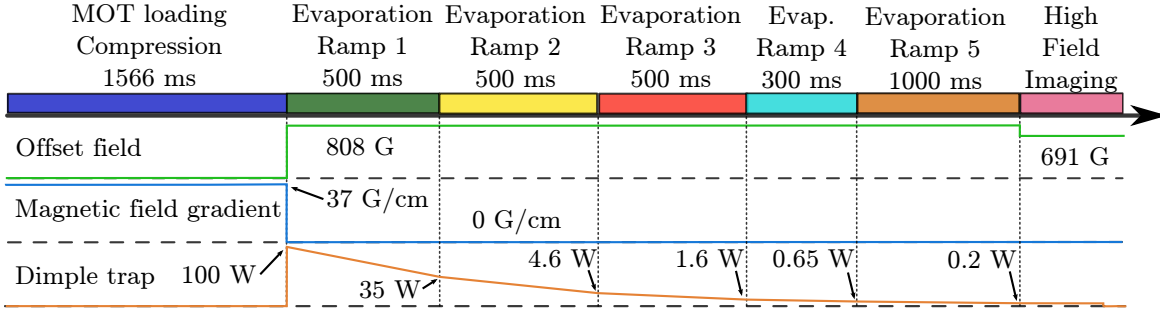


Figure 2.18: Experimental sequence for loading of a ^6Li mBEC. Schematic diagram for the timings of selected parameters. For more details see text.

distribution follows Eq. (2.12) and their energetically lowest state can be occupied macroscopically. A molecular BEC (mBEC) occurs when the molecular peak phase-space density [Chin and Grimm, 2004]

$$D_{mol} = D_P^2 e^{\epsilon_B/(k_B T)} \quad (2.25)$$

becomes slightly larger than one.

In Sect. 2.4.1 we present our experimental scheme for the creation of such a mBEC, which follows closely the approach by the Jochim group in Heidelberg [Ottensstein, 2010; Lompe, 2011; Kohnen, 2008]. The production process and the properties of the degenerate gas are analyzed in Sect. 2.4.2.

2.4.1 Experimental Scheme for Loading a ^6Li mBEC

We start our preparation of the mBEC by loading a ^6Li MOT for 1566 ms including subsequent compression in a similar procedure as described in Sect. 2.2.1. 7 ms before we turn off the MOT lasers, we illuminate the sample with the light from the dimple trap (see Sect. 2.1.3) at a power of ~ 100 W, thus loading $\sim 1.5 \times 10^6$ atoms in the two lowest hyperfine states into the trap. Immediately afterwards, we turn on the magnetic offset field at 808 G, where the scattering length amounts to $15600 a_0$. We begin the forced evaporation by ramping the dipole trap laser power to 35 W within 0.5 s. In three further ramps with a total duration of 1.3 s we bring the sample of 2.5×10^5 atoms to a temperature of 900 nK. We finally ramp the laser power to values P_{end} between 70 mW and 220 mW. Depending on P_{end} the two-component gas is either at the onset of condensation, or deeply in the condensed regime. We then ramp to a field value of 691 G, where $a_{\text{Li}} = 1450 a_0$. The binding energy of dimers at this scattering length amounts to $7 \mu\text{K}$. We allow the system to thermalize within 100 ms, and image the sample using our high-field

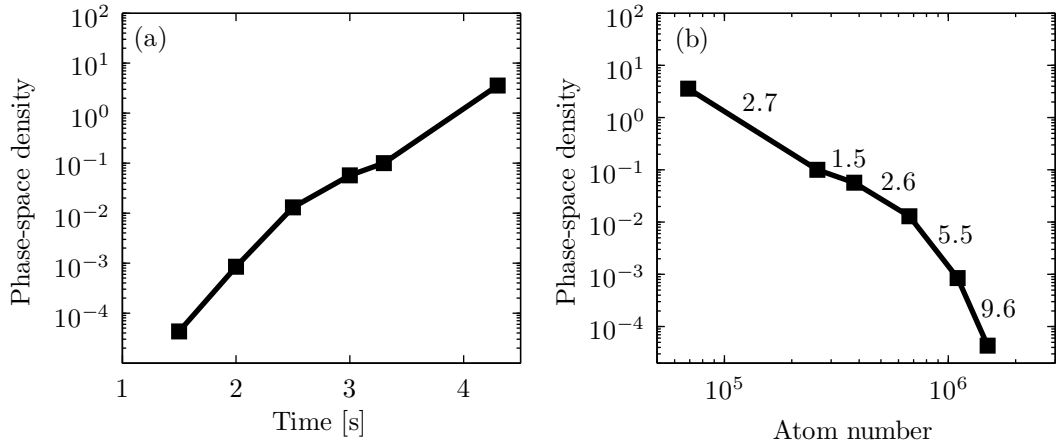


Figure 2.19: Characterization of the ^6Li evaporation process. (a) Phase-space density as a function of time, where $t = 0$ marks the start of the MOT loading procedure. (b) Phase-space density as a function of atom number. The numbers in the plot indicate the evaporation efficiency Γ (see Eq. (2.16)) of each evaporation ramp.

imaging scheme (see Sect. 2.1.5). The sequence described above is summarized in Fig. 2.18, and the results and the characterization of this procedure are given in the subsequent section.

2.4.2 Characterization of the ^6Li mBEC

The time evolution of the PSD during our evaporation is illustrated in Fig. 2.19(a). The value at 4.3 s is taken from an ensemble which is just at the onset of Bose-Einstein condensation, where the temperature is ~ 90 nK. At these temperatures, the sample is in a dynamic equilibrium between two competing processes. One of them is the formation of molecules via three-body collisions, the other one is dissociation of molecules into atoms [Jochim et al., 2003; Chin and Grimm, 2004]. Nonetheless, we use the definition in Eq. (2.15) of the atomic PSD for all points in Fig. 2.19, in order to provide a more direct comparison of the different evaporation steps. Within four seconds, we increase the atomic PSD by four orders of magnitude. The evaporation efficiency Γ (see Eq. (2.16)) is shown in Fig. 2.19(b), where the PSD is given as a function of atom number. In the ^6Li case, the total evaporation efficiency is higher than for ^{133}Cs , which can mainly be attributed to the more favorable ratio of elastic to inelastic collisions.

The transition from a thermal gas to a mBEC is summarized in Fig. 2.20. The atomic column density is shown for three different values of the laser powers P_{end}

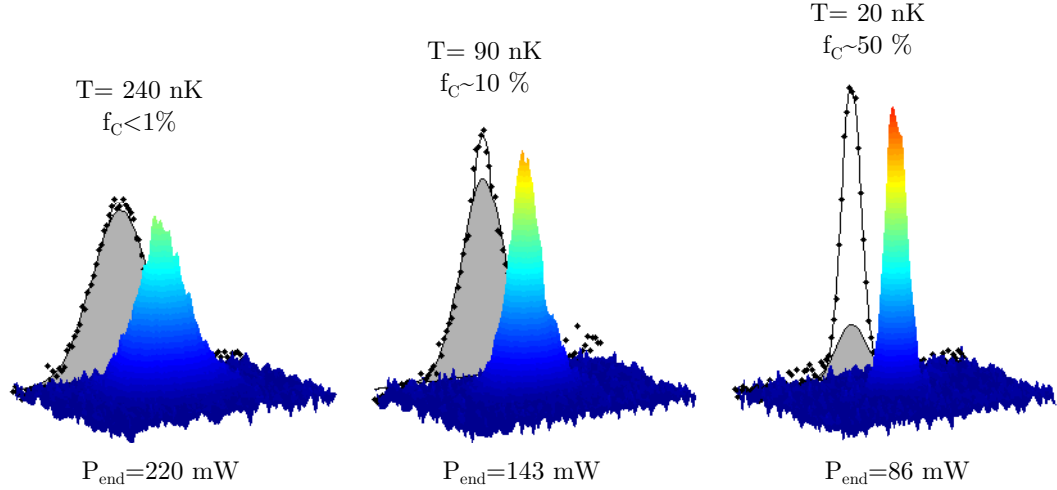


Figure 2.20: Bose-Einstein condensation of ${}^6\text{Li}$. The two dimensional column density for the three indicated dipole trap laser powers P_{end} illustrate the transition from a thermal to a bimodal distribution. The projections show a cut through the vertical axis (points), the fitted bimodal distribution (solid line), and the thermal Gaussian profile (grey shaded area). The temperature is obtained via time-of-flight measurements, and the condensate fraction f_C by a fit to Eq. (2.26).

at the end of the last evaporation ramp. One can clearly see how the peak density increases for lower values of P_{end} , which corresponds to lower trap depths and lower temperatures. The density distribution for $P_{\text{end}} = 220$ mW is well described by a thermal Gaussian distribution, as shown by the projection of a vertical cut through the center of the cloud in Fig. 2.20. For lower laser powers, as for example $P_{\text{end}} = 86$ mW, the cut through the vertical column density is described by the bimodal distribution in the Thomas-Fermi limit

$$n(z) = \frac{1 - f_c}{\sqrt{2\pi}w_{th}} A e^{-z^2/w_{th}^2} + \frac{15}{16w_c} A f_c \left(1 - \left(\frac{z}{w_c} \right)^2 \right)^2. \quad (2.26)$$

In this case, w_c denotes the half-width of the condensate where the density goes to zero. A fit to this function (analogous to the fit performed in Sect. 2.3) is shown in Fig. 2.20, for which we obtain condensate fractions on the order of 50 %.

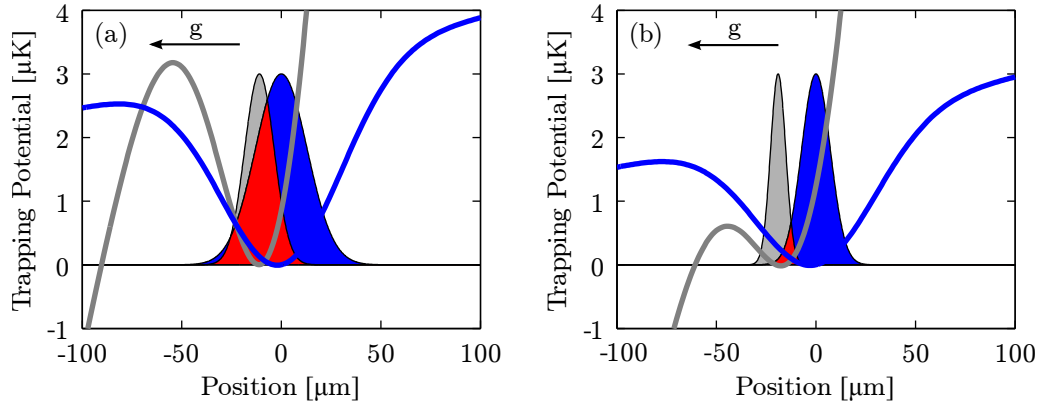


Figure 2.21: Role of the gravitational sag for different trap depth. (a) The vertical component of the trapping potentials for ^6Li (blue line) and ^{133}Cs (gray line) are plotted for a laser power of 150 mW. The overlap (red area) for typical density distributions at temperatures of 450 nK of ^6Li (blue) and ^{133}Cs (gray) is $\sim 80\%$. (b) For a laser power of 106 mW and resulting temperatures below 100 nK, the overlap is reduced to 12 %. The direction of the gravitation 'g' is shown by the arrow in both plots.

2.5 Requirements for Combination of Both Species at Higher Phase Space Densities

Bringing both species together to quantum degeneracy is not straightforward. One can not simply load them in a double MOT and evaporate them in the same optical dipole trap to quantum degeneracy, because of the following two complications. Firstly, the atom numbers in a double MOT are severely limited by inelastic collisions with loss rate constants on the order of $\gamma_{\text{LiCs}} \approx 10^{-10} \text{ cm}^3/\text{s}$ [Schlöder et al., 1999]. For the MOT densities in our experiment we measure fast, approximately exponential ^6Li losses with time constants below 100 ms, when we hold ^6Li in a dipole trap and load a ^{133}Cs MOT at the same position. The second complication is the difference in trapping potential that both species experience. One reason for this is the fact that the polarizability of ^{133}Cs for a laser of 1070 nm wavelength is a factor of four larger than that of ^6Li , as will be discussed further within this section (cf. Sect. 2.2.2). The second reason is the mass difference. While the ^6Li mass only plays a negligible role, the heavier ^{133}Cs experiences a gradient in the trapping potential due to gravitation. At sufficiently low laser powers, this gradient reduces the trapping potential significantly and shifts the equilibrium position of ^{133}Cs away from the one of ^6Li . At trap depths on the order of $3 \mu\text{K}$, both species experience approximately the same trap depth and temperatures. The spatial overlap at this

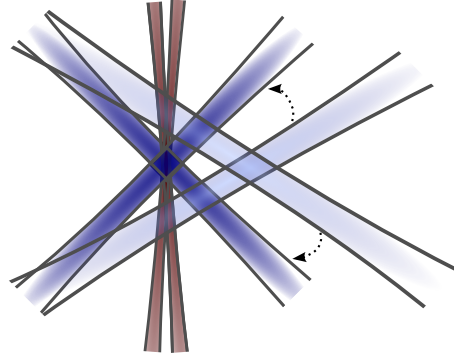


Figure 2.22: Displacement of reservoir. The reservoir trap is loaded at a displaced position (light blue), and then superposed with the dimple trap (red) via a piezo driven mirror. The final position of the reservoir is illustrated in dark blue.

stage is calculated to be on the order of 80% (see Fig. 2.21(a)). Lowering the laser power further then quickly reduces the overlap, and yields a shallower trap depth for ^{133}Cs as compared to ^6Li . This scenario is shown in Fig. 2.21(b). The vertical overlap (red area) is reduced significantly to $\sim 12\%$ for ^{133}Cs temperatures of ~ 100 nK, which are required in order to reach Bose-Einstein condensation. A comparison of the temperatures at the lowest P_{end} values in Fig. 2.17 and Fig. 2.20 shows that for dimple trap powers on the order of ~ 100 mW the confinement of ^6Li is stronger as that for ^{133}Cs , causing the ^6Li temperature to be higher than that of ^{133}Cs . For laser powers on the order of a few hundred mW, as shown e.g. in Fig. 2.12, the situation is reversed, and the ^6Li sample is colder than the ^{133}Cs sample.

A scheme that avoids the limitations discussed above is presented as follows. Instead of loading the species at the same position, we load both species subsequently with sufficient displacement. In principle, this has been already done for mixing the species in Sect. 2.2 by adding an offset field during loading of the ^{133}Cs MOT while ^6Li was already stored in a dimple trap. However, the ^{133}Cs MOT loading time was limited to $t < 200$ ms. For longer loading times, the extension of the ^{133}Cs cloud becomes large enough to overlap with the ^6Li MOT, yielding fast inelastic losses. Displacing the ^{133}Cs MOT further by increasing the offset field is not an option, as the loading efficiency of the optical lattice for DRSC, which is in this case still overlapped with the dimple trap containing ^6Li , then becomes insufficient. In order to resolve this, we displace the position of the optical lattice and the reservoir trap sufficiently far away from the dimple trap, and load both species subsequently at displaced positions into different dipole traps. The ^{133}Cs atoms in the reservoir

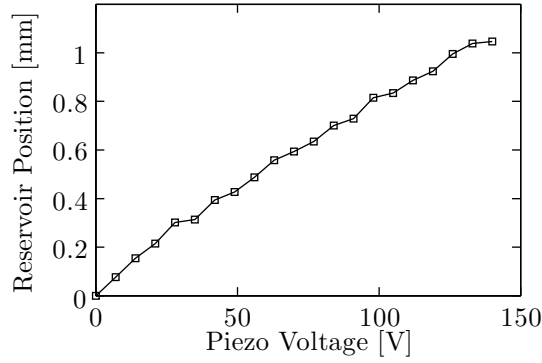


Figure 2.23: Reservoir position as a function of piezo voltage. The reservoir trap can be displaced up to 1 mm from the position of the dimple trap by help of a piezo driven mirror.

trap can then be superposed with the dimple trap by use of a piezo driven mirror that allows for shifting of the reservoir trap beams. We illustrate this process schematically in Fig. 2.22. We implement the piezo driven mirror into our setup and illustrate the measured position of the ^{133}Cs cloud in the reservoir as a function of the voltage supplied to the piezo element in Fig. 2.23. With a maximum piezo voltage of 150 V, we are able to shift the position of the ^{133}Cs reservoir by ~ 1 mm, which is sufficient for subsequent loading of both species without inducing inelastic losses, as performed in Chap. 4.

The problem of the vanishing overlap is approached by using an additional dipole trap laser that allows for a species selective manipulation of the atoms. In Fig. 2.24 we display the wavelength dependent ^6Li and ^{133}Cs polarizabilities

$$\alpha(\omega) = \sum_{\beta} \frac{2\omega_{\beta\alpha} |\langle \alpha | \hat{e} \cdot \mathbf{d} | \beta \rangle|^2}{\hbar(\omega_{\beta\alpha}^2 - \omega^2)} \quad (2.27)$$

for the ground state $|\alpha\rangle$, where \hat{e} denotes the unit polarization vector of the light field, \mathbf{d} represents the dipole operator, and the sum is performed over the relevant states $|\beta\rangle$. The polarizability for ^{133}Cs vanishes at a wavelength of 880.18 nm, because the contributions from the D_1 and the D_2 lines cancel, when these are the only states used in Eq. (2.27). Adding a laser at this wavelength to the existing dimple trap allows us to apply an additional trapping potential only for ^6Li without affecting the trapping potential of ^{133}Cs . At low dimple trap powers, which yield gravitational shifts for ^{133}Cs (see Fig. 2.21), the ^6Li potential can be adjusted with this tune-out trap so that it still overlaps with ^{133}Cs . Alternatively, one can select a wavelength where for a desired trap depth both species experience the same potential, since the

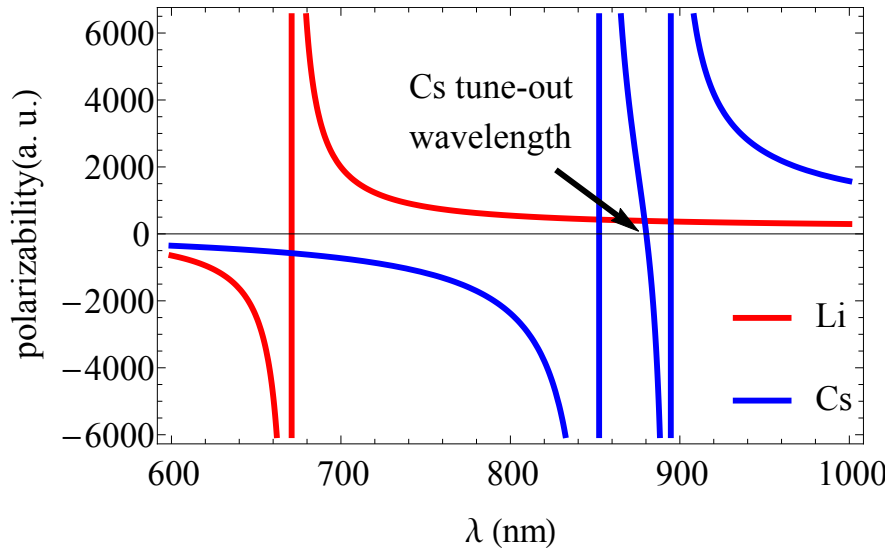


Figure 2.24: Polarizabilities $\alpha(\omega)$ for ${}^6\text{Li}$ (red) and ${}^{133}\text{Cs}$ (blue). The tune-out wavelength $\lambda_{0,\text{Cs}} = 880.18$ nm for ${}^{133}\text{Cs}$ is indicated by an arrow. Only the contributions from the D_1 and D_2 line have been used for the calculation of $\alpha(\omega)$ (Eq. (2.27)), which is given in atomic units. Figure taken from Häfner, 2013.

laser used for this scheme is tunable over a large range of wavelengths.

In a first set of preliminary experiments³² we analyze the behavior of the ${}^{133}\text{Cs}$ sample in the tune-out trap with a crossing angle of 90° . The trapping frequencies are measured for different wavelengths and laser powers, as summarized in Fig. 2.25. Close to the tune-out wavelength λ_0 we cannot measure ${}^{133}\text{Cs}$ trapping frequencies, because the trapping potential vanishes. However, as expected, we observe that the frequencies decrease for wavelengths approaching λ_0 , following the calculated theory curves for the expected behavior. We illustrate three different curves, because the beam waist changes slightly with wavelength, as discussed in Häfner, 2013. We also measure the ac Stark shift on the $6S_{1/2} |f = 4\rangle \rightarrow 6P_{3/2} |f' = 5\rangle$ imaging transition caused by the tune-out trap. As this laser shifts both states of this transition, we show the results for the difference of the ac Stark shifts of both states in Fig. 2.26. This shift also decreases for values approaching λ_0 . More details on the experiments with the tune-out trap can be found in Häfner, 2013.

The measurements described above prove that the tune-out wavelength trap can be employed for a species selective trapping of only ${}^6\text{Li}$, while the ${}^{133}\text{Cs}$ trapping potential remains unaffected. However, the ${}^{133}\text{Cs}$ atoms still scatter light, which

³²These measurements have been performed by S. Häfner within the scope of his master's thesis [Häfner, 2013]. At the time of the described measurement, the ${}^6\text{Li}$ sample could not be probed for technical reasons.

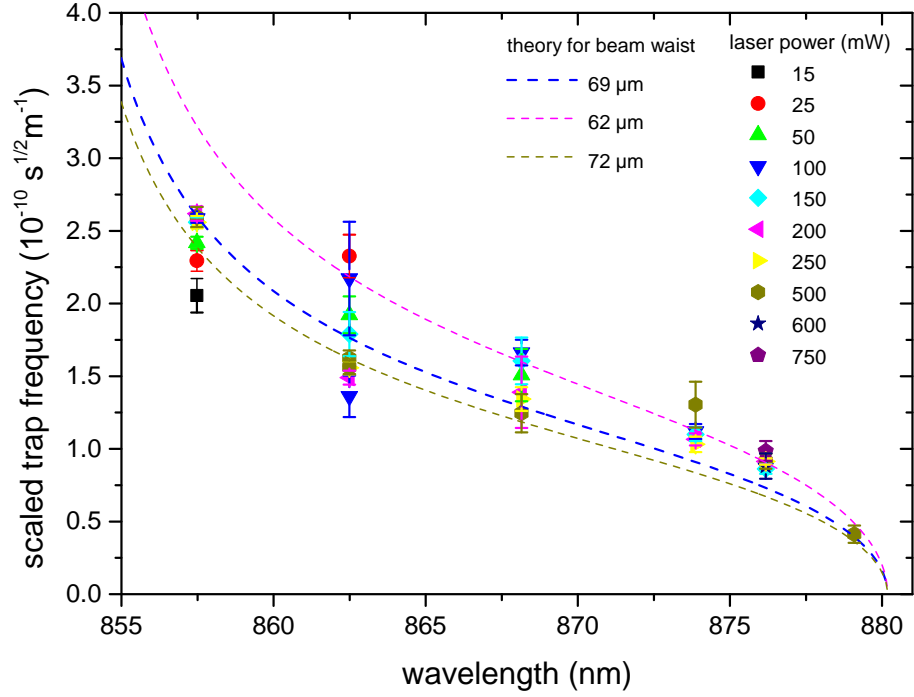


Figure 2.25: Scaled trap frequency as a function of laser wavelength. The frequencies are scaled as $\nu_{\text{scaled}} = \nu / (4\sqrt{P/(\pi m_{Cs})})$, where P denotes the laser power. The expected behavior $\sqrt{-\text{Re}[\alpha(\omega)]/2\epsilon_0 c/(2\pi\omega_0^2)}$ is shown (dashed lines) for the three indicated beam waists since this parameter slightly changes with wavelength (see Häfner, 2013). Figure taken from Häfner, 2013.

leads to heating of the atoms. For typical laser intensities, this effect can be on the order of 100 nK/s, which limits the atom lifetime in the trap. Thus, the time for experiments with mixed species close to or at quantum degeneracy is also limited to values on the order of 1 s.

A planned step for the near future is to superpose the tune-out trap with the dimple trap by use of dichroic mirrors. Once this has been implemented, we expect to bring the mixture to quantum degeneracy simultaneously, while maintaining a high spatial overlap of both gases via the tune-out trap.

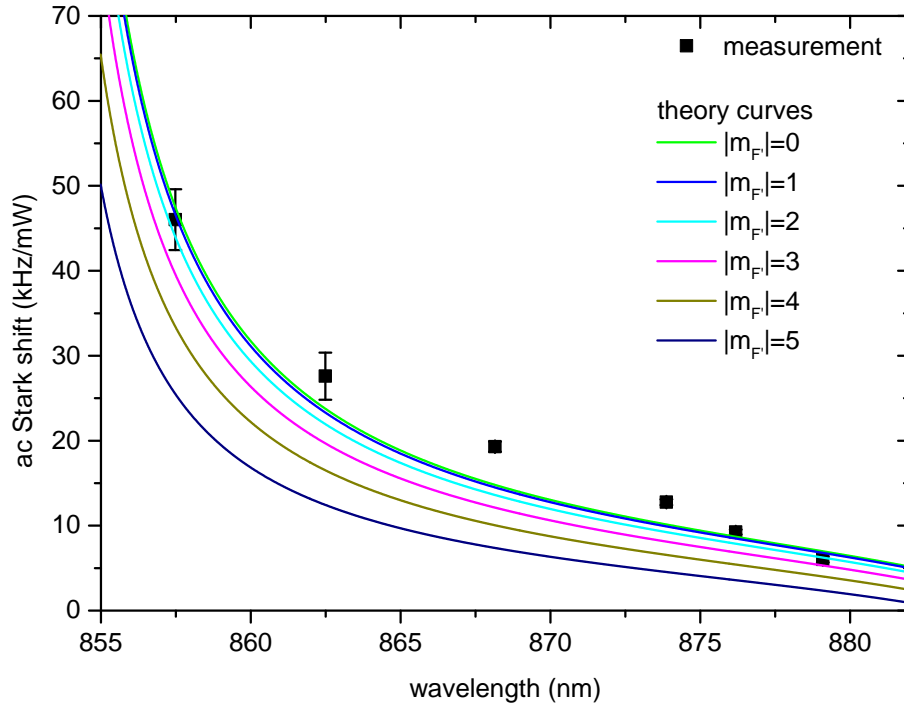


Figure 2.26: Differential ac Stark shift as a function of wavelength. The measured difference of the ac Stark shift between the $6S_{1/2} |f = 4\rangle$ and $6P_{3/2} |f' = 5\rangle$ states, induced by the tune-out trap, is illustrated as black squares. The lines show the expected behavior for the different m_f sublevels in the $6P_{3/2} |f' = 5\rangle$ state. For a discussion on the small discrepancies, we refer to Häfner, 2013. Figure taken from Häfner, 2013.

Chapter 3

Analyzing Feshbach Resonances

Parts of this chapter are based on the following publications:

R. Pires, M. Repp, J. Ulmanis, E.D. Kuhnle, M. Weidemüller, T.G. Tiecke, C.H. Greene, B.P. Ruzic, J.L. Bohn and E. Tiemann

Analyzing Feshbach Resonances - A LiCs Case Study

Manuscript in preparation

M. Repp, R. Pires, J. Ulmanis, R. Heck, E.D. Kuhnle, M. Weidemüller, E. Tiemann

Observation of interspecies ${}^6\text{Li}$ - ${}^{133}\text{Cs}$ Feshbach resonances

Physical Review A **87**, 010701 (2013)

For the quantitative study of phenomena that depend on particle interactions, e.g. Efimov resonances, precise knowledge of the field-dependent scattering lengths is essential. In principle, this property can be calculated from accurate interatomic potentials. However, in the case of ${}^6\text{Li}$ - ${}^{133}\text{Cs}$ the available potentials, constructed from Fourier-transform spectroscopy in Staunum et al., 2007, contain mainly deeper lying singlet states, from which the majority are associated with the ${}^7\text{Li}$ - ${}^{133}\text{Cs}$ combination. The sensitivity of these measurements to the ${}^6\text{Li}$ - ${}^{133}\text{Cs}$ potential in the region of the dissociation threshold, which is the critical part for the position of Feshbach resonances (FRs), is not sufficient for an accurate prediction of the field dependent scattering length $a(B)$. A powerful tool for obtaining appropriate experimental data for the calculation of $a(B)$ is Feshbach spectroscopy.

A straightforward numerical coupled channels calculation (CC), which often em-

employs a large number of channels N , can then be used to calculate the appropriate wavefunctions and the scattering lengths from this data. As the time for the matrix operation required to solve this problem is on the order of N^3 [Croft et al., 2011], such a calculation can be computationally expensive. However, sufficient insight into the resonance structure can be gained by applying models that approximately describe the scattering properties, while reducing the computational effort enormously. Two such models have been proven as powerful alternatives.

One of these models is the asymptotic bound state model (ABM), which uses only the bound states close to the asymptote to describe observables like FRs and the scattering length, neglecting the spatial part of the Schrödinger equation and the continuum of scattering states. A second approach to calculate scattering observables is the multichannel quantum defect theory (MQDT), which uses the separation of length and energy scales to facilitate the calculation.

Even though FRs have been extensively reviewed in Chin et al., 2010, the literature is currently lacking a detailed juxtaposition of the aforementioned models. The goal of the present chapter is to fill this gap by comprehensively comparing the approaches of CC calculation, ABM, and MQDT and by providing quantitative results based on the example of the ^6Li - ^{133}Cs system.

The motivation for this comparison originates from a disagreement between CC calculation and ABM, as reported in Repp et al., 2013. The CC calculation¹ allows to accurately assign measured FRs (see Sect. 3.1) with a root mean square (rms) deviation δB^{rms} (for a definition see Eq. (3.51)) of 39 mG for the field positions of the observed resonances. An application of the crudest version of the ABM with six free fit parameters, similar to the one done in Repp et al., 2013, yields a rms deviation of 877 mG. However, leaving all six parameters as free parameters in the fit yields unphysical fit values which are not consistent with those of the CC calculation because the parameters are significantly correlated. Therefore, we demonstrate how this deviation can be reduced by minimizing the amount of free fit parameters and by including magnetic dipole-dipole interaction, yielding a slightly increased $\delta B^{rms} = 965$ mG but parameters that are physically consistent with the CC values.

The ^6Li - ^{133}Cs combination is a good system for the illustration of this extended ABM, because its small reduced mass leads to a large spacing between vibrational states. Therefore, only the least bound states need to be included, which keeps the number of parameters low, and minimizes the computational effort. Other systems

¹Calculations performed by E. Tiemann.

with higher reduced mass would require a larger number n of bound states, which results in $2n+n^2$ fit parameters ($2n$ bound states in singlet and triplet potentials and n^2 respective overlap parameters). For example in Rb-Cs at least five vibrational levels have to be included. The required 35 parameter fit to the observed resonances is asking for an appropriate number of observations if no further theoretical input is available.

We additionally apply the dressed ABM², which includes the coupling of the bound molecular state to the scattering state of the incoming atoms [Tiecke et al., 2010], to improve the agreement with experimental FR positions in the ^6Li - ^{133}Cs system even further. The application of this model is not straightforward due to a subtlety in the ^6Li - ^{133}Cs triplet potential. A virtual state, which is close to the atomic threshold, is not resonant enough to dominate the scattering behavior in the open channel. Therefore, neither the limiting case where a bound state dominates [Tiecke et al., 2010], nor the case where only the virtual state dictates the behavior [Marcelis et al., 2004] is applicable. We will bridge this gap by demonstrating a phenomenological method that includes both effects, leading to a convincing description of the observed FRs with a rms deviation of 265 mG.

Unlike the ABM, the MQDT handles the spatial part of the scattering problem at large separation r explicitly, and the formalism does not differentiate between dominating bound or virtual states. Thus, the latest version of the MQDT as described in Ruzic et al., 2013 can be directly applied³ without extension, resulting in a rms deviation of 40 mG. Besides giving the results for the ^6Li - ^{133}Cs case, we demonstrate how a frame transformation (FT) in a MQDT ansatz can be applied⁴ to a system where no accurate potentials and only experimental data for FR positions are available, in order to assign these resonances and predict other resonance positions. The rms deviation of the FT approximation for the ^6Li - ^{133}Cs system becomes 48 mG.

This chapter is organized as follows. We present the measurement of interspecies FRs in Sect. 3.1. We review the basic concepts of scattering physics in Sect. 3.2 before we explain the basic approach and the underlying assumptions of the applied models to the scattering problem in Sect. 3.3. In Sect. 3.4 we discuss the results of the three models and finally, in Sect. 3.5 we provide the quantitative comparison of the models and summarize our findings.

²Calculations performed by T. Tiecke.

³Calculations performed by B. Ruzic, J. Bohn and C. Greene.

⁴Calculations performed by C. Greene.

3.1 Measurement of Feshbach Resonances

In the following section we show how a mixture of ultracold ${}^6\text{Li}$ - ${}^{133}\text{Cs}$ atoms, prepared in the way presented in Sect. 2.2, can be used to perform Feshbach spectroscopy. This allows to improve existing ${}^6\text{Li}$ - ${}^{133}\text{Cs}$ molecular potentials [Staanum et al., 2007] and therefore to calculate accurate values for the field dependent scattering length by use of a coupled channels calculation (see Sect. 3.4.1). We start by outlining the loss processes we expect in an ultracold mixture in Sect. 3.1.1. Our procedure for calibration of magnetic fields is explained in Sect. 3.1.2, and details on our trap loss measurements, as given in a previous publication [Repp et al., 2013], are illustrated in Sect. 3.1.3. The unique applications for favorably positioned resonances are described in Sect. 3.1.4.

3.1.1 Loss Processes of Ultracold ${}^6\text{Li}$ - ${}^{133}\text{Cs}$ Atoms in a Dipole trap

As we want to find FRs by observing losses in our ${}^6\text{Li}$ - ${}^{133}\text{Cs}$ mixture, we list the dominating loss processes that can occur in our trapped ultracold sample:

- **One-body losses.** Collisions between particles from the background gas and trapped atoms lead to exponential losses of the latter from our trap. Due to non optimal vacuum conditions, these losses occur with a relatively small time constant of $\tau \sim 4$ s. However, since our hold times in the trap are shorter than this time, they do not limit our experiments, but only lead to a constant offset in our loss spectra.
- **Two-body losses.** The ${}^6\text{Li}|1/2, 1/2\rangle \oplus {}^{133}\text{Cs}|3, 3\rangle$ channel is the energetically lowest channel, which excludes inelastic losses caused by two body collisions. For all other channels, however, inelastic two body losses are energetically possible. While the K_2 loss coefficient in the ${}^6\text{Li}|1/2, -1/2\rangle \oplus {}^{133}\text{Cs}|3, 3\rangle$ channel of $\sim 10^{-18}\text{cm}^3/\text{s}$ is negligible away from resonance [Tung et al., 2013], spin-dipolar coupling to exit channel d-waves can cause transitions to the energetically lowest channel, thus resulting in additional losses.
- **Losses caused by elastic collisions.** In our setup, a dominant loss mechanism is caused by elastic interspecies collisions. As explained in Sect. 2.2.2 and Sect. 2.5, the temperature of the ${}^{133}\text{Cs}$ atoms is a factor of four higher than that of the ${}^6\text{Li}$ atoms, which experience a much shallower trapping potential

(see Fig. 2.12). This leads to additional losses of ${}^6\text{Li}$ due to heating by ${}^{133}\text{Cs}$. As the scattering cross section scales with a^2 (see Sect. 3.2.1 and Eq. (3.9)), we expect increased ${}^6\text{Li}$ losses at the position of a FR, because here the scattering length diverges (see Fig. 3.8). This is one of the main reasons why we use the ${}^6\text{Li}$ instead of ${}^{133}\text{Cs}$ atom number for our trap loss measurements.

- **Three-body losses.** A further loss mechanism occurs during a three-body collision. When two of the atoms form a molecule, its binding energy is carried away by all three particles, thus leading to strong losses. It can be shown that the loss coefficient L_3 scales as [Fedichev et al., 1996; D’Incao and Esry, 2005; Weber et al., 2003a]

$$L_3 \propto C(a, T)a^4, \quad (3.1)$$

where the coefficient $C(a, T)$ depends on the microscopic details of the involved atoms. At low temperatures, $C(a, T)$ shows a modulation that corresponds to the Efimov effect. In fact, a minimum of $C(a, T)$ at 21 G for ${}^{133}\text{Cs}$ allowed us to create a BEC in Sect. 2.3 (c.f. [Kraemer et al., 2004]). The Efimov effect and three-body losses are discussed in more detail in Chap. 4. On a Feshbach resonance, the power law scaling of the three-body loss coefficient with a^4 leads to significant losses due to the diverging scattering length (see Fig. 3.8). Hence, increased losses at certain magnetic fields can be associated with FRs, as shown in Sect. 3.1.3.

Besides the above mentioned loss processes, there are also higher-order loss processes. An n -body loss process requires n particles to approach within distances on the order of the van der Waals range (see Eq. (3.29)). However, as the probability to find $n > 3$ atoms in this region is small, these processes are suppressed for the densities of the experiments discussed in this work.

3.1.2 Magnetic Field Calibration

For a precise determination of the FR positions it is important to calibrate the magnetic fields accurately. This is achieved by inducing microwave transitions to the ${}^6\text{Li}$ $m_J = 1/2$ manifold (see Fig. 3.1(a)) by a small coil inside our vacuum chamber. The frequency of the microwave field is scanned for a fixed magnetic field, and for a resonant frequency we see a significant reduction in atom number caused by transitions to the $m_J = 1/2$ state. A comparison of the energies from the Breit-Rabi formula (see Fig. 3.1(a)) to the peak position of a Gaussian fit allows us to

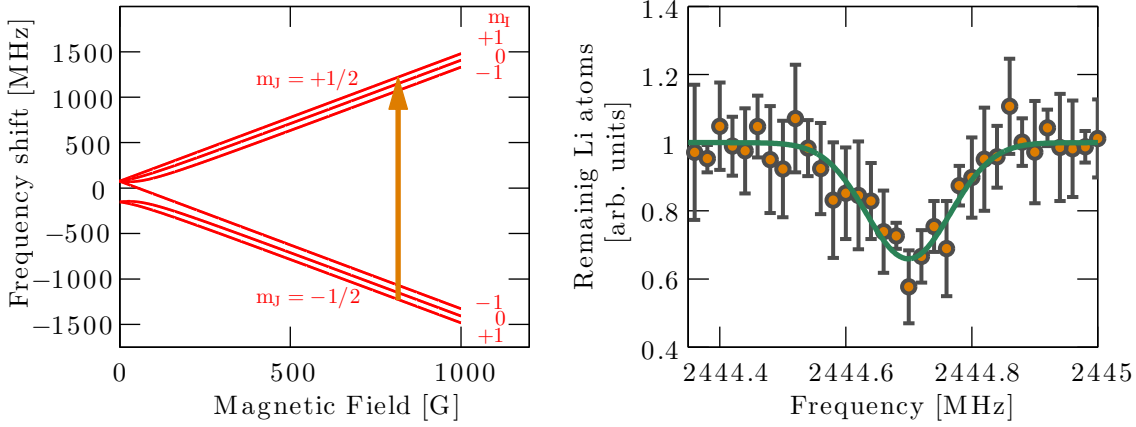


Figure 3.1: Rf transition for the magnetic field calibration. Left: The field dependent level splitting of ^6Li is depicted. The orange arrow indicates the transition used for calibration via the energetically lowest ^6Li state. Right: A typical trap loss spectrum, including a Gaussian fit is shown. The FWHM of 156 kHz at 816.24 G corresponds to a field accuracy of 110 mG. The error bars represent the standard error of the mean atom number determined by several measurements. Figure taken from Repp, 2013.

deduce the magnetic field that corresponds to the measured transition frequency, thus calibrating our magnetic fields. As the width of the atom distribution along the weak axis of confinement is on the order of $\sim 100 \mu\text{m}$, we expect a broadening of the loss feature due to field inhomogeneities. While we cannot distinguish between fast fluctuations of the field and inhomogeneity across the sample, we can give an upper limit for the combined effect of both. For the largest measured field of 950 G a Gaussian fit to the loss feature yields a full width at half maximum (FWHM) of 200 kHz, which corresponds to a magnetic field accuracy of 140 mG across the sample. We perform this measurement at all fields where a FR occurs and conclude that the width scales approximately linear with magnetic field. A typical loss spectrum is shown in Fig. 3.1(b). We observe slow drifts of up to 200 mG on the time scales of a day. For the calculations of the errors in Sect. 3.4 we include this systematic error.

3.1.3 Trap Loss Spectroscopy

In order to observe FRs via two and three-body losses, as described in Sect. 3.1.1, we prepare a mixture of ^6Li and ^{133}Cs atoms as given in Sect. 2.2. We then hold the atoms at a certain field for a variable hold time. Performing this procedure for different magnetic fields and observing the ^6Li atom number via high field imaging

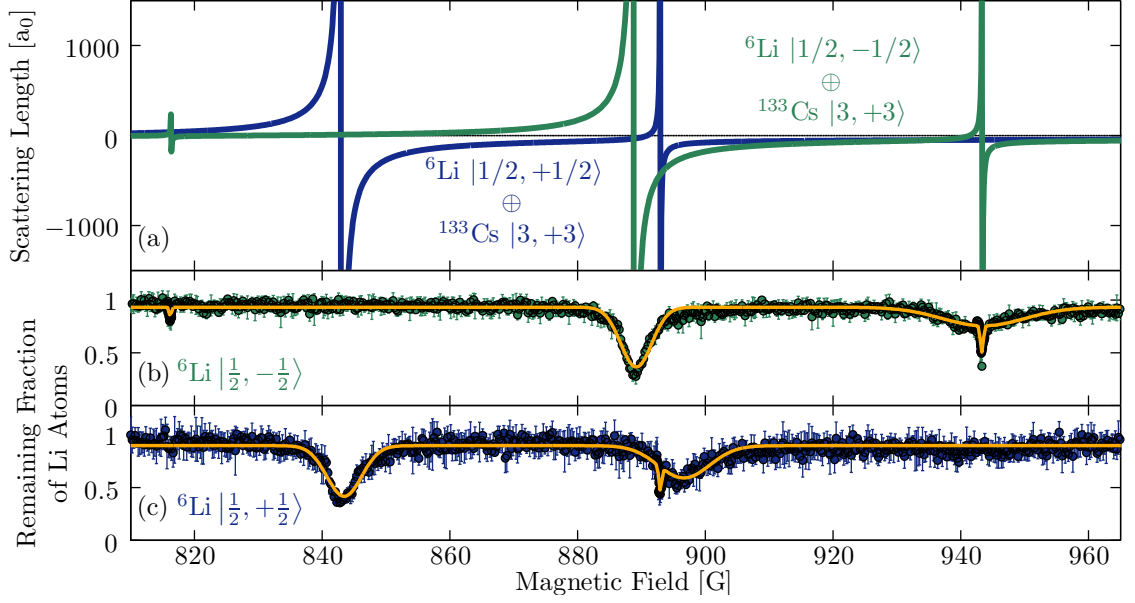


Figure 3.2: S-wave resonances and scattering lengths for the two energetically lowest hyperfine channels. (a) Scattering length for both channels as calculated by a coupled channels calculation (see Sect. 3.4.1). (b) Trap loss measurement and Gaussian profile fits for the ${}^6\text{Li}|1/2, -1/2\rangle$ channel. (c) Trap loss measurement and Gaussian profile fits for the ${}^6\text{Li}|1/2, 1/2\rangle$ channel.

(see Sect. 2.1.5) yields loss spectra as e.g. given in Fig. 3.2. We adjust the ${}^{133}\text{Cs}$ density by changing the ${}^{133}\text{Cs}$ MOT loading times, and vary the hold times t_{Hold} between 60 ms and 2000 ms in a way that produces a relative ${}^6\text{Li}$ atom loss of 15 - 55 % on resonance, which provides a clear, non-saturated loss signal that allows for fitting of a Gaussian profile. The ${}^{133}\text{Cs}$ atom number and t_{Hold} is given for each resonance measurement in Table 3.1.

For the four ${}^6\text{Li}|1/2, \pm 1/2\rangle$ and ${}^{133}\text{Cs}|3, f = 2, 3\rangle$ channels, connected to the two energetically lowest hyperfine states of each species, we detect a total of 19 loss features in the field range between 650 G and 950 G. In order to unambiguously assign the loss feature to interspecies FRs in each observed channel, we repeat the exact measurement sequence, but remove ${}^{133}\text{Cs}$ with a resonant light pulse during DRSC, which makes the loss features disappear. We also repeat the measurement with a mixture containing the respective other ${}^6\text{Li}$ spin state, and with only ${}^{133}\text{Cs}$ in the trap in order to assure that the loss is not connected with intraspecies FRs. The result of the trap loss spectroscopy from 810 G to 965 G, where the broadest loss features are observed, is given in Fig. 3.2. These features are assigned to s-wave resonances via the theoretical analysis reported in the remainder of this chapter. Several of the narrow loss features, which are assigned to p-wave resonances via the CC (see

Entrance channel	$B_{\text{res}}^{\text{exp}} [\text{G}]$	$\Delta B^{\text{exp}} [\text{G}]$	N_{Cs}	$t_{\text{hold}} [\text{ms}]$	Li Loss [%]	$\delta [\text{G}]$	$\Delta [\text{G}]$	$a_{\text{bg}} [a_0]$	m_f	f	G	1
${}^6\text{Li} 1/2, +1/2\rangle$ $\oplus {}^{133}\text{Cs} 3, +3\rangle$	662.79(1)	0.10(2)	5×10^4	500	30	-0.04	-	-	7/2	9/2	7/2	1
	663.04(1)	0.17(2)	5×10^4	500	50	-0.02	-	-	9/2	9/2	7/2	1
	713.63(2)	0.10(3)	5×10^4	1000	15	-0.05	-	-	7/2	7/2	7/2	1
	714.07(1)	0.14(3)	5×10^4	1000	30	-0.05	-	-	9/2	7/2	7/2	1
	843.5(4)	6.4(1)	5×10^4	100	50	0.51	60.4	-28.5	7/2	9/2	7/2	0
	892.87(7)*	0.4(2)	5×10^4	60	20	-0.11	4.6	-28.5	7/2	7/2	7/2	0
${}^6\text{Li} 1/2, -1/2\rangle$ $\oplus {}^{133}\text{Cs} 3, +3\rangle$	658.21(5)	0.2(1)	14×10^4	1000	20	0.07	-	-	7/2	9/2	7/2	1
	708.63(1)	0.10(2)	5×10^4	500	30	-0.05	-	-	5/2	7/2	7/2	1
	708.88(1)	0.18(2)	5×10^4	500	45	-0.03	-	-	7/2	7/2	7/2	1
	764.23(1)	0.07(3)	5×10^4	2000	20	-0.06	-	-	5/2	5/2	7/2	1
	764.67(1)	0.11(3)	5×10^4	2000	25	-0.05	-	-	7/2	5/2	7/2	1
	816.24(2)	0.20(4)	5×10^4	250	45	-0.12	0.36	-28.4	5/2	9/2	7/2	0
	889.2(2)	5.7(5)	5×10^4	100	55	0.46	59.9	-28.4	5/2	7/2	7/2	0
	943.26(3)	0.38(7)	5×10^4	100	45	-0.12	4.3	-28.4	5/2	5/2	7/2	0
${}^6\text{Li} 1/2, +1/2\rangle$ $\oplus {}^{133}\text{Cs} 3, +2\rangle$	704.49(3)	0.35(9)	8×10^4	1000	30	0.07	-	-	7/2	9/2	7/2	1
	896.6(7)	10(2)	5×10^4	100	30	0.68	-	-	5/2	9/2	7/2	0
${}^6\text{Li} 1/2, -1/2\rangle$ $\oplus {}^{133}\text{Cs} 3, +2\rangle$	750.06(6)	0.4(2)	8×10^4	1000	25	0.06	-	-	5/2	7/2	7/2	1
	853.85(1)	0.15(3)	8×10^4	500	40	-0.17	-	-	3/2	9/2	7/2	0
	943.5(1.1)**	15**(3)	5×10^4	100	20	2.21	-	-	3/2	7/2	7/2	0

Table 3.1: List of interspecies ${}^6\text{Li}$ - ${}^{133}\text{Cs}$ Feshbach resonances for combinations of the entrance channels ${}^{133}\text{Cs}|3, 2\rangle$, ${}^{133}\text{Cs}|3, 3\rangle$, ${}^6\text{Li}|1/2, -1/2\rangle$ and ${}^6\text{Li}|1/2, 1/2\rangle$. We fit Gaussian profiles to the experimentally observed resonances in order to deduce resonance positions $B_{\text{res}}^{\text{exp}}$ and widths ΔB^{exp} . The 95% confidence interval of the fit yields the statistical errors. An additional error of 0.2 G is expected due to inhomogeneities and drifts of the magnetic field. The deviations $\delta = B_{\text{res}}^{\text{exp}} - B_{\text{res}}^{\text{theo}}$ between the resonance positions from experiment and from coupled channels calculations ($B_{\text{res}}^{\text{theo}}$), as well as the calculated width Δ are also given. The background scattering lengths a_{bg} for the purely elastic channels of two body collisions, as well as ${}^{133}\text{Cs}$ atoms numbers (N_{Cs}), hold times (t_{hold}) and relative ${}^6\text{Li}$ loss are also presented. For an explanation of the assigned quantum numbers we refer to the text. Two errors of the quantum numbers of previous versions of this table [Repp et al., 2013; Repp, 2013] are corrected in this table. (*) A ${}^{133}\text{Cs}$ 3-body loss minimum at 893(1) G [Berringer et al., 2011b] overlaps with the observed loss feature, which changes the ${}^{133}\text{Cs}$ densities and thus affects the ${}^6\text{Li}$ losses. (**) Due to the broad feature, the fit depends on the amount of data points around the small loss feature at 943.26 G. An averaged value of 942.6(1.0) G was used for the CC calculation.

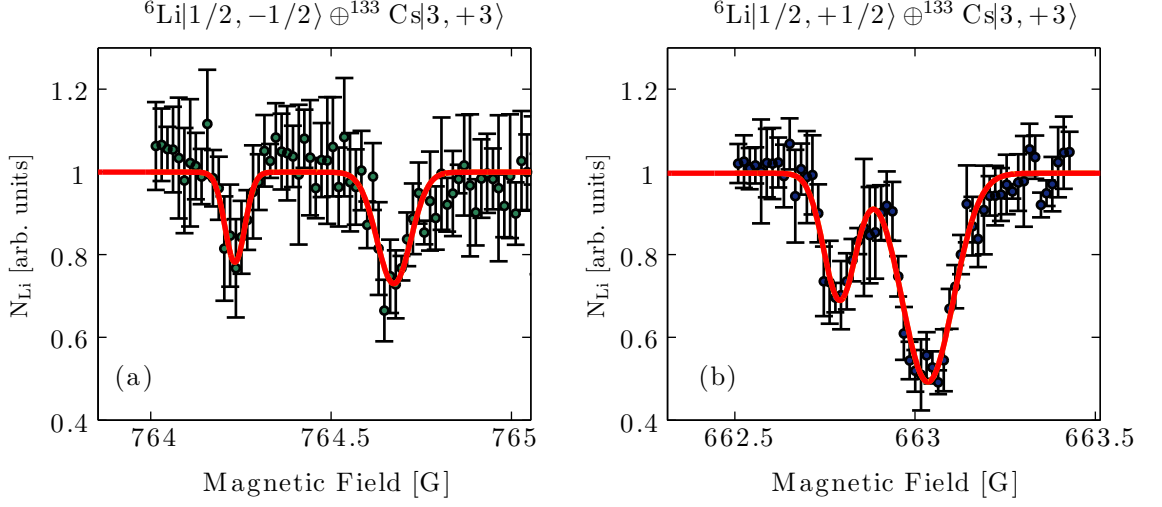


Figure 3.3: Trap loss measurement for selected p-wave resonances with resolved splitting. The remaining atom number in dependence of the magnetic field, as well as double Gaussian profile fits to the observed loss features are shown for the indicated channels. Adapted from Repp, 2013.

Sect. 3.4.1) show a splitting. This is depicted in Fig. 3.3 and is a direct consequence of the second-order spin-orbit and magnetic spin dipole-dipole interaction. In Table 3.1 we provide all resonance positions and loss feature widths, as determined by magnetic field calibration via rf spectroscopy (see Sect. 3.1.2) and fits of Gaussian profiles to the loss features. In a measurement with a step size of 150 mG and 500 ms hold time in the field region between 0 G and 1300 G containing atoms of all the relevant hyperfine states, we observe no additional loss features. We note that the five s-wave FRs which have also been measured by the Chin group at the University of Chicago [Tung et al., 2013] shortly after our experiments, are consistent with our findings. We assign all resonances via a full coupled channels calculation⁵ by adjusting the potentials obtained via laser induced fluorescence Fourier-transform spectroscopy [Staanum et al., 2007]. As these calculations are extensively described in Sect. 3.4.1, we only state the results at this point. The field dependent scattering lengths in the region from 810 G to 965 G are depicted in Fig. 3.2(a) for the ${}^6\text{Li}|1/2, 1/2\rangle \oplus {}^{133}\text{Cs}|3, 3\rangle$ and ${}^6\text{Li}|1/2, -1/2\rangle \oplus {}^{133}\text{Cs}|3, 3\rangle$ channels. In Table 3.1 we assign the resonances to s- and p-wave, and give the deviation $\delta = B_{\text{res}}^{\text{exp}} - B_{\text{res}}^{\text{theo}}$ between experimentally and theoretically determined resonance positions, the FR width Δ and the background scattering length a_{bg} , as defined in Eq. (3.42). The total angular momentum f , which does not include l at zero magnetic field, as well

⁵Performed by E.Tiemann, University of Hannover.

as $G = S + i_{Cs}$, which is also a good quantum number due to the strong ^{133}Cs hyperfine coupling, are also given in Table 3.1 for a unique assignment.

3.1.4 Unique Properties of ^6Li - ^{133}Cs Feshbach Resonances

Several of the observed loss features provide a unique tunability of intra- and interspecies scattering lengths. For example, the ^{133}Cs zero crossing at 880.2 G [Lee et al., 2007; Berninger et al., 2013] is close to the ^6Li - ^{133}Cs resonance at 889.2 G. Due to the Pauli blocking of spin polarized ^6Li , a sample containing atoms in the $^6\text{Li}|1/2, -1/2\rangle \oplus ^{133}\text{Cs}|3, 3\rangle$ states experiences strong interspecies interaction, while intraspecies scattering for both species is suppressed. In Repp, 2013 an interesting application for the simulation of Fröhlich polarons [Fröhlich, 1954; Tempere et al., 2009; Cucchiatti and Timmermans, 2006] via this FR is discussed. The vicinity of the FR at 843.5 G to the broad intraspecies $^6\text{Li}|1/2, -1/2\rangle \oplus ^6\text{Li}|1/2, 1/2\rangle$ resonance at 832.18 G [Zürn et al., 2012] allows to create a sample with strong $^6\text{Li}|1/2, 1/2\rangle \oplus ^{133}\text{Cs}|3, 3\rangle$ and $^6\text{Li}|1/2, -1/2\rangle \oplus ^6\text{Li}|1/2, 1/2\rangle$ interactions, while the $^6\text{Li}|1/2, -1/2\rangle \oplus ^{133}\text{Cs}|3, 3\rangle$ interactions are small. Furthermore, two ^6Li - ^{133}Cs resonances are close to a three-body loss minimum at 893 G. This allows for sympathetic cooling between ^6Li and ^{133}Cs (c.f.[Mudrich et al., 2002]), with minimized three-body losses in the ^{133}Cs sample. However, for this approach one requires similar trapping potentials for ^6Li and ^{133}Cs (see Sect. 2.5.).

3.2 Formalism for Scattering at Ultracold Temperatures

A recurring theme of this thesis is the concept of the scattering length. It is the only parameter needed to describe the interaction between two atoms in the realm of ultracold physics. In this section we revisit the underlying principles of scattering phenomena which are necessary for the theoretical treatment of such systems. The Schrödinger equation and its general solutions are introduced in Sect. 3.2.1, deriving the formulas for experimentally relevant observables in the process. The scattering length is formally introduced in Sect. 3.2.2, where we start by examining the one dimensional finite potential well as text book example for the understanding of the scattering length. The scattering wavefunctions, which are the solution of the Schrödinger equation, are then related to the sign of the scattering length. The divergence due to a shape resonance is presented, as well, which is relevant for the

new approach of the ABM presented in Sect. 3.4.2, because the incoming triplet channel of the ${}^6\text{Li}-{}^{133}\text{Cs}$ potential is close to such a resonance. In Sect. 3.2.3 we introduce the appropriate Hamiltonian for the description of scattering phenomena in ultracold atoms and give a detailed discussion of its individual terms.

3.2.1 Key Concepts of Scattering Theory

We start our summary of the quantum mechanical scattering theory by introducing the general Schrödinger equation for a collision between two particles:

$$\left[-\frac{\hbar^2}{2\mu} \nabla^2 + U(\vec{r}) \right] \psi(\vec{r}) = \frac{\hbar^2 k^2}{2\mu} \psi(\vec{r}), \quad (3.2)$$

where $|k| = \sqrt{2\mu|E|}/\hbar$ is the collision wavevector,

$$\mu = \frac{m_1 m_2}{m_1 + m_2} \quad (3.3)$$

is the reduced mass, and $U(\vec{r})$ is an interaction potential. For the investigated systems, $U(\vec{r})$ vanishes for sufficiently large interparticle spacings r . Thus we can write the wavefunction $\Psi(\vec{r})$ as a superposition of incoming plane wave and outgoing spherical wave with scattering amplitude $f(\theta, k)$:

$$\psi(\vec{r}) = e^{ikz} + f(\theta, k) \frac{e^{ikr}}{r}. \quad (3.4)$$

For all interactions considered in this thesis, we can assume a spherical symmetric potential, which allows us to expand the wavefunction in the basis of spherical harmonics $Y_l^m(\theta, \phi)$:

$$\psi(\vec{r}) = \sum_{l=0}^{\infty} \sum_{m=-l}^l Y_l^m(\theta, \phi) \frac{\chi_{k,l,m}(r)}{r}, \quad (3.5)$$

where $\chi_{k,l,m}(r)$ is a radial function that depends on k, l and m . It should be noted that the assumption of a spherically symmetric potential is not valid for experiments with species that exhibit a permanent dipole moment (e.g. [Aikawa et al., 2012; Stellmer et al., 2009; Stuhler et al., 2007; Lu et al., 2011]), as this alters the symmetry of the scattering process. Inserting Eq.(3.5) into Eq.(3.2) returns the solution

$$f(\theta, k) = \frac{1}{2ik} \sum_{l=0}^{\infty} (2l+1) (e^{2i\delta_l} - 1) P_l(\cos(\theta)) \quad (3.6)$$

for the scattering amplitude at large r , where P_l is the well known Legendre polynomial. This partial wave expansion introduces the phase shift δ_l , which contains all information of the systems interaction. As we demonstrate in Sect. 3.2.3, at the ultracold conditions of our experiment, s-wave ($l = 0$) scattering is the only component of the partial wave expansion that is necessary to describe the interaction between atoms, due to the low collision energies. It is convenient to introduce the s-wave scattering length

$$a = \lim_{k \rightarrow 0} \frac{-\eta_0}{k}, \quad (3.7)$$

where $\eta_0 = \tan(\delta_0(k))$, as the only parameter for the description of the scattering behavior.

Until now, we have not considered the specific nature of the colliding particles. Imposing the requirement of symmetric (anti-symmetric) wavefunctions for bosons (fermions), yields the expression for the differential cross section

$$\frac{d\sigma(k)}{d\Omega} = |f(\theta, k) + \epsilon f(\pi - \theta, k)|^2, \quad (3.8)$$

where $\epsilon = +1$ ($\epsilon = -1$) describes the case of identical bosons (fermions). Employing Eq. (3.7) in this equation yields the following cross sections:

$$\sigma_0 = \begin{cases} \frac{4\pi a^2}{1+k^2 a^2}, & \text{for distinguishable particles} \\ 0, & \text{for identical fermions} \\ \frac{8\pi a^2}{1+k^2 a^2} & \text{for identical bosons.} \end{cases} \quad (3.9)$$

3.2.2 Exploration of the Scattering Length

Considering a simple model potential gives a pedagogical introduction to the scattering length as defined in Eq. (3.7). Despite the vast simplification, the basic physics is still preserved in real systems. Using the partial-wave expansion in Eq. (3.5) allows us to separate radial and angular coordinates of Eq. (3.2). The solution of the angular part is straightforward, and inserting its result back into the Schrödinger equation yields simple equations for the radial wavefunctions $R_l(r) = \chi_l(r)/r$. As this is subject to many introductory textbooks of quantum mechanics [Schwabl,

2007; Merzbacher, 1998; Petrov, 2013]⁶, we state the solutions without derivation:

$$R_l''(r) + \frac{2}{r}R_l'(r) + \frac{2\mu}{\hbar^2}[E - V_l(r)]R_l(r) = 0. \quad (3.10)$$

Here, the collision energy is given by E , and the potential $V_l(r) = U(r) + \frac{\hbar^2 l(l+1)}{2\mu r^2}$ contains the centrifugal term with angular momentum quantum number l . We substitute $\chi_l(r) = r \cdot R_l(r)$, and rescale $\epsilon = 2\mu E/\hbar^2$ and $\bar{V}(r) = 2\mu V_l(r)/\hbar^2$ in order to get the simplified equation

$$\chi_l''(r) + [\epsilon - \bar{V}(r)]\chi_l(r) = 0. \quad (3.11)$$

For the remainder of this section, we consider the case $l = 0$ and drop the subscript l for simplification. For free atoms, where $\bar{V}(r) = 0$, and $E = \hbar^2 k^2/2\mu$ we obtain the obvious solution

$$\chi(r) = \sin(kr), \quad (3.12)$$

when the boundary condition $\chi(0) = 0$ is imposed for regularity of $R(r)$.

As we will see in the following discussion, a non-zero potential \bar{V} changes the shape of the scattering function in the interaction region, and thus leads to a phase shift η_0 in the wavefunction $\chi(r)$ for large distances r , where the interaction potential is approximately zero:

$$\chi(r) = \sin(kr + \eta_0). \quad (3.13)$$

η_0 can be related to the s -wave scattering length a via Eq. (3.7). We demonstrate, that a is the only quantity needed to describe the scattering between ultracold alkali atoms in Sect. 3.2.3. In order to clarify the meaning of η_0 , we chose the figurative example of the finite potential well as interatomic interaction potential

$$U(r) = \begin{cases} -V_0, & \text{if } 0 < r \leq r_0 \\ 0, & \text{otherwise,} \end{cases} \quad (3.14)$$

as depicted in Fig. 3.4, where we also demonstrate a convenient division of the radial wavefunction into the two components χ_I and χ_{II} .

We first consider the case of a hard-sphere potential, where $V_0 \rightarrow -\infty$. The wavefunction cannot penetrate into the region $r < r_0$, hence $\chi_I(r) = 0$. Given the

⁶In this section we follow the line of thought of Petrov, 2013, which is also similar to the treatment in Schuster, 2012.

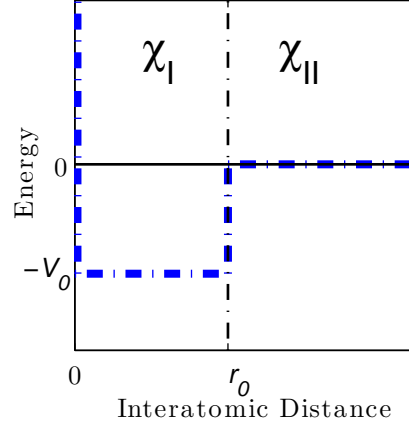


Figure 3.4: Finite potential well. The potential well of depth $-V_0$ and range r_0 as given in Eq.(3.14) is plotted as blue dash-dotted line. The region for the wavefunctions χ_I and χ_{II} is separated by a black dash-dotted line.

boundary condition $\chi_{II}(r_0) = 0$, the solution for $r > r_0$ is

$$\chi_{II}(r) = \sin(k(r - r_0)). \quad (3.15)$$

The imposed boundary condition is a direct consequence of our requirement for a continuous differentiable wavefunction at $r = r_0$:

$$\begin{aligned} \chi_I(r_0) &= \chi_{II}(r_0) \\ \chi'_I(r_0) &= \chi'_{II}(r_0). \end{aligned} \quad (3.16)$$

Here, the scattering length as defined in Eq. (3.7) is simply given by the range of the potential r_0 , as is expected for this classical limit.

Taking the more pragmatic example of a finite potential well with $V_0 = \frac{\hbar^2 k_0^2}{2\mu} > 0$, we also get a finite solution in the region $r < r_0$

$$\chi(r) = \begin{cases} C_1 \sin(k_+ r), & \text{if } 0 < r \leq r_0 \\ C_2 \sin(kr + \eta_0), & \text{otherwise,} \end{cases} \quad (3.17)$$

with $k_+^2 = k_0^2 + k^2$. Again, the regularity of $R(r)$ at $r = 0$ has been imposed. Applying the boundary conditions of Eq. (3.16), we get

$$a = r_0 - \frac{\tan(k_0 r_0)}{k_0}. \quad (3.18)$$

This function is shown in Fig. 3.5, in the scenario as originally envisioned by

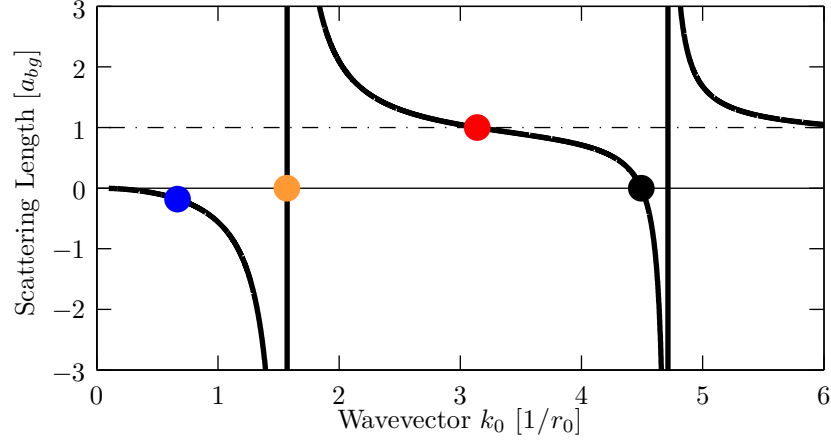


Figure 3.5: Scattering length a versus wavevector \mathbf{k}_0 . The behavior of the scattering length, as given by Eq. (3.18) is plotted. The positions where $a < 0$ (see Fig. 3.6(b)), $a > 0$ (see Fig. 3.6(c)), $a = 0$ (see Fig. 3.6(d)) and $a \rightarrow \infty$ (see Fig. 3.6(e)) are marked with a blue, red, black and orange dot, respectively.

Herman Feshbach [Feshbach, 1958], where the energy of the colliding particles is varied. For the cases where $k_0 r_0 = \pi/2 + n\pi$, with integer n , the scattering length diverges, and the interaction is significantly enhanced.

In Fig. 3.6 we depict the wavefunctions of Eq. (3.17) for typical parameters of our experiment. A temperature of 200 nK and a potential range of $r_0 = 45 a_0$ is assumed, which is on the order of typical temperatures and the van der Waals range of the ^6Li - ^{133}Cs interaction potential, respectively. For better visibility, we reduce the potential depth V_0 from ~ 200 THz to ~ 520 GHz, which decreases the oscillation period for $r < r_0$. For most values of V_0 the scattering length is $a = 45 a_0$ (see Fig. 3.6(c)). However, when we reduce V_0 , the scattering length goes through $a = 0$ (see Fig. 3.6(d)) to negative values (Fig. 3.6(b)). Right at the depth for V_0 where a new bound state occurs, the scattering length diverges (Fig. 3.6(e)). These special cases are also related to the general behavior of a via the colored dots in Fig. 3.5. When $r > r_0$, the radial wavefunction behaves as $\chi(r) \rightarrow C(r - a)$, which is also shown as the straight lines in Figs. 3.6(b)-(e). This means that for large distances, the wavefunction looks like there was an infinitely repulsive wall at $r = a$.

To illustrate this behavior, we also show the functions at larger interatomic distances (see Fig. 3.6(a)). The wavefunction for $a < 0$ (blue curve) is pulled to closer distances which corresponds to an attractive potential, while the wavefunction for positive a (red curve) is pushed away from $r = 0$, which mimics repulsive interaction. The wavefunction for $a = 0$ (black curve) corresponds to the wavefunction for atoms with zero interaction potential. The effect of the Feshbach resonance, where a

diverges, is seen in the orange curve, where the phase of the wavefunction is shifted by π .

The wavefunctions in Fig. 3.6 allow for an intuitive insight into the scattering behavior. However, the different scenarios are caused by fine-tuning of the underlying interaction potentials. In realistic systems, these potentials cannot be fine-tuned, but are given by nature. Thus, in order to obtain large scattering lengths, one relies on an accidental fine-tuning, which is for example the case for two neutron or proton-neutron systems [Braaten and Hammer, 2006]. Both ${}^6\text{Li}$ and ${}^{133}\text{Cs}$ are also good examples for an accidental fine-tuning. In these systems, the potential in the channel of the incoming atoms⁷ gives rise to a near resonant bound-state, which results in large background scattering length. The behavior of the phenomena described above, where $|a|$ increases due to a bound state in the same channel as the incoming atoms, is referred to as a shape resonance. As we show in Sect. 3.3.1, aside from shape resonances, a coupling of the incoming channel to a resonant, bound molecular state in a different scattering channel can have the same effect on the scattering length. The ${}^6\text{Li}$ - ${}^{133}\text{Cs}$ potential is close to a shape resonance in the triplet channel. Therefore, the existing approach of the ABM is not suited for an accurate treatment of this mixture. In Sect. 3.4.2 we extend the existing model in a phenomenological way, in order to precisely reproduce the observed resonance spectrum.

For completeness we consider the case of bound states with $\epsilon_B = -\frac{\hbar^2 k^2}{2\mu} < 0$ in the above described potentials. The solution for the wavefunction is given by

$$\chi(r) = \begin{cases} C_1 \sin(k_- r), & \text{if } 0 < r \leq r_0 \\ C_2 e^{-kr}, & \text{otherwise,} \end{cases} \quad (3.19)$$

where $k_- = k_0^2 - k^2$. Applying Eqs. (3.16), we get $k_- \cot(k_- r) = -r$. In the limit of weakly bound states, $k/k_0 \rightarrow 0$, we obtain the solution $k_0 r_0 = \pi/2 + n\pi$ which coincides with the poles found above. This demonstrates that the emergence of bound states coincides with the divergence of the scattering length.

At this point we can also introduce the universal limit $a \gg r_0$, in which the scattering length is much larger than the range of the potential. Using Eq. (3.18), we obtain

$$\epsilon_B = -\frac{\hbar^2}{2\mu a^2}, \quad (3.20)$$

for the binding energy, which is completely independent from r_0 and thus universal, as the atoms do not resolve the details of the interaction potential. The only effect

⁷We formally introduce the scattering channels in Sect. 3.2.3.

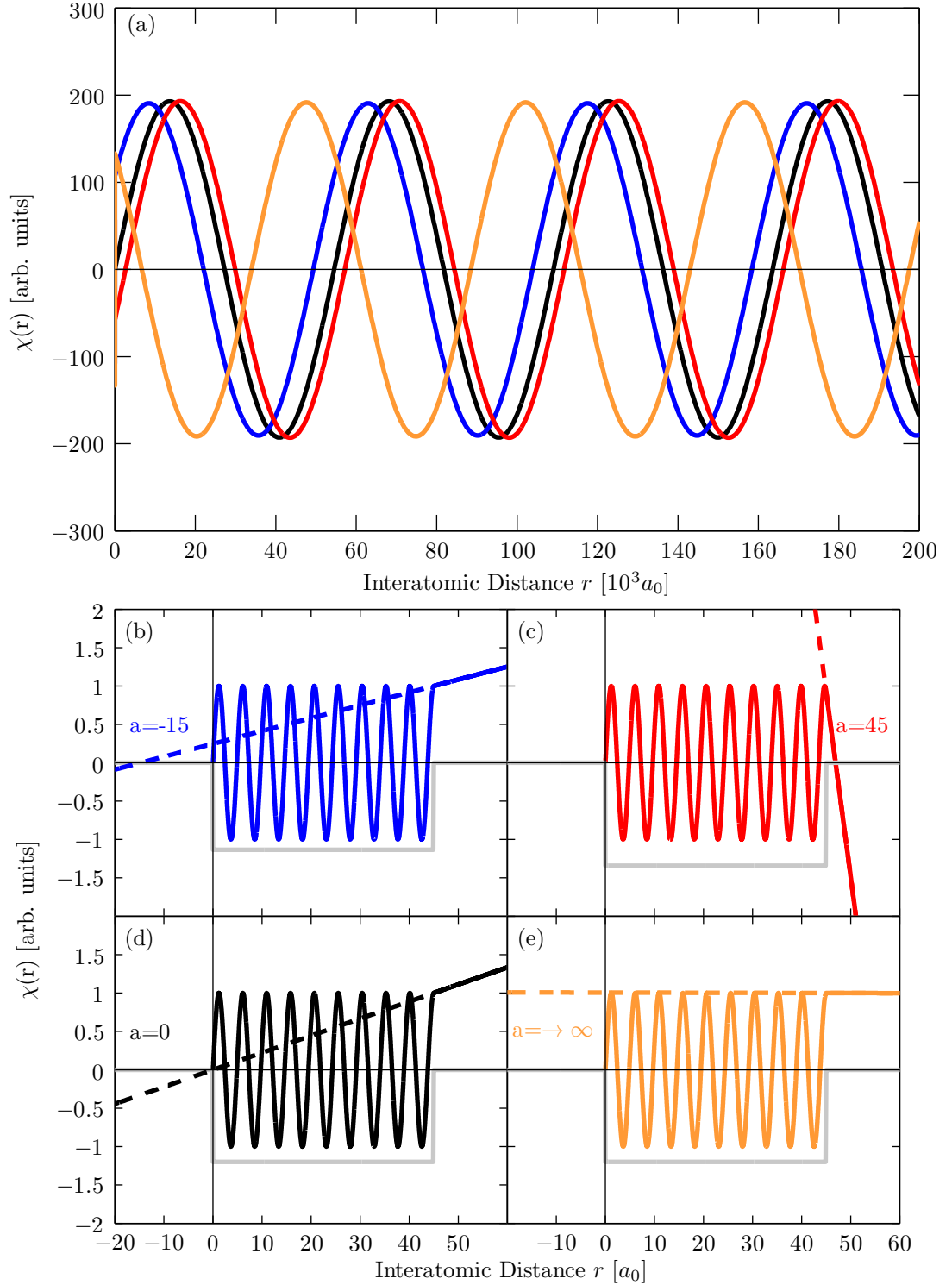


Figure 3.6: Radial wavefunctions for finite potential wells of different depths. The function in Eq. (3.17) for the special values of V_0 resulting in $a = -15 a_0$ (b), $a = 45 a_0$ (c), $a = 0$ (d) and $a \rightarrow \infty$ (e) is shown for small internuclear separations. The functions are also plotted for larger atomic distances (a), where the phase shifts for the wavefunctions with $a = -15 a_0$ (blue) and $a = 45 a_0$ (red) are exaggerated for better visibility. The dashed line shows the asymptotic form $C(r - a)$ of the wavefunction for $r > r_0$.

from the interaction potential is the phase imprinted on the wavefunction at large distances, and the atoms never probe the region where $r \sim r_0$. This can be seen directly by looking at $\chi(r)$, which reads

$$\chi(r) = \sqrt{\frac{2}{a}} e^{-\frac{r}{a}}. \quad (3.21)$$

Besides these two-body bound states, there are also universal three-body states, the so-called Efimov states, which are introduced in detail in Chap. 4.

3.2.3 The Scattering Hamiltonian in Ultracold Atomic Systems

The model potential of Sect. 3.2.2 introduces the effect of shape resonances on the scattering length. In atomic physics, however, the coupling between two different scattering channels gives rise to different scattering resonances, which can be tuned by magnetic fields (see Sect. 3.3.1). In order to understand this coupling mechanism, we extend the Hamiltonian of Eq. (3.2) and discuss each of its components in more detail in this section.

The scattering process of two colliding atoms can be described by the following Hamiltonian [Stoof et al., 1988]:

$$H = T + V + H_{\text{hf}} + H_Z + H_{\text{dd}}, \quad (3.22)$$

where $T = -\hbar^2 \Delta / (2\mu)$ denotes the relative kinetic energy term. The hyperfine energy operator

$$H_{\text{hf}} = \sum_{\beta=A,B} \alpha_{\beta}(r) \vec{s}_{\beta} \cdot \vec{i}_{\beta} / \hbar^2, \quad (3.23)$$

contains the electronic and nuclear spin operators \vec{s} and \vec{i} , respectively, and the summation is performed over the two atoms A and B. In the limit of large separations, the functions $\alpha_{\beta}(r)$, which depend on the internuclear separation r , approach the atomic hyperfine constant a_{hf} . The Zeeman interaction is given by

$$H_Z = \sum_{\beta=A,B} (g_{s,\beta} s_{z,\beta} + g_{i,\beta} i_{z,\beta}) \mu_B B / \hbar, \quad (3.24)$$

where g_s (g_i) is the electron (nuclear) g-factor, with respect to the Bohr magneton μ_B (see Arimondo et al., 1977). H_{dd} is the Hamiltonian describing direct magnetic spin-spin, as well as second-order spin-orbit interactions, which causes for example

the observed splitting of p -wave resonances in ${}^6\text{Li}$ - ${}^{133}\text{Cs}$ (see Sect. 3.1). It can be given in its effective form [Strauss et al., 2010]:

$$V_{\text{dip}}(r) = \frac{2}{3}\lambda(r)(3S_Z^2 - S^2), \quad (3.25)$$

where S_Z is a projection of total electron spin S onto the molecular axis. The function

$$\lambda(r) = -\frac{3}{4}\alpha^2 \left(\frac{1}{r^3} + a_{\text{SO}} \exp(-br) \right), \quad (3.26)$$

is given in atomic units with the universal fine structure constant α . The parameters b and a_{SO} for the assumed effective functional form of the second order spin-orbit interaction depend on the microscopic details of the constituent atoms, and will be used as fitting parameters in Sect. 3.4.

The interatomic interaction potential V contains a centrifugal term (cf. Sect. 3.2.2) and the Born-Oppenheimer potentials $U(r)$. The latter incorporates the assumption, that the electron motion occurs much faster than the motion of the heavy nuclei. Thus, the potential energy at each r is given by the ground-state energy of the electron clouds.

At short distances, the potential is strongly repulsive due to the interaction of positively charged atom cores and Pauli blocking of the electrons. In this region, the orientation of the valence electrons' spins of the two atoms becomes important. For alkali atoms, they can amount to a total spin $S = s_A + s_B$ of $S = 0$ (singlet) or $S = 1$ (triplet), which exhibit different potential depths, as depicted in Fig. 3.7(a). This behavior can be explained by the different symmetries of the two configurations. The triplet (singlet) state is symmetric (anti-symmetric), and thus, in order to obtain asymmetric electron wavefunctions, the spatial part must be anti-symmetric (symmetric). Hence, for the singlet configuration the probability of finding the electrons between the atom cores is greatly enhanced simply for symmetry reasons. This position of the negatively charged electrons leads to a screening of the positive nuclei and therefore to a stronger binding between the positive nuclei which results in a deeper molecular potential. The energy difference of the two configurations is given by the exchange part of the potential

$$U_{ex}(r) = \pm A_{ex} r^{\gamma_{ex}} e^{-\beta_{ex} r}, \quad (3.27)$$

where the plus (minus) sign applies for the singlet (triplet) potential. Here, γ_{ex} and β_{ex} , as well as the magnitude A_{ex} depend on the details of the electron clouds and

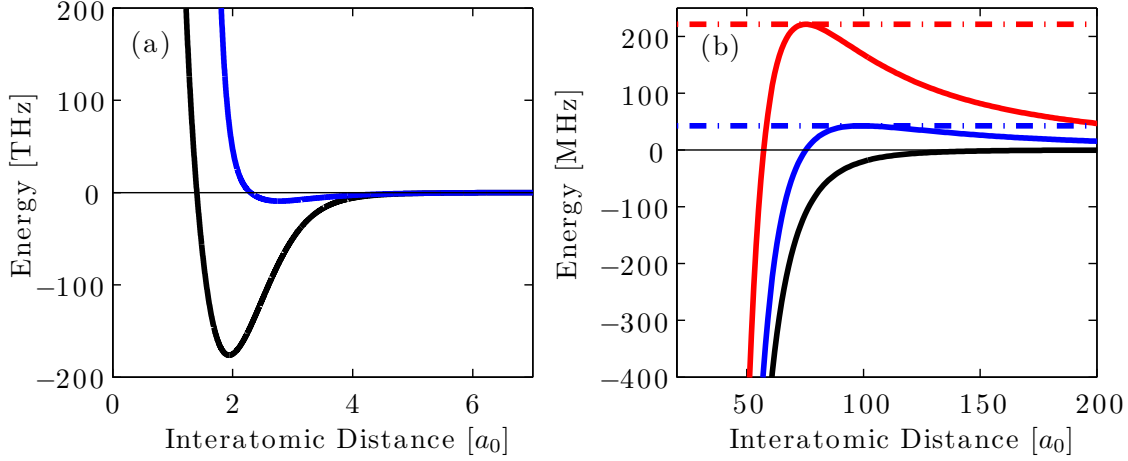


Figure 3.7: Interatomic interaction potentials for the LiCs mixture. (a) Full singlet (black) and triplet (blue) ground state potentials as calculated from a coupled channels calculation (see Sect. 3.4). (b) Long range potential with only van der Waals and centrifugal terms for $l = 0$ (black), $l = 1$ (blue) and $l = 2$ (red). The dash-dotted lines illustrate the rotational barrier (see Eq. (3.30)).

nuclei. The total potential $V = P_0 V_0 + P_1 V_1$ may be projected onto the singlet ($V_{S=0}$) and triplet ($V_{S=1}$) components by the projection operators P_0 and P_1 , respectively.

For distances that exceed the size of an electron cloud of an individual atom, the interaction between the atoms is attractive. The polarizability of the electron clouds induces dipoles, and their Coulomb interaction results in a power-law potential that has the asymptotic form

$$U(r) \rightarrow -\frac{C_6}{r^6} \quad \text{as } r \rightarrow \infty, \quad (3.28)$$

as plotted in Fig. 3.7(b). For systems with angular momentum, a centrifugal term has to be included, as well. The van der Waals coefficient C_6 depends on the details of the electronic configurations, and contains for example the atoms' ionization energies. In general, higher order terms (C_8, C_{10} , etc.) contribute to the potential at intermediate regimes, and retardation effects change the asymptotic potential to a $1/r^7$ form. However, both complications are not essential for the description of the phenomena discussed in this work.

The length scale of the van der Waals interaction

$$r_0 = \frac{1}{2} \left(\frac{2\mu C_6}{\hbar^2} \right)^{1/4}, \quad (3.29)$$

which is also called the van der Waals length, is typically on the order of tens of

Bohr radii for alkali atoms [Chin et al., 2010]. The ${}^6\text{Li}$ - ${}^{133}\text{Cs}$ van der Waals length of $r_0^{\text{LiCs}} = 45a_0$ is much smaller than the mean interatomic distance $n^{-1/3} \sim 1 \mu\text{m}$ for typical thermal cloud densities of $n = 10^{12} \text{ cm}^{-3}$, which describes the situation of a dilute system. This confirms our approach of describing the particle interactions only via collisions. The thermal de Broglie wavelength (see Eq (2.10)) $\lambda_{dB} \sim 1 \mu\text{m}$ for temperatures of $T = 450 \text{ nK}$ ⁸ is on the same order as the interparticle spacing. This means that the particles cannot be treated as point-like particles. Their wave nature has to be taken into consideration, justifying the quantum mechanical treatment presented in this chapter.

The height of the rotational barrier (see Fig. 3.7)

$$U_{rot} = \frac{1}{\sqrt{2C_6}} \left(\frac{\hbar^2 l(l+1)}{3\mu} \right)^{3/2} \quad (3.30)$$

is on the order of 11 mK for ${}^6\text{Li}$ - ${}^{133}\text{Cs}$ d-waves and 2 mK for p-waves. The temperatures used in the current experiments are well below these temperatures, and thus the s-wave components of the partial-wave expansion (see Eq. (3.5)) are sufficient to describe the scattering process.

The manifold of different internal states connected to the Hamiltonian of Eq. (3.22) defines a number of channels for a given space fixed projection M of the total angular momentum of the system. Unless otherwise stated, the coordinates connected to spin and angular momentum are characterized by use of an appropriate basis set like in Hund's coupling case (e) for an atom pair AB:

$$|\chi\rangle \equiv |(s_A, i_A)f_A, m_A; (s_B, i_B)f_B, m_B, l, M\rangle, \quad (3.31)$$

where the electron spin s couples with the nuclear spin i to the atomic angular momentum f with its projection m on the space fixed axis. l is the quantum number of the overall rotation of the atom pair. The basis vectors in Eq. (3.31) can be interpreted in two ways, namely for the field-free case, where f_A and f_B are good quantum numbers or in a magnetic field, where the pair is build up by the eigenvectors of the Breit-Rabi formula and f_A and f_B are approximate quantum numbers to label the corresponding eigenvector. The channel with the same spin state as the incoming atoms is called entrance channel. Those channels with an asymptotic ($r \rightarrow \infty$) energy larger than that of the entrance channel are called closed channels, all others are referred to as open channels.

⁸450 nK is the typical temperature of the gas for the experiments in Chpt 4.

3.3 Three Models for the Calculation of Feshbach Resonances

We begin this section by phenomenologically introducing the appearance of a FR in a simplified two-channel picture in Sect. 3.3.1, where we also identify the part of the Hamiltonian in Eq. (3.22) that causes the coupling between two scattering channels. In principle, it is impossible to solve the Schrödinger equation corresponding to this Hamiltonian without any approximations due to the fact that an infinite number of coupled equations, from an infinite number of basis states, are involved. In the following, we will give a general description how to overcome this difficulty in order to obtain an accurate description of resonance positions by the help of three different models, namely the CC calculation (Sect. 3.3.2), the ABM (Sect. 3.3.3) and the MQDT (Sect. 3.3.4).

3.3.1 Two-Channel Description of a Feshbach Resonance

Other than the shape resonances introduced in Sect. 3.2.2, where the bound-state that causes the divergence of the scattering length originates from the potential of the incoming channel, the situation for the magnetically tunable FRs employed in atomic physics is different. Here, the resonance is caused by a weak coupling to a bound-state in a different hyperfine channel. We explore the origin of the resonance in this scenario following Moerdijk et al., 1995, as this approach is the basis of the ABM model presented in Sect. 3.3.3.

We start by projecting the Hamiltonian of Eq. (3.22) onto the open and closed channel subspaces via the projection operators P and Q , respectively. This results in a set of coupled Schrödinger equations

$$(E - \mathcal{H}_{PP})\psi_P = \mathcal{H}_{PQ}\psi_Q \quad (3.32)$$

$$(E - \mathcal{H}_{QQ})\psi_Q = \mathcal{H}_{QP}\psi_P, \quad (3.33)$$

where P (Q) denotes the projection onto the open (closed) channel Hilbert space and $\mathcal{H}_{ij} = \hat{i}\mathcal{H}\hat{j}$ for $\{\hat{i}, \hat{j}\} = \{P, Q\}$. The energy E for this section is defined with respect to the incoming channel's dissociation threshold. Applying the Green operator $\frac{1}{E^+ - \mathcal{H}_{QQ}}$ with $E^+ = E + i\delta$, where δ approaches zero from positive values, to Eq. (3.33) yields

$$\psi_Q = \frac{1}{E^+ - \mathcal{H}_{QQ}}\mathcal{H}_{QP}\psi_P. \quad (3.34)$$

Substituting Eq. (3.34) into (3.32), results in the effective equation for the scattering process in the open channel

$$(E - \mathcal{H}_{\text{Eff}}) \psi_P = 0, \quad (3.35)$$

with $\mathcal{H}_{\text{Eff}} = \mathcal{H}_{PP} + \mathcal{H}_{PQ} \frac{1}{E^+ - \mathcal{H}_{QQ}} \mathcal{H}_{PQ}$. The second term in \mathcal{H}_{Eff} mimics a transition from the open to the closed channel, where the system propagates for a certain time, and then returns to the P -channel. The Green operator can be expanded to a complete set of eigenstates of \mathcal{H}_{PP} which contains bound-states and energy-normalized scattering states. In order to avoid the tedious treatment of continuum states, however, one can alternatively expand the propagator to Gamov resonances, which leads to a Mittag-Leffler expansion, as explained in Marcelis et al., 2004. This effective single channel treatment forms the validation for the ABM in Sect. 3.3.3. When a bound-state ϕ_B with energy ϵ_B is sufficiently close to the energy of the incoming atoms, so that all other terms of the expansion can be neglected, the solution of Eq.(3.35) reduces to

$$|\psi_P\rangle = |\psi_i^+\rangle + \frac{1}{E^+ - \mathcal{H}_{PP}} \mathcal{H}_{PQ} |\phi_B\rangle \frac{\langle \phi_B | \mathcal{H}_{QP} | \psi_i^+ \rangle}{E - \epsilon_B - \langle \phi_B | \mathcal{H}_{QP} \frac{1}{E^+ - \mathcal{H}_{PP}} \mathcal{H}_{PQ} | \phi_B \rangle}. \quad (3.36)$$

Here, $|\psi_i^+\rangle$ denotes an incoming wave in channel i , which is also an eigenstate of \mathcal{H}_{PP} . The transition amplitude for an incoming channel i and an outgoing channel j is given by

$$S_{ij} = S_{ji}^0 - 2\pi i \frac{\langle \psi_j^- | \mathcal{H}_{PQ} | \phi_B \rangle \langle \phi_B | \mathcal{H}_{QP} | \psi_i^+ \rangle}{E - \epsilon_B - \langle \phi_B | \mathcal{H}_{QP} \frac{1}{E^+ - \mathcal{H}_{PP}} \mathcal{H}_{PQ} | \phi_B \rangle}, \quad (3.37)$$

where S_{ji}^0 is a 'direct' term that describes the coupling within the P -channel. In our experiments, the atoms are often in their energetically lowest states, reducing the number of open channels to only one. Hence, the S -matrix for the only open P -channel with a coupling to a bound-state in the Q -channel can be written as

$$S(E) = S_P(E) \left(1 - 2\pi i \frac{|\langle \phi_Q | \mathcal{H}_{QP} | \psi_P^+ \rangle|^2}{E - \epsilon_Q - \mathcal{A}(E)} \right), \quad (3.38)$$

where the subscript for the bound-states now indicate their origin in the Q -space, and the direct matrix in P -space is denoted as $S_{ii}^0 = S_P(E) = S_P(k)$. The elastic S -matrix element in Eq (3.38) is related to the scattering phase shift $\delta(k)$ via $S(k) = e^{2i\delta(k)}$.

The complex energy shift

$$\mathcal{A}(E) = \langle \phi_Q | \mathcal{H}_{QP} \frac{1}{E^+ - \mathcal{H}_{PP}} \mathcal{H}_{PQ} | \phi_Q \rangle \quad (3.39)$$

describes the shift of the bare bound-state $|\phi_Q\rangle$ due to the coupling with the P -channel. $\mathcal{A}(E) = \Delta(E) + \frac{i}{2}\Gamma(E)$ can be decomposed into its real component $\Delta(E)$ and the imaginary part $\Gamma(E)$. For energies above the scattering threshold ($E > 0$), the unperturbed bound-state ϵ_Q can be interpreted as a quasi bound-state that is shifted by $\Delta(E)$ and has a finite width $\Gamma(E)$. For energies below the continuum threshold, the energy shift is purely real, and $\Gamma(E) = 0$.

The closed channel consists of a pair of atoms in a hyperfine channel (see Eq. (3.31)) with different nuclear and electron spin quantum numbers as compared to the incoming channel. Thus, the two channels exhibit different magnetic field dependent energy shifts (cf. Eq. (3.24)). When a bound-state in the closed channel is sufficiently close to the (threshold) energy of the incoming channel, one can bring both channels into degeneracy by applying a magnetic field B . In this situation the S -matrix of Eq. (3.38) has a pole, since its denominator becomes infinitely small, which results in a diverging scattering length a . In a simplified picture, one would expect the resonance to occur when the energy of the bare molecular bound-state is degenerate with the incoming atoms' energy. This is exactly the assumption of the bare ABM, as introduced in Sect. 3.3.3. This approximation is only appropriate when the coupling between the incoming atoms and the resonant channel is very small. In all other cases, Eq. (3.39) shows that the molecular energy including the shifts due to the coupling need to have the same energy as the incoming pair for a resonance to occur. This shift is approximated in the dressed ABM in Sect. 3.3.3.

At low collision energies, the surviving part of the incoming wave $|\psi_P^+\rangle$ is proportional to $\sqrt{k} \sim E^{1/4}$ in the range of the exchange interaction [Taylor, 1972]. When the direct S -matrix is described via a background scattering length a_{bg} , Eq (3.38) reduces to

$$S(k) = e^{-2ika_{bg}} \left(1 - \frac{2iCk}{iCk - \epsilon_{res}(B)} \right), \quad (3.40)$$

where the magnetic field dependence of $\epsilon_{res}(B) = \epsilon_Q(B) + \Delta(B)(E = 0)$ due to the Zeeman Hamiltonian in Eq. (3.24) has been included explicitly. C is a positive constant that characterizes the coupling strength between P and Q space. Setting Eq. (3.40) equal to $e^{-2i\delta(k)}$ yields

$$a(B) = a_{bg} - \frac{C}{\epsilon_{res}(B)}, \quad (3.41)$$

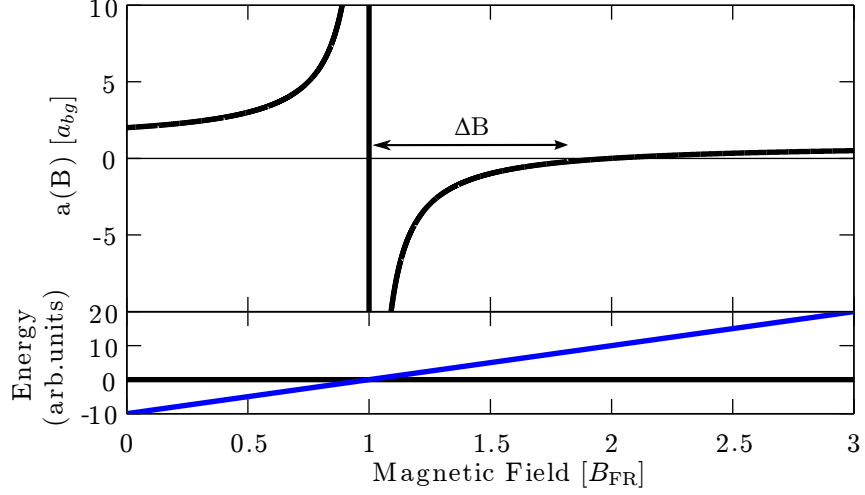


Figure 3.8: Scattering length and binding energy as a function of magnetic field. The upper panel shows the scattering length according to Eq. (3.42). The resonance width ΔB is indicated by the arrow. The lower panels plots the bound-state energy (blue line) with respect to the energy of the incoming channel (black line) as function of magnetic field. For simplicity, the coupling between bound-state and incoming channel has been neglected.

where a_{bg} and C are depending only weakly on B . The resonant part only plays an important role near the pole B_{FR} of the S -matrix. Taking the field dependence of $\epsilon_{\text{res}}(B) = (2\mu_P(B_{\text{FR}}) - \mu_Q(B_{\text{FR}}))(B - B_{\text{FR}})$ into account results in the well-known dispersive behavior

$$a(B) = a_{bg} - \frac{C}{2\mu_P(B_{\text{FR}}) - \mu_Q(B_{\text{FR}})} \frac{1}{B - B_{\text{FR}}} = a_{bg} \left(1 - \frac{\Delta B}{B - B_{\text{FR}}} \right), \quad (3.42)$$

Here, the FR width ΔB , which is the difference in field between scattering pole and zero crossing of the scattering length, has been introduced. $\mu_P(B_{\text{FR}})$ is the magnetic moment of the incoming channel that consists of two single atom magnetic moments, and $\mu_Q(B_{\text{FR}})$ is the magnetic moment of the two-atom resonant state. This behavior is schematically shown in Fig. 3.8, where we also illustrate the behavior of $\epsilon_Q(B)$ with respect to the energy of the incoming continuum.

Up to this point we have not considered which part of the Hamiltonian in Eq. (3.22) causes the coupling between different channels. In order to clarify the actual coupling mechanism, we go to a basis in which $T + V$ is diagonal, namely $|\beta\rangle = |\psi_{Sl}\rangle |\sigma\rangle$, where $|\psi_{Sl}\rangle$ handles the spatial dependency, and $|\sigma\rangle = |S, i_A, i_B\rangle$ denotes the spin degrees of freedom. For an $l = 0$ partial wave, H_{dd} of Eq. (3.22) couples to d -waves. For $l \neq 0$ H_{dd} leads to a coupling between different $|\beta\rangle$ states,

however, in both cases this coupling is extremely weak and results in FRs that are usually too narrow to be detected experimentally. Thus, H_{dd} is not the cause of the ${}^6\text{Li}$ - ${}^{133}\text{Cs}$ resonances found in Sect. 3.1 and merely leads to a lifting of the degeneracy of different l projections on the space fixed axis, resulting in a splitting of p -wave resonances, as analyzed in Sect. 3.4.2 and illustrated in Fig. 3.3. The Zeeman term in Eq. (3.24) is obviously diagonal in $|\beta\rangle$ and thus cannot explain the coupling between different channels. From the structure of the hyperfine interactions as given in Eq. (3.23), one can see that they mix the different $|\beta\rangle$ states. The inelastic collisions and FRs occur because this term does not commute with the potential operator of Eq. (3.22). As a result, we can identify the dominating components of \mathcal{H}_{PQ} and \mathcal{H}_{QP} with the hyperfine interaction. With the complete understanding of the underlying scattering processes, we can now proceed to explore different ways of calculating the positions of Feshbach resonances.

3.3.2 The Coupled Channels Calculation

The coupled channels calculation is a numerical approach to solve the Schrödinger equation resulting from the Hamiltonian of Eq. (3.22). For bound states, r is represented on a grid and the resulting matrix is diagonalized, while for scattering solutions, the logarithmic derivative of the wavefunction is propagated in discrete steps with optimized step size from low r to large r , from which the phase shift is determined by comparing with asymptotic wavefunctions. To calculate bound states, the wavefunctions at small separations r_{in} and large separations r_{out} (up to $10^4 a_0$ for the weakest bound levels, where a_0 represents the Bohr radius) are set to zero as boundary conditions. This is equivalent to adding an infinitely high potential wall at r_{in} and r_{out} , resulting in discretized continuum states, often referred to as box states. As this leads to shifts of the calculated resonance states, the size of the modeled box potential will be increased until achieving the desired accuracy.

Furthermore, in order to obtain a finite number of equations, the basis set is truncated, which is usually called close-coupling calculation. The attribute "close" refers to the fact that only states which are "close" in energy to each other, are retained. In the present approach the truncation is only in the space spanned by the rotational quantum number l and naturally by using only the two molecular ground states $X^1\Sigma^+$ and $a^3\Sigma^+$. We span all spin channels allowed by given s_A and s_B as well as i_A and i_B and the chosen space fixed projection M of the total molecular angular momentum. The coupling to higher electronic states exists but is weak and to some degree contained in H_{dd} . For collisions of alkali atoms in the

ground state at ultracold temperatures, only a limited number of partial waves l has to be included, owing to the small collision energy.

Performing the numerical procedure for a fine grid of magnetic fields yields the field dependent collisional properties, e.g. scattering lengths, collisional cross sections and collision rates. The procedure as we apply it, is specified in Marzok et al., 2009 and Schuster et al., 2012, and our results for ^6Li - ^{133}Cs are provided in Sect. 3.4.1.

3.3.3 The Asymptotic Bound State Model

The ABM simplifies the calculation of the coupled Schrödinger equations by replacing the kinetic energy term and the interatomic potentials in Eq. (3.22) by their bound-state energies as adjustable parameters for describing the observed FRs, and neglecting the scattering continuum [Tiecke et al., 2010; Goosen et al., 2010]. Therefore, neither accurate potentials, which are often not available, nor numerical integration of the spatial Schrödinger equation are needed. Solving the eigenvalue problem with the approximate Hamiltonian reduces to a simple matrix diagonalization of low dimension, which is the major benefit of the model. The ABM [Tiecke et al., 2010] has been introduced in Wille et al., 2008 and builds upon a model by Moerdijk et al. [Moerdijk et al., 1995]. Since then it has been extended to include various physical phenomena which has been applied to describe FRs in many systems [Wille et al., 2008; Li et al., 2008; Voigt et al., 2009; Deh et al., 2010; Knoop et al., 2011; Goosen et al., 2010; Tscherbul et al., 2010; Repp et al., 2013; Park et al., 2012; Goosen, 2011]. The ABM model is explained in detail in Tiecke et al., 2010 and here we present a summary and describe various extensions to the model.

We begin by considering zero-energy collisions ($E_{kin} = 0$) and restrict ourselves to s -wave collisions where $\langle H_{dd} \rangle = 0$. The model introduced by Moerdijk et al. [Moerdijk et al., 1995] neglected coupling of the singlet and triplet states reducing the Hamiltonian in Eq.(3.22) to: $H = \epsilon_{0,1} + H_{\text{hf}}^+ + H_Z$ where $\epsilon_{0,1}$ represent the singlet and triplet bound state energies and H_{hf}^+ is the part of the hyperfine interaction which does not couple singlet and triplet states. This is a valid approximation for the special case that the spacing between the singlet and triplet energies is larger than the hyperfine energy. In the ABM, the full hyperfine interaction $H = \epsilon_{0,1} + H_{\text{hf}} + H_Z$ is included, which generalizes the Moerdijk model to systems with arbitrary bound state energies, and the singlet triplet coupling is characterized by the overlap integral $\zeta_l = \langle \Psi_{S=0}^l | \Psi_{S=1}^l \rangle$ of the singlet ($|\Psi_{S=0}^l\rangle$) and triplet ($|\Psi_{S=1}^l\rangle$) wavefunctions times the nondiagonal part of the Hamiltonian.

In the ABM the Hilbert space consists of only bound states and no scattering states. Therefore, the calculation includes only the basis states

$$|\sigma\rangle \equiv |SM_S m_{iA} m_{iB} v_{n,S} l\rangle \quad (3.43)$$

of pure electron spin states $S = 0$ or $S = 1$, which will be related to the respective channels at a later stage for a pair of vibrational levels of the singlet and triplet state together. M_S, m_{iA} and m_{iB} are the projections onto the space fixed axis of the operators S, i_A and i_B , respectively, and $v_{n,S}$ is the n -th vibrational state in the $S = 1$ or $S = 0$ potential. The FRs are found at the magnetic fields for which an eigenstate at the energy of the incoming atom pair at that field exists. This condition corresponds to $E_{kin} = 0$. Additionally, if $\langle H_{dd} \rangle$ is small enough to be neglected, the Hamiltonian in Eq.(3.22) is diagonal in the partial wave quantum number l . As a result, the only parameters needed for the calculation of the FRs in each partial wave l are the energies of the bound states ϵ_S^l of the singlet ($S = 0$) and triplet ($S = 1$) potentials and their wavefunction overlap ζ_l . In fact, only a small number of such states has to be taken into consideration, because the FRs usually arise from the least bound states close to the asymptote. The energies ϵ_S^l and the overlap parameters ζ_l are the free parameters of the ABM and are typically obtained by fitting to experimentally observed FRs.

The resulting Schrödinger equation can be written in the form of a $N \times N$ matrix, denoted by \underline{M}_{ABM} , where N is determined by the number of spin channels and the number of selected vibrational states; N is on the order of a few tens. The diagonalization of this matrix for different fields provides the molecular energies as a function of the magnetic field. A comparison of this function to the energy sum of the two atoms yields the magnetic fields, at which the energies of bound-states and incoming free atoms are degenerate, thus marking the position of the FRs (as e.g. depicted in Fig. 3.10).

Close to a s -wave resonance, the molecular state –and therefore the resonance position– is shifted due to coupling to the scattering states of the open channel. These states are continuum states and hence not included in the ABM model as described above. However, in some systems, the coupling has such a severe effect on the resonance position that it cannot be neglected. It can be approximated by the coupling of the resonant molecular state to the least bound state of the open channel [Tiecke et al., 2010], which requires assigning the bound-states of \underline{M}_{ABM} to the scattering channels.

For this purpose, a rotation of the basis of \underline{M}_{ABM} is performed: from the $|\sigma\rangle$

basis to the basis formed by the eigenvectors of $H_{\text{hf}} + H_Z$ at the desired magnetic field (see Eq. (3.31)). This can be ordered in the block matrix

$$\underline{M}'_{ABM} = \begin{pmatrix} \mathcal{H}_{PP} & \mathcal{H}_{PQ} \\ \mathcal{H}_{QP} & \mathcal{H}_{QQ} \end{pmatrix}, \quad (3.44)$$

where the index P (Q) stands for the spin states which are associated with an open (closed) channel and it might include possible l partial waves. This form is equivalent to the treatment in Sect. 3.3.1. A diagonalization of the submatrix \mathcal{H}_{QQ} provides the bare molecular energies ϵ_Q , which are the energies of the molecular state when no coupling to the open channel bound state occurs. One of these states is the resonant state which causes the FR under consideration.

With the assumption that near a resonance the system can be described in a two channel picture, with one incoming, open channel and one resonant, closed channel, the total S -matrix of the scattering problem in the open channel can be written in the simple form of Eq. (3.38). For the calculation of the Feshbach resonances, which are given by the poles of the scattering matrix, the complex energy shift $\mathcal{A}(E)$ locating the pole needs to be estimated. Depending on whether a bound state or a virtual state dominates the scattering behavior, different expressions have to be used for $\mathcal{A}(E)$.

In ^{40}K - ^{40}K collisions, for example, a real bound state of the open channel (with wavenumber $k_p = i\kappa_{bs}$ with $\kappa_{bs} > 0$) occurs close to resonance resulting in a large positive background scattering length. In this case $\mathcal{A}(E)$ is given by [Tiecke et al., 2010]

$$\mathcal{A}(E) = \frac{\mu}{\hbar^2} \frac{-iA}{\kappa_{bs}(k - i\kappa_{bs})}, \quad (3.45)$$

where κ_{bs} is the wavevector associated with the bare energy of the open channel $\epsilon_{bs} < 0$, which is found on the diagonal of the submatrix \mathcal{H}_{PP} in Eq. (3.44). The coupling term A is the square of the appropriate off-diagonal matrix element in \mathcal{H}_{PQ} between the P -channel and the resonant Q -channel, after the Q subspace has been diagonalized and \underline{M}'_{ABM} has been transformed to the eigenvector of Q space. This procedure allows for a prediction of the resonance width (imaginary part of $\mathcal{A}(E)$) and shift (real part of $\mathcal{A}(E)$) arising from coupling to the continuum without additional parameters. Using the S -matrix, the scattering properties around the resonance can be derived. In the present case we consider only the positions of Feshbach resonances; these will appear at $E = 0$ and $k = 0$ for a magnetic field where the bare molecular energy satisfies $\epsilon_Q = -(\mu/\hbar^2)A/\kappa_{bs}^2 = -A/2|\epsilon_{bs}|$.

A virtual state, which is also often referred to as an anti-bound state ($k_p = -i\kappa_{vs}$ and $\kappa_{vs} > 0$ [Marcelis et al., 2004]) results in a large negative background scattering length. The ${}^6\text{Li}$ – ${}^6\text{Li}$ [Abraham et al., 1997] and ${}^{133}\text{Cs}$ – ${}^{133}\text{Cs}$ [Leo et al., 2000] systems are excellent examples for a system with a dominating virtual state. In this scenario, the complex energy shift is given by [Marcelis et al., 2004]

$$\mathcal{A}(E) = \frac{\mu}{\hbar^2} \frac{-iA_{vs}}{\kappa_{vs}(k + i\kappa_{vs})}, \quad (3.46)$$

where the coupling between virtual and bound state A_{vs} enters as new parameter, while κ_{vs} can be estimated from the van der Waals range r_0 via $a_{bg} = r_0 - 1/\kappa_{vs}$. To find the position of FRs one has to look for magnetic fields where the binding energy of the bare molecular state $\epsilon_Q = +(\mu/\hbar^2)A_{vs}/\kappa_{vs}^2$.

To calculate the background scattering length of the desired open channel a_{bg} , one requires the singlet (a_S) and triplet (a_T) background scattering lengths, as well as a decomposition of the ABM matrix eigenstates into singlet and triplet components. a_S and a_T can be estimated via the accumulated phase method, which employs a numerical calculation of the singlet and triplet wavefunctions from the asymptotic form of the inter-atomic potential V_{as} , using only the van der Waals tail plus adding the centrifugal barrier and the bound state energies. This procedure is described in Tiecke et al., 2010 and Verhaar et al., 2009. Obtaining the poles of the S -matrix for a system in which the virtual state dominates the scattering behavior has been utilized in Park et al., 2012 to explain FRs in a NaK mixture using the ABM.

The ${}^6\text{Li}$ – ${}^{133}\text{Cs}$ system, however, is in an intermediate regime, where both the bound state and the virtual state in the open channel are required to describe the FR positions. In Sect. 3.4.2 we demonstrate an extension of the existing models, that starts from the virtual state description, but includes the coupling to the bound state in a phenomenological way.

3.3.4 The Multichannel Quantum Defect Theory

The MQDT uses a separation of the solution to the Schrödinger equation into a long-range and a short-range part. It is based on a model by Seaton [Seaton, 1983], which was originally introduced to describe the properties of an electron in the field of an ion. However, it has been generalized in Greene et al., 1979 and Greene et al., 1982 and can now be applied to a variety of collisional partners, with all sorts of interaction potentials (see Croft et al., 2011 and references therein). For example, it has been applied successfully to various neutral atom pairs [Burke et al., 1998;

Gao et al., 2005; Raoult and Mies, 2004; Mies and Raoult, 2000; Julienne and Mies, 1989; Gao, 1998; Gao, 2001], and can, in general, be used for all alkali atom combinations without adaptation. The most recent modification improves the model for an accurate description of higher partial waves [Ruzic et al., 2013].

The main benefit of the model stems from the separate treatment of the long-range part of the scattering problem, where the van der Waals interaction dominates over exchange interactions and higher order terms. It can be solved accurately using the Milne phase amplitude method (see Burke et al., 1998 and references therein). This results in a linearly independent pair of functions (f^0, g^0) , referred to as base pair, which are smooth and analytic functions of energy. In the short-range part, the coupled Schrödinger equation at energy E is numerically integrated outwards to a radius r_{lr} on the order of a few tens of atomic units (typically $30 a_0$), beyond which the exchange interaction is negligible. At r_{lr} it is then connected to the long-range part of the solution.

The calculation incorporates only those channels which have a non-negligible effect on the scattering behavior of the system by truncating the basis set of Eq. (3.31) in the same manner as for the CC model. The solution is given by the square matrix $\underline{M}(r)$, which contains the independent solutions of each channel in its columns. Beyond r_{lr} , $\underline{M}(r)$ can be given as superposition of the base pair:

$$\underline{M}(r) = \underline{f}^0(r) - \underline{g}^0 \underline{K}^{sr}, \quad (3.47)$$

where \underline{f}^0 and \underline{g}^0 are diagonal matrices which contain the base pair evaluated at the appropriate channel energies $\epsilon_i = E - E_i$. In this notation E_i is the energy of the asymptote of channel i . The short-range reaction matrix \underline{K}^{sr} contains all the system specific information for the scattering behavior at low energies. Besides the short-range reaction matrix, one needs four coefficients in order to construct the S -matrix, which delivers the physical observables. Detailed instructions on how to obtain these coefficients, which are often noted⁹ as A , \mathcal{G} , γ and η , is given in Ruzic et al., 2013, Burke et al., 1998, and Burke, 1999.

The next level of simplification of the MQDT is the assumption that \underline{K}^{sr} depends only very weakly on energy. Thus it only needs to be calculated for a few energies, and can then be interpolated between these values. In the best case, a \underline{K}^{sr} matrix which is only calculated for one energy (typically close to threshold) and at zero magnetic field can be utilized to describe the scattering properties over a wide range of energies and magnetic fields. However, for obtaining \underline{K}^{sr} , one still has to solve

⁹Note that the Ruzic et al., 2013 paper changed the notation from $\tan\beta$ to $\cot\gamma$.

the coupled channel equations at short-range.

Nevertheless, the calculation can be facilitated further by using a frame transformation (FT) approach. The general form of the FT theory as applied to ultracold collisions of two alkali atoms has been written in Burke et al., 1998, Burke, 1999, and Gao et al., 2005. The main simplification is to neglect the hyperfine interaction at short-range. This is justified by the fact that the exchange splitting is much larger than the hyperfine and Zeeman energy. In this case the atomic motion is described by a set of uncoupled channel equations, whose numerical calculation is much less complex as compared to coupled equations. Matching the solutions to the analytic base pair allows one to determine the short-range energy-analytic scattering information in terms of quantum defects $\mu_S^{sr}(\epsilon_S)$ in the single-channel singlet-triplet basis (equivalently the singlet and triplet scattering lengths recast as quantum defects) in a diagonal short-range reaction matrix $K_{\text{diag}}^{sr} = \tan(\pi\mu)$. An energy independent real orthogonal transformation turns this short-range single-channel scattering information into the final channel structure applicable at $r \rightarrow \infty$, namely the representation of hyperfine plus Zeeman atomic energy eigenstates. This procedure, delivers the real, symmetric, short-range reaction matrix K^{sr} (or corresponding smooth quantum defect matrix μ^{sr}):

$$K_{ij}^{sr} = \sum_{\alpha} U_{i,\alpha} \tan(\pi\mu_{\alpha}) \tilde{U}_{\alpha,j}. \quad (3.48)$$

Here the tilde denotes the matrix transpose. The dissociation channel index i represents the set of quantum numbers according to Eq. (3.31) needed to characterize the internal energies of the separating atoms as well as their relevant angular momentum couplings with each other and with the orbital angular momentum quantum number l and its projection m_l .

As was stressed by Bo Gao in his "angular momentum insensitive" form of quantum defect theory for a van der Waals long-range potential, the l -dependence is known approximately [Gao, 2001] as $\mu_{S,l}^{sr} \approx \mu_S^{sr} - l/4$ [Ruzic et al., 2013]. When higher accuracy is needed, a small l -dependent correction α_l can be introduced to this equation, which leads to:

$$\mu_{S,l}^{sr} \approx \mu_S^{sr} - l/4 + \alpha_l, \quad (3.49)$$

where $\alpha_0 \equiv 0$ by definition. The FT then simply approximates the real, orthogonal matrix that diagonalizes K^{sr} as the angular momentum recoupling matrix that connects the short-range eigenstates with those appropriate at large r . Specifically, in the absence of any magnetic field, good quantum numbers of the atomic energy

levels are given by Eq. (3.31). In the presence of an external magnetic field B directed along the z -axis, f_A and f_B are no longer good quantum numbers but m_A, m_B are still conserved for the atoms at infinite separation. However one must diagonalize the atomic hyperfine plus Zeeman Hamiltonian to obtain a numerical eigenvector $\langle f_A m_A, f_B m_B | m_A k_A, m_B k_B \rangle \equiv \langle i | j \rangle$ and the corresponding field-dependent channel energies, $E_{m_A k_A, m_B k_B}(B) \equiv E_j(B)$ (see also the extended interpretation for the basis given in Eq. (3.31)). We indicate the short-range collision eigenstates by $|(s_A s_B) S(i_A, i_B) I f m_f \rangle \equiv |\alpha \rangle$. We can now write out the final FT matrix $U_{i\alpha}$ between the long- and short-range channels, which is needed in Eq. (3.48). Recall that in the present notation, the long-range scattering channels in the presence of a magnetic field B are written as $i = \{m_A, k_A, m_B, k_B\}$, and the short-range collision eigenchannels are $\alpha = \{(s_A, s_B) S(i_A, i_B) I, f m_f\}$, and the unitary transformation between these is given explicitly in terms of standard angular momentum coefficients (Clebsch-Gordan and Wigner 9-j symbol) and the Breit-Rabi eigenvectors such as $\langle k_A | f_A \rangle^{(m_A)}$, etc. as:

$$U_{i\alpha} = \sum_{f_A f_B f} \langle k_A | f_A \rangle^{(m_A)} \langle k_B | f_B \rangle^{(m_B)} \langle f_A m_A, f_B m_B | f m_f \rangle \times \langle (s_A i_A) f_A (s_B i_B) f_B | (s_A, s_B) S(i_A, i_B) I \rangle^{(f)} \quad (3.50)$$

Note that in the FT approximation, this matrix is independent of l , so this quantum number is not explicitly represented. The transformation mentioned for the ABM is constructed in the same way.

Note that the final step of computing scattering or bound state observables such as the FRs at zero incident energy in various scattering channels requires solving the MQDT equations as a function of energy and/or magnetic field. As usual in MQDT studies, this is the step where exponential decay of the large- r closed-channel radial solutions is imposed. The determinantal condition for a resonance to occur at an energy just above an open-channel threshold is $\det(K_{QQ}^{sr} + \cot \gamma) = 0$, where the notation K_{QQ}^{sr} indicates just the closed-channel partition of the full short-range K -matrix. In this equation, γ is a diagonal matrix of long-range negative energy phase parameters as used above for the MQDT.

The energy- and field-analytic nature of the single-channel solutions allows them to be constructed on a very coarse mesh of energy and magnetic field. In its most simple form, the energy dependence of the quantum defects can be dropped, and the quantum defects, which are calculated at a specific energy only once, can be used throughout the entire energy and magnetic field range of interest. Burke et al.,

1998 and Gao et al., 2005 demonstrate how the quantum defects can be represented by only two parameters, namely a_S and a_T , in the FT formalism. This yields the crudest, but also computationally lightest realization of the MQDT.

The details for a calculation of ${}^6\text{Li}$ - ${}^{133}\text{Cs}$ FRs using the MQDT are given in Sec. 3.4.3. Additionally, we introduce a slightly modified MQDT-FT approach, which allows us to calculate FRs for systems that are lacking a detailed microscopic model.

3.4 Application of the models to the ${}^6\text{Li}$ - ${}^{133}\text{Cs}$ System

In this chapter we apply the models described in Sect. 3.3 as a case study to the ${}^6\text{Li}$ - ${}^{133}\text{Cs}$ system. Throughout the entire section, we use the C_6 coefficient from Derevianko et al. [Derevianko et al., 2001] for the description of the van der Waals interaction, which has been calculated with sufficient accuracy. In order to compare the models among themselves and with experiment, we calculate the weighted rms deviation δB^{rms} on the resonance positions, which is defined as

$$\delta B^{rms} = \frac{\sqrt{(\sum_i^N \delta_i^2 / \delta B_i^2) / N}}{\sqrt{\sum_i^N \delta B_i^{-2}}}. \quad (3.51)$$

The summation is performed over N resonances, $\delta = B_{\text{res}}^{\text{exp}} - B_{\text{res}}^{\text{theo}}$ is the deviation of experimental ($B_{\text{res}}^{\text{exp}}$) and theoretical ($B_{\text{res}}^{\text{theo}}$) resonance positions, and δB_i contains the experimental uncertainty of the measured resonance positions, which are given in Table 3.1, and a 200 mG drift of the magnetic field for all resonances.

3.4.1 The Coupled Channels Calculation

We have provided details of the CC calculation for a mixture of ${}^6\text{Li}$ and ${}^{133}\text{Cs}$ atoms elsewhere (see Repp et al., 2013 and references therein). Here, we review the method of our CC calculation and summarize its results, as they are used as benchmark for the other approximate models presented in the subsections below.

For the CC matrix, the Hamiltonian of Eq. (3.22) is employed, where the effective form of H_{dd} (Eq. (3.25)) is used. Only basis states with partial waves up to $l = 2$ are included, which is sufficient for the descriptions of alkali atoms in the μK regime. Besides the atomic constants, which are readily available in the liter-

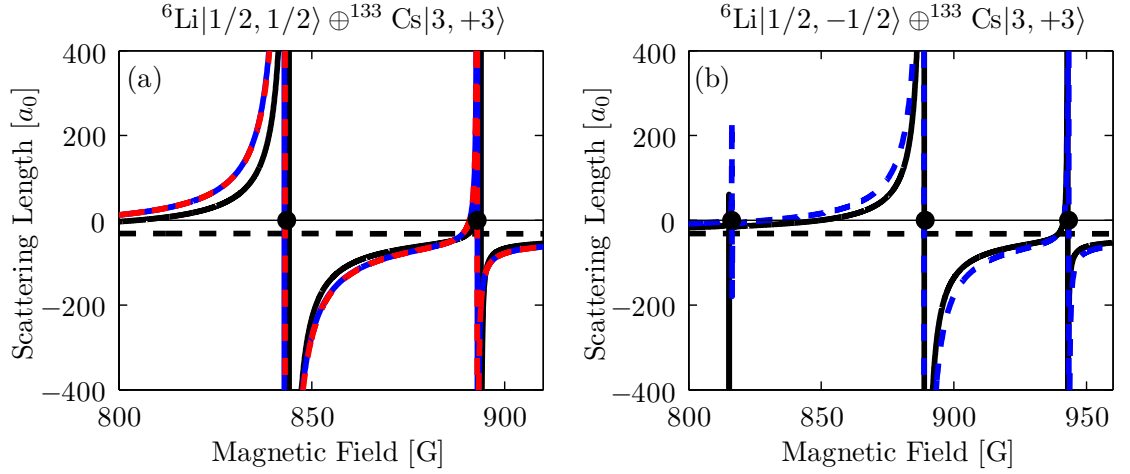


Figure 3.9: Scattering length for the two energetically lowest channels.

The scattering lengths (black solid lines) and the background scattering lengths (black dashed lines) deduced from the ABM are shown for the energetically lowest (a) and second lowest (b) channels indicated in the figure title. For comparison, the scattering lengths from the CC calculation are also plotted (blue dashed lines), as well as the MQDT values (red dashed line) in (a). The experimentally measured FR positions are indicated by a black dot.

ature [Arimondo et al., 1977], accurate potentials are crucial in order to precisely determine the position of FRs. For this purpose, the relevant potential curves for the $\alpha^3\Sigma^+$ and $X^1\Sigma^+$ states of ${}^6\text{Li}-{}^{133}\text{Cs}$ are expanded in a power series of the internuclear separation r (similar to Gerdes et al., 2008), where r is mapped onto a Fourier grid following Tiesinga et al., 1998. Then, the expansion coefficients, which were initially determined via Fourier-transform spectroscopy [Staanum et al., 2007], are modified iteratively in such a way that both the calculated maxima of binary collision rates and the rovibrational transition frequencies are in agreement with the measured FRs and with the 6498 previously observed molecular transitions [Staanum et al., 2007], respectively. The potential parameters are summarized in the online material of Pires et al., 2014a, the parameters of the bound states, which are involved in the observed FRs, are given in Table 3.2 and the resulting resonance positions in Table 3.3. The rms deviation for this model is 39 mG. The obtained s -wave scattering lengths are depicted in Fig. 3.9, and the molecular energy levels for the ${}^6\text{Li}|1/2, -1/2\rangle \oplus {}^{133}\text{Cs}|3, 3\rangle$ channel with respect to the incoming channel are given in Figure 3.10.

Model	ϵ_0^0 (MHz)	ϵ_1^0 (MHz)	ζ_0	ϵ_0^1 (MHz)	ϵ_1^1 (MHz)	ζ_1	a_S (a_0)	a_T (a_0)
CC	1566	3942	0.866	1159	3372	0.866	30.3(1)	-34.3(2)
bABM	1592	4189	0.866	1191	3641	0.860	29.6	-42.4
dABM	1543	4155	0.870	1191	3641	0.860	30.7	-40.8
MQDT	1565	3945	0.866	1158	3375	0.862	30.3	-34.4
MQDT-FT	-	-	-	-	-	-	30.1	-39.2

Table 3.2: List of bound state energies ϵ_S^l , wavefunction overlaps ζ_l and background scattering lengths as for singlet ($S = 0$) and triplet ($S = 1$) potentials and $l = 0, 1$. The fit results for the CC calculation, the bare ABM (bABM), the dressed ABM (dABM), the MQDT, and the MQDT-FT are tabulated. Note that the $l = 1$ values for the bABM and the dABM are taken from the same fit. The scattering lengths indicated for the ABM are derived from the binding energies using the accumulated phase method.

Entrance channel	1	$B_{\text{res}}^{\text{exp}}$ (G)	ΔB^{exp} (G)	δ_{CC} (G)	δ_{bABM} (G)	δ_{dABM} (G)	δ_{MQDT} (G)	$\delta_{MQDT-FT}$ (G)
${}^6\text{Li} 1/2, +1/2\rangle$ $\oplus {}^{133}\text{Cs} 3, +3\rangle$	1	662.79(1)	0.10(2)	-0.04	-0.04	—	-0.11	-0.26
	1	663.04(1)	0.17(2)	-0.02	-0.37	—	-0.01	0.01
	1	713.63(2)	0.10(3)	-0.05	-0.82	—	-0.09	-0.22
	1	714.07(1)	0.14(3)	-0.05	-1.35	—	0.10	0.22
	0	843.5(4)	6.4(1)	0.51	8.32	-0.64	0.38	0.00
	0	892.87(7)	0.4(2)	-0.11	-7.03	-1.20	-0.04	-0.39
${}^6\text{Li} 1/2, -1/2\rangle$ $\oplus {}^{133}\text{Cs} 3, +3\rangle$	1	658.21(5)	0.2(1)	0.07	-3.02	—	0.04	-0.06
	1	708.63(1)	0.10(2)	-0.05	1.24	—	-0.11	-0.19
	1	708.88(1)	0.18(2)	-0.03	0.91	—	-0.01	0.06
	1	764.23(1)	0.07(3)	-0.06	0.83	—	-0.06	-0.09
	1	764.67(1)	0.11(3)	-0.05	0.29	—	0.12	0.35
	0	816.24(2)	0.20(4)	-0.12	-5.19	1.51	-0.26	-0.02
	0	889.2(2)	5.7(5)	0.46	9.31	0.31	0.34	0.00
	0	943.26(3)	0.38(7)	-0.12	-5.68	0.1	-0.04	-0.34
	1	704.49(3)	0.35(9)	0.07	0.67	—	0.01	-0.01
	0	896.6(7)	10(2)	0.68	19.51	-0.35	0.07	-0.21
${}^6\text{Li} 1/2, -1/2\rangle$ $\oplus {}^{133}\text{Cs} 3, +2\rangle$	1	750.06(6)	0.4(2)	0.06	1.47	—	-0.01	0.01
	0	853.85(1)	0.15(3)	-0.17	-7.34	-0.29	-0.41	0.15
	0	943.5(1.1)	15(3)	2.21	21.69	1.59	1.64	1.4
δB^{rms} (G)				0.039	0.965	0.265	0.040	0.048

Table 3.3: Comparison of the resulting Li-Cs FR positions from the various models to the observed resonances.

The experimental positions $B_{\text{res}}^{\text{exp}}$ and widths ΔB^{exp} are taken from Repp et al., 2013 (see also Table 3.1). The resonance positions $B_{\text{res}}^{\text{theo}}$ derived from CC calculation (δ_{CC}), bare ABM (δ_{bABM}), dressed ABM (δ_{dABM}), MQDT (δ_{MQDT}) and MQDT-FT ($\delta_{MQDT-FT}$) are given as deviations $\delta = B_{\text{res}}^{\text{exp}} - B_{\text{res}}^{\text{theo}}$ with respect to the observations. We also state the rms deviation δB^{rms} (see Eq. (3.51)) for all models. For the dressed ABM the p -wave values are identical to the bare ABM, therefore not repeated in the table. The splitting of the p -wave resonances has not been considered in $\delta_{MQDT-FT}$.

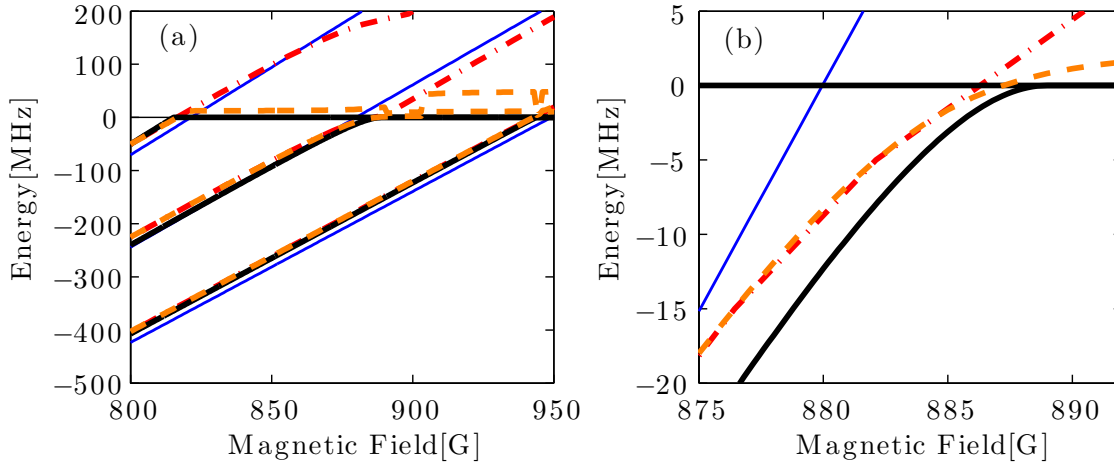


Figure 3.10: Molecular energy levels for the ${}^6\text{Li} |1/2, -1/2\rangle \oplus {}^{133}\text{Cs} |3, 3\rangle$ channel. (a) The energies with respect to the open channel asymptote for the bare ABM (blue line), dressed ABM (black line), MQDT (red dash-dotted line) and CC (orange line) are depicted. The horizontal line at zero energy represents the continuum threshold. The energies of the box states of the CC model (see Sect. 3.3.2) are also visible for $E > 0$. (b) A zoom into the region of the resonance at 889 G is presented. The different crossings of the molecular channels with the threshold at $E = 0$ mark the positions of the FRs and show the deviations of the models.

3.4.2 The Asymptotic Bound State Model

For the ABM calculation of ${}^6\text{Li}$ - ${}^{133}\text{Cs}$ FR positions, we begin using the ABM in its simplest form starting from the Hamiltonian of Eq. (3.22), replacing $T + V$ by the bound-state energies and neglecting H_{dd} . The latter is incorporated at a later stage. Because the spacing of the vibrational states in the ${}^6\text{Li}$ - ${}^{133}\text{Cs}$ potential is large compared to the hyperfine energy, we only include the least bound vibrational state of the singlet and triplet potential and neglect the role of deeper bound states. This yields a fit of only three parameters per partial wave. However, the three fit parameters are not independent with the present set of data, as will be explained below.

As a prelude to the new fits in this section, we start with the ABM as practiced in Repp et al., 2013, where the ABM was applied leaving five parameters (ϵ_0^0 , ϵ_1^0 , ζ_0 , ϵ_0^1 , ϵ_1^1) as free fit parameters, while ζ_1 was taken to be equal to ζ_0 ¹⁰. In this thesis we redo the fit, utilizing ζ_1 also as a free parameter, thus using six parameters

¹⁰Also, the atomic masses in the calculation were not accurate enough, which also had minor effects on the fitting results. In the present work we use atomic masses from [(version 3.0). [Online] Available: <http://physics.nist.gov/Comp> [2013, 12 09]. National Institute of Standards and Technology, Gaithersburg, MD.]

as fit parameters to minimize δB^{rms} (see Eq. (3.51)). This quantity gives intuitive and quantitative insight into the deviations of calculated from measured resonance positions. In ${}^6\text{Li}-{}^{133}\text{Cs}$ the hyperfine interaction gives rise to a very strong singlet-triplet mixing, which is indicated by an expectation value for the total spin S of $\langle S \rangle \simeq 0.6 - 0.7$ on the resonances. This results in a strong correlation of the fit parameters and the resonances can be fit with similar rms deviations over a large range (within a few GHz) of binding energies. The best fit has a rms deviation of 877 mG with the parameters $\epsilon_0^0 = 5824$ MHz, $\epsilon_1^0 = 2995$ MHz, $\zeta_0 = 0.559$, $\epsilon_0^1 = 1844$ MHz, $\epsilon_1^1 = 3575$ MHz and $\zeta_1 = 0.821$. However, since the singlet and triplet binding energies and their overlap parameter are related to each other through the interaction potential, the obtained overlap parameter of $\zeta_0 = 0.559$ is unphysical for the fitted binding energies. Additionally, the p -wave shift is unreasonably large for the singlet channel binding energy, while it has opposite sign for the triplet binding energy, which are clear indications that the fit results are unphysical.

In order to obtain a fit restrained to physical parameters, we demonstrate how these discrepancies of binding energies and overlap parameters can be reduced in the bare ABM (bABM) in three steps. The first step is to reduce the number of independent fit parameters by deriving the wavefunction overlaps from the two binding energies via the accumulated phase method (as described in Verhaar et al., 2009) instead of leaving them as a free parameter, thereby restricting ourselves to only the physical range of the fit parameters and reducing the fit to two parameters. The coupling of the bound state to the continuum, which is neglected at this stage, results in significant shifts for s -wave resonances. Therefore, we use only the narrow p -wave resonances for the initial fit, because their widths are not acquired by coupling to the continuum but rather by tunneling through the centrifugal barrier which is suppressed at low collision energies. The fit results of $\epsilon_0^1 = 1193$ MHz, $\epsilon_1^1 = 3638$ MHz and the calculated $\zeta_1 = 0.861$ agree much better with the CC values in Table 3.2. The p -wave resonances are reproduced with a rms deviation of 560 mG, where the mean was used for resonances which are split due to the magnetic spin-spin and second-order spin-orbit coupling. This demonstrates how the bare ABM model, which extensively simplifies the spatial part of the scattering problem, satisfactorily reproduces resonances which are not shifted due to coupling to the open channel scattering wavefunction.

Since we obtain the asymptotic wavefunctions from the accumulated phase method in the procedure described above, in the second step it is now also possible to include the magnetic dipole-dipole and second-order spin-orbit coupling term into the ABM Hamiltonian (similar to Goosen et al., 2010) in its effective form (see Eq. (3.25)).

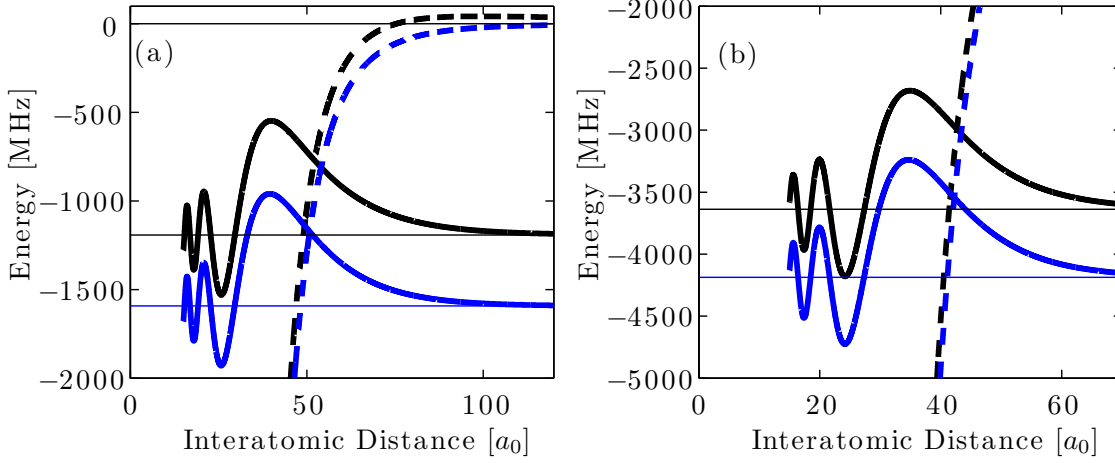


Figure 3.11: Wavefunctions for singlet (a) and triplet (b) long-range potentials. The long-range potentials (containing only van der Waals and centrifugal terms) (dashed lines) and the wavefunctions (solid lines) for $l = 0$ (blue) and $l = 1$ (black) are depicted. Note the similarity for wavefunctions with different l at short-range, which justifies the use of the accumulated phase method.

With a rms deviation of 375 mG, a fit containing H_{dd} improves the prediction of the p -wave resonances by about 185 mG, which is the expected order of magnitude, considering that the splitting is only on the order of a few hundred mG at most. For calculating the expectation value of H_{dd} only the long range part of the wavefunction was used. Thus the spin-orbit contribution does not play a role and a_{SO} in Eq. (3.26) could be set to zero.

In order to include the s -wave resonances in the third and final step of the bABM, the s -wave binding energies are deduced from the fitted p -wave binding energies using the accumulated phase method as follows. We numerically solve the Schrödinger equation containing only the van der Waals term in the interaction potential and using the phases of the obtained p -wave functions at r_i and $\psi \rightarrow 0$ for $r \rightarrow \infty$ as boundary conditions. Here, r_i is the radius where the van der Waals energy is larger than the hyperfine energy, and the exchange energy is large enough to split the singlet-triplet manifold [Verhaar et al., 2009]. This approach neglects the l -dependence of the phase-shift at r_i which is a small correction in our case [Verhaar et al., 2009]. For comparison, we illustrate the obtained singlet and triplet wavefunctions for $l = 0$ and $l = 1$ in Fig. 3.11. One can see that for small internuclear separations, the wavefunctions are approximately equal, which justifies the use of the accumulated phase method. The rms deviation for all resonances in the case where the p -wave resonances are fit and the s -wave resonances are calculated is 1.26 G

when H_{dd} is neglected. Including H_{dd} into this fit results in the lowest attainable rms deviation value of 965 mG for a physically meaningful bare ABM fit. The resulting molecular energy levels for the ${}^6\text{Li } |1/2, -1/2\rangle \oplus {}^{133}\text{Cs } |3, 3\rangle$ are shown in Fig. 3.10. As one can see, the positions where the bound state energies cross the threshold are not shifted due to interactions, as is the case for the other models. Thus, compared to the measured values, the broad FRs are systematically shifted to lower magnetic fields, as illustrated in Table 3.3, where the resonance positions are given in the "bABM" column. The positions of the narrow resonances are shifted to higher values most likely because of the application of the accumulated phase methods, which introduces errors in the determination of the s -wave binding energies. The latter are given together with the p -wave binding energies as "bABM" values in Table 3.2. If one needs a more accurate prediction for the narrow resonances, one could also fit them using ϵ_0^0 and ϵ_1^0 as additional parameters.

The binding energies can be used to derive background scattering lengths via the accumulated phase method [Verhaar et al., 2009], by propagating the wavefunction with the known phase at r_i to large internuclear separations and then comparing to a long-range wavefunction which is not shifted by an interaction potential. This procedure introduces additional errors on the order of $\sim 10\%$, which are errors related to the accumulated phase method and not to the ABM. By including the energy dependence of the accumulated phase as described in Verhaar et al., 2009 the scattering length might be calculated with better accuracy. However, calculating these derived quantities allows for a comparison with the MQDT-FT (see Sect. 3.4.3) where no binding energies were derived directly, and yields an additional test of consistency among the three different models.

In order to achieve higher accuracy, we include the coupling of the closed channel responsible for the FR to the open channel, which is referred to as dressed ABM (dABM). In Sect. 3.3.3 we discuss the limiting cases, where the coupling of the closed channel bound state to either the least bound state, or to a virtual state in the open channel can be used as an estimate for the shift of the resonance position. The ${}^6\text{Li}$ - ${}^{133}\text{Cs}$ system, however, is in an intermediate regime, where both of the approaches do not deliver satisfactory results. The background scattering length of the triplet channel of $a_T = -34.3(2) a_0$ indicates this regime. On the one hand, it is significantly far from the van der Waals range of $r_0 = 45 a_0$, which would indicate a non-resonant open channel, but on the other hand, it is also not dominating the scattering process, which would lead to a much larger magnitude of the background scattering length.

Therefore, we introduce an extension to the ABM similar to the approach pre-

sented in Park, et al. [Park et al., 2012], which includes both effects in a phenomenological manner. We use the complex energy shift of Eq. (3.46), just as in a system with a resonant open channel [Marcelis et al., 2004; v. Kempen et al., 2004]. To calculate $A_{vs} = \mathcal{K}^2 \zeta_{vs}$, we multiply the square of the appropriate matrix element of \mathcal{H}_{PQ} taken from the matrix \underline{M}'_{ABM} in the form where \mathcal{H}_{QQ} is diagonalized (denoted by \mathcal{K}^2) with an additional scaling factor ζ_{vs} , which handles the spatial part of the matrix element and is equal for all FRs. However, in contrast to Marcelis et al., 2004, the molecular energy ϵ_Q is not taken to be the bare energy from the submatrix \mathcal{H}_{QQ} , but we rather diagonalize the full matrix \underline{M}_{ABM} and replace ϵ_Q in the S -matrix of Eq. (3.38) with the dressed resonant molecular state ϵ_{ABM} . In doing so, ϵ_{ABM} contains the coupling to the open channel bound state. Therefore, both the influence of the coupling to the bound and the virtual states in the P -channel are accounted for. The FR positions are now simply obtained at magnetic fields where the following identity is satisfied:

$$\epsilon_{ABM} = \frac{\mu}{\hbar^2} \frac{\zeta_{vs} \mathcal{K}^2}{\kappa_{vs}^2}. \quad (3.52)$$

κ_{vs} is obtained as described in Sect. 3.3.3 and ζ_{vs} is left as a free fit parameter. Within this approach the FRs, including coupling to the (near-resonant) scattering states, can be found by simple matrix operations and linear equations.

We note that the full scattering properties around the resonance (including the resonance width and for the case of overlapping resonances [Park et al., 2012]), can be obtained from the S -matrix by using the complex energy shift A_{vs} as given above.

We start the calculation by only fitting the narrow s -wave resonances, where the coupling to the open channel is small, in order to fit ϵ_0^0 and ϵ_1^0 . Their overlap ζ_0 is obtained with the same method as for the bare ABM. The results of this fit are given in Table 3.2 as "dABM", where the background scattering lengths for the specific incoming channels are deduced in the same manner as described above. The next step is the fitting of the scaling factor ζ_{vs} by performing a weighted least squares minimization on all observed s -wave resonances, additionally allowing the overlap parameter to vary by $< 0.1\%$. The result of $\zeta_{vs} = 0.025$ yields a rms deviation of 321 mG on all s -wave resonances. Combining with the results of the bare ABM for the p -wave resonances we obtain a total rms deviation of $\delta B^{rms} = 265$ mG on all resonances. The resonance positions are listed in Tab. 3.3, and selected molecular energy levels are given as a function of magnetic field in Fig. 3.10 for comparison. The largest deviation between the CC and ABM approach is seen at the broad resonances, e.g. at 890 G (see inset Fig. 3.10). The coupling to the continuum is

obvious by the nonlinear function of the energy with respect to the magnetic field.

In Fig. 3.9 we illustrate the scattering length, which can be obtained by inserting the fit results into Eq. (3.38). Comparing the the results of the CC calculation, it is obvious that the widths of the FRs are underestimated. This is expected, because the dressed ABM takes into account only the coupling with one closed channel bound state. For more accurate results, the couplings to more states should be included, which would also increase the widths of the FRs.

While the ABM assigns the FRs with a sub-1 G accuracy, there is a significant deviation of the triplet binding energy ϵ_1^0 from the CC value. This could arise from the fact that the coupling to the (near resonant) triplet channel is only included phenomenologically by adding a single virtual state. Also, only one bound state is taken into account and we treat the resonances as being non-overlapping.

An additional approximation is introduced by using the accumulated phase method to derive the overlap parameters, and to relate the s -wave and p -wave binding energies enlarges the uncertainty. We characterize the accuracy of the accumulated phase method by comparing the obtained binding energies with the bound states of the full ${}^6\text{Li}$ - ${}^{133}\text{Cs}$ potentials. Using the boundary conditions at r_i from the s -wave binding energies we find that the accumulated phase method reproduces the p -wave binding energies to $\sim 1 - 2\%$ for both the singlet and triplet potentials. Changing the binding energies on the order of $\sim 1 - 2\%$ increases δB^{rms} on the FRs with more than a factor 2, indicating that at this level of accuracy the inner part of the potential has a significant effect. Extending the ABM to use more information of the full potentials to link the s - and p -wave binding energies is straightforward, however, by this step we would lose the advantage of the simple calculations of the ABM. We also note that a more rigorous method to include both the bound and the virtual state is the Resonant State Model as presented in Goosen, 2011. Also, the accumulated phase methods leads to an error in the derivation of the background scattering lengths. While this is on the order of $\sim 10\%$, a significant part of the deviation of a_T is a result of the systematic shift of ϵ_1^0 , in both the bare and the dressed ABM.

3.4.3 The Multichannel Quantum Defect Theory

We apply the *ab initio* MQDT treatment, using the potentials of the CC calculation from Sect. 3.4.1 as input for the calculation. We then slightly modify the inner wall of these potential in order to minimize the deviation from the experiment. The present calculation only requires solving the coupled differential equations out to

$r_0 = 40 a_0$, and very little difference is seen if this matching radius to the long-range single-channel QDT solutions is reduced to $30 a_0$. Table 3.3 shows the accuracy of the FR positions in comparison with the experimentally determined resonances from Sect. 3.1, and Fig. 3.10 plots three of the obtained energy levels for comparison with the other models. The close agreement between CC and MQDT is very satisfying. The same holds for the resulting scattering lengths, which are illustrated in Fig. 3.9(a) for the energetically lowest channel. The bound state energies (see Table 3.2), which do not play the same central role in the MQDT calculation as in the ABM model, can be extracted from the underlying modified potentials for comparison. They show excellent agreement with the CC values and give a measure as to what degree the potentials from the CC calculation have been modified. This agreement and the small rms deviation of the FR positions from the experimental values demonstrate, that MQDT and CC calculation are asymptotically consistent with regard to δB^{rms} but for the description of individual resonances the two models deviate up to ~ 100 mG. This might also indicate the limit for predicting new FRs.

In the present study we test an alternative way to utilize the FT plus MQDT formulation; the idea is to empirically fit the single-channel singlet and triplet quantum defects so as to achieve optimum agreement with a few measured FRs. In this treatment, if the long-range van der Waals coefficient is already known to sufficient accuracy, as is believed to be the case for ${}^6\text{Li}$ - ${}^{133}\text{Cs}$, then with two fitted parameters it is possible to achieve good agreement with all of the s -wave resonances that have been measured to date, and to predict additional resonances. The l -dependence of the fitted quantum defects is approximately known, but to achieve sub-1 G accuracy on other partial waves, it appears to be necessary to fit one small additional correction for p -waves (see Eq. (3.49)). While the MQDT has been shown in a number of studies to give a highly efficient way to calculate ultracold scattering observables when the interaction potentials are known, there is increasing demand for a robust method for analyzing new, complex systems where FRs have been measured but not yet analyzed to the level of yielding a detailed microscopic model. The present test of the semi-empirical MQDT frame transformation (MQDT-FT) is encouraging in its potential for such problems, as is seen from the results presented below for the ${}^6\text{Li}$ - ${}^{133}\text{Cs}$ interaction.

In our implementation of the frame-transformed version of MQDT utilized for the present study, the long-range parameters (A , \mathcal{G} , γ and η) are determined once and for all for a pure van der Waals potential at long-range, $-C_6/r^6$. The long-range MQDT parameters are standard and can be used for any alkali atom collision, because they are tabulated as functions of the single dimensionless variable which is the product

of the van der Waals length and the wavenumber k (see e.g. Ruzic et al., 2013). Two energy-independent and field-independent short-range quantum defects, namely $\mu_{S,l}^{sr}$ for $S = 0, 1$, were adjusted until optimum agreement was achieved with the experimental resonance positions. Note that a global search was not carried out over all values of the $0 \leq \mu_S^{sr} < 1 \pmod{1}$. The starting values of the search came from quantum defects extracted from the ${}^6\text{Li}$ - ${}^{133}\text{Cs}$ potentials of Sect. 3.4.1 and only small adjustments of those values were needed in the MQDT-FT fit to achieve the quoted level of agreement with the experimental resonance locations. In contrast with the MQDT calculation and the full CC calculation, this MQDT-FT calculation did not include the magnetic dipole-dipole interaction nor the second-order spin-orbit interaction term. Nevertheless, the fit with three adjustable parameters (adding α_1 of Eq. (3.49)) gives a small rms deviation with experimental resonance positions in Table 3.3, namely 48 mG. The fitted p -wave correction is $\alpha_1 = 0.00208$ and the $l = 0$ quantum defects are $\{\mu_0^{sr}, \mu_1^{sr}\} = \{0.092115, 0.346848\}$. These can be used to derive the background scattering lengths of the singlet and triplet potential, which are given in Table 3.2. Because the bound state energies are only expected to be accurate when the binding is quite small, no comparisons with bound levels obtained in the other methods are presented here. In Table 3.2 one sees that the largest deviations of the scattering lengths appear for the triplet state. Despite the very different qualities of the fit for the ABM and MQDT-FT approach, their results for the triplet scattering lengths are fairly close but deviate significantly from the result of CC and MQDT. Similarly, the fit quality of MQDT and MQDT-FT are comparable but the derived scattering lengths deviate strongly. No physical reason for this behavior is known at present.

3.5 Comparison of the Performance of the Three Models

In this chapter we have applied three different models for the assignment of the measured FRs. All three models describe the observed resonances with a sub-1 G accuracy. However, depending on the desired degree of precision and the availability of accurate interaction potentials, the models serve different purposes.

In some cases a phenomenon under investigation requires highly accurate knowledge of scattering observables that are not measured but rather deduced from theory, as for example the scattering length in dependence of the magnetic field. In these cases it is inevitable to use the CC calculation. This demands either accurate *ab*

initio potentials or sufficient experimental data to construct such potentials. The high accuracy of the CC calculation stems from the fact that it incorporates the least amount of assumptions out of the three models. The rms deviation of 39 mG is the lowest of all three models. It is a rigorous and straightforward numerical approach, which comes at the cost of computational power and complex codes. The potentials for the CC calculations were mainly determined by spectroscopic data and here the data set for the triplet state is fairly sparse. The minimum is not well characterized because the vibrational levels from $v = 0 - 4$ are not yet observed. Thus, predictions of FR for $^7\text{Li}-^{133}\text{Cs}$ may be less accurate than for $^6\text{Li}-^{133}\text{Cs}$. Measurements would be very desirable.

There are situations where the required precision of scattering observables is less stringent. One example is evaporative cooling of ultracold gases or sympathetic cooling of ultracold mixtures to quantum degeneracy by means of a FR, or for initial characterization of FRs. In these cases, the processes are often optimized experimentally, and it is not necessary to know the exact value of the scattering length for the start of the optimization. Under these circumstances the two other simplified models are much more appropriate.

With a rms deviation of 965 mG, the bare ABM explains the FR structure already on the level of ~ 1 G. Only two parameters are sufficient for the description of the FR positions. The relatively large deviation is related to the fact that couplings to continuum states are neglected, which results in shifts on the order of the FR width of broad resonances. The fact that the rms deviation of p -wave resonances is only 560 mG, and can be further reduced to 375 mG when the spin-spin interaction is included, shows that narrow resonances are predicted sufficiently well. An advantage of the bare ABM is that no molecular information is required, as it builds solely on atomic constants and few fit parameters. Additionally, the code for the calculation is extremely simple since it only involves the numerical diagonalization of a small matrix, which is included in standard computational software programs. Therefore, it can be applied at low programming expense for all systems, in order to assign or predict FRs, or quickly map out all resonances of a system. In fact, it was used to estimate whether there are any FRs expected in experimentally achievable field regions for the $^6\text{Li}-^{133}\text{Cs}$ system before the experiment was set up. Also, it can be used to optimize the starting conditions for a CC calculation [Li et al., 2008]. We remark that the open channels for $M = 5/2$ and $M = 3/2$ have overlapping continua, $|1/2, -1/2\rangle \oplus |3, +3\rangle$ with $|1/2, 1/2\rangle \oplus |3, +2\rangle$ or $|1/2, -1/2\rangle \oplus |3, +2\rangle$ with $|3/2, -3/2\rangle \oplus |3, +3\rangle$, respectively. Thus the two-state approach for the S -matrix derived in Sect. 3.3.1 might not be completely justified.

For the calculation of scattering properties and an accurate description of broad resonances, the dressed ABM has to be applied. With a rms deviation of 265 mG it is somewhat less accurate than the MQDT-FT. Yet, since it does not solve the Schrödinger equation numerically but rather utilizes an analytical expression of the S -matrix, it is still computationally not demanding. In cases where the background scattering lengths for the incoming channel are known, the implementation is simple, since a comparison with the van der Waals length directly shows whether the analytical expressions for bound or virtual state or –as is the case for ${}^6\text{Li}$ - ${}^{133}\text{Cs}$ – for an intermediate regime are appropriate. If this information is not available, we suggest first fitting the narrow resonances, in order to deduce background scattering lengths from the fitted bound state energies via the accumulated phase method, as explained in Sect. 3.4.2. Then the right choice of the analytical expression to be used will become evident by a comparison with the van der Waals range.

In order to gain accurate information from the MQDT, the interaction potentials have to be known sufficiently well. However, compared to the CC calculation, it reduces the complexity of the problem enormously. As it is still a full scattering physics approach, employing a coupled-channel solution at short-range, the code is more complex and lengthy than the ABM code. Yet, once this code is available, it can be used for any alkali system without adaptation to the system specifics and solves the scattering problem efficiently. The accuracy of the final results with a rms deviation of 40 mG is nearly indistinguishable from that of the full CC calculation. Also, both yield smaller values for the FR positions of the broad resonances as compared to the observations. This deviation stems from the fact that for the experimental determination of the position, a Gaussian profile was fit to the loss spectrum, which neglects its asymmetric line shape and therefore returns slightly larger values than the actual resonance positions. As a result, the current investigation does not indicate a model problem of CC and MQDT for the broad resonances.

Many of the above mentioned properties of the MQDT are also true for the MQDT-FT. The latter is especially useful for systems with little knowledge of interaction potentials and only a few experimentally measured FRs. A two parameter fit for only s -waves (three-parameters for $s + p$ etc.) allows to assign the resonances and to investigate the existence of possibly broader or for specific applications more appropriate FRs. While the rms deviation of 48 mG is comparable to MQDT and CC models, the predicted values of the bare singlet and triplet scattering lengths is less accurate. Because the variation of the quantum defects compensates for deviations introduced by the assumptions of the MQDT-FT (see Sect. 3.4.3) in order to recreate the FR positions, the accuracy of other scattering properties should be

tested in future studies. As it relies on only three parameters for the prediction or assignment of FR, it is appropriate in systems that are currently lacking accurate interaction potentials.

In conclusion, depending on the knowledge of molecular parameters, the required accuracy of the predicted scattering parameters, the complexity of code and the computational expense, each model has its own strength in applicability.

Chapter 4

Observation of Efimov Resonances

Parts of this chapter are based on the following publication:

R. Pires, J. Ulmanis, S. Häfner, M. Repp, A. Arias, E.D. Kuhnle and M. Weidemüller

Observation of Efimov Resonances in a Mixture with Extreme Mass Imbalance

Submitted, arXiv:1403.7246

The control of interactions in ultracold atomic systems via magnetically tunable Feshbach resonances (FRs) opens up new pathways for the investigation of few- and many-body physics [Chin et al., 2010]. One intriguing example is the access to the universal regime, which is characterized by a magnitude of the scattering length a exceeding all other length scales of the system. In the limit of at least two resonant pairwise interactions, an infinite series of three-body bound-states, the so called Efimov states, exists [Efimov, 1971; Braaten and Hammer, 2006; Zinner and Jensen, 2013]. Counterintuitively, these trimers persist even for $a < 0$, where the two body potential does not support a bound-state. The ratio between two subsequent trimer energies follows a discrete scale invariance with a universal factor of $\exp(-2\pi/s_0)$. Here, s_0 only depends on the quantum statistics of the constituent atoms, their mass ratio, and the number of resonant pairwise interactions [D’Incao and Esry, 2006; Braaten and Hammer, 2006; Esry et al., 2008]. This scale invariance also reflects in those values of a , where the energy of the bound-states coincides with the threshold of three free atoms for $a < 0$, resulting in an enhanced three-body loss. When the position of the first resonance is given by $a_-^{(0)}$, the N -th excited state

is found at the scattering length $a_-^{(N)} = a_-^{(0)} \exp(\pi N/s_0)$. It has been shown that for homonuclear systems $a_-^{(0)}$ only depends on the characteristic range r_0 of the interatomic van der Waals potential [Berninger et al., 2011a; Roy et al., 2013; Wang et al., 2012a; Sørensen et al., 2012; Schmidt et al., 2012; Naidon et al., 2014]. The universal scaling factor acquires a value of 22.7 for equal mass constituents and features a drastic reduction in heteronuclear mass-imbalanced systems of two heavy and one light particle [Braaten and Hammer, 2006; D’Incao and Esry, 2006; Esry et al., 2008], resulting e.g. in a factor of 4.9 for a ${}^6\text{Li}$ - ${}^{133}\text{Cs}$ mixture.

In ultracold atom experiments, Efimov resonances become evident in the three-body loss coefficient L_3 in the rate equation for atom loss $\dot{n} = -L_3 n^3$. Here, n denotes the number density of atoms, and $L_3 \propto C(a)a^4$. The Efimov physics are contained in the dimensionless, log-periodic coefficient $C(a)$. Thus far, Efimov resonances have been explored in several equal mass systems [Kraemer et al., 2006; Gross et al., 2009; Ottenstein et al., 2008; Pollack et al., 2009; Wild et al., 2012; Huckans et al., 2009; Zaccanti et al., 2009; Berninger et al., 2011a; Roy et al., 2013], where the scaling between different resonances is predicted to follow $C(a) = C(22.7a)$. This large scaling factor demands a regime of temperature and magnetic field control that makes the observation of an excited Efimov state highly involved. There had been indication of such an excited state in a three-component Fermi gas of ${}^6\text{Li}$ atoms [Williams et al., 2009] exhibiting the same scaling as equal mass bosons [Braaten et al., 2010]. A finite temperature model [Rem et al., 2013] suggests that the observation of a second Efimov resonance in bosonic ${}^7\text{Li}$ is feasible at current experimental conditions [Rem et al., 2013; Dyke et al., 2013]. During the completion of this thesis, the Grimm group in Innsbruck succeeded in measuring an excited Efimov state in a homonuclear ${}^{133}\text{Cs}$ sample [Huang et al., 2014], confirming the prediction of the scaling for the equal mass boson case. In heteronuclear systems, only the K-Rb mixtures have been investigated so far [Barontini et al., 2009; Bloom et al., 2013], where a scaling factor of ~ 131 obstructs the observation of an excited Efimov state. In ${}^6\text{Li}$ - ${}^{133}\text{Cs}$ the predicted scaling factor of 4.9 [Braaten and Hammer, 2006; D’Incao and Esry, 2006; Esry et al., 2008] and the ability to tune the scattering length over a large range due to broad FRs [Repp et al., 2013; Tung et al., 2013] favor the observability of a series of Efimov resonances.

This chapter describes our observation of Efimov resonances in this system with extreme mass imbalance. We start by outlining the phenomenon of an Efimov resonance in the hyperspherical representation in Sect. 4.1. We then demonstrate our experimental approach to the measurement of Efimov resonances in Sect. 4.2. Finally, the observation of two Efimov resonances in the three-body loss coefficient of

${}^6\text{Li}-{}^{133}\text{Cs}-{}^{133}\text{Cs}$ with a scaling ratio of $a_-^{(1)}/a_-^{(0)} = 5.8(1.0)$ are discussed in Sect. 4.3.

4.1 The Efimov Effect

The three-body problem is of interest in various fields of physics, and therefore unites groups with a variety of frameworks for its theoretical treatment, as for example effective field theory, renormalization group methods and the hyperspherical formalism. An excellent summary of these methods can be found in Braaten and Hammer, 2006 and Wang et al., 2013. In this work we follow closely the discussion in Braaten and Hammer, 2006 of the hyperspherical approach, as it delivers an intuitive picture in a similar fashion as the treatment of the two-body problem in Chap. 3. Several different approaches and degrees of approximations have been proven useful for tackling the three-body problem using this method [Botero and Greene, 1986; Bohn et al., 1998; Lin, 1981; Koyama et al., 1989; Zhou et al., 1993; Esry et al., 1996b; D’Incao et al., 2009; Blume and Greene, 2000; Rittenhouse et al., 2010; von Stecher and Greene, 2009].

We start by separating angular and radial hyperspherical coordinates in Sect. 4.1.1 in order to derive a single simplified Schrödinger equation for the three-body problem and discuss the solutions for this equation for several scenarios. A separation of length scales allows to obtain simplified expressions for the S -matrix in Sect. 4.1.2, based on simple arguments of probability conservation. This matrix allows for the calculation of physical observables for the manifestation of Efimov resonances, which is also presented in the latter section.

4.1.1 The Hyperspherical Formalism

We start our discussion by considering the well-known case of three identical bosons for reasons of simplicity. The appropriate changes for the mass-imbalanced case are then given at the end of the section.

The time-independent Schrödinger equation

$$\left(-\frac{\hbar^2}{2m} \sum_{i=1}^3 \nabla_i^2 + V(\mathbf{r}_1, \mathbf{r}_2, \mathbf{r}_3) \right) \Psi(\mathbf{r}_1, \mathbf{r}_2, \mathbf{r}_3) = E \Psi(\mathbf{r}_1, \mathbf{r}_2, \mathbf{r}_3) \quad (4.1)$$

contains six degrees of freedom, once the equation has been transformed into the center of mass frame. With the help of the hyperspherical coordinates and appropriate approximations, the degrees of freedom can be reduced drastically, while the

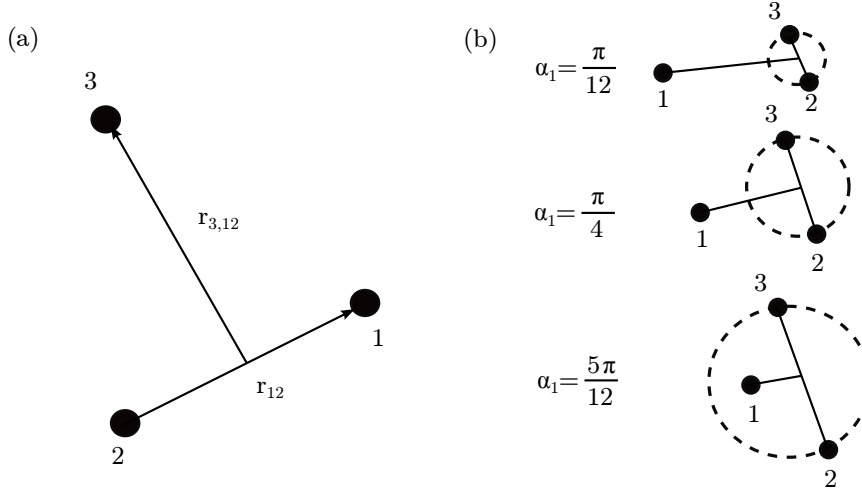


Figure 4.1: Jacobi coordinates and Delves hyperangle. (a) One of three possible variants of the Jacobi coordinates given by Eq. (4.2). (b) Three different configurations for Delves hyperangle, as defined in Eq. (4.4), in the relevant range between 0 and $\pi/2$.

essential key properties of the problem are still contained in the resulting equation. Using the Jacobi coordinates

$$\mathbf{r}_{ij} = \mathbf{r}_i - \mathbf{r}_j, \quad \mathbf{r}_{k,ij} = \mathbf{r}_k - \frac{1}{2}(\mathbf{r}_i + \mathbf{r}_j) \quad (4.2)$$

(see Fig. 4.1(a)), we can define the hyperradius R as the root-mean-square separation of the three atoms:

$$R^2 = \frac{1}{3}(\mathbf{r}_{12}^2 + \mathbf{r}_{23}^2 + \mathbf{r}_{31}^2) = \frac{1}{2}\mathbf{r}_{ij}^2 + \frac{2}{3}\mathbf{r}_{k,ij}^2. \quad (4.3)$$

Three different configurations for the Delves hyperangles [Delves, 1960]

$$\alpha_k = \arctan \left(\frac{\sqrt{3}\mathbf{r}_{ij}}{2\mathbf{r}_{k,ij}} \right) \quad (4.4)$$

in the possible range between 0 and $\pi/2$ are also shown in Fig. 4.1(b). One of these angles together with the unit vectors $\hat{\mathbf{r}}_{ij}$ and $\hat{\mathbf{r}}_{k,ij}$ yield the additional five independent coordinates besides R for the description of the three-body problem. These dimensionless variables will be denoted Ω in the following discussion. With the help of hyperspherical coordinates introduced above, we can rewrite Eq. (4.1) as

$$\left(T_R + T_\alpha + \frac{\Lambda_{k,ij}^2}{2mR^2} + V(R, \Omega) \right) \Psi = E\Psi, \quad (4.5)$$

where T_R and T_α denote hyperradial and hyperangular kinetic operators¹, respectively, and $\Lambda_{k,ij}^2 = \mathbf{L}_{ij}^2/\sin^2\alpha_k + \mathbf{L}_{k,ij}^2/\cos^2\alpha_k$ is a generalized angular momentum operator. Here, \mathbf{L}_{ij} and $\mathbf{L}_{k,ij}$ are the conventional angular momentum operators connected to \mathbf{r}_{ij} and $\mathbf{r}_{k,ij}$, respectively. The formula in Eq. (4.5) is equivalent to Eq. (4.1) when the latter is transformed to the center of mass system. The following simplifications reduce the complexity of the problem enormously.

For two-atom clusters where the third atom is sufficiently far away, the potential can be written as

$$V(\mathbf{r}_1, \mathbf{r}_2, \mathbf{r}_3) = V(r_{12}) + V(r_{23}) + V(r_{31}). \quad (4.6)$$

While this assumption seems excessively restrictive, Eq. (4.6) describes the low-energy behavior of a universal sample surprisingly well, because at the large distances involved in such problems, the potential is well-described by pair-wise terms. In certain cases where the short-range effects need to be included, an additional term that incorporates real three-body effects at short separations can be added [Braaten and Hammer, 2006; Wang et al., 2013]. The wavefunction can be assumed to take on the form

$$\Psi(\mathbf{r}_1, \mathbf{r}_2, \mathbf{r}_3) = \psi^{(1)}(\mathbf{r}_{23}, \mathbf{r}_{1,23}) + \psi^{(2)}(\mathbf{r}_{31}, \mathbf{r}_{2,31}) + \psi^{(3)}(\mathbf{r}_{12}, \mathbf{r}_{3,12}), \quad (4.7)$$

where each of the summands is a solution to the appropriate Fadeev equation

$$\left(T_R + T_{\alpha_k} + \frac{\Lambda_{k,ij}^2}{2mR^2}\right) \psi^{(k)} + V(r_{ij}) (\psi^{(k)} + \psi^{(i)} + \psi^{(j)}) = E\psi^{(k)}. \quad (4.8)$$

At this point it is convenient to neglect all subsystem angular momentum, which yields a further simplification for the solution of the three-body problem. The coupling between different subsystem angular momenta only enters at second order for the potential as given by Eq. (4.6), while it enters at first order in Eq. (4.1), which clarifies why it has been implemented only after simplifying the potential. The subsequent results can in principle also be obtained when the subsystem angular momentum is included, as shown in Nielsen et al., 2001. For the phenomenological introduction, however, we refrain from including it, and thus simplify the wavefunction of Eq. (4.7) to Braaten and Hammer, 2006

$$\Psi(\mathbf{r}_1, \mathbf{r}_2, \mathbf{r}_3) = \psi(R, \alpha_1) + \psi(R, \alpha_2) + \psi(R, \alpha_3). \quad (4.9)$$

¹For their explicit formulas we refer to Braaten and Hammer, 2006.

The three Faddeev equations simplify to²

$$(T_R + T_{\alpha_k} - E) \psi(R, \alpha_k) + V(\sqrt{2}R \sin \alpha_k) (\psi(R, \alpha_k) + \psi(R, \alpha_i) + \psi(R, \alpha_j)) = 0 \quad (4.10)$$

which can be reduced further to only one equation. To this end, we chose $k = 1$ and average $\psi(R, \alpha_2)$ and $\psi(R, \alpha_3)$ over the angular variables $\hat{\mathbf{r}}_{23}$ and $\hat{\mathbf{r}}_{1,23}$, which allows us to express them as integral operators acting on $\psi(R, \alpha_1)$:

$$\langle \psi(R, \alpha_2) \rangle_{\hat{\mathbf{r}}_{23}, \hat{\mathbf{r}}_{1,23}} = \langle \psi(R, \alpha_3) \rangle_{\hat{\mathbf{r}}_{23}, \hat{\mathbf{r}}_{1,23}} = \frac{2}{\sqrt{3}} \int_{\pi/3-\alpha_1}^{\pi/2-|\pi/6-\alpha_1|} \frac{\sin(2\alpha')}{\sin(2\alpha_1)} \psi(R, \alpha') d\alpha'. \quad (4.11)$$

Inserting Eq. (4.11) into Eq. (4.10) yields the single integro-differential *low energy Faddeev equation*

$$(T_R + T_\alpha - E) \psi(R, \alpha) = -V(\sqrt{2}R \sin \alpha) \left[\psi(R, \alpha) + \frac{4}{\sqrt{3}} \int_{\pi/3-\alpha}^{\pi/2-|\pi/6-\alpha|} \frac{\sin(2\alpha')}{\sin(2\alpha)} \psi(R, \alpha') d\alpha' \right] \quad (4.12)$$

for the three-body problem, which now only depends on one of the hyperangles $\alpha_1 = \alpha$.

The hyperspherical expansion

$$\psi(R, \alpha) = \frac{1}{R^{5/2} \sin(2\alpha)} \sum_n f_n(R) \phi_n(R, \alpha) \quad (4.13)$$

separates radial and angular coordinates, and the functions $\phi_n(R, \alpha)$ define a set of channel potentials

$$V_n(R) = [\lambda_n(R) - 4] \frac{\hbar^2}{2mR^2} \quad (4.14)$$

via the solutions to the α -dependent integro-differential equation

$$\left[-\frac{\partial^2}{\partial \alpha^2} - \lambda_n(R) \right] \phi_n(R, \alpha) = -\frac{2mR^2}{\hbar^2} V(\sqrt{2}R \sin \alpha) \left[\phi_n(R, \alpha) + \frac{4}{\sqrt{3}} \int_{\pi/3-\alpha}^{\pi/2-|\pi/6-\alpha|} \phi_n(R, \alpha') d\alpha' \right], \quad (4.15)$$

where $\lambda_n(R)$ denotes the eigenvalue as a function of the hyperradius R , which

²This equation has to be obtained for each permutation of i, j and k , which results in a total of three equations.

is treated as a parameter. The potentials of Eq. (4.14) can be understood as adiabatic potentials controlling the evolution of the system in R , similar as the Born-Oppenheimer potentials for the two-body system introduced in Chap. 3. Inserting the channel potentials and the hyperspherical expansion of Eq. (4.13) into the low energy Fadeev equation, we obtain a set of coupled differential equation

$$\left[\frac{\hbar^2}{2m} \left(-\frac{\partial^2}{\partial R^2} + \frac{15}{4R^2} \right) + V_n(R) \right] f_n(R) + \sum_m \left[2P_{nm}(R) \frac{\partial}{\partial R} + Q_{nm}(R) \right] f_m(R) = E f_n(R), \quad (4.16)$$

where the couplings P_{nm} and Q_{nm} between different channels depend on the first and second order partial derivative of $\lambda_n(R)$ with respect to R , respectively. When $\lambda_n(R)$ varies only slowly with R , we can make the adiabatic hyperspherical approximation which neglects the coupling between channels. Neglecting also the diagonal coupling terms in Eq. (4.16), we obtain a reduced radial Schrödinger equation for each of the hyperspherical potentials

$$\left[\frac{\hbar^2}{2m} \left(-\frac{\partial^2}{\partial R^2} + \frac{15}{4R^2} \right) + V_n(R) \right] f_n(R) \approx E f_n(R). \quad (4.17)$$

Due to the assumptions made in the derivation, this equation is only valid in the region $r_0 \ll R \ll a$. For $R \sim r_0$, the previously neglected short range physics affect the behavior of the system, and the simplifying assumptions are no longer valid. For $R \sim a$, the coupling between different hyperangular channels can no longer be neglected, and Eq. (4.17) loses its validity.

The challenging part of the three-body problem is the solution of Eq. (4.15). Various numerical methods for its solution are discussed in Braaten and Hammer, 2006 and Wang et al., 2013. One way to obtain the eigenvalues is to assume the resonant limit, where the scattering length $|a|$ is much larger than the two-body potential range r_0 . Solving Eq. (4.15) in regions of extremely small and large values of $R \sin \alpha$, in which Eq. (4.15) simplifies, and matching these solutions at small α yields the following transcendental matching equation for the channel eigenvalues:

$$\cos \left(\lambda^{1/2} \frac{\pi}{2} \right) - \frac{8}{\sqrt{3}} \lambda^{-1/2} \sin \left(\lambda^{1/2} \frac{\pi}{6} \right) = \sqrt{2} \lambda^{-1/2} \sin \left(\lambda^{1/2} \frac{\pi}{2} \right) \frac{R}{a}. \quad (4.18)$$

The numerical solutions of Eq. (4.18) can be inserted into Eq. (4.14) to obtain channel potentials, which are shown in Fig. 4.2. As can be seen in this figure, the only eigenvalues of interest for the Efimov effect are the lowest ones for the two

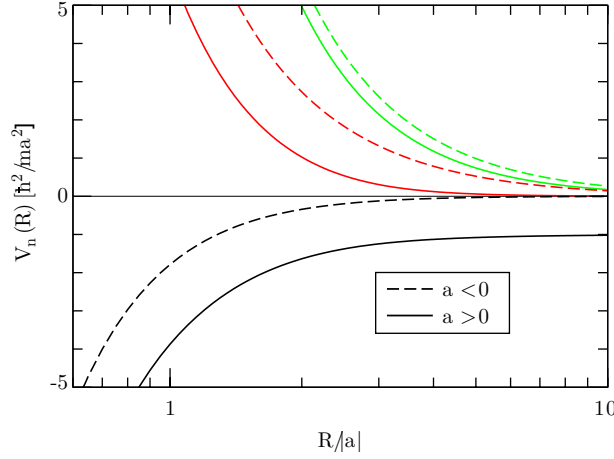


Figure 4.2: The three lowest hyperspherical potentials for positive and negative scattering lengths. The channel potentials $V_n(R)$ are scaled by \hbar^2/ma^2 for $a > 0$ (solid lines) and $a < 0$ (dashed lines). Reprinted and adapted from Braaten and Hammer, 2006 with permission from Elsevier.

cases $a < 0$ and $a > 0$, named $\lambda_0(R)$, because they are the only eigenvalues that yield attractive potentials which support bound-states. In the limit $R/a \rightarrow 0$, this eigenvalue is given by

$$\lambda_0 \rightarrow -s_0^2 \left(1 + 1.897 \frac{R}{a} \right), \quad (4.19)$$

where $s_0 = 1.00624$. Inserting this expression into Eq. (4.17) and neglecting the R/a term yields

$$\frac{\hbar^2}{2m} \left[\frac{\partial^2}{\partial R^2} - \frac{s_0^2 + 1/4}{R^2} \right] f_0(R) = E f_0(R). \quad (4.20)$$

The Efimov effect arises from the long-range nature of the attractive effective potential $-\frac{s_0^2+1/4}{R^2}$ in Eq. (4.20), which features an infinite amount of bound-states. The solution of Eq. (4.20) can be identified as exponentially decaying Bessel functions with imaginary argument and imaginary order. The bound-state energies are then given by

$$E_T^n = \left(e^{-2\pi/s_0} \right)^{n-n_*} \frac{\hbar^2 \kappa_*^2}{m}, \quad (4.21)$$

where κ_* denotes the wave vector of an arbitrary bound state labeled by $n = n_*$.

Obtaining the position of the first bound state κ_0 requires an accurate treatment of the interactions at short distance. However, due to the assumptions made in the derivation of the low-energy Fadeev equation, this information is lost, and needs to be reintroduced by choosing appropriate boundary conditions of the wavefunction in the region of $R \sim r_0$. Equivalently, one can choose a convenient cutoff R_0 of the effective potential in Eq. (4.20). Specifying the derivative $R_0 f'(R_0)/f(R_0)$ then

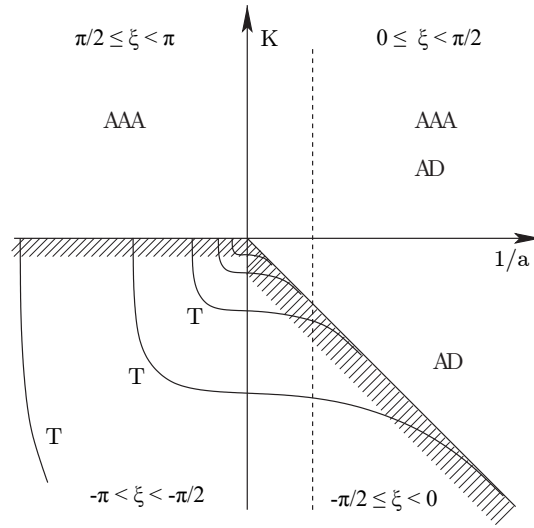


Figure 4.3: Efimov scenario. The Efimov state energies are plotted in the K - $1/a$ plane, which is actually given as $H^{1/4} \sin \xi$ versus $H^{1/4} \cos \xi$ for better visibility. The regions where three-body (atom-dimer) scattering states are allowed are labeled AAA (AD) and its threshold is indicated by cross-hatching. The dashed line indicates a fixed finite a value, for which only a limited number of Efimov states can be found. The relevant range for ξ is also shown in each quadrant. Reprinted and adapted from Braaten and Hammer, 2006 with permission from Elsevier.

yields the position of the first bound state. Once this has been fixed, all other energies are given by the universal Eq. (4.21).

This so called Efimov scenario is demonstrated in Fig. 4.3, where we plot $K = \text{sign}(E)(m|E|/\hbar^2)^{1/2}$ as a function of $1/a$. The exact dependence of the energies on $1/a$ is derived in Sect. 4.1.2, and our discussion so far only treats the region $a \rightarrow \infty$, where $1/a \rightarrow 0$. For the understanding of this figure, it is also convenient to introduce the polar coordinates H and ξ , which are defined via

$$1/a = H \cos \xi, \quad K = H \sin \xi. \quad (4.22)$$

Fig. 4.3 can then be understood as a plot of $H \sin \xi$ versus $H \cos \xi$. In order to fit more of the Efimov bound states into the figure, the axes were rescaled and show actually $H^{1/4} \sin \xi$ versus $H^{1/4} \cos \xi$. The angle ξ varies between $-\pi$ and π . The appropriate quadrants in the plot can be classified by the range of ξ , as indicated in Fig. 4.3. The straight line that represents the dimer threshold lies exactly on $\xi = -\pi/4$. The regions where three atom scattering states (AAA) and atom-dimer scattering states (AD) are possible, are also labeled. Some of the trimer states are labeled by T, and it should be noted that for better visibility only a limited number

of these states are shown. The Efimov states merge with the dimer threshold on the positive a side, and the three free atom threshold on the $a < 0$ side. As we will see in the next section, the number of experimentally accessible bound-states is ultimately limited due to finite temperature effects.

The discussion so far has introduced the Efimov effect using the simple example of three equal mass bosons. For the description of the resonances in systems with unequal masses, as for example the ^6Li - ^{133}Cs system, the general derivation is still valid, however, one must introduce slightly changed hyperspherical coordinates, which alters the matching condition in Eq. (4.18). In the remainder of this section we will outline how to generalize this treatment for such a mass-imbalanced system.

The \mathbf{r}_{ij} Jacobi coordinate of Eq. (4.2) remains unchanged, while

$$\mathbf{r}_{k,ij} = \mathbf{r}_k - \frac{m_i \mathbf{r}_i + m_j \mathbf{r}_j}{m_i + m_j} \quad (4.23)$$

now contains the masses m_i and m_j . The hyperradius

$$R^2 = \frac{m_1 m_2 r_{12}^2 + m_2 m_3 r_{23}^2 + m_3 m_1 r_{31}^2}{m_1 m_2 + m_2 m_3 + m_3 m_1}, \quad (4.24)$$

the hyperangles

$$\tan \alpha_k = \left(\frac{m_{ij}^2 (m_1 + m_2 + m_3)}{m_1 m_2 m_3} \right)^{1/2} \frac{r_{ij}}{r_{k,ij}}, \quad (4.25)$$

and the magnitudes of the vectors

$$r_{ij} = \left(\frac{m_1 m_2 m_3}{m_{ij} m_{123} (m_1 + m_2 + m_3)} \right)^{1/2} R \sin \alpha_k \quad (4.26)$$

and

$$r_{k,ij} = \left(\frac{m_{ij}}{m_{123}} \right)^{1/2} R \cos \alpha_k \quad (4.27)$$

are also redefined, using

$$m_{123} = \frac{m_1 m_2 m_3}{m_1 m_2 + m_2 m_3 + m_3 m_1} \quad (4.28)$$

and the well-known two-body reduced mass m_{ij} (as denoted by μ in Eq. (3.3)). The Fadeev wavefunction in Eq. (4.9) must be generalized to the form

$$\Psi(\mathbf{r}_1, \mathbf{r}_2, \mathbf{r}_3) = \psi^{(1)}(R, \alpha_1) + \psi^{(2)}(R, \alpha_2) + \psi^{(3)}(R, \alpha_3) \quad (4.29)$$

and the channel potentials now read³

$$V_n(R) = -\frac{(\lambda_n(R) - 1/4)\hbar^2(m_1 + m_2 + m_3)}{2(m_1m_2 + m_2m_3 + m_3m_1)R^2}. \quad (4.30)$$

If $R \sin \alpha_k$ is large enough that the two-body potential $V(R \sin \alpha_i)$ can be neglected in the generalized version of Eq. (4.15), the i -th Fadeev equation must be of the form

$$\psi^{(i)}(R, \alpha_i) \approx F^{(i)} \frac{\sin[\lambda^{1/2}(R)((\pi/2) - \alpha_i)]}{\sin(2\alpha_i)}, \quad (4.31)$$

where the R dependent functions $F^{(i)}$ are defined in Nielsen et al., 2001. This leads to the generalized version of the matching conditions (cf. (4.18))

$$\begin{aligned} & \left[\cos\left(\lambda^{1/2}\frac{\pi}{2}\right) - \left(\frac{m_1m_2m_3}{m_{jk}m_{123}(m_1 + m_2 + m_3)}\right)^{1/2} \lambda^{-1/2} \sin\left(\lambda^{1/2}\frac{\pi}{2}\right) \frac{R}{a_{jk}} \right] F^{(i)} \\ & - 2\lambda^{-1/2} \left[\frac{\sin[\lambda^{1/2}((\pi/2) - \gamma_{ij})]}{\sin(2\gamma_{ij})} F^{(j)} + \frac{\sin[\lambda^{1/2}((\pi/2) - \gamma_{ik})]}{\sin(2\gamma_{ik})} F^{(k)} \right] = 0, \end{aligned} \quad (4.32)$$

for the solutions at small and large $R \sin \alpha_k$, where a_{jk} denotes the scattering length between particle j and k . Here, i, j, k are permutations of 1, 2, 3 and the angle γ_{ij} satisfies

$$\tan \gamma_{ij} = \left(\frac{m_k(m_1 + m_2 + m_3)}{m_i m_j} \right)^{1/2}. \quad (4.33)$$

The equations for the three cyclic permutations of i, j, k can also be written in matrix form with a vector $\mathcal{F} = (F^{(1)}, F^{(2)}, F^{(3)})$:

$$\underline{\mathcal{M}} \mathcal{F} = 0. \quad (4.34)$$

This matrix equation has a non trivial solution only when the consistency equation

$$\det(\underline{\mathcal{M}}) = 0 \quad (4.35)$$

for the 3×3 coefficient matrix $\underline{\mathcal{M}}$ is fulfilled. The solutions of the matrix equation are the eigenvalues $\lambda_n(R)$.

The mass-imbalanced system exhibits the Efimov effect, when the lowest eigenvalue of Eq. (4.32) is negative at $R = 0$ and $r_0 \rightarrow 0$, because then the effective channel potential has the attractive $-1/R^2$ behavior that supports an infinite num-

³The leading minus sign is also given in Braaten and Hammer, 2006. It is possible that this is a typographical error.

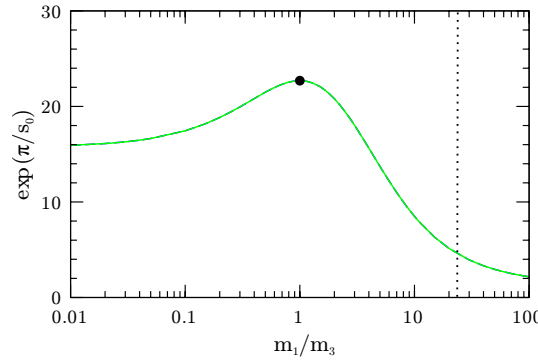


Figure 4.4: Mass dependence of the discrete scaling factor for three resonant pairs. The factor e^{π/s_0} is shown in dependence of the mass ratio m_1/m_3 for the scenario of two equal mass particles $m_1 = m_2$ in the case where the interactions between all pairs are resonant. The dotted line indicates the ${}^6\text{Li}$ - ${}^{133}\text{Cs}$ mass ratio. Reprinted and adapted from Braaten and Hammer, 2006 with permission from Elsevier.

ber of bound states. It should be noted that in this limit, Eq. (4.35) is independent of the scattering lengths.

For the case where the s -wave scattering length between all pairs is large⁴, Eq. (4.32) always has a negative single channel eigenvalue $\lambda_0(0) = -s_0^2$. Therefore, the Efimov effect occurs for all mass ratios. When $m_1 = m_2$, the scaling factor e^{π/s_0} ranges from 15.7 in the limit $m_1 = m_2 \ll m_3$ to 1 for $m_1 = m_2 \gg m_3$, as depicted in Fig. 4.4. It takes its maximum value of 22.7 for $m_1 = m_2 = m_3$ and it does not matter whether particle 1 and 2 are identical bosons or distinguishable particles.

When only two of the pairs exhibit large s -wave scattering lengths, e.g. a_{31} and a_{23} , the equation for $F^{(3)}$ in Eq.(4.32) can be ignored, and $F^{(3)}$ can be set to zero [Braaten and Hammer, 2006] for the equations in $F^{(1)}$ and $F^{(2)}$. Eq. (4.35) then reduces to

$$\begin{aligned} & \left[\cos\left(\lambda^{1/2}\frac{\pi}{2}\right) + \frac{2\lambda^{-1/2}\sin[\lambda^{1/2}((\pi/2) - \gamma_{12})]}{\sin(2\gamma_{12})} \right] \\ & \times \left[\cos\left(\lambda^{1/2}\frac{\pi}{2}\right) - \frac{2\lambda^{-1/2}\sin[\lambda^{1/2}((\pi/2) - \gamma_{12})]}{\sin(2\gamma_{12})} \right] = 0 \end{aligned} \quad (4.36)$$

for distinguishable equal mass particles 1 and 2. This equation has a single negative eigenvalue $\lambda_0(0) = -s_0^2$, and therefore exhibits the Efimov states regardless of the values of the masses. While the first factor in Eq. (4.36) does not have a negative

⁴This assumption inhibits the three particles from being identical fermions.

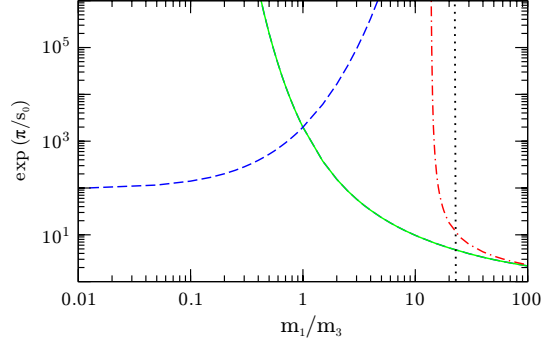


Figure 4.5: Mass dependence of the discrete scaling factor for two resonant pairs. The factor e^{π/s_0} is shown in dependence of the mass ratio m_1/m_3 for the scenario of two equal mass particles $m_1 = m_2$ in the case where only two of the inter particle interactions are resonant. For large a_{23} and a_{31} , particles 1 and 2 can be identical bosons or distinguishable particles (solid line) or identical fermions (dash-dotted line). For large a_{12} and a_{31} , the two equal mass particles must be distinguishable (dashed line). The dotted vertical line indicates the ${}^6\text{Li}$ - ${}^{133}\text{Cs}$ mass ratio. Reprinted and adapted from Braaten and Hammer, 2006 with permission from Elsevier.

solution, the second one gives rise to the negative eigenvalue and the Efimov effect.

The second factor in Eq. (4.36) also arises for the case when particle 1 and 2 are identical bosons. Thus, the Efimov states are also present in such systems, with the same discrete scaling factor as for the previous example. The first factor in Eq. (4.36) also appears for the case of two identical fermions. Since it has no negative eigenvalues, there is no Efimov effect in the discussed limit of vanishing subsystem angular momentum. When the mass ratio m_1/m_3 is larger than a critical value $\delta_c = 13.6$, the Efimov effect connected to nonzero subsystem angular momentum occurs. When a_{12} and a_{31} or equivalently a_{12} and a_{23} are large, the matching equation has negative solutions only for distinguishable equal mass particles 1 and 2. The scaling factor for all the possible scenarios with two resonant interactions, where two of the particles have equal mass, are summarized in Fig. 4.5.

For the case of ${}^6\text{Li}$ - ${}^{133}\text{Cs}$ the limits of two or three resonant pairwise interactions do not differ severely. Based on the treatment in Braaten and Hammer, 2006, we expect a scaling factor of ~ 4.3 for three, and ~ 4.8 for two resonant pairs. The treatment in D’Incao and Esry, 2006 finds a consistent value of 4.88 for two resonant pairs, and the authors of Wang et al., 2012b state agreeing scaling factors of 4.88 for two and 4.30 for three resonant pairwise interactions.

4.1.2 Efimov's Radial Law and Scattering Observables

In order to obtain experimental observables of interest, as for example the three-body recombination rate or the Efimov trimer binding energies, we have to proceed to a more realistic situation with finite a , and therefore relax our requirement of the resonant limit $a \rightarrow \infty$. For this treatment, we go back to the case of three identical bosons. While the derivation for mass imbalanced particles can be performed analogous to the following discussion, it does not bring any new insights. We refer to the literature [Braaten and Hammer, 2006; Wang et al., 2013 and references therein] for this procedure. The effects of deeply-bound dimers are neglected in the beginning of the discussion, as they can be added later in a quite simple fashion.

Instead of solving the Schrödinger equation for the whole range of R , we look at the evolution of incoming low energy scattering state from large to small values, and then to large values again. This can typically be described by a 2×2 symmetric unitary matrix

$$\begin{pmatrix} S_{AAA,AAA} & S_{AAA,AD} \\ S_{AD,AAA} & S_{AD,AD} \end{pmatrix} \begin{pmatrix} |AAA\rangle_{in} \\ |AD\rangle_{in} \end{pmatrix} = \begin{pmatrix} |AAA\rangle_{out} \\ |AD\rangle_{out} \end{pmatrix}, \quad (4.37)$$

where the entries $S_{i,j}$ describe the amplitude of the evolution from state i to state k . The subscript *in* (*out*) denotes the incoming (outgoing) wavefunction. The advantage in this approach lies in the fact that for the regions where the derivation of the wavefunction is not straightforward, we can simply apply probability conservation arguments in order to acquire information on the total reactive behavior of the system.

We start by dividing the range of the hyperradius R into four characteristic regions:

- The asymptotic region $R \gg |a|$.
- The long-distance region $R \sim |a|$.
- The scale-invariant region $r_0 \ll R \ll |a|$.
- The short-distance region $R \sim r_0$.

The interaction potential in the asymptotic region is negligible. This justifies the simple choice of the S -matrix in Eq. (4.37), as the only possible solutions are atom-dimer and free atom scattering states. The former is a product of a universal

dimer wavefunction similar⁵ to Eq. (3.21) and a free atom scattering wavefunction. The latter can be expressed in terms of Bessel functions. These states are of course only supported for positive energies, or for negative energies above the atom-dimer threshold when $a > 0$ (see Fig. 4.3). In the region where only one (none) of them is allowed, only one (none) of the matrix elements of Eq. (4.37) is nontrivial, which further simplifies the treatment in this region.

In the scale-invariant region, Eq. (4.20) describes the hyperradial wave. Sufficiently deep in this region, E in Eq. (4.20) can be neglected, and the solution

$$\psi_{hw}(R, \alpha) = \frac{\sinh[((\pi/2) - \alpha_1)R/a]}{R^2 \sin(2\alpha_1)} [Ae^{is_0 \ln(HR)} + Be^{-is_0 \ln(HR)}], \quad (4.38)$$

can be written as an incoming and an outgoing hyperradial wave with arbitrary amplitudes A and B .

Obtaining a solution for the wavefunction in the short-distance region is more involved than for the two regions discussed above. However, when the system does not decay to deep bound-states, and no coupling to other hyperradial channels exists, probability must be conserved. Therefore, instead of trying to find an explicit solution, we only consider the effect of the short-distance region on the wavefunction of the scale-invariant region. For a complete reflection, the outgoing amplitude A in Eq. (4.38) must be equal in magnitude as the incoming amplitude B ,

$$A = e^{2i\theta_*} B, \quad (4.39)$$

and might only differ by a phase

$$\theta_* = -s_0 \ln(cH/\Lambda_0) \quad (4.40)$$

which is picked up during the reflection at short range. Here, c is a numerical constant, and Λ_0 is connected to the wave vector of the ground-state Efimov trimer⁶. Thus, θ_* is fully specified by the boundary condition at short range, or equivalently by specifying $R_0 f'(R_0)/f(R_0)$ at the short-range cutoff R_0 .

The long-distance region does not allow for simplifications that ease the acquisition of an explicit wavefunction. Therefore, we also base our treatment on arguments of probability conservation. The incoming and outgoing probability flux can only derive from the scale-invariant and asymptotic regions, for which we know the explicit wavefunctions. Thus, we describe the evolution in the long-distance region by

⁵The expression in Eq. (3.21) must simply be transformed to the hyperspherical basis.

⁶See Eq.(217) in Braaten and Hammer, 2006.

a unitary, symmetric⁷ 3×3 matrix

$$s_{ij} = \langle i \text{ in} | \hat{U} | j \text{ out} \rangle, \quad (4.41)$$

where \hat{U} describes the evolution of a wavefunction through the long-distance region. The label in (out) denotes an incoming (outgoing) wave with respect to the long-distance region. The indices $i, j = 1, 2, 3$ denote hyperradial waves from the scale invariant region, asymptotic dimer states and asymptotic three-atoms states, respectively. The diagonal entries s_{ii} describe reflections of the wave i , and the off-diagonal elements s_{ij} represent the coupling between the waves i and j .

By use of the long-distance s -matrix, we can now state the terms of the S -matrix in Eq. (4.37) explicitly:

$$S_{AD,AD} = s_{22} + s_{21} \frac{1}{1 - e^{2i\theta_*} s_{11}} e^{2i\theta_*} s_{12} \quad (4.42)$$

$$S_{AD,AA} = s_{23} + s_{21} \frac{1}{1 - e^{2i\theta_*} s_{11}} e^{2i\theta_*} s_{13} \quad (4.43)$$

$$S_{AAA,AAA} = s_{33} + s_{31} \frac{1}{1 - e^{2i\theta_*} s_{11}} e^{2i\theta_*} s_{13}. \quad (4.44)$$

The first summand in each of the equations represents a direct reflection of the incoming wave in the long-distance region. When the second summand is expanded in a power series of s_{11} , the n -th term describes transmission through the long-distance region, n cycles of back and forth reflection at short- and long-distance regions, and finally transmission through the long-distance region.

As found by Efimov [Efimov, 1979], the radial variable H enters only through the angle θ_* into the S -matrix. Additionally, he demonstrated strict constraints for the dependence of the matrix on ξ . Thus, the calculation of specific properties of the S -matrix for all values of E , a and κ_* reduces to the calculation of a few universal functions depending on ξ .

One example of such a property is the calculation of binding energies. As the bound-states require a standing wave, they can only occur when the reflected wave at the short-distance region is resonant with the reflected wave from the long-distance region. This can be expressed in the condition

$$\exp(2i\theta_*) s_{11} = 1, \quad (4.45)$$

which is equivalent to setting the denominators in Eqs. (4.42)- (4.44) to zero. In

⁷The symmetric property of the matrix is a consequence of time reversal invariance.

the region $-\pi < \xi < -\pi/4$, where the Efimov states can occur (see Fig. 4.3), both AAA and AD states are forbidden, which allows us to set $s_{22} = s_{33} = 1$ and $s_{12} = s_{31} = s_{23} = 0$. Due to the unitarity of s , we can write s_{11} in the form

$$s_{11} = \exp(i\Delta(\xi)), \quad (4.46)$$

with $\Delta(\xi)/2$ being the hyperradial phase-shift from the reflection of the long-distance region. Combining these two conditions, we can obtain bound-states via the solution of

$$2\theta_* + \Delta(\xi) = 0 \pmod{2\pi}. \quad (4.47)$$

Inserting the appropriate expression for H, ξ and θ_* , we obtain the solution for the energy of an Efimov state

$$E_T + \frac{\hbar^2}{ma^2} = (e^{-2\pi/s_0})^{n-n_*} \exp[\Delta(\xi)/s_0] \frac{\hbar^2 \kappa_*^2}{m}, \quad (4.48)$$

where $\tan \xi = -(mE_T/\hbar^2)^{1/2}a$. We have derived the dependence of the Efimov energies on the scattering length a . Eq. (4.48) recovers the spectrum of Eq. (4.21) in the resonance limit $a \rightarrow \pm\infty$, because in this case $\xi = -\pi/2$ and $\Delta(\xi) \rightarrow 0$. For all other cases, the universal functions $\Delta(\xi)$ have been calculated numerically via renormalized zero-range models or effective field theory, and a simple set of parametrizations for $\Delta(\xi)$ is given in Braaten and Hammer, 2006. The scattering length dependence of the trimer energies is illustrated in Fig. 4.3

So far, the effect of deeply bound states has been neglected. However, due to the separation of length scales, its treatment is facilitated enormously. For the transitions into deep dimers, the three particles have to be sufficiently close together, because the size of the bound-state is on the order of r_0 . When $E_{\text{deep}} \gtrsim \hbar^2/mr_0^2$ is the energy of the bound state, energy and momentum conservation require the third atom to acquire a momentum of $(4mE_{\text{deep}}/3)^{1/2}$. As this is on the order \hbar/r_0 , this momentum kick can only be delivered when all three atoms are within a range of r_0 . Therefore, the only relevant region for this process is the short-range region, where the coupling between incoming scattering channel and outgoing deeply bound-state channel is significant. We can simply include the decay by accounting for the lost fraction $e^{-4\eta_*}$ of the reflected probability at short range by adding an appropriate factor to the reflected amplitude of Eq. (4.39). The parameter η_* describes the cumulative effect of the decay to all deeply-bound states. The

equivalent of Eq. (4.39) then reads

$$A = -e^{-2\eta_* + 2i\theta_*} B. \quad (4.49)$$

The S -matrix can be built up analogous to Eqs. (4.42)-(4.44), when all angles θ_* are replaced by $\theta_* + i\eta_*$. Like in Eq. (4.41), a matrix

$$t_{ij} = \langle i \text{ in} | \hat{U} | j \text{ out} \rangle \quad (4.50)$$

for the long-distance region can be defined, where now an additional pair of incoming and outgoing states, labeled with subscript X , are added for each deeply bound state. Similar to Eqs. (4.42)-(4.44), we can now write the S -matrix elements for transitions from the S_{AAA} and S_{AD} states to the deeply bound atom-molecule scattering state X as

$$\sum_X |S_{X,AD}|^2 = \frac{(1 - e^{-4\eta_*})|s_{12}|^2}{|1 - e^{-2\eta_* + 2i\theta_*} s_{11}|^2} \quad (4.51)$$

$$\sum_X |S_{X,AAA}|^2 = \frac{(1 - e^{-4\eta_*})|s_{13}|^2}{|1 - e^{-2\eta_* + 2i\theta_*} s_{11}|^2}, \quad (4.52)$$

where the sum is performed over all deeply bound states X .

The condition for a bound-state, analogous to Eq. (4.47), becomes

$$2(\theta_* + i\eta_*) + \Delta(\xi) = 0 \pmod{2\pi}, \quad (4.53)$$

which yields the solutions

$$E_T + \frac{i}{2}\Gamma_T + \frac{\hbar^2}{ma^2} = (e^{-2\pi/s_0})^{n-n_*} \exp\left[\frac{\Delta(\xi) + 2i\eta_*}{s_0}\right] \frac{\hbar^2 \kappa_*^2}{m}, \quad (4.54)$$

where $\tan \xi = -(m(E_T + i\Gamma_T/2)/\hbar^2)^{1/2}a$. Here, the Efimov states are no longer sharp, but exhibit a finite width Γ_T due to the decay into deeply bound states. This width is given by

$$\Gamma_T \approx \frac{4\eta_*}{s_0} \left(E_T + \frac{\hbar^2}{ma^2} \right) \quad (4.55)$$

for sufficiently small η_* .

Our main motivation for the introduction of Efimov's radial law is the derivation of the experimentally observable three-body loss coefficient L_3 . It is typically defined

via

$$\frac{d}{dt}n = -L_3 n^3 \quad (4.56)$$

for a thermal gas, and is the most commonly used method to examine the Efimov effect, which reveals itself via modulations in L_3 . With the help of the previous derivations, it is straightforward to obtain an analytic expression for L_3 . As our experiments focus on the region $a < 0$, we will not discuss the three-body loss rates for positive values of a , where both decay into shallow and deep dimers can occur. In the negative a region, the scattering state can only decay to deeply bound states, because there are no universal two-body bound states (see Sect. 3.2.2).

Hence, the L_3 coefficient is directly proportional to $\sum_X |S_{X,AAA}|^2$ as given in Eq. (4.52). The s -matrix elements s_{11} and s_{13} can be expanded in powers of K , and in the low energy limit $K \rightarrow 0$, the resulting expression for L_3 in a thermal gas on the negative a side taking only the leading order into account, reads

$$L_3 = 3 \frac{4590 \sinh(2\eta_*)}{\sin^2[s_0 \ln(a/a_*)] + \sinh^2 \eta_*} \frac{\hbar a^4}{m} \quad (a < 0). \quad (4.57)$$

Here, a_* is the position where an Efimov trimer merges with the three free atom continuum.

The behavior of this function is schematically shown⁸ in Fig. 4.6 for three-different values of η_* . For increasing η_* values, the peaks become less pronounced, and for $\eta_* \rightarrow \infty$ the loss rate would just become a straight line in this plot. One can clearly see the characteristic logarithmic scaling in a , where the loss rate is increased for those values of a that coincide with an Efimov state merging into the three-body scattering threshold (see Fig. 4.3). An intuitive explanation for this behavior can be found in Esry and D’Incao, 2007 and D’Incao and Esry, 2005, where the enhanced loss rate is interpreted as a shape resonance due to a barrier in the incoming three free atom channel.

In order to understand this barrier, we have to reanalyze the effective channel potentials of Fig. 4.2. The derivation of these potentials holds only for the region $r_0 \ll R \ll |a|$. The Efimov effect arises from the bound-states found in this region. For $R \sim |a|$, D’Incao and Esry, 2005 have shown that the potential takes on the form

$$V(R) \propto \frac{\lambda(\lambda + 4) + 15/4}{2\mu_{ijk} R^2}, \quad (4.58)$$

where λ is a positive integer and μ_{ijk} is a three-body reduced mass, as e.g. defined

⁸In reality we use Eq.(25) of Helfrich et al., 2010, since this work gives analytical formulas to calculate the desired parameters for the heteronuclear case.

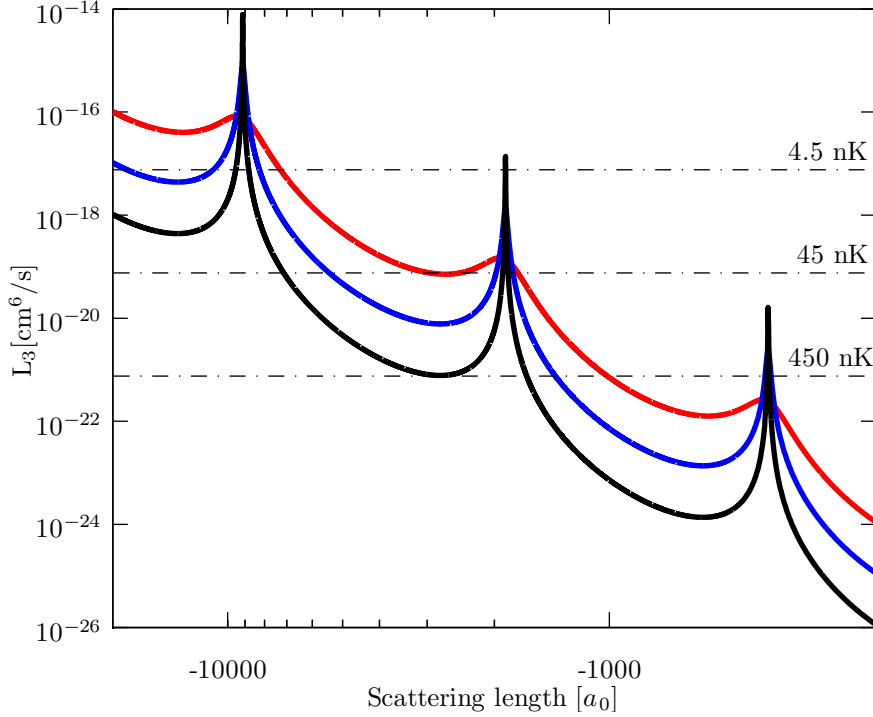


Figure 4.6: Three-body loss coefficient as a function of scattering length.

L_3 of Eq. (4.57) for a ${}^6\text{Li}$ - ${}^{133}\text{Cs}$ mixture is schematically plotted for $\eta_* = 0.0024$ (black solid line), $\eta_* = 0.024$ (blue solid line), and $\eta_* = 0.24$ (red solid line). The dashed horizontal lines represent the unitarity limit given by Eq. (4.60) for the indicated temperatures. Instead of using the explicit form of Eq. (4.57), we employ the analytic form of Eq.(25) in Helfrich et al., 2010, because here the involved parameters for the heteronuclear case are given explicitly.

in Nielsen et al., 2001. This potential yields a barrier with a position proportional to $|a|$, and a height proportional to $1/a^2$. Tuning of a shifts the height and position of a quasi-bound state in the inner region of the barrier. When the energy of the incoming atoms is resonant with such a bound state, the tunneling through the barrier is enhanced, and the amplitude of the wavefunction behind the barrier is significantly increased. As explained above, this inner region also contains the coupling to the deeply bound dimers. The component of the incoming wavefunction that penetrates into this region can decay to deeply bound states, which explains the enhanced losses by three-body recombination.

Finally, we consider the limitations on the above derived properties. For the derivation of the geometric scaling formula in Eq. (4.21), we inherently used the scaling limit ($r_0 \rightarrow 0$) and the resonant limit ($a \rightarrow \infty$) simultaneously in order to obtain the channel potentials of Eq. (4.14) via solving Eq. (4.15). If we account for the finite range r_0 of the interaction potential, these solutions are valid only for

energies above $E \sim \hbar^2/(mr_0^2)$, which is also called ultraviolet cutoff. This gives a bound of the Efimov trimer energies from below.

Some calculations of physical quantities like the three-body loss rate in Eq. (4.57), require knowledge of the s -wave phase-shift⁹. For sufficiently low energies, the expression for the scattering length can be expanded in powers of k . This so-called effective range expansion

$$k \cot \delta_0(k) = -1/a + \frac{1}{2}r_s k^2 + \dots \quad (4.59)$$

is often truncated after the first summand on the right side of Eq. (4.59). However, above (below) a characteristic energy (distance) scale, higher-order terms, e.g. the term including the s -wave effective range r_s , have to be incorporated for an accurate calculation of the desired properties.

Last but not least, experiments are performed at finite temperatures. This adds corrections to several expressions, where the low-energy limit was assumed. Most importantly, the three-body loss rate will have an upper-bound, given by the saturation of the two-body cross section in Eq. (3.9). For sufficiently high a , the a^2 factors cancel, and the cross section is limited to the scattering length independent value $4\pi/k^2$. This phenomenon is referred to as unitarity limit. An order of magnitude estimate for the limit on the three-body loss rate has been calculated by D’Incao and Greene, 2014 for the case of two bosons and one fermion:

$$L_{3,\text{lim}} = \frac{8\pi^2 \hbar^5}{\mu^3 (k_B T)^2}, \quad (4.60)$$

where $\mu = \sqrt{m_B^2 m_F / (2m_B + m_F)}$ is the reduced mass containing the boson mass m_B and the fermion mass m_F . For this calculations, only the decay from scattering states in the lowest angular momentum ($J = 0$) channel to a few bound states has been included. For a more elaborate expression, one would have to include all bound states and higher angular momenta, which can significantly increase this limit [D’Incao et al., 2004]. When the scattering length is on the order of the thermal de Broglie wave length (see Eq. (2.10)), the three-body loss coefficient deviates from the behavior of Eq. (4.57) and merges to the value given by $L_{3,\text{lim}}$. In this case, no further modulation due to Efimov resonances can be clearly resolved. This behavior is a limiting factor in our experiment. $L_{3,\text{lim}}$ is depicted in Fig. 4.6 for

⁹The s -wave phase-shift for the derivation of Eq. (4.57) enters via an expansion of the s -matrix elements of Eq. (4.41), which is not explicitly discussed in this work. We refer to Braaten and Hammer, 2006 for a detailed description

several temperatures. Besides reaching the unitarity limit, the finite temperature also washes out the signal of the enhanced losses due to thermal averaging, which also leads to shifts of the peak position to smaller scattering lengths [D’Incao et al., 2004].

4.2 Experimental Procedure for the Detection of Efimov Resonances

We proceed to describe the experimental scheme that we apply for the measurement of the Efimov states in a ${}^6\text{Li}$ - ${}^{133}\text{Cs}$ mixture. The previously described measurement of the FRs (see Chap. 3) were performed at ${}^6\text{Li}$ (${}^{133}\text{Cs}$) temperatures of $2\ \mu\text{K}$ ($8\ \mu\text{K}$). The resulting unitarity limited three-body collision rate does not allow for the detection of Efimov related modulations. Hence, we present a new approach to reach colder temperatures in the following section. The method is somewhat similar to the one present in Sects. 2.3 and 2.4, with the main difference being a spatial displacement of the ${}^{133}\text{Cs}$ reservoir trap.

We start by loading a ${}^{133}\text{Cs}$ MOT in typically 2 s, followed by DRSC into the reservoir trap at 35 W. The atoms at the wings of the trap are heated due to conversion of potential to kinetic energy. We counteract this effect by adding an additional Raman cooling pulse. To this end, the lattice and the optical pumping beam are turned off and after 5.1 ms of propagation in the dipole trap potential towards the trap center, where the kinetic energy is at its maximum, we turn both lasers back on for 1.5 ms to remove the excess kinetic energy. We then ramp the fields and laser powers of the Raman lasers down (see Sect. 2.2.2), and apply an offset field of $\sim 4.5\ \text{G}$ in order to provide a quantization axis that keeps the sample polarized.

We continue by loading a ${}^6\text{Li}$ MOT for 1.8 s with a sufficient displacement from the ${}^{133}\text{Cs}$ atoms. The ${}^6\text{Li}$ atoms are loaded into the dimple trap at $\sim 1\ \text{mm}$ distance from the reservoir trap, and the offset field is set to 943 G, where the scattering length between the two lowest hyperfine states of ${}^6\text{Li}$ is $-5400\ a_0$ and the ${}^{133}\text{Cs}$ intraspecies scattering length amounts to $900\ a_0$. The high a values ensure rapid thermalization, while ${}^6\text{Li}$ three-body losses are strongly suppressed due to Pauli blocking.

Subsequently, we apply forced evaporation on each of the species in their respective traps. The ${}^6\text{Li}$ atoms are evaporated in the dimple trap by ramping the power from $\sim 100\ \text{W}$ to $200\ \text{mW}$ within 3.7 s. Simultaneously, the reservoir trap is ramped

4.2. Experimental Procedure for the Detection of Efimov Resonances

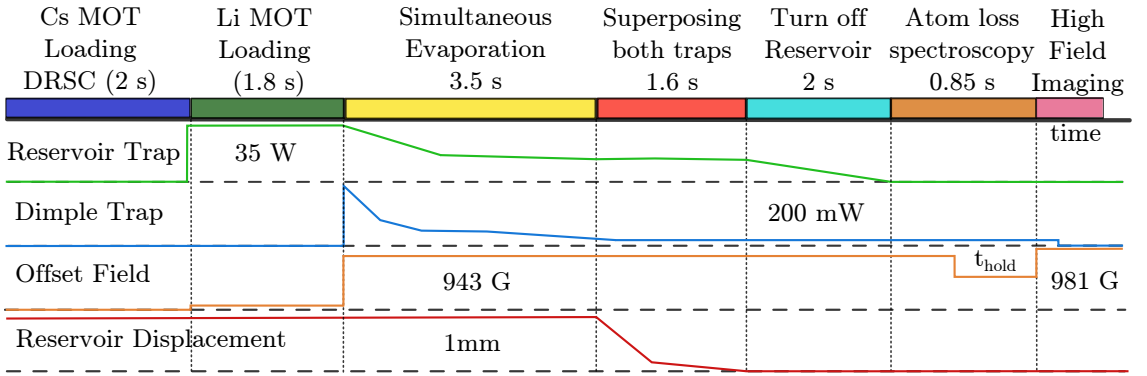


Figure 4.7: Experimental sequence for atom loss spectroscopy. The reservoir and dimple trap laser powers, offset field, and reservoir trap position are schematically illustrated as a function of time. For details see text.

from 35 W to 21 W within 3.5 s in order to evaporatively cool ^{133}Cs . Right after the latter evaporation ramp both traps are superposed. This is performed by moving the reservoir laser beams with a piezo driven mirror within 600 ms to the direct vicinity of the dimple trap. The clouds are finally brought together by superposing the reservoir sufficiently slow within 1 s, in order to ensure approximately an adiabatic merging of both traps and thus reduce heating. In order to load the ^{133}Cs atoms into the dimple trap, the reservoir is turned off in a ramp of 2 s. In this step, the ^6Li and ^{133}Cs clouds overlap, and a FR between the $^6\text{Li}|f = 1/2, m_f = -1/2\rangle$ and $^{133}\text{Cs}|3, 3\rangle$ hyperfine states leads to sympathetic cooling of ^{133}Cs by expelling all $^6\text{Li}|1/2, -1/2\rangle$ atoms from the trap. This is a convenient effect, because the remaining ^6Li atoms are only those that are in their energetically lowest $|1/2, 1/2\rangle$ state. After allowing for thermalization within 450 ms, we finally arrive at an excellent starting point for our Efimov resonance measurements, with typically 4×10^4 ^6Li and 1.6×10^4 ^{133}Cs atoms at trap frequencies of $275 \times 308 \times 33$ Hz and $114 \times 123 \times 11$ Hz, respectively. The temperatures of both species are approximately 400 nK.

For the atom loss spectroscopy, we quickly ramp the field to a selected variable value close to the FR at 843 G. The atom number is then recorded after a fixed hold time t_{hold} at the specific field value. Both species are then detected at a field of 981 G using the high field imaging technique as discussed in Sect. 2.1.5. This sequence is summarized in Fig. 4.7.

The measurement of the three-body loss coefficient is performed in a similar fashion as the atom loss spectroscopy, with only the following three differences. Firstly, instead of the atom numbers given above, we load a mixture of 2×10^4 (3×10^4) ^{133}Cs (^6Li) atoms. The difference in ^6Li atom number is caused by degrading of the ^6Li MOT laser TA chip, which results in a lower total power available for the

optical cooling and trapping of ^6Li atoms. Secondly, 200 ms after turning off the reservoir trap, we increase the dimple trap laser power by $\sim 10\%$ within 200 ms, in order to increase the ratio $U/k_B T$ of trap depth U to temperature T . In doing so, we reduce residual evaporation, but also increase the temperature of both species to ~ 450 nK. We then ramp the offset field to the vicinity of the FR at 843 G. The third difference is that instead of holding the atoms at the offset field for a fixed time t_{hold} , we vary this parameter in order to track the time evolution of the atom number, which allows us to extract the three-body loss coefficient (see Eq.(4.56)). The results of both the atom loss and three-body loss coefficient measurements are presented in the subsequent section.

4.3 Three-Body Loss Coefficient and Atom Loss Measurements

We start analyzing the Efimov resonances by assessing the atom number after a fixed hold time in the trap at various fields close to the FR at ~ 843 G. The results of these measurements are summarized in Fig. 4.8. We clearly observe a modulation in the ^{133}Cs losses after a storage time of 1 s in Fig. 4.8(b). In the discussion below, we identify this feature as the first Efimov resonance.

Due to the a^4 scaling of the three-body loss coefficient (see Eq. (4.57)), the atomic losses occur much faster close to the FR, where a increases (see Fig. 3.2(a)). Therefore, we reduce the hold time to 400 ms for the ^{133}Cs atom number measurements in the direct vicinity of the FR, which is shown in Fig. 4.8(a). Besides the global loss maximum, which can be associated with the pole of the FR, we observe a clear loss feature near 844 G and an additional small atom number decrease at 843 G (see inset in Fig. 4.8(a)). The former one is identified as the excited Efimov state in the following paragraphs, and the latter one is presumably the second excited state.

We determine the exact position of the three loss features by fitting Gaussian profiles with a linear background to each feature. The result of this fit yields $B_0 = 849.12(6)_{\text{stat}}(3)_{\text{sys}}$ and $B_1 = 844.89(1)_{\text{stat}}(3)_{\text{sys}}$ for the position of the first two Efimov resonances, where the first errors denote the statistic uncertainty in the fit, and the second errors result from the systematic uncertainty in the absolute magnetic field value. For the very narrow feature we obtain the field value $B_2 = 843.03(5)_{\text{stat}}(3)_{\text{sys}}$, where the first error contains the width of the Gaussian profile instead. This is probably the second excited Efimov resonance.

Under the experimental conditions of the measurements in Fig. 4.8(a) and (b),

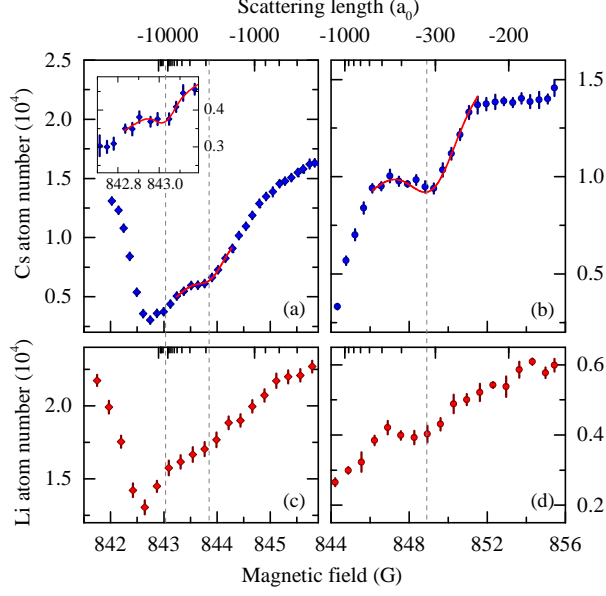


Figure 4.8: Magnetic field dependent atom loss measurements of the Li-Cs mixture at a temperature of 400 nK. The ^{133}Cs atom number after a hold time of 400 ms (a) and 1 s (b) is illustrated. The inset in (a) is a zoom into the region where a third loss feature can be seen. The ^6Li atoms show resonances at consistent positions after a hold time of 1.2 s (c) and (d), when the initial ^6Li atom number is reduced by a factor of two as compared to the measurements in (a) and (b). Each of the values are the mean of at least six independent measurements, and the error bars represent the standard error. The dashed vertical lines indicate the position of the Efimov resonances. The resonance positions are determined via a fit of Cs atoms with Gaussian profiles with linear background (red solid lines). The scattering length scale has been assigned via radio frequency association of universal dimers.

the relative loss fraction of ^6Li at B_0 and B_1 is too small to be discerned from atom number fluctuations caused by instabilities in the experiment. However, lowering the ^6Li atom number by a factor of two as compared to the previous measurements allows us to increase the relative loss fraction. Hence, we recover the loss features at consistent magnetic fields, as presented in Fig. 4.8(c) and (d) for storage times of 1.2 s. The fact that the ^6Li atom number losses occur on much slower time scales already hint at a three-body loss process that is dominated by two ^{133}Cs and one ^6Li atom. This is the most probable loss process, as Pauli blocking reduces the likeliness of finding two ^6Li atoms in the same spin state at a sufficiently close distance for three-body recombination to occur.

Even though the above described atom loss features are strong hints of Efimov resonances, it is inevitable to measure L_3 (see Eq. (4.57)) in order to verify that

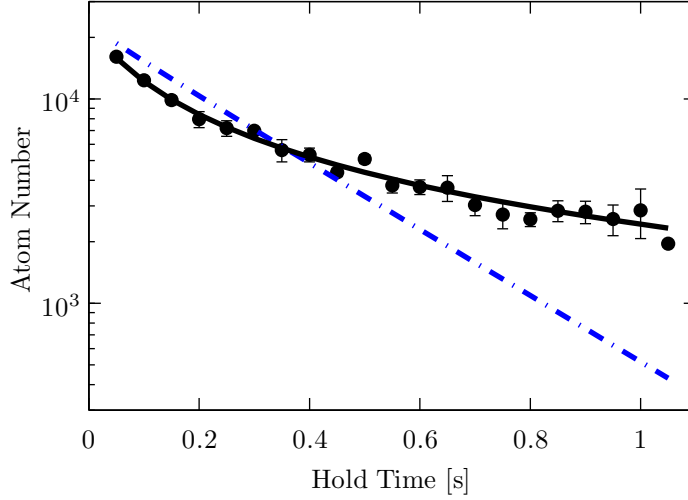


Figure 4.9: Time-dependent atom losses in a ${}^6\text{Li}$ - ${}^{133}\text{Cs}$ mixture at a field of 843.9 G. The dots show the ${}^{133}\text{Cs}$ atom number, where the error is given by the standard error from five measurements. The black solid line shows the results of a fit to Eq. (4.62), where only Li+Cs+Cs and Cs intraspecies three-body losses have been included. The blue dash-dotted line demonstrates a fit to Eq. (4.62) when the Li+Cs+Cs loss channel is replaced by Li+Li+Cs losses which scale as $n_{\text{Li}}^2 n_{\text{Cs}}$.

the observed Efimov resonances are indeed caused by a three-body process with the same ratio of Cs to Li atoms involved. For this purpose, we now evaluate the temporal evolution of the atom numbers via the experimental scheme described in the previous section. A typical result of such a measurement is shown in Fig. 4.9 for the ${}^{133}\text{Cs}$ atom number. While we lose $\sim 90\%$ of the ${}^{133}\text{Cs}$ atoms for typical hold times on the order of a few seconds, we only lose $\sim 30\%$ of the ${}^6\text{Li}$ atoms. The temperature of the mixture remains unaffected within the uncertainties of our temperature determination ($\sim 15\%$).

The evolution of n_{Cs} is given by the rate equation

$$\dot{n}_{\text{Cs}} = -L_1^{\text{Cs}} n_{\text{Cs}} - L_3^{\text{LiCsCs}} n_{\text{Li}} n_{\text{Cs}}^2 - L_3^{\text{Cs}} n_{\text{Cs}}^3. \quad (4.61)$$

Here, L_1^{Cs} , L_3^{LiCsCs} and L_3^{Cs} are the loss coefficients for ${}^{133}\text{Cs}$ background collisions, ${}^6\text{Li}+{}^{133}\text{Cs}+{}^{133}\text{Cs}$ three-body collisions, and ${}^{133}\text{Cs}+{}^{133}\text{Cs}+{}^{133}\text{Cs}$ three-body collisions, respectively. The inter- and intraspecies two-body losses are ignored in Eq. (4.61), because the atoms are in the energetically lowest states and thus only exhibit elastic collisions. Under the conditions of the experiment the temperature dependence of the three-body loss coefficients [Rem et al., 2013] can be neglected, and n_{Li} can be assumed constant to a good approximation. Because the tempera-

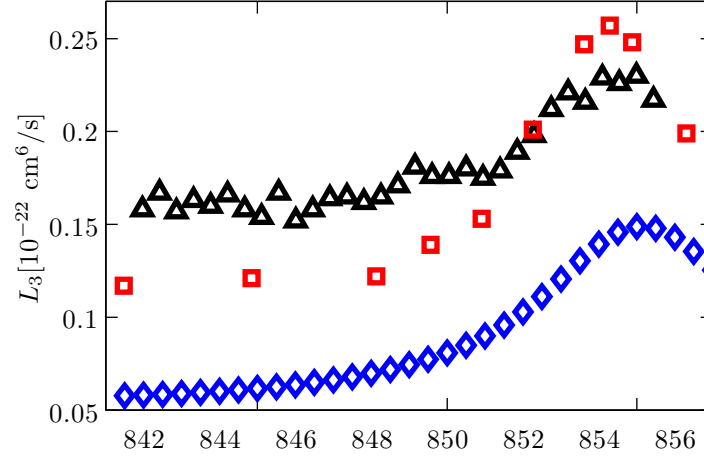


Figure 4.10: ^{133}Cs intraspecies three-body loss coefficient. The black triangles illustrate the results of our measurements at a temperature of 410 nK in the relevant field region. For comparison, we also present independent data taken at Innsbruck [Huang and Grimm, 2014] for a sample temperature of 330 nK (red squares). A calculation based on the finite temperature model by Rem et al., 2013 for 410 nK (blue diamonds) [Huang and Grimm, 2014] yields values that are within our systematic error of $\sim 80\%$. The ^{133}Cs Efimov resonance at 853 G [Berninger et al., 2013] does not influence the system in the relevant field region between 842 G and 852 G.

ture is nearly constant, the change in density can be directly linked to the change in atom number.

A comparison of the description of the atom losses via $\text{Li}+\text{Li}+\text{Cs}$ and $\text{Li}+\text{Cs}+\text{Cs}$ losses is shown in Fig. 4.9. For the calculation of the former process we numerically solve Eq. (4.61) in the manner described below, replacing the summand containing L_3^{LiCsCs} by $L_3^{\text{LiLiCs}} n_{\text{Li}}^2 n_{\text{Cs}}$. The fit to $\text{Li}+\text{Cs}+\text{Cs}$, as also described below, is plotted in Fig. 4.9, as well. It is obvious that the ^{133}Cs atom loss curves are described by $\text{Li}+\text{Cs}+\text{Cs}$ and $\text{Cs}+\text{Cs}+\text{Cs}$ losses (black solid line in Fig. 4.9), while a description via $\text{Li}+\text{Li}+\text{Cs}$ and $\text{Cs}+\text{Cs}+\text{Cs}$ loss rates (blue dash-dotted line in Fig. 4.9) does not reproduce the shape of the loss curves. This observation verifies that $\text{Li}+\text{Li}+\text{Cs}$ three-body losses are indeed strongly suppressed due to Fermi statistics and confirms that the observed Efimov resonances originate from the $\text{Li}+\text{Cs}+\text{Cs}$ channel, which is the only channel for this mixture that is predicted to support universal three-body bound states [Braaten and Hammer, 2006; D’Incao and Esry, 2006]. This is also reflected in the loss ratio of Li to Cs atom numbers of $\sim 1:2$ in the entire range of the probed magnetic fields.

In order to extract the loss rates from our measurements, we integrate Eq. (4.61)

over the density distributions given in Eq. (2.3), which yields an equivalent equation for the atom number evolution:

$$\frac{dN_{\text{Cs}}}{dt} = -L_1^{\text{Cs}} N_{\text{Cs}} - L_3^{\text{LiCsCs}} C_1 N_{\text{Li}} N_{\text{Cs}}^2 - L_3^{\text{Cs}} C_2 N_{\text{Cs}}^3. \quad (4.62)$$

The constants

$$C_1 = \prod_{i=x,y,z} \frac{(\sigma_{i,\text{Li}}^2 + \sigma_{i,\text{Cs}}^2)^{-1/2}}{2\pi\sigma_{i,\text{Cs}}} \quad (4.63)$$

and

$$C_2 = \left(24\sqrt{3}\pi^3 \sigma_{x,\text{Cs}}^2 \sigma_{y,\text{Cs}}^2 \sigma_{z,\text{Cs}}^2 \right)^{-1} \quad (4.64)$$

are determined by a direct measurement of the trapping frequencies and temperatures, which are required for the determination of the widths σ_i (see Eq. (2.4)).

The coefficient L_1^{Cs} is measured in a ^{133}Cs single species experiment with very long hold times and low ^{133}Cs densities near a zero crossing of a_{Cs} , where one-body losses are the dominant loss mechanism. A fit to the time dependent atom number including only the first summand on the right side of Eq. (4.62) yields $L_1^{\text{Cs}} = 1/28 \text{ s}^{-1}$.

In order to reduce the number of free fit parameters in Eq. (4.62) further, we also measure L_3^{Cs} in a single species experiment by observing the time-dependent losses for fields near the FR at 843 G. For these measurements, the temperature of the ^{133}Cs sample is $\sim 410 \text{ nK}$. The results of a fit to Eq. (4.62), where the summand containing L_3^{LiCsCs} is removed, are summarized in Fig. 4.10. The ^{133}Cs three-body loss coefficients are approximately constant for the fields where the ^6Li - ^{133}Cs Efimov resonances occur. The close-by ^{133}Cs intraspecies Efimov resonance at 853 G [Berninger et al., 2013] does not affect our analysis, as it becomes important only for the region $a_{\text{LiCs}} > -250 a_0$, which is not relevant for the ^6Li - ^{133}Cs Efimov resonances found in this work. Our results for L_3^{Cs} are consistent with independent measurements from the Innsbruck group [Huang and Grimm, 2014] taken at temperatures of 330 nK and a theoretical curve for our temperatures based on the model by Rem et al., 2013¹⁰, as shown in Fig. 4.10. The small discrepancy of our measurements, which are expected to yield slightly smaller values as compared to the measurements at colder temperatures from the Grimm group and the deviations from the calculated values, are within the systematic error of $\sim 80 \%$, given by uncertainties in measured atom numbers, temperatures, and trap frequencies. For the analysis of L_3^{LiCsCs} , we employ the average of L_3^{Cs} in the range from 842 – 852 G as a fixed parameter.

¹⁰The calculation has been performed by Bo Huang [Huang and Grimm, 2014].

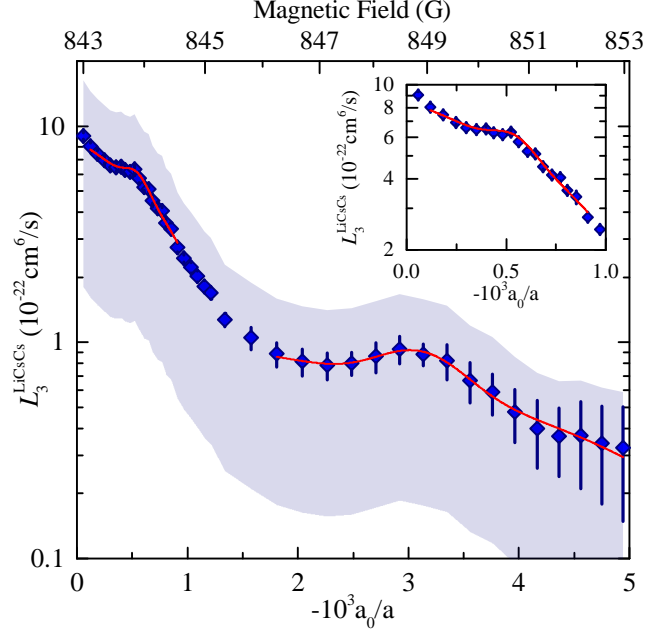


Figure 4.11: Three-body loss coefficient L_3^{LiCsCs} plotted versus inverse scattering length $1/a$. The blue diamonds show the mean of three L_3^{LiCsCs} measurements, where the error bars are given by the standard errors. The red solid lines show Gaussian profiles with linear background fitted to the data to determine the position of the two Efimov resonances. The grey area illustrates the systematic error of 80% for the absolute value of L_3^{LiCsCs} . The inset shows a zoom into the region of the first excited Efimov resonance.

As a result, our analysis of the ${}^6\text{Li}$ - ${}^{133}\text{Cs}$ three-body losses is reduced to a single parameter fit of the time-dependent atom number to the numerical solution of Eq. (4.62). The obtained L_3^{LiCsCs} coefficients are displayed in Fig. 4.11. The systematic error of this value is on the same order of magnitude as that of L_3^{Cs} , as it also contains atom numbers, temperatures, and trap frequencies. Using the experimentally determined value of L_3^{Cs} which is slightly higher than expected, possibly leads to a systematic underestimation of L_3^{LiCsCs} . Additionally, the gravitational sag reduces the spatial overlap of the atomic cloud. We estimate that this effect reduces the spatial integral over the densities in Eq. (4.62) by $\sim 20\%$, and include this effect into our analysis. Day to day drifts in the beam pointing of the dimple trap might cause fluctuations of the overlap.

A precise determination of the field dependent scattering length $a(B)$ is essential for a quantitative analysis. In particular the exact value of the scattering pole B_{FR} , where $|a|$ diverges, plays a crucial role. We measure this value via radio

frequency spectroscopy of universal dimers¹¹, which yields $B_{\text{FR}} = 842.90(20)$ G and $\Delta B = 61.4(7)$ G for the resonance position and width, respectively. These values are in agreement with the extensive study of ${}^6\text{Li}$ - ${}^{133}\text{Cs}$ FRs via the three different models presented in Chap. 3. Inserting these results into the relation

$$a(B) = a_{bg} \left(\frac{\Delta B}{B - B_{\text{FR}}} + 1 \right) \quad (4.65)$$

which is the equivalent of Eq. (3.42) for negative a_{bg} , allows us to determine the abscissa in Fig. 4.8 and Fig. 4.11, where a_{bg} is taken from Repp et al., 2013.

We observe two distinct resonances of L_3^{LiCsCs} , which are the cause of the enhanced atom losses in Fig. 4.8. For large values of the scattering length, the loss rate approaches a value that is consistent with an order of magnitude estimate [D’Incao and Greene, 2014] for the unitarity limit L_3^{Lim} of Eq. (4.60) yielding $L_3^{\text{Lim}} \approx 10^{-21}\text{cm}^6/\text{s}$ for the temperatures in our experiments.

Due to the lack of a heteronuclear finite temperature model similar to the one in Rem et al., 2013, the position of the resonances is determined via a fit of a Gaussian profile with linear background, which results in $B_0 = 848.90(6)_{\text{stat}}(3)_{\text{sys}}$ G and $B_1 = 843.85(1)_{\text{stat}}(3)_{\text{sys}}$ G. Using Eq. (4.65), we assign the scattering lengths $a_-^{(0)} = -320(3)_{\text{stat}}(2)_{\text{sys}}(10)_{\text{rf}}$ a_0 and $a_-^{(1)} = -1871(19)_{\text{stat}}(58)_{\text{sys}}(388)_{\text{rf}}$ a_0 for the Efimov resonance positions, where the last error accounts for the uncertainties of FR position and width resulting as extracted from the radio frequency spectroscopy. All errors are obtained by error propagation of Eq. (4.65).

For the scaling between the first and second Efimov resonance position, we obtain $a_-^{(1)}/a_-^{(0)} = 5.8(0.1)_{\text{stat}}(0.2)_{\text{sys}}(1.0)_{\text{rf}}$. This value is close to the predicted scaling of 4.9 [Braaten and Hammer, 2006; D’Incao and Esry, 2006] for a zero temperature gas in the resonant limit ($|a| \gg r_0$).

The assumption of universal behavior is not strictly justified for the first resonance, since $a_-^{(0)}$ is only a factor of ~ 7 (~ 3) larger than the ${}^6\text{Li}$ - ${}^{133}\text{Cs}$ (${}^{133}\text{Cs}$ - ${}^{133}\text{Cs}$) van der Waals length $r_0^{\text{LiCs}} = 45$ a_0 ($r_0^{\text{Cs}} = 101$ a_0), possibly resulting in the necessity to include finite range corrections. In fact, early predictions have shown that the ratio between the first and second resonance departs from the universal value and yields larger values due to finite range corrections [D’Incao and Esry, 2006]. However, these calculations, like the prediction in Braaten and Hammer, 2006, did not take the actual inter- and intraspecies scattering lengths at the Efimov resonance positions in ${}^6\text{Li}$ - ${}^{133}\text{Cs}$ into account, which were not available at the time of

¹¹These measurements are performed by Juris Ulmanis and will be explained in detail in his PhD thesis. A short summary is also given in the Supplemental Material of Pires et al., 2014b.

the publications.

The second resonance is already influenced by the unitarity limit at the temperatures achievable in the current experiment, which leads to a broadening of the resonance feature and might also cause additional shifts to lower values of a [D’Incao et al., 2004]. In addition, the fact that the ^{133}Cs intraspecies scattering length varies between $-1200\ a_0$ at B_0 and $-1500\ a_0$ at B_1 [Berninger et al., 2013] still needs to be accounted for in the theoretical determination of the expected scaling ratio. Preliminary calculations [Wang et al., 2014] based on the model of Wang et al., 2012b seem to be consistent with a slightly increased value for the ratio. However, these results are subject to ongoing investigation and are beyond the scope of this thesis.

The position of the third resonance is indicated by a modulation of the atom losses at $B_2 = 843.03(5)_{\text{stat}}(3)_{\text{sys}}\text{ G}$ in Fig. 4.8, for which we assign scattering length $a_-^{(2)} = -13.5(5.2)_{\text{stat}}(3.1)_{\text{sys}} \times 10^3\ a_0$. The error due to uncertainties in B_{FR} is on the order of $a_-^{(2)}$ and can even result in positive scattering lengths at B_2 . In a dedicated measurement of L_3^{LiCsCs} in the vicinity of B_2 , we cannot resolve an additional loss feature that can be associated with the third resonance. The resonance is in a regime where the scattering length is on the order of the thermal wavelength, and therefore not the dominating length scale anymore. Hence, we expect the peak height of the Efimov feature to be significantly reduced to the point where we cannot resolve it due to technical limitations. As a result, we cannot exclude that the losses at B_2 in Fig. 4.8 are caused by $^6\text{Li}+^6\text{Li}+^{133}\text{Cs}$ collisions or other loss processes, e.g. four-body losses.

After having found clear evidence for consecutive Efimov resonances in the loss rate coefficient of a mixture with large mass imbalance, the next sensible experimental step is the creation of a $^6\text{Li}-^{133}\text{Cs}$ mixture at significantly lower temperatures. The unitarity-limited regime will be pushed towards larger values of the scattering length due to its scaling with $\propto 1/T^2$ (see Eq.(4.60)), and the resonances should become narrower and exhibit smaller shifts. In the current experiment, the gravitational sag due to the large mass of ^{133}Cs leads to a separation of the atom clouds, which limits the lowest achievable temperatures of the mixture. Therefore, a dedicated engineering of trap potentials with species selective trapping forces [LeBlanc and Thywissen, 2007] is required to overcome this limitation, as discussed in Sect. 2.5.

Based on calculations by C. Greene et al. [Wang et al., 2014] we estimate that temperatures on the order of 30 nK result in a unitarity-limited three-body loss coefficient of $\sim 2 \times 10^{-19}\text{cm}^6/\text{s}$, which is more than two orders of magnitude larger than the current limit. In this case, calculations based on the zero-range model [Helfrich

et al., 2010] predict the three-body loss coefficient to be below the unitarity limit. In order to avoid the influence of the unitarity limit on the third resonance, one would actually require temperatures on the order of ~ 1 nK. Extending the model presented in Rem et al., 2013 to the case of heteronuclear mixtures, however, might allow for a detailed analysis of the influence of unitarity even at higher temperatures. Another intriguing perspective is the study of finite size effects on the Efimov trimers [Portegies and Kokkelmans, 2011], as the size of the second excited Efimov trimer of $\sim 0.2 \mu\text{m}$ is not much smaller than the oscillator length of $2 \mu\text{m}$ of the trapping potential used in the present experiments.

A second major improvement over the current investigations will be a more precise determination of the magnetic field scattering pole B_{FR} in order to reduce the uncertainties in the assignment of scattering lengths to the observed resonances. Here, we expect an improvement by an order of magnitude in the near future by performing additional more accurate spectroscopy on the binding of the universal dimer, since we have recently reduced our magnetic field uncertainties from ~ 200 mG to below 30 mG. A more accurate determination of the resonance positions would shed new light onto application of universal few-body theories to mixed systems with large mass imbalance addressing, e.g., the question to which extent the position of the first resonances also features universal scaling as recently found in homonuclear systems [Berninger et al., 2011a; Roy et al., 2013].

Besides our experiments, the Chin group at the University of Chicago also recently reported on the observation of excited Efimov states. Atomic loss features in ^6Li - ^{133}Cs under comparable experimental conditions are presented in a preprint [Tung et al., 2014]. While two of the atom loss features agree reasonably well with our measurements, the position of the first Efimov resonance is shifted by ~ 0.5 G. The reason for this shift is currently not clear, but its effect on $a_-^{(0)}$ is only on the order of a few percent. The main difference between this work and Tung et al., 2014 is the determination of the scattering pole position. While we measure rf association, the authors of Tung et al., 2014 simply chose the global minimum of the loss spectrum as the scattering pole. However, one has to be cautious which such an assumption. Molecule formation on the $a > 0$ side of the FR coupled with atom-dimer scattering might lead to an increase of losses, thus shifting the global loss maximum, as shown in Dieckmann et al., 2002 and Khramov et al., 2012. If one assumes the scattering pole to be at the field found in this work, the pole determined in Tung et al., 2014 would be on the $a > 0$ side. Molecules at this field have a binding energy on the order of the temperature sample, hence three-body collisions can result in significant losses. Of course, the stability and

lifetime of such molecules also has to be taken into consideration, which is beyond the scope of this thesis. The authors of Tung et al., 2014 also claim finding universal scaling for similar temperatures as ours, due to the position of the third resonance. Based on our analysis of the three-body loss-rate coefficients, we cannot confirm that ${}^6\text{Li}+{}^{133}\text{Cs}+{}^{133}\text{Cs}$ three-body collisions are the cause for the third atom loss feature. Therefore, we refrain from discussing this resonance in terms of universal scaling. For comparison, we perform an analysis analogous to Tung et al., 2014, where a Gaussian profile fit to the global loss minimum is used to determine B_{FR} . Using the positions of atom loss features, we obtain $a_-^{(1)}/a_-^{(0)} = 5.07(6)_{\text{stat}}(13)_{\text{sys}}(2)_{\text{FR}}$ and $a_-^{(2)}/a_-^{(1)} = 3.79(23)_{\text{stat}}(39)_{\text{sys}}(6)_{\text{FR}}$ for the scaling ratios, where the errors labeled FR are given by the fit uncertainty of $B_{\text{FR}} = 842.73(1)_{\text{stat}}(3)_{\text{sys}}$.

Chapter 5

Conclusion and Outlook

Within the scope of this thesis we investigate both two- and three-body interactions in a system with extreme mass imbalance. For this purpose, we built a new experimental apparatus, which allows to bring both gases to quantum degeneracy separately. In a ${}^6\text{Li}$ - ${}^{133}\text{Cs}$ mixture, 19 interspecies Feshbach resonances have been identified in the two energetically lowest spin channels of each species via atom loss spectroscopy. A coupled-channels calculation, multichannel quantum defect theory and the asymptotic bound-state model have been applied for the assignment of the resonances, yielding rms errors of 39 mG, 40 mG and 263 mG, respectively. Considering the level of simplification of each of the models, the agreement with the measured positions is excellent. Part of the deviations can be ascribed to the usage of Gaussian profile fit for the determination of the measured Feshbach resonance position, which does not account for asymmetries in the shape of the loss features due to differences of the three-body loss rate on the $a < 0$ and $a > 0$ side [D’Incao et al., 2004]. Thus, the precision of the determination of the scattering pole is limited to a few hundred mG for the broad resonances with this method. For a more precise determination, several different methods for a more direct measurement of the scattering length, e.g. rf association of dimers or magnetic field modulation spectroscopy should be employed. Excellent examples for such measurements of ${}^6\text{Li}$ and ${}^{133}\text{Cs}$ are given in Zürn et al., 2012 and Berninger et al., 2013, respectively. In our group, we are currently applying rf association on several of the resonances, in order to obtain more accurate scattering pole positions. Additional measurements, for example the observation of coherent oscillations in a harmonic trapping potential would allow for a direct observation of scattering length magnitude and sign [Schuster et al., 2012].

The three-body loss rates are measured at a 61 G broad resonance near 843 G in the energetically lowest ${}^6\text{Li}$ - ${}^{133}\text{Cs}$ hyperfine channel, yielding clear evidence for two

consecutive Efimov resonances. This constitutes the first measurement of an excited Efimov resonance in a heteronuclear mixture. While the Efimov feature is obvious in the ^{133}Cs three-body loss coefficients, its signal-to-noise in ^6Li , which is the majority species in our experiments, is too low for a more detailed study. Therefore, a major improvement would be the increase of the ^{133}Cs atom number, which is currently a limiting factor. With an increased ^{133}Cs atom number, the ^6Li loss signal would improve, and the three-body loss coefficient could be measured analogously to the ^{133}Cs three-body loss coefficient, which would yield additional confirmation of our measurements.

The obtained scaling ratio of 5.8(1.0) between the scattering length values of the Efimov resonances is consistent with zero temperature models [D’Incao and Esry, 2006; Braaten and Hammer, 2006; Esry et al., 2008]. However, it is not clear to what extent the assumptions in these models are fulfilled. For example, typical calculations assume the resonant limit $a \gg r_0$. For the first resonance, this is not appropriate, as the scattering length is only a factor of 7 (3) larger than the ^6Li - ^{133}Cs (^{133}Cs - ^{133}Cs) van der Waals range. Currently, there is no systematic study to what degree this affects the universal scaling ratio. In Fig. 2 of D’Incao and Esry, 2006, a slightly larger scaling ratio has been illustrated for exactly this scenario, though not further quantified. The further exploration of mixed species systems in this context is an interesting challenge for theorists specialized in this field.

The second resonance is not in the threshold regime $a \ll \lambda_{dB}$ for our experiments at 450 nK, which means that the zero temperature assumption also breaks down. Thus, the resonant feature is broadened and possibly also shifted due to finite temperature effects and the resulting unitarity limit. In order to further investigate this feature in the zero temperature limit, we estimate required temperatures in the order of tens of nK. A scheme to reach this temperature regime using a species selective trap is also presented in this thesis. In the near future, we plan to implement this trap for the manipulation of ^6Li , thus allowing to overcome the limits given by the gravitational sag in order to reach the required temperatures in the mixture.

Obtaining a mixture at temperatures on the order of one nK, which is necessary in order to observe a third resonance in the zero temperature limit, is experimentally more challenging. However, an extension of a finite temperature model [Rem et al., 2013] to heteronuclear systems would allow for a study of the third resonance even for higher temperatures. Even at the temperatures employed in our experiments we observe a hint of a third resonance in the atomic losses. The scaling ratio of 7.2 is afflicted with a large error, due to the uncertainties in the position of the resonance pole. Accordingly, the rf measurements mentioned above are essential for

a quantitative comparison with theory.

The effect of the ^{133}Cs - ^{133}Cs background scattering length on the scaling factor is also an interesting aspect for future studies. Its value varies between the first and second observed resonance from $-1200\ a_0$ to $-1500\ a_0$. The question is whether these values are already large enough to justify universality, so that the behavior does not depend on the explicit background scattering length value. Measurement of Efimov resonances at different Feshbach resonances, where the ^{133}Cs - ^{133}Cs background scattering length takes on different values, are planned in order to address this question. This will allow to test the predictions given in D’Incao and Esry, 2009, where three-body collisions properties for several regimes of intra- and interspecies scattering lengths in a Bose-Fermi mixture are discussed. These measurements would also allow to investigate whether or not the three-body parameters, which are linked to the appearance of the first Efimov resonance, are universal. A recent study predicts that for a system with two heavy and one light particle, the three-body parameter is indeed universal, and its specific value is given by the heavy-heavy interparticle interactions [Wang et al., 2012b].

Besides the understanding of three-body loss processes, an intriguing possibility is also the study of higher order loss processes. Before each Efimov trimer becomes bound (when scanning the scattering length), two four-body bound states should be formed [von Stecher et al., 2009; Ferlaino et al., 2009]. The energies of these four-body states are completely determined by the energy of the three-body Efimov state, and require no further parameter. In the presented experiments we have not observed any indications of such resonances. However, this can possibly be ascribed to the relatively high temperatures. Once our scheme for obtaining colder samples has been realized, a study of universal bound states involving more than three constituents could also be performed.

It is indisputable that with the presented experiments a new chapter in the investigation of universal physics in the mixed species case has opened up. While the findings in this sector will certainly help to sharpen the theoretical methods for the treatment of the universal three-body problem in the realm of atomic physics, it will be interesting to see to what extent they will lead to a better understanding of three-body processes in other fields (see e.g. Zhukov et al., 1993 and Nielsen et al., 2001).

Bibliography

- [Abraham et al., 1997] Abraham, E. R. I., McAlexander, W. I., Gerton, J. M., Hulet, R. G., Côté, R., and Dalgarno, A. (1997). Triplet s-wave resonance in ${}^6\text{Li}$ collisions and scattering lengths of ${}^6\text{Li}$ and ${}^7\text{Li}$. *Phys. Rev. A*, 55:R3299–R3302.
- [Aikawa et al., 2012] Aikawa, K., Frisch, A., Mark, M., Baier, S., Rietzler, A., Grimm, R., and Ferlaino, F. (2012). Bose-Einstein Condensation of Erbium. *Phys. Rev. Lett.*, 108:210401.
- [Amado and Noble, 1971] Amado, R. and Noble, J. (1971). On Efimov’s effect: A new pathology of three-particle systems. *Physics Letters B*, 35(1):25 – 27.
- [Amado and Noble, 1972] Amado, R. D. and Noble, J. V. (1972). Efimov’s Effect: A New Pathology of Three-Particle Systems. II. *Phys. Rev. D*, 5:1992–2002.
- [Arias, 2014] Arias, A. (2014). Master’s thesis, University of Heidelberg.
- [Arimondo et al., 1977] Arimondo, E., Inguscio, M., and Violino, P. (1977). Experimental determinations of the hyperfine structure in the alkali atoms. *Rev. Mod. Phys.*, 49:31–75.
- [Arlt et al., 1998] Arlt, J., Bance, P., Hopkins, S., Martin, J., Webster, S., Wilson, A., Zetie, K., and Foot, C. J. (1998). Suppression of collisional loss from a magnetic trap. *Journal of Physics B: Atomic, Molecular and Optical Physics*, 31(7):L321.
- [Bang and Thompson, 1992] Bang, J. and Thompson, I. (1992). Three body calculations for ${}^{11}\text{Li}$. *Physics Letters B*, 279(3–4):201 – 206.
- [Barontini et al., 2009] Barontini, G., Weber, C., Rabatti, F., Catani, J., Thalhammer, G., Inguscio, M., and Minardi, F. (2009). Observation of Heteronuclear Atomic Efimov Resonances. *Phys. Rev. Lett.*, 103:043201.

- [Bedaque et al., 2000] Bedaque, P. F., Braaten, E., and Hammer, H.-W. (2000). Three-body Recombination in Bose Gases with Large Scattering Length. *Phys. Rev. Lett.*, 85:908–911.
- [Bedaque and D’Incao, 2009] Bedaque, P. F. and D’Incao, J. P. (2009). Superfluid phases of the three-species fermion gas. *Annals of Physics*, 324(8):1763 – 1768.
- [Bell et al., 2010] Bell, S. C., Junker, M., Jasperse, M., Turner, L. D., Lin, Y.-J., Spielman, I. B., and Scholten, R. E. (2010). A slow atom source using a collimated effusive oven and a single-layer variable pitch coil Zeeman slower. *Review of Scientific Instruments*, 81(1):013105.
- [Benvenuti et al., 1999] Benvenuti, C., Cazeneuve, J., Chiggiato, P., Cicoira, F., Escudeiro Santana, A., Johaneck, V., Ruzinov, V., and Fraxedas, J. (1999). A novel route to extreme vacua: The non-evaporable getter thin film coatings. *Vacuum*, 53(1-2):219–225.
- [Bergeman et al., 1987] Bergeman, T., Erez, G., and Metcalf, H. J. (1987). Magnetostatic trapping fields for neutral atoms. *Phys. Rev. A*, 35:1535–1546.
- [Berninger et al., 2011a] Berninger, M., Zenesini, A., Huang, B., Harm, W., Nägerl, H.-C., Ferlaino, F., Grimm, R., Julienne, P. S., and Hutson, J. M. (2011a). Universality of the Three-Body Parameter for Efimov States in Ultracold Cesium. *Phys. Rev. Lett.*, 107:120401.
- [Berninger et al., 2011b] Berninger, M., Zenesini, A., Huang, B., Harm, W., Nägerl, H.-C., Ferlaino, F., Grimm, R., Julienne, P. S., and Hutson, J. M. (2011b). Universality of the Three-Body Parameter for Efimov States in Ultracold Cesium. *Phys. Rev. Lett.*, 107:120401.
- [Berninger et al., 2013] Berninger, M., Zenesini, A., Huang, B., Harm, W., Nägerl, H.-C., Ferlaino, F., Grimm, R., Julienne, P. S., and Hutson, J. M. (2013). Feshbach resonances, weakly bound molecular states, and coupled-channel potentials for cesium at high magnetic fields. *Phys. Rev. A*, 87:032517.
- [Bjorklund et al., 1983] Bjorklund, G. C., Levenson, M. D., Lenth, W., and Ortiz, C. (1983). Frequency Modulation (FM) Spectroscopy. *Applied Physics B*, 32:145.
- [Bloom et al., 2013] Bloom, R. S., Hu, M.-G., Cumby, T. D., and Jin, D. S. (2013). Tests of Universal Three-Body Physics in an Ultracold Bose-Fermi Mixture. *Phys. Rev. Lett.*, 111:105301.

- [Blume and Greene, 2000] Blume, D. and Greene, C. H. (2000). Monte Carlo hyperspherical description of helium cluster excited states. *The Journal of Chemical Physics*, 112(18):8053–8067.
- [Bogoliubov, 1947] Bogoliubov, N. (1947). On the theory of superfluidity. *J. Phys.*, 11:23.
- [Bohn et al., 1998] Bohn, J. L., Esry, B. D., and Greene, C. H. (1998). Effective potentials for dilute Bose-Einstein condensates. *Phys. Rev. A*, 58:584–597.
- [Boiron et al., 1996] Boiron, D., Michaud, A., Lemonde, P., Castin, Y., Salomon, C., Weyers, S., Szymaniec, K., Cognet, L., and Clairon, A. (1996). Laser cooling of cesium atoms in gray optical molasses down to 1.1 μK . *Phys. Rev. A*, 53:R3734–R3737.
- [Bongs and Sengstock, 2002] Bongs, K. and Sengstock, K. (2002). *Interactions in Ultracold Gases*, chapter Introduction to Bose-Einstein Condensation. Wiley-VCH, Weinheim.
- [Botero and Greene, 1986] Botero, J. and Greene, C. H. (1986). Resonant Photodetachment of the Positronium Negative Ion. *Phys. Rev. Lett.*, 56:1366–1369.
- [Braaten and Hammer, 2001] Braaten, E. and Hammer, H.-W. (2001). Three-Body Recombination into Deep Bound States in a Bose Gas with Large Scattering Length. *Phys. Rev. Lett.*, 87:160407.
- [Braaten and Hammer, 2006] Braaten, E. and Hammer, H.-W. (2006). Universality in few-body systems with large scattering length. *Physics Reports*, 428(5–6):259 – 390.
- [Braaten et al., 2008] Braaten, E., Hammer, H.-W., Kang, D., and Platter, L. (2008). Three-body recombination of identical bosons with a large positive scattering length at nonzero temperature. *Phys. Rev. A*, 78:043605.
- [Braaten et al., 2010] Braaten, E., Hammer, H. W., Kang, D., and Platter, L. (2010). Efimov physics in ^6Li atoms. *Phys. Rev. A*, 81:013605.
- [Burke, 1999] Burke, J. P. (1999). *Theoretical Investigation of Cold Alkali Atom Collisions*. PhD thesis, University of Colorado.

- [Burke et al., 1998] Burke, J. P., Greene, C. H., and Bohn, J. L. (1998). Multichannel Cold Collisions: Simple Dependences on Energy and Magnetic Field. *Phys. Rev. Lett.*, 81:3355–3358.
- [Carlson and Schiavilla, 1998] Carlson, J. and Schiavilla, R. (1998). Structure and dynamics of few-nucleon systems. *Rev. Mod. Phys.*, 70:743–841.
- [Catelani and Yuzbashyan, 2008] Catelani, G. and Yuzbashyan, E. A. (2008). Phase diagram, extended domain walls, and soft collective modes in a three-component fermionic superfluid. *Phys. Rev. A*, 78:033615.
- [Cherng et al., 2007] Cherng, R. W., Refael, G., and Demler, E. (2007). Superfluidity and Magnetism in Multicomponent Ultracold Fermions. *Phys. Rev. Lett.*, 99:130406.
- [Chin and Grimm, 2004] Chin, C. and Grimm, R. (2004). Thermal equilibrium and efficient evaporation of an ultracold atom-molecule mixture. *Phys. Rev. A*, 69:033612.
- [Chin et al., 2010] Chin, C., Grimm, R., Julienne, P., and Tiesinga, E. (2010). Feshbach resonances in ultracold gases. *Rev. Mod. Phys.*, 82:1225–1286.
- [Cornelius and Glöckle, 1986] Cornelius, T. and Glöckle, W. (1986). Efimov states for three ^4He atoms? *The Journal of Chemical Physics*, 85(7):3906–3912.
- [Courteille et al., 1998] Courteille, P., Freeland, R. S., Heinzen, D. J., van Abeelen, F. A., and Verhaar, B. J. (1998). Observation of a Feshbach Resonance in Cold Atom Scattering. *Phys. Rev. Lett.*, 81:69–72.
- [Croft et al., 2011] Croft, J. F. E., Wallis, A. O. G., Hutson, J. M., and Julienne, P. S. (2011). Multichannel quantum defect theory for cold molecular collisions. *Phys. Rev. A*, 84:042703.
- [Cucchietti and Timmermans, 2006] Cucchietti, F. M. and Timmermans, E. (2006). Strong-Coupling Polarons in Dilute Gas Bose-Einstein Condensates. *Phys. Rev. Lett.*, 96:210401.
- [Dalfovo et al., 1999] Dalfovo, F., Giorgini, S., Pitaevskii, L. P., and Stringari, S. (1999). Theory of Bose-Einstein condensation in trapped gases. *Rev. Mod. Phys.*, 71:463–512.

- [Deh et al., 2010] Deh, B., Gunton, W., Klappauf, B. G., Li, Z., Semczuk, M., Van Dongen, J., and Madison, K. W. (2010). Giant Feshbach resonances in ^6Li - ^{85}Rb mixtures. *Phys. Rev. A*, 82:020701.
- [Delves, 1960] Delves, L. (1960). Tertiary and general-order collisions (II). *Nuclear Physics*, 20(0):275 – 308.
- [DePue et al., 2000] DePue, M. T., Winoto, S. L., Han, D. J., and Weiss, D. S. (2000). Transient compression of a MOT and high intensity fluorescent imaging of optically thick clouds of atoms. *Opt. Comm.*, 180:73.
- [Derevianko et al., 2001] Derevianko, A., Babb, J. F., and Dalgarno, A. (2001). High-precision calculations of van der Waals coefficients for heteronuclear alkali-metal dimers. *Phys. Rev. A*, 63:052704.
- [Dieckmann et al., 2002] Dieckmann, K., Stan, C. A., Gupta, S., Hadzibabic, Z., Schunck, C. H., and Ketterle, W. (2002). Decay of an Ultracold Fermionic Lithium Gas near a Feshbach Resonance. *Phys. Rev. Lett.*, 89:203201.
- [D’Incao and Esry, 2005] D’Incao, J. P. and Esry, B. D. (2005). Scattering Length Scaling Laws for Ultracold Three-Body Collisions. *Phys. Rev. Lett.*, 94:213201.
- [D’Incao and Esry, 2006] D’Incao, J. P. and Esry, B. D. (2006). Enhancing the observability of the Efimov effect in ultracold atomic gas mixtures. *Phys. Rev. A*, 73:030703.
- [D’Incao and Esry, 2009] D’Incao, J. P. and Esry, B. D. (2009). Ultracold Three-Body Collisions near Overlapping Feshbach Resonances. *Phys. Rev. Lett.*, 103:083202.
- [D’Incao and Greene, 2014] D’Incao, J. P. and Greene, C. H. (2014). Private Communication.
- [D’Incao et al., 2009] D’Incao, J. P., Greene, C. H., and Esry, B. D. (2009). The short-range three-body phase and other issues impacting the observation of Efimov physics in ultracold quantum gases. *Journal of Physics B: Atomic, Molecular and Optical Physics*, 42(4):044016.
- [D’Incao et al., 2004] D’Incao, J. P., Suno, H., and Esry, B. D. (2004). Limits on Universality in Ultracold Three-Boson Recombination. *Phys. Rev. Lett.*, 93:123201.

- [Drewsen et al., 1994] Drewsen, M., Laurent, P., Nadir, A., Santarelli, G., Clairon, A., Castin, Y., Grison, D., and Salomon, C. (1994). Investigation of sub-Doppler cooling effects in a cesium magneto-optical trap. *Applied Physics B*, 59:283.
- [Dyke et al., 2013] Dyke, P., Pollack, S. E., and Hulet, R. G. (2013). Finite-range corrections near a Feshbach resonance and their role in the Efimov effect. *Phys. Rev. A*, 88:023625.
- [Efimov, 1970] Efimov, V. (1970). Energy levels arising from resonant two-body forces in a three-body system. *Physics Letters B*, 33(8):563 – 564.
- [Efimov, 1971] Efimov, V. (1971). Weakly-bound states of three resonantly-interacting particles. *Sov. J. Nucl. Phys.*, 12:589–595.
- [Efimov, 1979] Efimov, V. (1979). Low-energy properties of three resonantly interacting particles. *Sov. J. Nucl. Phys*, 29(4):546–553.
- [Esry and D’Incao, 2007] Esry, B. D. and D’Incao, J. P. (2007). Efimov physics in ultracold three-body collisions. *Journal of Physics: Conference Series*, 88(1):012040.
- [Esry et al., 1999] Esry, B. D., Greene, C. H., and Burke, J. P. (1999). Recombination of Three Atoms in the Ultracold Limit. *Phys. Rev. Lett.*, 83:1751–1754.
- [Esry et al., 1996a] Esry, B. D., Greene, C. H., Zhou, Y., and Lin, C. D. (1996a). Role of the scattering length in three-boson dynamics and Bose - Einstein condensation. *Journal of Physics B: Atomic, Molecular and Optical Physics*, 29(2):L51.
- [Esry et al., 1996b] Esry, B. D., Lin, C. D., and Greene, C. H. (1996b). Adiabatic hyperspherical study of the helium trimer. *Phys. Rev. A*, 54:394–401.
- [Esry et al., 2008] Esry, B. D., Wang, Y., and D’Incao, J. P. (2008). Alternative paths to observing Efimov physics. *Few-Body Systems*, 43(1-4):63–68.
- [Fano, 1961] Fano, U. (1961). Effects of Configuration Interaction on Intensities and Phase Shifts. *Phys. Rev.*, 124:1866–1878.
- [Fedichev et al., 1996] Fedichev, P. O., Reynolds, M. W., and Shlyapnikov, G. V. (1996). Three-Body Recombination of Ultracold Atoms to a Weakly Bound s Level. *Phys. Rev. Lett.*, 77:2921–2924.

- [Fedorov et al., 1994a] Fedorov, D. V., Jensen, A. S., and Riisager, K. (1994a). Efimov States in Halo Nuclei. *Phys. Rev. Lett.*, 73:2817–2820.
- [Fedorov et al., 1994b] Fedorov, D. V., Jensen, A. S., and Riisager, K. (1994b). Three-body halos: Gross properties. *Phys. Rev. C*, 49:201–212.
- [Fedorov et al., 1994c] Fedorov, D. V., Jensen, A. S., and Riisager, K. (1994c). Three-body halos. II. From two- to three-body asymptotics. *Phys. Rev. C*, 50:2372–2383.
- [Ferlaino et al., 2009] Ferlaino, F., Knoop, S., Berninger, M., Harm, W., D’Incao, J. P., Nägerl, H.-C., and Grimm, R. (2009). Evidence for Universal Four-Body States Tied to an Efimov Trimer. *Phys. Rev. Lett.*, 102:140401.
- [Feshbach, 1958] Feshbach, H. (1958). Unified theory of nuclear reactions. *Annals of Physics*, 5(4):357 – 390.
- [Feshbach, 1962] Feshbach, H. (1962). A unified theory of nuclear reactions. {II}. *Annals of Physics*, 19(2):287 – 313.
- [Fröhlich, 1954] Fröhlich, H. (1954). Electrons in lattice fields. *Advances in Physics*, 3(11):325–361.
- [Gacesa et al., 2008] Gacesa, M., Pellegrini, P., and Côté, R. (2008). Feshbach resonances in ultracold ${}^6,7\text{Li}+{}^{23}\text{Na}$ atomic mixtures. *Phys. Rev. A*, 78:010701.
- [Gao, 1998] Gao, B. (1998). Quantum-defect theory of atomic collisions and molecular vibration spectra. *Phys. Rev. A*, 58:4222–4225.
- [Gao, 2001] Gao, B. (2001). Angular-momentum-insensitive quantum-defect theory for diatomic systems. *Phys. Rev. A*, 64:010701.
- [Gao, 2008] Gao, B. (2008). General form of the quantum-defect theory for $1/r^\alpha$ type of potentials with $\alpha>2$. *Phys. Rev. A*, 78:012702.
- [Gao et al., 2005] Gao, B., Tiesinga, E., Williams, C. J., and Julienne, P. S. (2005). Multichannel quantum-defect theory for slow atomic collisions. *Phys. Rev. A*, 72:042719.
- [Gehm, 2003] Gehm, M. (2003). Properties of ${}^6\text{Li}$. Unpublished.
- [Gerdes et al., 2008] Gerdes, A., Hobein, M., Knöckel, H., and Tiemann, E. (2008). Ground state potentials of the NaK molecule. *Eur. Phys. J. D*, 49(1):67–73.

- [Goosen, 2011] Goosen, M. R. (2011). *Universal relations between Feshbach resonances and molecules*. PhD thesis, Technische Universiteit Eindhoven.
- [Goosen et al., 2010] Goosen, M. R., Tiecke, T. G., Vassen, W., and Kokkelmans, S. J. J. M. F. (2010). Feshbach resonances in $^3\text{He}^*$ - $^4\text{He}^*$ mixtures. *Phys. Rev. A*, 82:042713.
- [Greene, 2010] Greene, C. (2010). Universal insights from few-body land. *physicstoday*, 63.
- [Greene et al., 1979] Greene, C., Fano, U., and Strinati, G. (1979). General form of the quantum-defect theory. *Phys. Rev. A*, 19:1485–1509.
- [Greene et al., 1982] Greene, C. H., Rau, A. R. P., and Fano, U. (1982). General form of the quantum-defect theory. II. *Phys. Rev. A*, 26:2441–2459.
- [Grimm et al., 2000] Grimm, R., Weidemüller, M., and Ovchinnikov, Y. B. (2000). Optical Dipole Traps for Neutral Atoms. *Advances In Atomic, Molecular, and Optical Physics*, 42:95 – 170.
- [Gross, 1961] Gross, E. (1961). Structure of a quantized vortex in boson systems. *Il Nuovo Cimento Series 10*, 20(3):454–477.
- [Gross et al., 2009] Gross, N., Shotan, Z., Kokkelmans, S., and Khaykovich, L. (2009). Observation of Universality in Ultracold ^7Li Three-Body Recombination. *Phys. Rev. Lett.*, 103:163202.
- [Guéry-Odelin et al., 1998] Guéry-Odelin, D., Söding, J., Desbiolles, P., and Dalibard, J. (1998). Is Bose-Einstein condensation of atomic cesium possible? *EPL (Europhysics Letters)*, 44(1):25.
- [Guery-Odelin et al., 1998] Guery-Odelin, D., Soeding, J., Desbiolles, P., and Dalibard, J. (1998). Strong evaporative cooling of a trapped cesium gas. *Opt. Express*, 2(8):323–329.
- [Häfner, 2013] Häfner, S. (2013). A tunable optical dipole trap for ^6Li and ^{133}Cs . Master’s thesis, University of Heidelberg.
- [Hansen et al., 1995] Hansen, P. G., Jensen, A. S., and Jonson, B. (1995). Nuclear Halos. *Annual Review of Nuclear and Particle Science*, 45(1):591–634.

- [Heck, 2012] Heck, R. (2012). All-Optical Formation of an Ultracold Gas of Fermionic Lithium Close to Quantum Degeneracy. Master’s thesis, Ruprecht-Karls-Universität Heidelberg, Germany.
- [Heiselberg et al., 2000] Heiselberg, H., Pethick, C. J., Smith, H., and Viverit, L. (2000). Influence of Induced Interactions on the Superfluid Transition in Dilute Fermi Gases. *Phys. Rev. Lett.*, 85:2418–2421.
- [Helfrich et al., 2010] Helfrich, K., Hammer, H.-W., and Petrov, D. S. (2010). Three-body problem in heteronuclear mixtures with resonant interspecies interaction. *Phys. Rev. A*, 81:042715.
- [Honerkamp and Hofstetter, 2004] Honerkamp, C. and Hofstetter, W. (2004). BCS pairing in Fermi systems with N different hyperfine states. *Phys. Rev. B*, 70:094521.
- [Honvault and Launay, 1998] Honvault, P. and Launay, J.-M. (1998). Quantum mechanical study of the $F + D_2 \rightarrow DF + D$ reaction. *Chemical Physics Letters*, 287(3–4):270 – 274.
- [Hopkins et al., 2000] Hopkins, S. A., Webster, S., Arlt, J., Bance, P., Cornish, S., Maragò, O., and Foot, C. J. (2000). Measurement of elastic cross section for cold cesium collisions. *Phys. Rev. A*, 61:032707.
- [Huang and Grimm, 2014] Huang, B. and Grimm, R. (2014). Private Communication.
- [Huang et al., 2014] Huang, B., Sidorenkov, L. A., Grimm, R., and Hutson, J. M. (2014). Observation of the Second Triatomic Resonance in Efimov’s Scenario. *Phys. Rev. Lett.*, 112:190401.
- [Huckans et al., 2009] Huckans, J. H., Williams, J. R., Hazlett, E. L., Stites, R. W., and O’Hara, K. M. (2009). Three-Body Recombination in a Three-State Fermi Gas with Widely Tunable Interactions. *Phys. Rev. Lett.*, 102:165302.
- [Hung et al., 2008] Hung, C.-L., Zhang, X., Gemelke, N., and Chin, C. (2008). Accelerating evaporative cooling of atoms into Bose-Einstein condensation in optical traps. *Phys. Rev. A*, 78:011604.
- [Hutson, 1994] Hutson, J. M. (1994). Coupled channel methods for solving the bound-state Schrödinger equation. *Computer Physics Communications*, 84(1–3):1 – 18.

- [Inouye et al., 1998] Inouye, S., Andrews, M. R., Stenger, J., Miesner, H.-J., Stamper-Kurn, D. M., and Ketterle, W. (1998). Observation of Feshbach resonances in a Bose-Einstein condensate. *Nature*, 392(6672):151–154.
- [Jochim et al., 2003] Jochim, S., Bartenstein, M., Altmeyer, A., Hendl, G., Riedl, S., Chin, C., Hecker Denschlag, J., and Grimm, R. (2003). Bose-Einstein Condensation of Molecules. *Science*, 302(5653):2101–2103.
- [Jochim et al., 2002] Jochim, S., Bartenstein, M., Hendl, G., Denschlag, J. H., Grimm, R., Mosk, A., and Weidemüller, M. (2002). Magnetic Field Control of Elastic Scattering in a Cold Gas of Fermionic Lithium Atoms. *Phys. Rev. Lett.*, 89:273202.
- [Johannsen et al., 1990] Johannsen, L., Jensen, A., and Hansen, P. (1990). The ^{11}Li nucleus as a three-body system . *Physics Letters B*, 244(3–4):357 – 362.
- [Julienne and Mies, 1989] Julienne, P. S. and Mies, F. H. (1989). Collisions of ultracold trapped atoms. *J. Opt. Soc. Am. B*, 6(11):2257–2269.
- [Kastberg et al., 1995] Kastberg, A., Phillips, W. D., Rolston, S. L., Spreew, R. J. C., and Jessen, P. S. (1995). Adiabatic Cooling of Cesium to 700 nK in an Optical Lattice. *Phys. Rev. Lett.*, 74:1542–1545.
- [Kerman et al., 2000] Kerman, A. J., Vuletić, V., Chin, C., and Chu, S. (2000). Beyond Optical Molasses: 3D Raman Sideband Cooling of Atomic Cesium to High Phase-Space Density. *Phys. Rev. Lett.*, 84:439–442.
- [Ketterle et al., 1999] Ketterle, W., Durfee, D. S., and Stamper-Kurn, D. M. (1999). Making, probing and understanding Bose-Einstein condensates. In M. Inguscio, S. S. and Wieman, C., editors, *Proceedings of the International School of Physics "Enrico Fermi"*, Course CXL, pages 67–176. IOS Press, Amsterdam.
- [Ketterle and van Druten, 1996] Ketterle, W. and van Druten, N. J. (1996). Evaporative cooling of atoms. *Advances in Atomic, Molecular, and Optical Physics*, 37:181.
- [Khramov et al., 2012] Khramov, A. Y., Hansen, A. H., Jamison, A. O., Dowd, W. H., and Gupta, S. (2012). Dynamics of Feshbach molecules in an ultracold three-component mixture. *Phys. Rev. A*, 86:032705.

- [Knoop et al., 2011] Knoop, S., Schuster, T., Scelle, R., Trautmann, A., Appmeier, J., Oberthaler, M. K., Tiesinga, E., and Tiemann, E. (2011). Feshbach spectroscopy and analysis of the interaction potentials of ultracold sodium. *Phys. Rev. A*, 83:042704.
- [Kohnen, 2008] Kohnen, M. (2008). Ultracold Fermi Mixtures in an Optical Dipole Trap. Master’s thesis, Ruprecht-Karls-Universität Heidelberg, Germany.
- [Koyama et al., 1989] Koyama, N., Takafuji, A., and Matsuzawa, M. (1989). Highly doubly excited states of H - and He II. 1 P 0 states. *Journal of Physics B: Atomic, Molecular and Optical Physics*, 22(4):553.
- [Kraemer et al., 2004] Kraemer, T., Herbig, J., Mark, M., Weber, T., Chin, C., Nägerl, H.-C., and Grimm, R. (2004). Optimized production of a cesium Bose-Einstein condensate. *Applied Physics B: Lasers and Optics*, 79:1013–1019. 10.1007/s00340-004-1657-5.
- [Kraemer et al., 2006] Kraemer, T., Mark, M., Waldburger, P., Danzl, J. G., Chin, C., Engeser, B., Lange, A. D., Pilch, K., Jaakkola, A., Nägerl, H. C., and Grimm, R. (2006). Evidence for Efimov quantum states in an ultracold gas of caesium atoms. *Nature*, 440(7082):315–318.
- [Launay and Dourneuf, 1982] Launay, J. M. and Dourneuf, M. L. (1982). Hyper-spherical description of collinear reactive scattering. *Journal of Physics B: Atomic and Molecular Physics*, 15(13):L455.
- [LeBlanc and Thywissen, 2007] LeBlanc, L. J. and Thywissen, J. H. (2007). Species-specific optical lattices. *Phys. Rev. A*, 75:053612.
- [Lee et al., 2007] Lee, M. D., Köhler, T., and Julienne, P. S. (2007). Excited Thomas-Efimov levels in ultracold gases. *Phys. Rev. A*, 76:012720.
- [Leo et al., 1998] Leo, P. J., Tiesinga, E., Julienne, P. S., Walter, D. K., Kadlec, S., and Walker, T. G. (1998). Elastic and Inelastic Collisions of Cold Spin-Polarized ^{133}Cs Atoms. *Phys. Rev. Lett.*, 81:1389–1392.
- [Leo et al., 2000] Leo, P. J., Williams, C. J., and Julienne, P. S. (2000). Collision Properties of Ultracold ^{133}Cs Atoms. *Phys. Rev. Lett.*, 85:2721–2724.
- [Li and Lin, 1999] Li, Y. and Lin, C. D. (1999). Calculations of some weakly bound diatomic molecular negative ions. *Phys. Rev. A*, 60:2009–2014.

- [Li et al., 2008] Li, Z., Singh, S., Tscherbul, T. V., and Madison, K. W. (2008). Feshbach resonances in ultracold ^{85}Rb - ^{87}Rb and ^6Li - ^{87}Rb mixtures. *Phys. Rev. A*, 78:022710.
- [Lim et al., 1977] Lim, T. K., Duffy, S. K., and Damer, W. C. (1977). Efimov State in the ^4He Trimer. *Phys. Rev. Lett.*, 38:341–343.
- [Lin, 1981] Lin, C. D. (1981). Analytical channel functions for two-electron atoms in hyperspherical coordinates. *Phys. Rev. A*, 23:1585–1590.
- [Lompe, 2011] Lompe, T. (2011). *Efimov Physics in a three-component Fermi gas*. PhD thesis, Ruprecht-Karls-Universität Heidelberg, Germany.
- [Lu et al., 2011] Lu, M., Burdick, N. Q., Youn, S. H., and Lev, B. L. (2011). Strongly Dipolar Bose-Einstein Condensate of Dysprosium. *Phys. Rev. Lett.*, 107:190401.
- [Mandl, 1988] Mandl, F. (1988). *Statistical Physics*. The Manchester Physics Series. Books on Demand.
- [Marcelis et al., 2004] Marcelis, B., van Kempen, E. G. M., Verhaar, B. J., and Kokkelmans, S. J. J. M. F. (2004). Feshbach resonances with large background scattering length: Interplay with open-channel resonances. *Phys. Rev. A*, 70:012701.
- [Marzok et al., 2009] Marzok, C., Deh, B., Zimmermann, C., Courteille, P. W., Tiemann, E., Vanne, Y. V., and Saenz, A. (2009). Feshbach resonances in an ultracold ^7Li and ^{87}Rb mixture. *Phys. Rev. A*, 79:012717.
- [McCarron et al., 2008] McCarron, D. J., King, S. A., and Cornish, S. L. (2008). Modulation transfer spectroscopy in atomic rubidium. *Measurement Science and Technology*, 19(10):105601.
- [Mehta et al., 2009] Mehta, N. P., Rittenhouse, S. T., D’Incao, J. P., von Stecher, J., and Greene, C. H. (2009). General Theoretical Description of N-Body Recombination. *Phys. Rev. Lett.*, 103:153201.
- [Merzbacher, 1998] Merzbacher, E. (1998). *Quantum Mechanics*. John Wiley & Sons Inc.
- [Metcalf and van der Straten, 1999] Metcalf, H. and van der Straten, P. (1999). *Laser Cooling and Trapping*. Graduate Texts in Contemporary Physics. Springer New York.

-
- [Mies and Raoult, 2000] Mies, F. H. and Raoult, M. (2000). Analysis of threshold effects in ultracold atomic collisions. *Phys. Rev. A*, 62:012708.
- [Mies et al., 1996] Mies, F. H., Williams, C. J., Julienne, P. S., and Krauss, M. (1996). Estimating Bounds on Collisional Relaxation Rates of Spin-Polarized ^{87}Rb Atoms at Ultracold Temperatures. *Journal of Research of the National Institute of Standards and Technology*, 101:521.
- [Moerdijk et al., 1995] Moerdijk, A. J., Verhaar, B. J., and Axelsson, A. (1995). Resonances in ultracold collisions of ^6Li , ^7Li , and ^{23}Na . *Phys. Rev. A*, 51:4852–4861.
- [Monroe et al., 1993] Monroe, C. R., Cornell, E. A., Sackett, C. A., Myatt, C. J., and Wieman, C. E. (1993). Measurement of Cs-Cs elastic scattering at $T=30\text{ }\mu\text{K}$. *Phys. Rev. Lett.*, 70:414–417.
- [Mudrich et al., 2002] Mudrich, M., Kraft, S., Singer, K., Grimm, R., Mosk, A., and Weidemüller, M. (2002). Sympathetic Cooling with Two Atomic Species in an Optical Trap. *Phys. Rev. Lett.*, 88:253001.
- [Müller, 2011] Müller, R. (2011). Towards an ultracold mixture of ^6Li and ^{133}Cs . Master’s thesis, Ruprecht-Karls-Universität Heidelberg, Germany.
- [Naidon et al., 2014] Naidon, P., Endo, S., and Ueda, M. (2014). Microscopic Origin and Universality Classes of the Efimov Three-Body Parameter. *Phys. Rev. Lett.*, 112:105301.
- [Nielsen et al., 2001] Nielsen, E., Fedorov, D., Jensen, A., and Garrido, E. (2001). The three-body problem with short-range interactions. *Physics Reports*, 347(5):373 – 459.
- [Nielsen et al., 1998] Nielsen, E., Fedorov, D. V., and Jensen, A. S. (1998). The structure of the atomic helium trimers: halos and Efimov states. *Journal of Physics B: Atomic, Molecular and Optical Physics*, 31(18):4085.
- [Nielsen and Macek, 1999] Nielsen, E. and Macek, J. H. (1999). Low-Energy Recombination of Identical Bosons by Three-Body Collisions. *Phys. Rev. Lett.*, 83:1566–1569.
- [O’Hara et al., 2002] O’Hara, K. M., Hemmer, S. L., Gehm, M. E., Granade, S. R., and Thomas, J. E. (2002). Observation of a Strongly Interacting Degenerate Fermi Gas of Atoms. *Science*, 298(5601):2179–2182.

- [Ottenstein, 2010] Ottenstein, T. B. (2010). *Few-body physics in ultracold Fermi gases*. PhD thesis, Ruprecht-Karls-Universität Heidelberg, Germany.
- [Ottenstein et al., 2008] Ottenstein, T. B., Lompe, T., Kohnen, M., Wenz, A. N., and Jochim, S. (2008). Collisional Stability of a Three-Component Degenerate Fermi Gas. *Phys. Rev. Lett.*, 101:203202.
- [Paananen et al., 2006] Paananen, T., Martikainen, J.-P., and Törmä, P. (2006). Pairing in a three-component Fermi gas. *Phys. Rev. A*, 73:053606.
- [Park et al., 2012] Park, J. W., Wu, C.-H., Santiago, I., Tiecke, T. G., Will, S., Ahmadi, P., and Zwierlein, M. W. (2012). Quantum degenerate Bose-Fermi mixture of chemically different atomic species with widely tunable interactions. *Phys. Rev. A*, 85:051602.
- [Petrov, 2013] Petrov, D. S. (2013). The Few-atom problem. In *Many-Body Physics with Ultracold Gases: Lecture Notes of the Les Houches Summer School: Volume 94, July 2010*. OUP Oxford.
- [Pinkse et al., 1997] Pinkse, P. W. H., Mosk, A., Weidemüller, M., Reynolds, M. W., Hijmans, T. W., and Walraven, J. T. M. (1997). Adiabatically Changing the Phase-Space Density of a Trapped Bose Gas. *Phys. Rev. Lett.*, 78:990–993.
- [Pires et al., 2014a] Pires, R., Repp, M., Ulmanis, J., Kuhnle, E., Weidemüller, M., Tiecke, T., Greene, C., Ruzic, B. P., Bohn, J. L., and Tiemann, E. (2014a). Analyzing Feshbach Resonances - A Li Cs Case Study. To be submitted.
- [Pires et al., 2014b] Pires, R., Ulmanis, J., Häfner, S., Repp, M., Arias, A., Kuhnle, E., and Weidemüller, M. (2014b). Observation of Efimov Resonances in a Mixture with Extreme Mass Imbalance. *arXiv preprint arXiv:1403.7246*.
- [Pitaevskii, 1961] Pitaevskii, L. P. (1961). Vortex lines in an imperfect Bose gas. *Sov. Phys. JETP*, 13:451.
- [Pollack et al., 2009] Pollack, S. E., Dries, D., and Hulet, R. G. (2009). Universality in Three- and Four-Body Bound States of Ultracold Atoms. *Science*, 326(5960):1683–1685.
- [Portegies and Kokkelmans, 2011] Portegies, J. and Kokkelmans, S. (2011). Efimov Trimers in a Harmonic Potential. *Few-Body Systems*, 51(2-4):219–234.

-
- [Raoult and Mies, 2004] Raoult, M. and Mies, F. H. (2004). Feshbach resonance in atomic binary collisions in the Wigner threshold law regime. *Phys. Rev. A*, 70:012710.
- [Rapp et al., 2008] Rapp, A., Hofstetter, W., and Zaránd, G. (2008). Trionic phase of ultracold fermions in an optical lattice: A variational study. *Phys. Rev. B*, 77:144520.
- [Rapp et al., 2007] Rapp, A., Zaránd, G., Honerkamp, C., and Hofstetter, W. (2007). Color Superfluidity and “Baryon” Formation in Ultracold Fermions. *Phys. Rev. Lett.*, 98:160405.
- [Rem et al., 2013] Rem, B. S., Grier, A. T., Ferrier-Barbut, I., Eismann, U., Langen, T., Navon, N., Khaykovich, L., Werner, F., Petrov, D. S., Chevy, F., and Salomon, C. (2013). Lifetime of the Bose Gas with Resonant Interactions. *Phys. Rev. Lett.*, 110:163202.
- [Repp, 2013] Repp, M. (2013). *Interspecies Feshbach Resonances in an Ultracold, Optically Trapped Bose-Fermi Mixture of Cesium and Lithium*. PhD thesis, Universität Heidelberg.
- [Repp et al., 2013] Repp, M., Pires, R., Ulmanis, J., Heck, R., Kuhnle, E. D., Weidemüller, M., and Tiemann, E. (2013). Observation of interspecies ${}^6\text{Li}$ - ${}^{133}\text{Cs}$ Feshbach resonances. *Phys. Rev. A*, 87:010701.
- [Repp et al., 2014] Repp, M., Pires, R., Ulmanis, J., Schmidt, S., Müller, R., Meyer, K., Heck, R., Kuhnle, E., and Weidemüller, M. (2014). A helical Zeeman slower for sequential loading of two elements with large mass difference into optical dipole traps. *Manuscript in preparation*.
- [Richard, 1992] Richard, J.-M. (1992). The nonrelativistic three-body problem for baryons. *Physics Reports*, 212(1):1 – 76.
- [Riisager, 1994] Riisager, K. (1994). Nuclear halo states. *Rev. Mod. Phys.*, 66:1105–1116.
- [Rittenhouse et al., 2010] Rittenhouse, S. T., Mehta, N. P., and Greene, C. H. (2010). Green’s functions and the adiabatic hyperspherical method. *Phys. Rev. A*, 82:022706.
- [Robicheaux, 1999] Robicheaux, F. (1999). Simple asymptotic potential model for finding weakly bound negative ions. *Phys. Rev. A*, 60:1706–1709.

- [Roy et al., 2013] Roy, S., Landini, M., Trenkwalder, A., Semeghini, G., Spagnolli, G., Simoni, A., Fattori, M., Inguscio, M., and Modugno, G. (2013). Test of the Universality of the Three-Body Efimov Parameter at Narrow Feshbach Resonances. *Phys. Rev. Lett.*, 111:053202.
- [Ruzic et al., 2013] Ruzic, B. P., Greene, C. H., and Bohn, J. L. (2013). Quantum defect theory for high-partial-wave cold collisions. *Phys. Rev. A*, 87:032706.
- [Salzmann, 2007] Salzmann, W. (2007). *Photoassociation and coherent control of ultracold molecules by femtosecond pulses*. PhD thesis, Albert-Ludwigs-Universität Freiburg, Germany.
- [Schlöder et al., 1999] Schlöder, U., Engler, H., Schünemann, U., Grimm, R., and Weidemüller, M. (1999). Cold inelastic collisions between lithium and cesium in a two-species magneto-optical trap. *The European Physical Journal D*, 7:331–340.
- [Schmidt et al., 2012] Schmidt, R., Rath, S., and Zwerger, W. (2012). Efimov physics beyond universality. *The European Physical Journal B*, 85(11):1–6.
- [Schmidt, 2011] Schmidt, S. (2011). Aufbau und Charakterisierung eines frequenzstabilisierten Diodenlasersystems zur Kühlung und Speicherung von Cs-Atomen. Master’s thesis, Ruprecht-Karls-Universität Heidelberg, Germany.
- [Schöllkopf and Toennies, 1996] Schöllkopf, W. and Toennies, J. P. (1996). The nondestructive detection of the helium dimer and trimer. *The Journal of Chemical Physics*, 104(3):1155–1158.
- [Schönhals, 2013] Schönhals, A. (2013). Imaging of ultracold Cesium atoms at high magnetic fields. Master’s thesis, University of Heidelberg.
- [Schünemann et al., 1999] Schünemann, U., Engler, H., Grimm, R., Weidemüller, M., and Zielonkowski, M. (1999). Simple scheme for tunable frequency offset locking of two lasers. *Review of Scientific Instruments*, 70(1):242–243.
- [Schuster, 2012] Schuster, T. (2012). *Feshbach Resonances and Periodic Potentials in Ultracold Bose-Fermi Mixtures*. PhD thesis, University of Heidelberg.
- [Schuster et al., 2012] Schuster, T., Scelle, R., Trautmann, A., Knoop, S., Oberthaler, M. K., Haverhals, M. M., Goosen, M. R., Kokkelmans, S. J. J. M. F., and Tiemann, E. (2012). Feshbach spectroscopy and scattering properties of ultracold Li + Na mixtures. *Phys. Rev. A*, 85:042721.

- [Schwabl, 2007] Schwabl, F. (2007). *Quantenmechanik*. Springer-Verlag.
- [Seaton, 1983] Seaton, M. J. (1983). Quantum defect theory. *Reports on Progress in Physics*, 46(2):167.
- [Söding et al., 1998] Söding, J., Guéry-Odelin, D., Desbiolles, P., Ferrari, G., and Dalibard, J. (1998). Giant Spin Relaxation of an Ultracold Cesium Gas. *Phys. Rev. Lett.*, 80:1869–1872.
- [Sørensen et al., 2012] Sørensen, P. K., Fedorov, D. V., Jensen, A. S., and Zinner, N. T. (2012). Efimov physics and the three-body parameter within a two-channel framework. *Phys. Rev. A*, 86:052516.
- [Staanum et al., 2007] Staantum, P., Pashov, A., Knöckel, H., and Tiemann, E. (2007). $X^1\Sigma^+$ and $a^3\Sigma^+$ states of LiCs studied by Fourier-transform spectroscopy. *Phys. Rev. A*, 75:042513.
- [Stamper-Kurn et al., 1998] Stamper-Kurn, D. M., Miesner, H.-J., Chikkatur, A. P., Inouye, S., Stenger, J., and Ketterle, W. (1998). Reversible Formation of a Bose-Einstein Condensate. *Phys. Rev. Lett.*, 81:2194–2197.
- [Stan and Ketterle, 2005] Stan, C. A. and Ketterle, W. (2005). Multiple species atom source for laser-cooling experiments. *Review of Scientific Instruments*, 76(6):063113.
- [Stan et al., 2004] Stan, C. A., Zwierlein, M. W., Schunck, C. H., Raupach, S. M. F., and Ketterle, W. (2004). Observation of Feshbach Resonances between Two Different Atomic Species. *Phys. Rev. Lett.*, 93:143001.
- [Steck, 2008] Steck, D. A. (2008). Cesium D Line Data. available online at [HTTP://STECK.US/ALKALIDATA](http://STECK.US/ALKALIDATA)(revision 2.0.1, 2 May 2008).
- [Stellmer et al., 2009] Stellmer, S., Tey, M. K., Huang, B., Grimm, R., and Schreck, F. (2009). Bose-Einstein Condensation of Strontium. *Phys. Rev. Lett.*, 103:200401.
- [Stoof et al., 1988] Stoof, H. T. C., Koelman, J. M. V. A., and Verhaar, B. J. (1988). Spin-exchange and dipole relaxation rates in atomic hydrogen: Rigorous and simplified calculations. *Phys. Rev. B*, 38:4688–4697.
- [Strauss et al., 2010] Strauss, C., Takekoshi, T., Lang, F., Winkler, K., Grimm, R., Hecker Denschlag, J., and Tiemann, E. (2010). Hyperfine, rotational, and vibrational structure of the $a^3\Sigma_u^+$ state of $^{87}\text{Rb}_2$. *Phys. Rev. A*, 82:052514.

- [Stuhler et al., 2007] Stuhler, J., Griesmaier, A., Werner, J., Koch, T., Fattori, M., and Pfau, T. (2007). Ultracold chromium atoms: from Feshbach resonances to a dipolar Bose–Einstein condensate. *Journal of Modern Optics*, 54(5):647–660.
- [Stwalley, 1976] Stwalley, W. C. (1976). Stability of Spin-Aligned Hydrogen at Low Temperatures and High Magnetic Fields: New Field-Dependent Scattering Resonances and Predissociations. *Phys. Rev. Lett.*, 37:1628–1631.
- [Tang et al., 1995] Tang, K. T., Toennies, J. P., and Yiu, C. L. (1995). Accurate Analytical He-He van der Waals Potential Based on Perturbation Theory. *Phys. Rev. Lett.*, 74:1546–1549.
- [Tanihata, 1996] Tanihata, I. (1996). Neutron halo nuclei. *Journal of Physics G: Nuclear and Particle Physics*, 22(2):157.
- [Taylor, 1972] Taylor, J. R. (1972). *Scattering Theory: The Quantum Theory On Nonrelativistic Collisions*. Wiley, New York.
- [Tempere et al., 2009] Tempere, J., Casteels, W., Oberthaler, M. K., Knoop, S., Timmermans, E., and Devreese, J. T. (2009). Feynman path-integral treatment of the BEC-impurity polaron. *Phys. Rev. B*, 80:184504.
- [Thomas, 1935] Thomas, L. H. (1935). The Interaction Between a Neutron and a Proton and the Structure of H^3 . *Phys. Rev.*, 47:903–909.
- [Tiecke et al., 2010] Tiecke, T. G., Goosen, M. R., Walraven, J. T. M., and Kokkelmans, S. J. J. M. F. (2010). Asymptotic-bound-state model for Feshbach resonances. *Phys. Rev. A*, 82:042712.
- [Tiesinga et al., 1993] Tiesinga, E., Verhaar, B. J., and Stoof, H. T. C. (1993). Threshold and resonance phenomena in ultracold ground-state collisions. *Phys. Rev. A*, 47:4114–4122.
- [Tiesinga et al., 1998] Tiesinga, E., Williams, C. J., and Julienne, P. S. (1998). Photoassociative spectroscopy of highly excited vibrational levels of alkali-metal dimers: Green-function approach for eigenvalue solvers. *Phys. Rev. A*, 57:4257–4267.
- [Treutlein et al., 2001] Treutlein, P., Chung, K. Y., and Chu, S. (2001). High-brightness atom source for atomic fountains. *Phys. Rev. A*, 63:051401.

-
- [Tscherbul et al., 2010] Tscherbul, T. V., Calarco, T., Lesanovsky, I., Krems, R. V., Dalgarno, A., and Schmiedmayer, J. (2010). rf-field-induced Feshbach resonances. *Phys. Rev. A*, 81:050701.
- [Tung et al., 2014] Tung, S.-K., Jimenez-Garcia, K., Johansen, J., Parker, C. V., and Chin, C. (2014). Observation of geometric scaling of Efimov states in a Fermi-Bose Li-Cs mixture. *arXiv preprint arXiv:1402.5943*.
- [Tung et al., 2013] Tung, S.-K., Parker, C., Johansen, J., Chin, C., Wang, Y., and Julienne, P. S. (2013). Ultracold mixtures of atomic ^6Li and ^{133}Cs with tunable interactions. *Phys. Rev. A*, 87:010702.
- [v. Kempen et al., 2004] v. Kempen, E. G. M., Marcelis, B., and Kokkelmans, S. J. J. M. F. (2004). Formation of fermionic molecules via interisotope Feshbach resonances. *Phys. Rev. A*, 70:050701.
- [Verhaar et al., 2009] Verhaar, B. J., van Kempen, E. G. M., and Kokkelmans, S. J. J. M. F. (2009). Predicting scattering properties of ultracold atoms: Adiabatic accumulated phase method and mass scaling. *Phys. Rev. A*, 79:032711.
- [Voigt et al., 2009] Voigt, A.-C., Taglieber, M., Costa, L., Aoki, T., Wieser, W., Hänsch, T. W., and Dieckmann, K. (2009). Ultracold Heteronuclear Fermi-Fermi Molecules. *Phys. Rev. Lett.*, 102:020405.
- [von Stecher, 2010] von Stecher, J. (2010). Weakly bound cluster states of Efimov character. *Journal of Physics B: Atomic, Molecular and Optical Physics*, 43(10):101002.
- [von Stecher et al., 2009] von Stecher, J., D’Incao, J. P., and Greene, C. H. (2009). Signatures of universal four-body phenomena and their relation to the Efimov effect. *Nature Physics*, 5(6):417–421.
- [von Stecher and Greene, 2009] von Stecher, J. and Greene, C. H. (2009). Correlated Gaussian hyperspherical method for few-body systems. *Phys. Rev. A*, 80:022504.
- [Wang et al., 2014] Wang, J., D’Incao, J., and Greene, C. (2014). Private Communication.
- [Wang et al., 2012a] Wang, J., D’Incao, J. P., Esry, B. D., and Greene, C. H. (2012a). Origin of the Three-Body Parameter Universality in Efimov Physics. *Phys. Rev. Lett.*, 108:263001.

- [Wang et al., 2013] Wang, Y., D’Incao, J. P., and Esry, B. D. (2013). Chapter 1 - Ultracold Few-Body Systems. In Ennio Arimondo, P. R. B. and Lin, C. C., editors, *Advances in Atomic, Molecular, and Optical Physics*, volume 62 of *Advances In Atomic, Molecular, and Optical Physics*, pages 1 – 115. Academic Press.
- [Wang et al., 2012b] Wang, Y., Wang, J., D’Incao, J. P., and Greene, C. H. (2012b). Universal Three-Body Parameter in Heteronuclear Atomic Systems. *Phys. Rev. Lett.*, 109:243201.
- [Weber et al., 2003a] Weber, T., Herbig, J., Mark, M., Nägerl, H.-C., and Grimm, R. (2003a). Three-Body Recombination at Large Scattering Lengths in an Ultracold Atomic Gas. *Phys. Rev. Lett.*, 91:123201.
- [Weber et al., 2003b] Weber, T., Herbig, J., Mark, M., Nägerl, H.-C., and Grimm, R. (2003b). Bose-Einstein Condensation of Cesium. *Science*, 299(5604):232–235.
- [Weiner et al., 1999] Weiner, J., Bagnato, V. S., Zilio, S., and Julienne, P. S. (1999). Experiments and theory in cold and ultracold collisions. *Rev. Mod. Phys.*, 71:1–85.
- [Wenz et al., 2013] Wenz, A. N., Zürn, G., Murmann, S., Brouzos, I., Lompe, T., and Jochim, S. (2013). From Few to Many: Observing the Formation of a Fermi Sea One Atom at a Time. *Science*, 342(6157):457–460.
- [Wild et al., 2012] Wild, R. J., Makotyn, P., Pino, J. M., Cornell, E. A., and Jin, D. S. (2012). Measurements of Tan’s Contact in an Atomic Bose-Einstein Condensate. *Phys. Rev. Lett.*, 108:145305.
- [Wille et al., 2008] Wille, E., Spiegelhalder, F. M., Kerner, G., Naik, D., Trenkwalder, A., Hendl, G., Schreck, F., Grimm, R., Tiecke, T. G., Walraven, J. T. M., Kokkelmans, S. J. J. M. F., Tiesinga, E., and Julienne, P. S. (2008). Exploring an Ultracold Fermi-Fermi Mixture: Interspecies Feshbach Resonances and Scattering Properties of ^6Li and ^{40}K . *Phys. Rev. Lett.*, 100:053201.
- [Williams et al., 2009] Williams, J. R., Hazlett, E. L., Huckans, J. H., Stites, R. W., Zhang, Y., and O’Hara, K. M. (2009). Evidence for an Excited-State Efimov Trimer in a Three-Component Fermi Gas. *Phys. Rev. Lett.*, 103:130404.
- [Yamazaki, 1999] Yamazaki, T. (1999). An Exotic Three-Body System - Antiprotonic Helium Atomcules. In Desplanques, B., Protasov, K., Silvestre-Brac, B., and Carbonell, J., editors, *Few-Body Problems in Physics ’98*, volume 10 of *Few-Body Systems*, pages 151–160. Springer Vienna.

- [Yuan and Lin, 1998] Yuan, J. and Lin, C. D. (1998). Weakly bound triatomic He 2 Li and He 2 Na molecules. *Journal of Physics B: Atomic, Molecular and Optical Physics*, 31(15):L637.
- [Zaccanti et al., 2009] Zaccanti, M., Deissler, B., D’Errico, C., Fattori, M., Jonas-Lasinio, M., Müller, S., Roati, G., Inguscio, M., and Modugno, G. (2009). Observation of an Efimov spectrum in an atomic system. *Nature Physics*, 5(8):586–591.
- [Zhai, 2007] Zhai, H. (2007). Superfluidity in three-species mixtures of Fermi gases across Feshbach resonances. *Phys. Rev. A*, 75:031603.
- [Zhou et al., 1993] Zhou, Y., Lin, C. D., and Shertzer, J. (1993). Hyperspherical approach to Coulombic three-body systems with different masses. *Journal of Physics B: Atomic, Molecular and Optical Physics*, 26(21):3937.
- [Zhukov et al., 1993] Zhukov, M., Danilin, B., Fedorov, D., Bang, J., Thompson, I., and Vaagen, J. (1993). Bound state properties of Borromean halo nuclei: ^6He and ^{11}Li . *Physics Reports*, 231(4):151 – 199.
- [Zinner and Jensen, 2013] Zinner, N. T. and Jensen, A. S. (2013). Comparing and contrasting nuclei and cold atomic gases. *Journal of Physics G: Nuclear and Particle Physics*, 40(5):053101.
- [Zürn et al., 2012] Zürn, G., Lompe, T., Wenz, A. N., Jochim, S., Julienne, P. S., and Hutson, J. M. (2012). Precise characterization of ^6Li Feshbach resonances using trap-sideband resolved RF spectroscopy of weakly bound molecules.

Acknowledgements

This thesis is a product of a great team effort, involving a large number of people without whom it would not have been possible to succeed. It is impossible to explicitly thank every individual who has directly or indirectly contributed to my work in Heidelberg, but in this section I would like to express gratitude to at least some of the people who have supported me.

First and foremost I would like to thank you, **Prof. Dr. Matthias Weidelmüller** for giving me the opportunity to complete my PhD in your group, and trusting me with the new Li-Cs experiment. While showing great organizational talent and an excellent intuition for the direction of our research, you also gave me enough freedom to grow as a scientist. I also thank you for teaching skills that go beyond physics. Your way of approaching difficult or complex question in a very structured and analytic way will surely prove helpful in other areas of life, as well.

I would like to thank **Prof. Dr. Selim Jochim** for being my thesis examiner and advisor. You provided excellent help in all sorts of questions, and had a fitting answer for any of our problems. I'm also grateful that you took the time to 'pimp' our imaging system.

Prof. Dr. Chris Greene for taking the time to be on my thesis committee, and also for an extreme amount of scientific (and personal) exchange. You took the time to answer many of my questions regarding two- and three-body physics, and I learned a lot from you in this field.

Prof. Dr. Peter Bachert for being a part of my thesis committee, and for several excellent tutorials in the early stages of my student life.

Next I would like to acknowledge the Mixtures team for the outstanding team effort, especially in the 'crunch time' of the Efimov project. Thank you **Dr. Marc (le) Repp** for the whole planing of the experiment, and also for its implementation. Even though we didn't quite keep the time line for the creation of a Cs BEC in our first Gantt diagram, we were only behind a few years. Those years have been great fun, both in and out of the laboratory. Your Zeeman 'Slauer' a.k.a zebra

leg is an excellent loading source, and together with the vacuum system (I will not mention the 'all-metal valves' here) essential for the success of the experiment. **Juris Ulmanis**, you were the perfect addition to the mixtures team. With your strict JUTÜV, you helped us optimize all the technical details. Especially the experiment control was crucial. I think you implemented our dictum 'just make no mistakes' excellently, and I could learn a lot from your technical expertise. **Dr. Eva Kuhnle**, I also thank you for taking the lead on the project, and taking some of the load off our backs. Besides working in the lab, you also handled much of the organizational part of the work, for which I am very grateful. Thanks to you, I also felt perfectly safe in the institute, knowing that a distinct karate fighter is standing in harms way. **Stephan Häfner**, you started the PhD right on time for the rush hour of the Efimov results. Thank you for staying late in the Institute many nights in order to get the Efimov paper done. I hope you will have a lot of fun with the setup in the future. **Alda Arias**, I appreciate the great work on the reservoir trap, and the excellent Colombian breakfasts. I am not a 'Memme'!!! I am also obligated to the other people who worked on the project, namely **Carmen Renner** for the imaging system, **Stefan Schmidt** and **Romain Müller** for setting up the MOT lasers, **Stefan Arnold** for the setup of the Feshbach coils, **Robert Heck** for the ^6Li dipole trap, **Kristina Meyer** for the first generation reservoir trap, **Thomas Kirchner** for getting started on the magic wavelength trap, **Arthur Schönhals** for the high-field imaging, **Jian-Pei Ang** for writing the ABM code and **Andy McCulloch**, **Silvania Alves de Carvalho** and **Rodrigo Figueredo Shiozaki** for visiting and helping in the lab. Also **Dr. Johannes Deiglmayr** has been very helpful in the beginning stages of the experiment, especially with his binding energy calculations.

Prof. Dr. E. Tiemann for an excellent collaboration and also taking the time to teach me a great deal of molecular theory over the phone and in person. **Dr. Tobias Tiecke**, without whom I would know only half as much about the ABM, thanks for explaining things over many interesting skype sessions. **Prof. Dr. John Bohn** and **Brandon Ruzic** for the MQDT calculations and many great discussions.

Gratitude also to the members of the Rydberg experiments. Especially in the beginning stages of both experiments the exchange was very helpful. **Dr. Thomas Amthor**, **Dr. Christoph Hofmann**, **Dr. Georg Günter**, **Hanna Schempp**, **Dr. Martin Robert-de-Saint-Vincent**, **Nele Müller** and the rest of the team have been great co-workers, both inside and outside the institute. I wish all the best to the new generation of Rydbergers.

It has also been great fun working with the MOTRIMS team, around **Bastian**

Höltkemeier, Henry Lopez, Pascal Weckesser, Julian Glässel and the other members.

I would like to show courtesy to **Dominic Litsch** for the technical help with our lasers, and to **Claudia Krämer** for the excellent organizational work.

Dr. Shannon Whitlock, thanks for taking the time to also help us with some of the experimental problems. Good luck with your experiments to you and your group! Also good luck to the Strontium team with the experiments in China. All of the people who have been in the QD-group, I thank you for the great atmosphere.

The Jochim group around **Dr. Gerhard Zürn, Dr. Thomas Lompe, Dr. Andre Wenz, Martin Ries** and all the other members I am grateful for the help on the ^6Li system, for sharing many of their technological inventions (except for the Hip4081 module) and for many interesting and helpful discussions.

Also the group around **Prof. Dr. Markus Oberthaler**, for many fruitful discussions. Especially **Dr. Tobias Schuster** and **Dr. Steven Knoop** for the collaboration on the ABM model. **Dr. Raphael Scelle** for the interesting exchange, and **Ion Stroescu** for the joint leadership in the IMPRS-QD.

The realization of many technical aspects has only been possible because of the great work of the technical staff. Thanks to the members of the **mechanical workshop**, lead by **Ralf Ziegler**, for the excellent collaboration. You managed to get all the components done exactly to our desires, even when the technical drawings I gave you were not perfect. Among others, **Simon Rabenecker, Thomas Fießer, Oliver Hornberger** and **Maximilian von Klot** have been very helpful with some of the required components. I also thank the **construction team** around **Dr. Windelband, Jürgen Gerhäuser, Stefan Hetzel** and **Kevin Stumpf** for help in many of the developments. The **electronic workshop** around **Dr. Venelin Angelov** and **Peter von Walter** has been extremely helpful. **Klaus Layer** it has always been fun visiting you, thanks for giving me one of your desks as my own working space. **Niklas Lehr, Nicole Kupfer** and **Frank Schumacher**, thank you for assembling, repairing, designing and helping with many of the components in my experiment. I would also like to thank the **EDV team** for the IT help.

We also have many friends in physics outside of the Heidelberg city lines. I would like to thank the team around **Prof. Dr. Rudolf Grimm** for the help on the ^{133}Cs setup, and many interesting discussions regarding coils, Feshbach resonances and Efimov resonances. Especially **Dr. Francesca Ferlaino, Dr. Alessandro Zenesini, Dr. Martin Berninger** and **Bo Huang** should be mentioned in this context. **Dr. Jose D’Incao, Dr. Jia Wang, Prof. Dr. P. Julienne** and **Dr. Yujun Wang**, I am very thankful for your help and your calculations regarding the Efimov re-

sonances we found. Especially **Jose D’Incao** was able to answer many questions that came up during our investigation of Efimov resonances. Thanks also to **Prof. Dr. Christophe Salomon**, **Prof. Dr. Licoln Carr** and **Dr. Nikolaj Zinner** for interesting and fruitful discussions regarding Efimov and molecular physics.

I appreciate the invitation to Brazil from **Prof. Dr. Vanderlei Bagnato**. I also had a lot of fun in your group, both inside and outside the physics building. Your yearly party and the summer school both were legendary, and if I ever start drinking beer, I will definitely try the one from your brewery. I also thank **Prof. Dr. Philippe Courteille** and his team for the great time in Brazil.

The time at UCONN in the group of **Prof. Dr. Phil Gould** has shaped me as a physicist, and I learned a lot from **Marco Ascoli** and **Prof. Dr. Edward Eyler**.

I am grateful to the **IMPRS-QD** and the **HGSFP** for providing a stipend, financial travel support, excellent teaching events, seminars and symposia and for making the University of Heidelberg such an excellent environment for studying.

I am obliged to **Tillmann Lang** for career advise, as well as **Ines Filz** and the **McKinsey recruiting team** for many interesting and fun events that allowed for some distraction from physics.

Thanks to all my friends who have been there for me and sometimes steered my attention away from physics, which is also necessary from time to time. I will not list all the names, but I think you know who you are.

I also would like to show my appreciation to my family. My Siblings **Rosario**, **Romeo**, **Rio**, **Julia**, **Ramon** and my niece **Ansuela**, as well as my parents **Rio** and **Julia**, thanks for helping and supporting me in all possible kind of ways. The same holds for my second family, **Gerhard**, **Anke**, **Caro** and **Janis**. I am thankful I could live and be so close to you, especially in the beginning of my student life. Not to forget my other brothers from other mothers, **Kevin Burleson** and **Geoffrey Person**, it’s great how after years or months of not seeing each other, everything is just as if we have been hanging out all along.

Last but not least I want to thank my girlfriend **Nora-Anissa Méliani**, who has been by my side during my entire master’s and PhD studies. Thanks for the strength, support and love during these awesome seven years.